

ACCEPTED MANUSCRIPT • OPEN ACCESS

Pushing the boundaries of lithium battery research with atomistic modelling on different scales

To cite this article before publication: Lucy Morgan *et al* 2021 *Prog. Energy* in press <https://doi.org/10.1088/2516-1083/ac3894>

Manuscript version: Accepted Manuscript

Accepted Manuscript is “the version of the article accepted for publication including all changes made as a result of the peer review process, and which may also include the addition to the article by IOP Publishing of a header, an article ID, a cover sheet and/or an ‘Accepted Manuscript’ watermark, but excluding any other editing, typesetting or other changes made by IOP Publishing and/or its licensors”

This Accepted Manuscript is © 2021 The Author(s). Published by IOP Publishing Ltd..

As the Version of Record of this article is going to be / has been published on a gold open access basis under a CC BY 3.0 licence, this Accepted Manuscript is available for reuse under a CC BY 3.0 licence immediately.

Everyone is permitted to use all or part of the original content in this article, provided that they adhere to all the terms of the licence <https://creativecommons.org/licenses/by/3.0>

Although reasonable endeavours have been taken to obtain all necessary permissions from third parties to include their copyrighted content within this article, their full citation and copyright line may not be present in this Accepted Manuscript version. Before using any content from this article, please refer to the Version of Record on IOPscience once published for full citation and copyright details, as permissions may be required. All third party content is fully copyright protected and is not published on a gold open access basis under a CC BY licence, unless that is specifically stated in the figure caption in the Version of Record.

View the [article online](#) for updates and enhancements.

Pushing the boundaries of lithium battery research with atomistic modelling on different scales

Lucy M. Morgan,^{†,‡,¶} Michael P. Mercer,^{†,§,¶} Arihant Bhandari,^{||,¶} Chao Peng,^{⊥,¶} Mazharul M. Islam,^{‡,¶} Hui Yang,^{#,¶} Julian Holland,^{||,¶} Samuel W. Coles,^{‡,¶} Ryan Sharpe,[‡] Aron Walsh,^{#,Ⓜ,¶} Benjamin J. Morgan,^{‡,¶} Denis Kramer,^{⊥,△,¶} M. Saiful Islam,^{‡,¶} Harry E. Hoster,^{§,¶} Jacqueline Sophie Edge,^{*,∇,¶} and Chris-Kriton Skylaris^{*,||,¶}

[†]*The two authors contributed equally to this review.*

[‡]*Department of Chemistry, University of Bath, Claverton Down, Bath BA2 7AY, UK*

[¶]*The Faraday Institution, Quad One, Harwell Campus, Didcot, OX11 0RA, UK*

[§]*Department of Chemistry, Lancaster University, Bailrigg, Lancaster, LA1 4YB, UK*

^{||}*School of Chemistry, University of Southampton, Southampton SO17 1BJ, UK*

[⊥]*School of Engineering, University of Southampton, Southampton SO17 1BJ, UK*

[#]*Department of Materials, Imperial College London, London SW7 2AZ, UK*

[Ⓜ]*Department of Materials Science and Engineering, Yonsei University, Seoul 03722, Korea*

[△]*Faculty of Mechanical Engineering, Helmut-Schmidt University, Holstenhofweg 85, 22043 Hamburg, Germany*

[∇]*Department of Mechanical Engineering, Imperial College London, London, SW7 2AZ, UK*

E-mail: j.edge@imperial.ac.uk; c.skylaris@soton.ac.uk

Abstract

Computational modelling is a vital tool in the research of batteries and their component materials. Atomistic models are key to building truly physics-based models of batteries and form the foundation of the multiscale modelling chain, leading to more robust and predictive models. These models can be applied to fundamental research questions with high predictive accuracy. For example, they can be used to predict new behaviour not currently accessible by experiment, for reasons of cost, safety, or throughput. Atomistic models are useful for quantifying and evaluating trends in experimental data, explaining structure-property relationships, and informing materials design strategies and libraries. In this review, we showcase the most prominent atomistic modelling methods and their application to electrode materials, liquid and solid electrolyte materials, and their interfaces, highlighting the diverse range of battery properties that can be investigated. Furthermore, we link atomistic modelling to experimental data and higher scale models such as continuum and control models. We also provide a critical discussion on the outlook of these materials and the main challenges for future battery research.

Contents

19	1 Introduction	6
20	2 Methods	14
21	2.1 Method overview	14
22	2.1.1 Density Functional Theory	14
23	2.1.2 Linear-Scaling DFT	17
24	2.1.3 Nudged Elastic Band	20
25	2.1.4 Cluster expansion	21
26	2.1.5 Lattice gas and Monte Carlo	23
27	2.1.6 Molecular Dynamics	25
28	2.2 Method Development	28
29	2.2.1 Continuum models of electrolyte solutions within Density Functional	
30	Theory	28
31	2.2.2 Fitting Potentials for Classical Molecular Dynamics	32
32	2.3 Calculating observable properties	34
33	2.3.1 Equilibrium voltage	34
34	2.3.2 Activity coefficients of electrolytes	37
35	2.3.3 Diffusion coefficients	37
36	2.3.4 Vibrational and Thermal Properties	40
37	3 Anodes	41
38	3.1 Introduction	41
39	3.2 Bulk Properties	43
40	3.2.1 Graphite structure and Li-graphite stages	43
41	3.2.2 Equilibrium potential and measured open circuit voltage	44
42	3.2.3 Entropy	49
43	3.2.4 Ion diffusion in Li-GIC	53

44	3.3	Graphite Surfaces and Interfaces	56
45	3.3.1	Possible graphite surfaces and their stability	56
46	3.3.2	Surface Effect on Intercalation Energy	57
47	3.3.3	The Surface Effect on Li Diffusion	60
48	3.3.4	Li deposition on graphite anodes	63
49	3.3.5	Solid-Electrolyte Interphase	64
50	3.4	C/Si composites	67
51	3.5	Outlook and challenges for anodes	69
52	4	Electrolytes	72
53	4.1	Introduction	72
54	4.2	Liquid Electrolytes	76
55	4.2.1	Introduction to liquid electrolyte materials	76
56	4.2.2	An introduction to modelling liquid electrolytes	77
57	4.2.3	<i>Ab initio</i> modelling of liquid electrolytes	78
58	4.2.4	Classical modelling of liquid electrolytes	81
59	4.2.5	Bulk Structure and Landscaping	83
60	4.2.6	Li-ion Diffusion	85
61	4.2.7	Solvation Energies	88
62	4.2.8	Activity coefficients of electrolytes	90
63	4.2.9	Interfacial Nanostructure of Electrolytes	90
64	4.2.10	Outlook and challenges	93
65	4.3	Solid Electrolytes	96
66	4.3.1	Introduction	96
67	4.3.2	Sulfides	99
68	4.3.3	Oxides	103
69	4.3.4	Interface stability	108
70	4.3.5	Outlook and challenges	113

1		
2		
3		
4	71	5 Cathodes 115
5	72	5.1 Introduction 115
6		
7	73	5.2 Bulk Properties 118
8		
9	74	5.2.1 Crystal Structure and Micro-Structure 118
10		
11	75	5.2.2 Lithium-ion Diffusion 120
12		
13	76	5.2.3 Redox and Electronic Properties 124
14		
15	77	5.2.4 TM Ordering in NMC Layered Oxides 127
16		
17	78	5.2.5 Vibrational and Thermal Properties 128
18		
19	79	5.3 Surfaces 129
20		
21	80	5.4 Interfaces 134
22		
23	81	5.5 Outlook and challenges for cathodes 135
24		
25		
26	82	6 Outlook 138
27		
28		
29	83	Acknowledgement 142
30		
31		
32	84	References 142
33		
34		
35		
36		
37		
38		
39		
40		
41		
42		
43		
44		
45		
46		
47		
48		
49		
50		
51		
52		
53		
54		
55		
56		
57		
58		
59		
60		

1 Introduction

Lithium-ion (Li-ion) batteries (LiBs) were first commercialised by Sony in 1991.¹ They are ubiquitous in portable electronic devices, are emerging in hybrid and all-electric vehicles,² and are starting to play a role in large scale stationary storage.³ Despite over 30 years of commercialisation and longer for development, not all factors dictating their capacity, performance, safety, and longevity are completely understood. The complexity of battery systems makes it time consuming and impractical to directly measure all of their physical attributes. The grand challenge is to construct a multiscale model, incorporating inputs across length- and time scales that can not only describe, but also predict, changes in behaviour.

To build a truly predictive modelling framework, a physical underpinning to battery models is required, incorporating physically correct descriptions of thermodynamic and kinetic battery behaviour. With sufficient accuracy built in, these models can provide insights on difficult-to-measure internal states, such as degree of Li intercalation and local electrolyte and ionic concentrations, as determined by the nanostructure of the materials used. By contrast, empirical models, which fit a curve to experimental data, are widely used in battery research, but have only a limited physical basis or, in some cases, no physical basis at all. For example, equivalent circuit models, which are widely used in industry, cannot be relied upon to predict battery behaviour over several charge-discharge cycles.

Physics-based continuum models attempt to describe the behaviour of whole cells, for example the widely used Doyle-Fuller-Newman (DFN) model.⁴⁻⁸ These models need to use drastic simplifications to enable them to run in real time, but their accuracy can be greatly improved by adopting parameters measured using more detailed, microscopic simulations. Atomistic models are key to building truly physics-based models and form the foundation of the multiscale modelling chain, leading to more robust and predictive models.

Atomistic models can also be applied to fundamental research questions with high predictive accuracy. For example, they can be used to predict new behaviour not currently accessible by experiment, for reasons of cost, safety, or throughput. They can be used to op-

1
2
3 112 timise experimental design and use resources more efficiently, determining whether particular
4
5 113 experiments are even worth performing and also provide unique insights into the behaviour
6
7 114 of materials that may not even be accessible, or are impractical to obtain, by experimental
8
9 115 probes. Atomistic models are useful for quantifying and evaluating trends in experimental
10
11 116 data, explaining structure-property relationships and informing materials design strategies
12
13 117 and libraries.

14
15 118 With the above in mind, we target this review to the following audiences. Non-atomistic
16
17 119 battery modellers, such as continuum and control modellers, who would benefit from an eas-
18
19 120 ily accessible summary of atomistic methods and how they connect with longer length scale
20
21 121 models. As atomistic models comprise a range of methods, it is also beneficial to summarise
22
23 122 how these interlink, since it is possible to be an expert in one area, whilst being unfamil-
24
25 123 iar with another. For this reason, it is instructive to summarise these different methods in
26
27 124 one place, so that non-specialists can understand these links. Recent developments in these
28
29 125 techniques, such as linear scaling Density Functional Theory (DFT), require summarising
30
31 126 standard DFT techniques. Likewise, longer length scale atomistic techniques can be parame-
32
33 127 terised using *ab initio* data. While DFT and other atomistic methods are widely known and
34
35 128 utilised individually, their other applications and connections to one another are often not
36
37 129 as thoroughly described, nor do these descriptions account for more recent developments.

38
39 130 This review also aims to reach those working in the battery area, such as experimental-
40
41 131 ists, who may not be experts in atomistic modelling and want to understand how atomistic
42
43 132 models can help to understand experimental behaviour. Likewise, we show examples of
44
45 133 behaviour currently out of reach with experiments. Similarly, this review is of benefit to
46
47 134 junior researchers new to the battery area, and those who are already familiar with atom-
48
49 135 istic methods but are new to lithium batteries. With these audiences in mind, we have
50
51 136 summarised applications of atomistic methods in lithium-ion batteries and all solid-state
52
53 137 batteries (ASSBs), which represent the most technologically advanced rechargeable battery
54
55 138 systems currently available.

1
2
3
4 139 The family of atomistic models itself represents a range of different length- and time
5
6 140 scales, from the level of electronic structure calculations through conventional and linear-
7
8 141 scaling DFT, to *ab initio* Molecular dynamics (MD) and on to longer length scale models,
9
10 142 such as classical MD, Monte Carlo (MC), and kinetic Monte Carlo (kMC) calculations, which
11
12 143 are parameterised by force field potentials or *ab initio* data. These techniques, along with re-
13
14 144 cent method developments and battery-specific observable properties, are summarised in the
15
16 145 methods section of this review, section 2.1. Specific applications to anodes, liquid and solid
17
18 146 electrolytes, and cathodes are broken down in the following sections. Links between different
19
20 147 methodologies are emphasised and this review may thus be of particular interest to those
21
22 148 looking, for example, to link DFT calculations to MC calculations, or apply linear-scaling
23
24 149 DFT to MD, bridging possible gaps in nomenclature at different length scales. Atomistic
25
26 150 models linking to *ab initio* calculations are summarised by Van der Ven et al.;⁹ also note-
27
28 151 worthy in this area is a review by Shi et al.,¹⁰ and an older review by Franco.¹¹ A recent
29
30 152 review of method development in the area of hybrid quantum-continuum solvation models
31
32 153 is presented by Herbert.¹²

33 154 The review covers mechanisms in both the conventional liquid electrolyte based and solid-
34
35 155 state based LiB, as shown schematically in Figure 1. In a single cell of a conventional LiB,
36
37 156 as shown here, the anode, or negative electrode, comprises a copper current collector and the
38
39 157 primary active material is graphite in the vast majority of commercial LiBs. Increasingly,
40
41 158 small amounts of silicon are being added to boost the gravimetric capacity. The electrode
42
43 159 material also comprises a binder, such as polyvinylidene fluoride (PVDF), and sometimes
44
45 160 a small fraction of conductive carbon is added to boost conductivity. The two electrodes
46
47 161 are divided by a separator soaked in an organic electrolyte, which is usually a mixture
48
49 162 of carbonates with dissolved LiPF₆ salt. The cathode, or the positive electrode, has an
50
51 163 aluminium current collector. Various different types of cathode material are utilised in
52
53 164 commercial LiBs, with the example shown here being the classic “rocking-chair” battery with
54
55 165 a LiCO₂ cathode.¹³ The low conductivity of these transition metal oxides requires addition
56
57
58
59
60

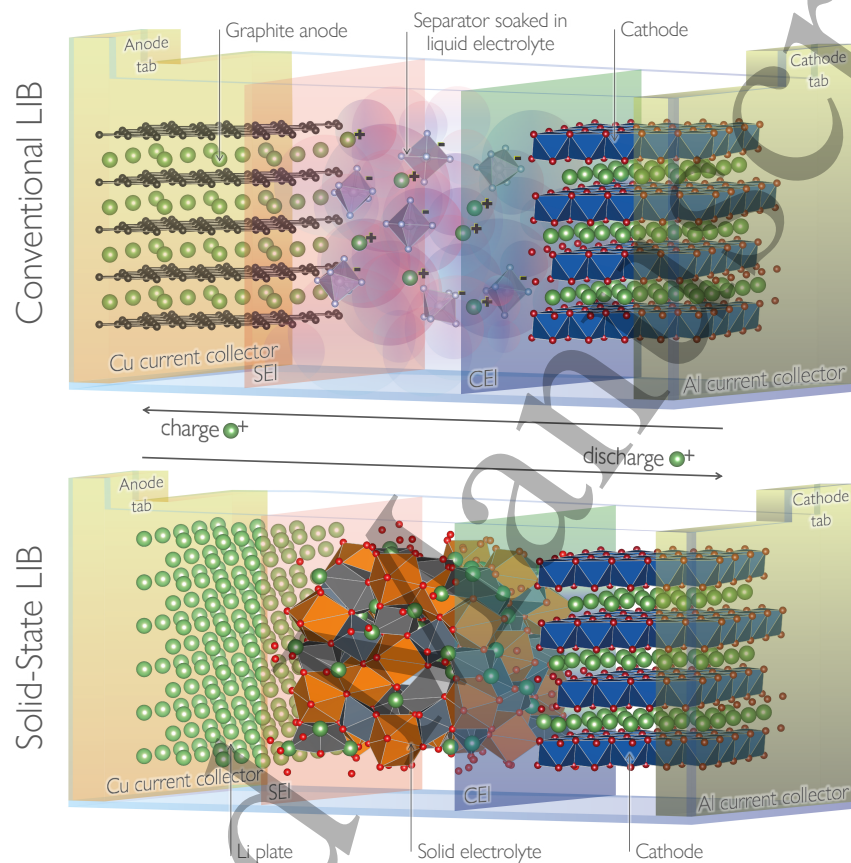


Figure 1: A schematic of a single cell of a conventional, liquid-based lithium-ion battery (LiB) and a solid-state LiB. The conventional LiB comprises an anode composed of a Cu current collector and an active anode material (graphite), a separator soaked in an organic electrolyte, and a cathode composed of a Al current collector and an active cathode material, for example, LiCo_2 , as shown here. The solid-state LiB comprises a similar cathode, a solid electrolyte, and an anode composed of a Li-ion plate and Cu current collector. The anode-electrolyte interphase (SEI) and cathode-electrolyte interphase (CEI) for both LiBs are represented as pink and blue transparent layers, respectively. The tabs are shown protruding from the top of the current collectors. Both LiB cells show all components as fully lithiated, with directional Li^+ movement during (dis)charge indicated with arrows.

1
2
3 166 of conductive carbon and, as with the anode material, the active cathode material is held
4
5 167 together with a binder, such as PVDF. When the cell is assembled, the cathode starts fully
6
7 168 lithiated and the anode is completely delithiated. On the first cell charge cycle (also known
8
9 169 as the formation cycle) lithium is removed from the cathode and the anode becomes filled
10
11 170 with lithium while the solid electrolyte interphase (SEI) and cathode electrolyte interphase
12
13 171 (CEI) are formed. While Figure 1 shows both electrodes in a fully lithiated state, Li is
14
15 172 transferred between the electrodes reversibly during (dis)charging, therefore allowing this
16
17 173 system to be rechargeable.

18
19 174 Although not yet commercialised, ASSBs are a promising future alternative to conven-
20
21 175 tional liquid electrolyte LiBs. Their anode, or negative electrode, comprises a copper current
22
23 176 collector and either a metallic lithium plate (Li-metal), as shown in Figure 1, or less com-
24
25 177 monly a graphite-based material (Li-ion). As there is no liquid, there is no longer a need
26
27 178 for separators, with the two electrodes being separated by the solid electrolyte material,
28
29 179 shown here with $\text{Li}_7\text{La}_3\text{Zr}_2\text{O}_{12}$ (LLZO). The cathode, or positive electrode, has an aluminium
30
31 180 current collector and, as with the conventional LiB, can accommodate various cathode mate-
32
33 181 rials, such as LiCoO_2 . The interfacial regions between the electrodes and the solid electrolyte
34
35 182 are known as the solid-solid interphase, or anode/cathode-solid interphase. Figure 1 shows
36
37 183 both electrodes in a fully lithiated state; however, the Li is transferred between the electrodes
38
39 184 reversibly, as in conventional LiBs.

40
41 185 The anodes section, section 3, heavily focuses on graphite, which is still the predominant
42
43 186 anode material in Li-ion cells. The section describes atomistic modelling of bulk graphite,
44
45 187 graphite edges where initial Li-ion insertion occurs, and the Solid-Electrolyte Interphase
46
47 188 (SEI). The bulk modelling discussion includes a direct comparison between experimental
48
49 189 and theoretical thermodynamic parameters, such as the open circuit voltage (OCV) and
50
51 190 entropy, which will also be of interest to battery control modellers. Kinetic predictions
52
53 191 are made and linked to DFT predictions of the influence of graphite edge morphology on
54
55 192 surface states, which may be of interest to those working on battery material development
56
57
58
59
60

1
2
3 and discovery. Recent work applying linear scaling DFT to complex interfaces will be of
4
5 interest to those at the forefront of DFT method development, focusing on the boundary
6
7 between atomistic and continuum modelling. Lastly, recent developments in silicides to
8
9 boost anode gravimetric capacity, along with their associated challenges, are summarised in
10
11 the outlook. Recent reviews in this area include Asenbauer et al.,¹⁴ summarising aspects of
12
13 lithiation/delithiation mechanisms and morphological aspects in graphite and silicon oxide
14
15 composites, and Zhang et al.,¹⁵ similar in scope but providing a more *ab initio* focus. Here,
16
17 our review here covers graphite structure and lithiation/delithiation mechanisms, including
18
19 surfaces and interfaces, which have tended to be neglected, although aspects of modelling
20
21 the SEI have been reviewed by Wang et al..¹⁶
22

23 The liquid electrolyte section, section 4.2, has a strong focus on the development of atom-
24
25 istic models, both *ab initio* and force field-based. This includes a pivotal discussion on the
26
27 atomic interactions between the components and method development to study electrolytes
28
29 via classical MD simulations. This will be of particular interest to those at the forefront of
30
31 classical MD method development. Liquid electrolytes are known to be limited by narrow
32
33 electrochemical windows, solvent toxicity, and material flammability/safety concerns. The
34
35 latter parts of this section describe the atomistic modelling of the bulk structure and land-
36
37 scaping, Li-ion diffusion, solvation energies, and activity coefficients of liquid electrolytes,
38
39 and the interfacial nanostructure relating to the interface with a solid electrode. These topics
40
41 cover the major aspects for improving liquid electrolytes for use in a battery and research
42
43 towards circumventing critical safety^{17,18} and energy density¹⁹ limitations. The challenges
44
45 and potential avenues for solving these issues are summarised in the outlook, including recent
46
47 developments to resolve these within the liquid electrolyte family and alternative materials.
48
49 Recent reviews in this area include Galiński et al.,²⁰ summarising the field of ionic liquids,
50
51 Wang et al.,²¹ reviewing the recent progress in water in salts electrolytes, and Logan and
52
53 Dahn,²² giving some recent developments in conventional electrolytes. Here, our review
54
55 covers the continued development of interatomic potentials for liquid electrolytes and a de-
56
57
58
59
60

220 scription of the solid electrode-liquid electrolyte interface from the perspective of the liquid,
221 which is not the conventional frame of reference.

222 Solid state electrolytes (SSEs) are becoming an increasingly popular avenue of research,
223 motivated by the rise of the electric vehicle (EV).²³ They have been proposed as an alterna-
224 tive to liquid electrolytes to resolve safety issues pertaining to the flammable organic liquid
225 electrolytes that are currently used,^{17,18} and also as a route to increased energy density.¹⁹
226 In the solid electrolyte section, section 4.3, we review a selection of the promising candidate
227 materials currently being investigated. Each material discussed has a different focus, high-
228 lighting a range of properties applicable to different SSE materials. In this section, we focus
229 on four material families, grouping them into sulfide and oxide based SSEs. Sulfide based
230 SSEs typically have a high Li-ion conductivity and poor electrochemical stability against
231 Li metal (the anode typically used in combination with SSEs).^{24,25} $\text{Li}_{10}\text{GeP}_2\text{S}_{12}$ (LGPS) is
232 reviewed, with a focus on how atomistic methods reveal the isotropic ion pathways, while
233 $\text{Li}_6\text{PS}_5\text{X}$ based Li-argyrodites are focused towards the relationship between ionic conduc-
234 tivity and anion substitution, as well as atomistic predictions of occupied Li sites. Oxides
235 typically have a higher electrochemical stability but still suffer from dendrite formation,
236 amongst other issues.²⁴ LLZO is also reviewed, with a focus on how multiple atomistic
237 methods have been applied to probe dendrite formation and ionic transport in the material.
238 State-of-the-art models of interfaces in oxide nanocomposites are reviewed. Lastly, the chal-
239 lenges of the SEI are discussed and an outlook to future modelling of SSEs is given. Related
240 reviews in the area include Zhang et al.,²⁶ summarising the future directions of ASSBs, and
241 Gurung et al.,²⁷ highlighting the advances and challenges in SSEs and ASSBs. Xiao et al.²⁸
242 and others^{29,30} provide a more specific review of the SEI. Ceder et al.³¹ outlines the prin-
243 ciples that should be employed when modelling SSEs. Here, our review discusses a broad
244 range of SSE properties, following the notion that these properties are applicable to range
245 of materials.

246 The cathodes section, section 5, covers a range of different cathode materials used in a

1
2
3
4 247 variety of Li-ion cells. This section describes atomistic modelling in the bulk, at the surfaces,
5
6 248 and the Cathode-Electrolyte Interphase (CEI). In discussing bulk modelling, a comparison
7
8 249 of the different cathode crystal structures, micro-structuring, and available diffusion path-
9
10 250 ways within the material are covered, as well as important properties, including redox and
11
12 251 electronic properties, transition metal ordering, and vibrational and thermal properties. Use
13
14 252 of electronic structure methods modelling techniques has been essential for investigating
15
16 253 crystalline structure, so will be of great interest to those who utilise DFT in their research.
17
18 254 Surface structures and morphologies of cathode particles can be difficult to determine using
19
20 255 experimental methods alone, which is where *ab initio* and potentials-based MD can pro-
21
22 256 vide vital insight. As with the SEI, linear-scaling DFT has recently been applied to CEI,
23
24 257 where discussions on CEI will be of interest to those doing state-of-the-art DFT method
25
26 258 development. Related reviews in the area include Ma,³² summarising modelling Li-ion bat-
27
28 259 tery cathode materials, Yan et al.,³³ focusing on DFT calculations of cathode materials,
29
30 260 and Wang et al.,³⁴ discussing closing the gap between theoretical and practical capacities
31
32 261 in layered oxide cathode materials. Our review includes a discussion on the CEI, which has
33
34 262 recently been reviewed by Maleki Kheimh Sari and Li.³⁵ Here, our review covers thermal,
35
36 263 electronic, dynamic, and structural properties for a range of prominent cathode materials
37
38 264 in terms of both electronic structure methods and potential-based modelling, which have
39
40 265 tended to be more isolated in other reviews.

41 266 Finally, we provide an outlook on the key remaining challenges for atomistic modelling
42
43 267 of LiBs and promising future directions for resolving them.
44
45
46
47
48
49
50
51
52
53
54
55
56
57
58
59
60

2 Methods

2.1 Method overview

2.1.1 Density Functional Theory

Density Functional Theory (DFT) is amongst the most accurate methods for atomistic simulations of materials, as it is a quantum mechanical method. This means that it is able to simulate the electrons in materials and how they result in all the observable processes and properties of a material. As electrons are microscopic particles, to simulate their properties we need to use the theory of quantum mechanics. However, the computational cost of calculations with this theory is very high, as all the observable properties are obtained from the wave function: a highly complicated function of many variables (proportional to the number of particles we are simulating) and, for exact solution, the computational effort scales exponentially with the number of particles. Approximate wave function based theories with more favourable computational scaling (such as $\sim N_e^5$ or $\sim N_e^7$, where N_e is the number of electrons in the calculation) have been developed, but the computational effort is still so high that they cannot be applied to molecules with more than a few atoms.

DFT is a reformulation of quantum electronic structure theory, where the central quantity is no longer the wave function, but instead the electronic density, $\rho(\mathbf{r})$, which is a comparatively simpler function of only one position variable, \mathbf{r} . As a result, DFT has lower computational scaling, allowing simulations of much larger systems (up to a few hundred atoms on supercomputers). Another advantage of DFT is that it is formally an exact theory. Due to these two significant advantages, DFT is today the method of choice for most simulations.

DFT was originally developed by Hohenberg and Kohn^{36,37} and reformulated by Kohn and Sham³⁸ into the mathematical description we use today, often called KS-DFT, where the energy of a material is expressed as:

$$E[\rho] = T_{KS}[\rho] + E_{\text{ext}}[\rho] + E_H[\rho] + E_{xc}[\rho]. \quad (1)$$

Here all the terms are expressed as functionals of the density and $T_{KS}[\rho]$ is the kinetic energy of the electrons, $E_{\text{ext}}[\rho]$ is the energy of attraction of the electrons to nuclei (also called external potential energy), $E_H[\rho]$ is the classical (Coulomb) electrostatic energy of the electronic density charge distribution (also called Hartree energy), and E_{xc} describes the purely quantum effects of exchange and correlation.

DFT calculations are performed in an iterative fashion, with electron density expressed as a sum of one-electron wave functions, $\{\psi_i\}$, called molecular orbitals (MOs):

$$\rho(\mathbf{r}) = \sum_{i=1}^{N_e} |\psi_i(\mathbf{r})| \quad (2)$$

and these MOs are obtained by solving the Kohn-Sham eigenvalue equation:

$$\left[-\frac{1}{2}\nabla^2 + v_{\text{ext}}(\mathbf{r}) + v_H[\rho](\mathbf{r}) + v_{xc}[\rho](\mathbf{r}) \right] = \varepsilon_i \psi_i(\mathbf{r}). \quad (3)$$

As we can see from eqn. 3, the Hartree, $v_H[\rho]$, and exchange-correlation, $v_{xc}[\rho]$, potentials are functionals of the density, thus ultimately functionals of the MOs, which provide the solutions of the equation. This equation cannot be solved directly, but must follow an iterative procedure called the *self-consistent field (SCF)* process. The simplest SCF method is to guess a set of $\{\psi_i\}$ and use these to build and solve (eqn. 3), obtaining a new set of $\{\psi_i\}$ and repeating this process until the $\{\psi_i\}$ and the energy (eqn. 1) no longer change.

KS-DFT is formally an exact theory, but it does not provide an explicit expression for the exchange-correlation energy, $E_{xc}[\rho]$. The exact exchange-correlation functional is unknown or, more precisely, unknowable. Thus a very active area of DFT development is to construct approximations of increasing accuracy for $E_{xc}[\rho]$. The simplest approximation is the local density approximation (LDA), where $E_{xc}[\rho(\mathbf{r})]$ is expressed as:

$$E_{xc}^{LDA}[\rho(\mathbf{r})] = \int \rho(\mathbf{r})\epsilon_{xc}[\rho(\mathbf{r})] d\mathbf{r} \quad (4)$$

312 The value of ϵ_{xc} at some position, \mathbf{r} , is computed exclusively from the value of ρ at that
313 position. In practice, $\epsilon_{xc}[\rho(\mathbf{r})]$ describes the exchange and correlation energy per particle of
314 a uniform electron gas of density ρ .³⁹

315 In general, the electron density in a molecular system is not spatially uniform, even at
316 small volumes of space, limiting the applicability of LDA. More accurate functionals are
317 obtained by the inclusion of a density gradient correction, known as the generalised gradient
318 approximation (GGA), or semi-local functionals. In the GGA, the functionals depend on
319 both the density and the gradient of the density, i.e. $v_{xc}^{GGA} = f(\rho, \nabla\rho)$. Popular examples
320 of GGA functionals are Perdew-Wang GGA (PWGGA) (both exchange and correlation),⁴⁰
321 Perdew-Burke-Ernzerhof GGA (PBEGGA),⁴¹ and Becke-Lee-Yang-Parr (BLYP).^{42,43} Func-
322 tionals including contributions from the second derivative of the density are called *meta*-GGA
323 functionals.⁴⁴

324 Standard DFT methods fail to describe dispersion effects that are of a non-local electron
325 correlation nature. Consequently, DFT methods are often inaccurate for the investigation
326 of molecular crystals, adsorption on surfaces, and other systems in which dispersion forces
327 due to van der Waals (vdW) gaps between layers play a significant role. Several versions
328 of dispersion corrected DFT (DFT-D) approaches are available, e.g. DFT-D2,⁴⁵ DFT-D3,⁴⁶
329 DFT-D4,⁴⁷ DFT-D3BJ,^{48,49} etc.

330 GGA functionals, however, still have problems with self interaction. The hybrid func-
331 tionals usually offer some improvement over the corresponding pure DFT functionals. Of
332 all modern functionals, the B3LYP method is the most popular to date.^{43,50} It works well
333 both for structural investigations and for the computation of electronic properties.⁵¹ An-
334 other popular hybrid functional, PW1PW,^{52,53} was parameterised to reproduce structural,
335 energetic, and electronic properties of solids. A more recent and popular hybrid functional
336 is HSE06, where the correlation part is defined by a PBE functional and a range-separation

337 approach is used for the exchange part.⁵⁴

338 The applicability of the hybrid functionals depends mainly on the type, size, and com-
339 plexity of the studied systems, as these functionals incur a huge computational cost. An
340 alternative approach is the DFT+U method, where the effects of strong intra-atomic elec-
341 tronic correlations are modelled by adding an on-site Coulomb repulsion, U , and site ex-
342 change term, J , to the DFT Hamiltonian.⁵⁵⁻⁵⁷ Parameters U and J can be extracted from
343 *ab initio* calculations, but are usually obtained semi-empirically. Inspired by the Hubbard
344 model, the DFT+U method is formulated to improve the ground state description of strongly
345 correlated systems. The Hubbard Hamiltonian describes the strongly correlated electronic
346 states (d and f orbitals), while the rest of the valence electrons are treated by normal DFT
347 approximations.

348 2.1.2 Linear-Scaling DFT

349 In conventional DFT, solving the Kohn-Sham eigenvalue equations, eqn. 3, subject to the
350 required orthonormality constraint, results in a computational cost scaling with the third
351 power (it is an $\mathcal{O}(N^3)$ procedure) with the number of atoms, N . This is demonstrated in the
352 example of Figure 2, showing the computation time as a function of the number of atoms for
353 slabs of graphite of increasing size. This unfavourable scaling is the reason why conventional
354 KS-DFT is practically unfeasible beyond several hundred atoms. However, there are many
355 grand challenges in materials research, where, due to their inherent complexity, building re-
356 alistic models requires thousands of atoms, such as simulations of defects, complex structures
357 of the Solid-Electrolyte Interphase (SEI), and metallic and semiconductor nanoparticles used
358 in catalysis and battery electrodes, among others. This need for large-scale DFT calcula-
359 tions has motivated the development of new theoretical methods which can scale linearly
360 with system size.⁵⁸ In these linear-scaling methods, conventional KS-DFT is reformulated in
361 terms of the one-particle density matrix, γ :

$$\gamma(\mathbf{r}, \mathbf{r}') = \sum_i f_i \psi_i(\mathbf{r}) \psi_i^*(\mathbf{r}'), \quad (5)$$

allowing us to exploit the principle of “nearsightedness of electronic matter”,⁵⁹ because the density matrix decays exponentially with the distance, $|\mathbf{r} - \mathbf{r}'|$,⁵⁹ while the MOs, $\{\psi_i\}$, are, in general, fully delocalised over the entire electronic system (molecule, nanoparticle, slab, etc.) and do not decay. The exponentially-decaying tail of the density matrix can be truncated to develop methods with reduced or linear-scaling computational cost. As the system size (number of atoms) is increased, it reaches a point where the remaining amount of information increases linearly with the size of the system. This can be implemented more efficiently with non-orthogonal, localised orbitals, $\{\phi_\alpha\}$.^{60,61} In this representation, the density matrix can be written as:

$$\gamma(\mathbf{r}, \mathbf{r}') = \phi_\alpha(\mathbf{r}) K^{\alpha\beta} \phi_\beta^*(\mathbf{r}'). \quad (6)$$

Here, the density kernel matrix, \mathbf{K} , is a generalisation of the MO occupancies, $\{f_i\}$, of equation 5, while implicit summation (Einstein convention) is assumed for repeated Greek indices.

The development of linear-scaling methods has proven to be a very challenging research topic, as the goal of developing methods that accommodate the conflicting requirements of orbital localisation with high accuracy is extremely difficult to achieve. Recent developments towards this goal have made this possible by using a dual resolution approach, where both $\{\phi_\alpha\}$ and \mathbf{K} are optimised self-consistently during the calculation, while subject to localisation constraints.⁶²⁻⁶⁴ The $\mathcal{O}(N)$ Electronic Total Energy Package (ONETEP),⁶⁵ has the unique capability of achieving linear-scaling computational cost, while maintaining the near-complete basis set accuracy of conventional DFT. The computational efficiency of this code is demonstrated on the graphite example in Figure 2, where the linear-scaling behaviour can be clearly seen. DFT calculations with tens of thousands of atoms can be performed

with ONETEP, opening avenues for simulating realistic models of materials and interfaces in lithium-ion batteries (LiBs) with DFT-scale accuracy. ONETEP is being actively developed and offers a large and diverse range of capabilities, including: different boundary conditions, various exchange–correlation functionals, finite electronic temperature methods for metallic systems, methods for strongly correlated systems, molecular dynamics, vibrational calculations, time-dependent DFT, electronic transport, core loss spectroscopy, implicit solvation, density of states calculations, and distributed multipole analysis.⁶⁵ Recent focus in ONETEP is on developing specific electrochemistry tools for battery simulations, aiming to develop the first atomistic simulation platform (in particular, the first linear-scaling DFT platform) for electrochemistry. Some of these developments are described in this review, in subsection 2.2.1.

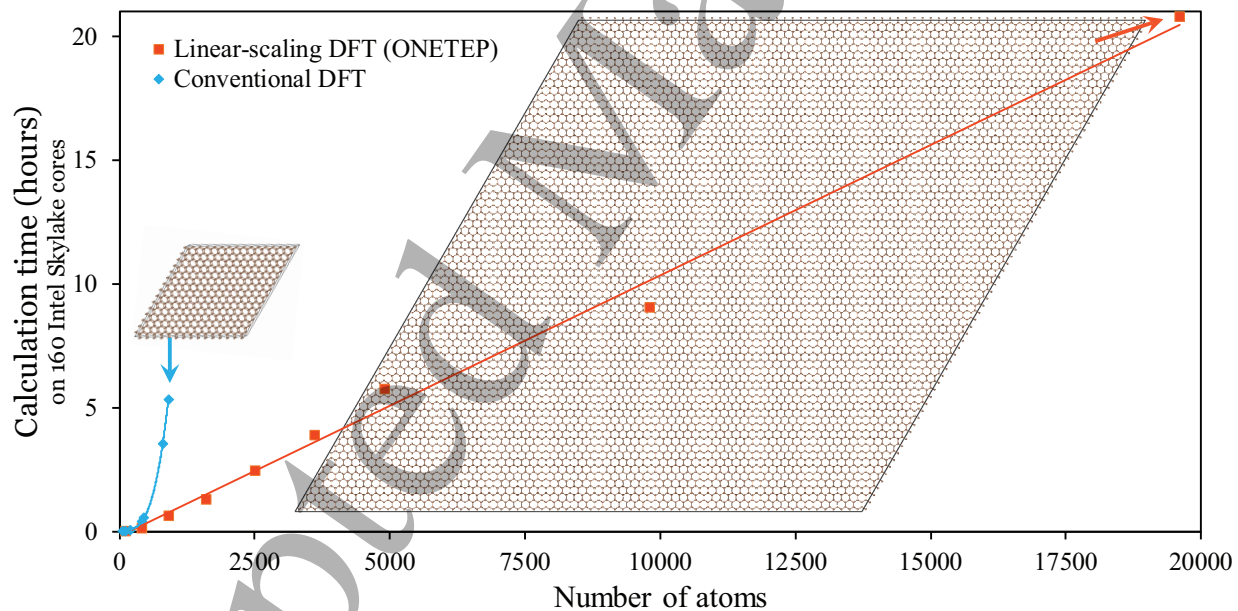


Figure 2: Comparison of the computational time with the number of atoms for slabs of graphite of increasing size using the ONETEP linear-scaling DFT code versus a conventional plane wave DFT code. The computations were performed on the Iridis 5 supercomputer at the University of Southampton on 40 MPI processes, with 4 OpenMP threads each (160 cores in total). Reprinted from Ref. 66, with the permission of AIP Publishing.

2.1.3 Nudged Elastic Band

Nudged elastic band (NEB) theory is a useful method based on transition state theory, seeking the minimum energy path and the saddle point (or transition state) between two minima (initial and final states).⁶⁷⁻⁶⁹ The energy difference between the lowest energy state and the saddle point is defined as the activation barrier (E_a), Figure 3.⁶⁹

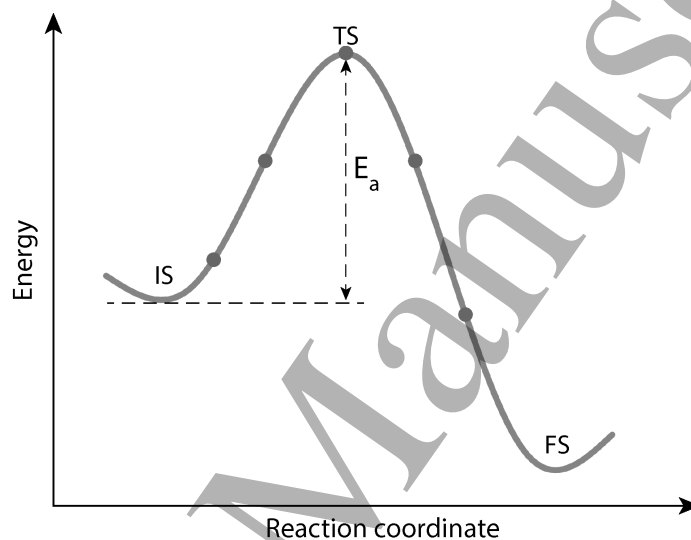


Figure 3: Energy profile of Nudged Elastic Band (NEB) calculation. The IS, TS, and FS are the initial state, transition state and final state, respectively. E_a denotes the activation barrier along the reaction path. The grey circles are the “images” in the NEB calculation.

The NEB approach initially guesses a number of configurations of several possible intermediate “images” that may occur along the reaction coordinate or diffusion path. This set of images can be created by linear interpolation between the initial and final states. The NEB algorithm further conducts constrained optimisation and converges those images along the minimum energy path. Furthermore, fictional spring forces are added between adjacent images to maintain the spacing and the continuity of the reaction or diffusion path. The NEB approach is widely applied in the studies of chemical transformations, such as catalytic reactions or ion diffusion in solid materials. The determined chemical reaction energy barriers can then be used in further, larger time- and length-scale models, such as microkinetic models.^{70,71}

2.1.4 Cluster expansion

The cluster expansion method enables a statistical approach to sample configurational phase space at finite temperature.⁷²⁻⁷⁴ This method aims to capture the energetics of mixing two or more atoms on a given set of lattice sites, typically with an accuracy close to DFT calculations. The approach borrows ideas from the Ising model,⁷⁵ where each lattice site is assigned as a spin variable to simulate the magnetic properties, but maps site occupancy onto spin variables instead.⁷⁶ For example, for a binary alloy system with atom types A and B, the occupation of each site can be described by a spin-like variable, i.e. $\sigma_i = +1$, if the site is occupied by atom A, and $\sigma_i = -1$ if the site is occupied by atom B, as shown in Figure 4. A configuration can then be written as $\sigma = (\sigma_1, \dots, \sigma_n)$. Accordingly, the energy of each configuration can be expressed as: $E \equiv E(\sigma_1, \dots, \sigma_n)$.

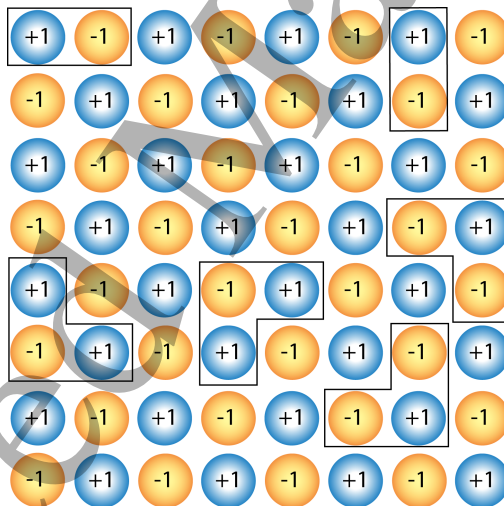


Figure 4: A 2D (8×8) structure including several clusters. $+1$ and -1 are the lattice sites assigned with different spins.

To compute $E(\sigma)$, all relevant interactions should be sampled. A set of interactions should be considered, such as nearest neighbouring pair interactions, second nearest neighbouring pair interactions, triplet interactions, quadruplet interactions, and so on, up to many body interactions (Figure 4). Further, all symmetry-equivalent interactions (including translations) can be grouped into “clusters (α)”. Including all relevant cluster interactions, the

energy can be expressed as:

$$E_\alpha = \sum_{\alpha} m_\alpha J_\alpha \bar{\Pi}_\alpha(\sigma), \quad (7)$$

where m_α is the multiplicity of the cluster, α , and can be obtained by considering all the point symmetries in the lattice cell. J_α is the effective cluster interaction (ECI) associated with a cluster, α . $\bar{\Pi}_\alpha(\sigma)$ is the correlation matrix of normalised spin-products for a particular cluster of the entire lattice, obtained via:

$$\bar{\Pi}_\alpha(\sigma) = \frac{1}{Nm_\alpha} \sum_{i \in \alpha} \Pi \sigma_i, \quad (8)$$

where N is the number of parent lattice cells required to generate the configuration σ . Theoretically, the expansion should include all possible clusters. However, that is not practical and one of the key features of cluster expansions is that they usually converge quickly after including a handful of terms.⁷⁷ Consequently, only a relatively small number of DFT calculations are therefore required to parameterise a handful of ECIs. For example, if we calculate the energy of an A-B alloy system and consider only four clusters and four configurations, the energy of each configuration can be expressed as:

$$\begin{pmatrix} E_1 \\ E_2 \\ E_3 \\ E_4 \end{pmatrix} = \begin{pmatrix} \Pi_1(1) & \Pi_2(1) & \Pi_3(1) & \Pi_4(1) \\ \Pi_1(2) & \Pi_2(2) & \Pi_3(2) & \Pi_4(2) \\ \Pi_1(3) & \Pi_2(3) & \Pi_3(3) & \Pi_4(3) \\ \Pi_1(4) & \Pi_2(4) & \Pi_3(4) & \Pi_4(4) \end{pmatrix} \begin{pmatrix} J_1 \\ J_2 \\ J_3 \\ J_4 \end{pmatrix} \quad (9)$$

In principle, the effective interaction coefficients, J_α , can be obtained via inverting the matrix above and using the energies from DFT calculations, but this is not commonly done. Rather, a larger training set is generated from DFT and the ECIs are fitted in a least-square sense. The set of considered clusters is usually obtained by cross-validation: the set of clusters with the highest accuracy for predicting configurations achieves the highest

cross-validation score and is selected.

Various codes exist to link the results of DFT calculations with cluster expansion codes, such as the Alloy Theoretic Automated Toolkit (AT-AT),⁷⁸⁻⁸⁰ the Clusters Approach to Statistical Mechanics (CASM),⁸¹ *Ab Initio* Random Structure Search (AIRSS),⁸² Integrated Cluster Expansion Toolkit (IceT),⁸³ and CLuster Expansion in Atomic Simulation Environment (CLEASE).⁸⁴ These codes usually provide a means to fit ECIs and include Monte Carlo (MC) features to sample phase spaces. They also allow the generation of DFT calculations to expand the training set. MC methods are explained in the next section.

2.1.5 Lattice gas and Monte Carlo

Lattice gas methods simulate the system state as an array of points.⁸⁵ This data structure is ideally suited to represent periodic, crystalline systems, but extensions to more complex systems are possible. In atomistic simulations, the array values denote the occupation of particular sites by certain types of atoms. The evolution of the system state can then be computed in terms of changes in those array values, i.e. site occupancies.⁸⁵

In the Ising Hamiltonian described in the previous section, each site can be in either a +1 or -1 state.⁸⁶ This data structure is suited to studying the thermodynamics and kinetics of binary alloys.^{87,88} Simplistically, a LiB intercalation material can be represented as a binary alloy of lithium atoms and vacancies within an Ising model.^{76,89,90}

The interaction Hamiltonian describes how the energy of the system depends on the configuration of the lattice. For a simple interaction model, it is possible to perform a direct evaluation of the partition function, Z , via:

$$Z = \sum_i e^{-\beta E_i}, \quad (10)$$

where E_i is the energy of state i , and $\beta = 1/kT$ (k = Boltzmann constant; T = absolute temperature). Once Z is known, the rest of the thermodynamic properties of the system can easily be determined.⁹¹⁻⁹³ In a two-level system,⁹² the number of states in equation 10 can

1
2
3
4 467 be reduced to scale linearly with the number of particles in the system, making the sum-
5
6 468 mation computationally tractable.⁹¹⁻⁹³ Measurable quantities, like the open circuit voltage
7
8 469 (OCV), voltammograms, and partial molar enthalpy and entropy can be simulated.⁹¹⁻⁹³ This
9
10 470 approach has been applied to lithium intercalation in lithium manganese oxide (LMO)⁹³ and
11
12 471 graphite,^{91,92} as demonstrated in section 3.2.3. The interactions between the particles can
13
14 472 be approximated by taking the average occupation in two levels, allowing ordered structures
15
16 473 like graphite stages to be modelled. This approach represents a step in complexity beyond
17
18 474 the assumption of simple solid solution behaviour, which is still commonly applied in con-
19
20 475 tinuum level models.⁹⁴ The approach is closely related to the phase field models applied by
21
22 476 Bazant to systems such as lithium iron phosphate (LFP) and graphite.⁹⁵⁻⁹⁷

23
24 477 For a more general and realistic interaction Hamiltonian, the number of energy states
25
26 478 precludes direct evaluation of equation 10. In that case, MC methods are useful for calcu-
27
28 479 lating thermodynamic properties. This is true for the Ising model defined in section 2.1.4,
29
30 480 when represented in more than one dimension, as is the case in most practical systems. It is
31
32 481 then more practical to obtain the thermodynamic properties by the Metropolis algorithm.⁹⁸
33
34 482 Following the Markov chain of states, the limiting distribution equals the probability distri-
35
36 483 bution of the thermodynamic ensemble. Properties of interest can be obtained from taking
37
38 484 the average of sampled configurations once the distribution has reached equilibrium.⁸⁸

39
40 485 Inputting a chemical potential, μ , in the grand canonical ensemble, the ground state
41
42 486 properties of the system are obtained as follows. For a LiB, μ represents the chemical
43
44 487 potential of intercalated Li in the host, i.e. the electrode potential, described in section 2.3.1.
45
46 488 Computing the average occupation, $\langle N \rangle$, of particles in the system at each μ value, therefore
47
48 489 allows the equilibrium potential to be simulated at any input temperature, T . Along with
49
50 490 $\langle N \rangle$, the average internal energy, $\langle E \rangle$, is a useful parameter to check the convergence of the
51
52 491 simulation results with respect to the system size.^{85,89,90,99}

53
54 492 Variances can be computed to check the system size convergence and derive experi-
55
56 493 mentally measurable parameters. For example, the configurational component of the heat

494 capacity at constant volume, C_V , given by:

$$C_V = \frac{\beta}{T} (\langle E^2 \rangle - \langle E \rangle^2) = \frac{\beta}{T} \text{var}(E), \quad (11)$$

495 where $\text{var}(E)$ is the variance of E . The vibrational and electronic components of C_V must
496 be determined by other means, such as the approaches outlined in section 2.3.4.

497 It is also possible to determine voltammograms from $\text{var}(N)$, as explained by Darling and
498 Newman and Mercer et al..^{89,99} If the covariance of U and N is also known, the partial molar
499 internal energy, $\partial U/\partial N$ and partial molar entropy $\partial S/\partial N$ can be obtained, as defined else-
500 where.^{89,90} These parameters can be compared with experimental parameters from “entropy
501 profiling” or calorimetry^{89,91,93,100,101} and input into a dynamic model such as kinetic Monte
502 Carlo (kMC),^{76,99,102,103} or Molecular Dynamics (MD) to describe temperature dependent
503 behaviour. A review of kMC has recently been published;¹⁰⁴ the technique is also briefly
504 described by Van der Ven et al..⁹ MD is described in the following section.

505 2.1.6 Molecular Dynamics

506 MD is an approach which probes the dynamic evolution of a system over time. The crucial
507 input for these simulations is the potential energy surface (PES), describing the interactions
508 between atoms. In *ab initio* MD (AIMD), this is described by solving the Schrödinger
509 equation, whereas in a classical (potentials-based) mechanics framework the interactions are
510 described using parameterised interatomic potentials. Here, we give an overview of both
511 frameworks.

512 AIMD is able to capture events that potentials-based MD cannot, including bond break-
513 ing, and bond formation. AIMD also assumes that the dynamics of particles can be treated
514 classically and that the equation of motion for all particles can be written as:

$$M_I \ddot{\mathbf{R}}_I = -\nabla_I [\varepsilon_0(\mathbf{R}) + V_{NN}(\mathbf{R})], \quad (12)$$

where M_I is the mass of a given nucleus, \mathbf{R} denotes all nuclear coordinates, ∇_I is the Laplacian operator of a given nucleus, $\varepsilon_0(\mathbf{R})$ represents the ground state energy of the system at that given nuclear configuration, and $V_{NN}(\mathbf{R})$ represents the nuclear-nuclear coulomb repulsion at that given nuclear configuration.

Most modern techniques use KS-DFT (c.f. section 2.1.1) to solve the Schrödinger equation which finds the ground state energy. AIMD can be broadly split up into two main categories: Born-Oppenheimer dynamics and Car-Parrinello extended Lagrangean. The Born-Oppenheimer dynamics method uses a symplectic integrator to numerically integrate the equation of motion in Eq. 12 for each time step. The Car-Parrinello extended Lagrangean method gives the Kohn-Sham orbitals an artificial time-dependence. To attain a minimum energy with each new \mathbf{R} , the orbital dynamics are kept at a temperature much lower than that of the nuclei, but still high enough for the orbitals to quickly relax as the equation of motion proceeds. The new orbitals and their dynamics can then be defined by the Lagrangean equation:¹⁰⁵

$$L = \mu \sum_i f_i \int d\mathbf{r} |\psi_i(\mathbf{r}, t)|^2 + \frac{1}{2} \sum_{I=1}^N M_I \dot{\mathbf{R}}_I^2(t) - E[\psi(t), \mathbf{R}(t)] + \sum_{i,j} \Lambda_{ij} \left[\int d\mathbf{r} \psi_i^*(\mathbf{r}, t) \psi_j(\mathbf{r}, t) - \delta_{ij} \right], \quad (13)$$

where μ is an artificial kinetic energy term (discussed further in Refs. 106 and 107), $\psi_x(\mathbf{r}, t)$ are the time-dependent Kohn-Sham orbitals, and Λ_{ij} contains a set of Lagrange multipliers to implement the orthonormality constraint on the orbitals.

Potentials-based MD is not able to capture some of the finer details of the system dynamics that AIMD is able to, however, it is able to reach longer time- and length- scales, providing information on long range diffusion properties. In classical potentials-based MD, the atomic interactions are described using parameterised interatomic potentials. There are multiple forms interatomic potentials can take, with their relevancy and accuracy relating to the system and study being conducted. Atoms are either attracted or repelled by one an-

538 other based on their interatomic distance, r , to reduce their potential energy to a minimum,
 539 r_{eq} . This is known as a pair-interaction, which can be used to calculate the force, \vec{F} , acting
 540 on each atom, given by:

$$\vec{F}_i = \sum_j \vec{\nabla} E(r_{ij}) \quad (14)$$

541 In complex systems, there is a “net effect” of the N surrounding atoms which can be
 542 accounted for by calculating the vector summation of each pair interaction contribution.
 543 Within ionic materials, the pair interactions are dominant and therefore it is computationally
 544 tractable to truncate the expression after the first term¹⁰⁸ to give an approximation of the
 545 pair potential. The charged nature of ions forms a coulombic interaction, where the relatively
 546 slow decay of $\frac{1}{r}$ as r increases, gives rise to the long range component of the potential. The
 547 general term for the total potential can therefore be written as:

$$E(r_{ij}) = \frac{Q_i Q_j}{4\pi\epsilon_0 r_{ij}} + \Phi_{sr}, \quad (15)$$

548 where i and j are ions of charge Q_i and Q_j at a distance of r_{ij} , and ϵ_0 is the permittivity
 549 of free space. Φ_{sr} is used to denote the remaining short-range interactions.

550 For ionic solids, including cathode materials, a common choice for an interatomic po-
 551 tential is a Coulomb-Buckingham potential,¹⁰⁹ derived from the Born model of the ionic
 552 solid,^{110,111} where the potential energy of the system can be expressed as:

$$E(r_{ij}) = \sum_{ij} \frac{Q_i Q_j}{4\pi\epsilon_0 r_{ij}} + \sum_{ij} A \exp\left(\frac{-r_{ij}}{\rho}\right) - C r_{ij}^{-6}, \quad (16)$$

553 where, A , ρ , and C are constants.

554 MD simulations can be performed using a range of ensembles, with the most commonly
 555 used being microcanonical (NVE), canonical (NVT), and isothermal-isobaric (NPT) ensem-
 556 bles.^{112–114} Here, the number of atoms (N), volume (V), energy (E), temperature (T), and
 557 pressure (P) are conserved within the respective ensembles. Within the NVT and NPT

1
2
3
4 588 ensembles the energy of endothermic and exothermic processes is exchanged with a ther-
5
6 589 mostat. A variety of thermostat algorithms are available, with some of the most popular
7
8 590 methods including the Nosé-Hoover, Berendsen, and Andersen thermostats.¹¹²⁻¹¹⁴ For NPT
9
10 591 ensembles, a barostat is also applied to control pressure.

11
12 592 The choice between AIMD and potentials-based MD is a trade-off between computational
13
14 593 cost, accuracy, and transferability. AIMD is highly accurate, however, it is computationally
15
16 594 expensive and scales poorly ($> O(N^3)$), making reachable system sizes and timescales rel-
17
18 595 atively small (< 1000 atoms, ~ 100 ps). On the other hand, potentials-based MD is less
19
20 596 computationally expensive and can be applied to much larger system sizes, up to millions
21
22 597 of atoms, with longer reachable time scales in the range of nanoseconds. However, the
23
24 598 potentials-based approach is generally less accurate, as developing an interatomic potential
25
26 599 which is sufficiently accurate enough to describe the specific system chemistry is challeng-
27
28 590 ing. The development of interatomic potentials is discussed in greater detail in section 2.2.2.
29
30 591 More recently, development of linear-scaling DFT approaches, as discussed in section 2.1.2,
31
32 592 has worked towards reducing this trade-off.

33 34 35 573 **2.2 Method Development**

36 37 38 574 **2.2.1 Continuum models of electrolyte solutions within Density Functional The-** 39 40 575 **ory**

41
42 576 Electrode-electrolyte interfaces are an important part of LiBs and an area of active re-
43
44 577 search.^{115,116} The complexity of the structure and formation of electrical double layers at
45
46 578 the interface has hindered the understanding of important electrochemical processes. While
47
48 579 DFT-based electronic structure methods have been successfully used to study the solid-state
49
50 580 physics in the bulk electrodes of LiBs, they are inadequate to describe the liquid state,
51
52 581 which lacks structural order. This has led to rapid development of methods to describe the
53
54 582 electrode-electrolyte interfaces.¹¹⁷

55
56 583 The liquid state can be described mainly via explicit solvation,¹¹⁸ implicit solvation,¹¹⁹

584 or both.¹²⁰ In the former, the surrounding solvent and electrolyte molecules are considered
 585 at the same level of chemical accuracy as the electrode atoms. The surrounding solvent and
 586 electrolyte molecules can not only neutralise the excess charge on the electrode surface, but
 587 also form bonds and adsorb on the electrode surface.^{121–123} The addition of a large number of
 588 solvent and electrolyte molecules to describe the liquid state drastically increases the config-
 589 uration degrees of freedom. Sampling this large configurational space is computationally
 590 demanding and often leads to loss of focus on the main region of interest: the interface.
 591 While consideration of the first bonding layer of explicit solvent and electrolyte molecules
 592 is necessary to describe the local effects of bonding and electric field,¹²⁴ the degrees of free-
 593 dom of the non-participating solvent and electrolyte molecules far away can be averaged out
 594 via an implicit model of the electrolyte solution.^{125,126} The electrostatic potential in these
 595 hybrid quantum-continuum models is obtained from the solution of the Poisson-Boltzmann
 596 equation (P-BE).¹²⁷ Recently, many DFT codes have integrated P-BE based continuum
 597 models.^{66,128–135}

598 The continuum electrolyte ions with space-dependent concentrations, $c_i(\mathbf{r})$, $i = 1 \dots p$,
 599 and charges, $\{z_i\}$, create a mobile electrolyte density, $\rho_{\text{mob}}(\mathbf{r}) = \sum_{i=1}^p z_i c_i(\mathbf{r})$, which interacts
 600 with the quantum charge density, $\rho(\mathbf{r})$, within a mean-field electrostatic potential, $\nu(\mathbf{r})$. This
 601 effect can be included in standard DFT by extending the standard free energy functional to
 602 include the mean-field electrostatic potential, $\nu(\mathbf{r})$, and the mobile charge concentrations,
 603 $c_i(\mathbf{r})$, as:¹³⁵

$$E[\rho(\mathbf{r})] \rightarrow \Omega[\rho(\mathbf{r}), \nu(\mathbf{r}), c_i(\mathbf{r})] \quad (17)$$

604 The variation of the free energy functional with the electrostatic potential, $\nu(\mathbf{r})$, gives
 605 the P-BE:

$$\nabla \cdot [\varepsilon(\mathbf{r}) \nabla \nu(\mathbf{r})] = -4\pi [\rho(\mathbf{r}) + \rho_{\text{mob}}(\mathbf{r})] \quad (18)$$

1
2
3
4
5
6
7
8
9
10
11
12
13
14
15
16
17
18
19
20
21
22
23
24
25
26
27
28
29
30
31
32
33
34
35
36
37
38
39
40
41
42
43
44
45
46
47
48
49
50
51
52
53
54
55
56
57
58
59
60

606 The P-BE not only includes the quantum charge density, $\rho(\mathbf{r})$, as in standard DFT
607 calculations in vacuum, but also the effect of the solvent in terms of a continuum dielectric
608 with permittivity function, $\varepsilon(\mathbf{r})$, and mobile charge density of electrolyte ions, $\rho_{\text{mob}}(\mathbf{r})$. The
609 permittivity function is chosen as a smooth function with value varying from 1 in the quantum
610 region to ε^∞ in the solvent region:¹³¹

$$\varepsilon(\mathbf{r}) = 1 + (\varepsilon^\infty - 1) s(\mathbf{r}), \quad (19)$$

611 where $s(\mathbf{r})$ is a smooth interface function varying from 0 in the quantum region to 1
612 in the solvent. Several choices for the interface function have been discussed by Andreussi
613 et al..¹³⁶ The variation of the free energy functional with ion concentrations, $c_i(\mathbf{r})$, gives the
614 Boltzmann expression for ionic concentrations:

$$c_i(\mathbf{r}) = c_i^\infty \lambda(\mathbf{r}) \exp\left(-\frac{z_i \nu(\mathbf{r})}{k_B T} + \frac{\mu_i^{\text{ex}}}{k_B T}\right), \quad i = 1 \dots p, \quad (20)$$

615 where $\{c_i^\infty\}$ and $\{\mu_i^{\text{ex}}\}$ are the bulk concentrations and excess chemical potentials of
616 the electrolyte ions. The mobile charge density of electrolyte ions, $\rho_{\text{mob}}(\mathbf{r}) = \sum_{i=1}^p z_i c_i(\mathbf{r})$, is
617 shown schematically in Fig. 5. As the interaction with mobile electrolyte charge is purely
618 electrostatic and excludes any quantum effects such as Pauli repulsion, there is a problem
619 of electrolyte charge accumulating infinitely close to the electrode. In order to prevent this
620 problem, the models include an electrolyte accessibility function, $\lambda(\mathbf{r})$, which varies from 0
621 near the electrode to 1 in the bulk electrolyte region.^{133,137,138} One of the ways of defining
622 such an accessibility function is as a product of atom-centred interlocking spheres of error
623 functions:¹³⁵

$$\lambda(\mathbf{r}) = \prod_k^{n_{\text{atoms}}} \frac{1}{2} \left[1 + \operatorname{erf} \left(\frac{|\mathbf{r} - \mathbf{R}_k| - R_k^{\text{solute}}(\rho_e^\lambda) - R_k^{\text{solvent}}}{\sigma} \right) \right], \quad (21)$$

624 where σ is a smearing width ($0 < \sigma < 0.5 a_0$). This description of the ion exclusion region
625 derives from a physical picture: the electrolyte ions are moved away from the quantum

$$\nabla \cdot [\varepsilon(\mathbf{r})\nabla v(\mathbf{r})] = -4\pi[\rho(\mathbf{r}) + \rho_{mob}(\mathbf{r})]$$

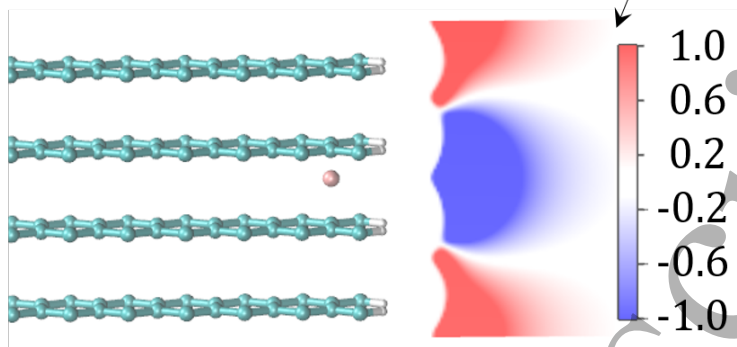


Figure 5: DFT simulation of a lithiated graphite interface in contact with an implicit electrolyte solution, based on the solution of the Poisson-Boltzmann equation. Reprinted with permission from Ref. 135. Copyright 2020 American Chemical Society.

electrode, up to a distance that incorporates not only the size of the species but also a solvation shell radius around the electrolyte ions. The species size can be described in terms of an isoradius of electronic density, ρ_e^λ . The solvation shell radius, R_k^{solvent} , depends on the solvent and is added to the species size, to calculate the overall radius of interlocking spheres for the accessibility function.

The electrostatic potential, $\nu(\mathbf{r})$, obtained from equation 18 is due to the entire electrode-electrolyte interface, where the electrode is treated quantum mechanically and the electrolyte solution as a continuum. Variation of the free energy functional with electronic density gives the Kohn-Sham equations in the total electrostatic potential, with additional terms for the variation of interface function with electronic density.^{130,139} Solvation energies are defined as:^{130,133}

$$\Delta\Omega = \Omega - \Omega_{\text{vac}} - \Omega_{\text{electrolyte}} \quad (22)$$

$$= \Omega[\rho(\mathbf{r}), \{c_i(\mathbf{r})\}, \nu(\mathbf{r})] \quad (23)$$

$$- \Omega[\rho_{\text{vac}}(\mathbf{r}), \{c_i(\mathbf{r})\} = 0, \nu_{\text{vac}}(\mathbf{r})]$$

$$- \Omega[\rho(\mathbf{r}) = 0, \{c_i(\mathbf{r})\} = \{c_i^\infty\}, \nu(\mathbf{r}) = 0],$$

637 where the respective terms can be computed as the total free energy in the electrolyte
 638 solution, the total free energy in vacuum, and the total free energy of the pure electrolyte.¹³⁵
 639 The electrolyte effect on solvation energies can be computed as the difference of solvation
 640 energy in electrolyte at $\{c_i^\infty\}$ and solvation energy in pure solvent at $\{c_i^\infty = 0\}$:

$$\Delta\Delta\Omega = \Delta\Omega[\{c_i^\infty\}] - \Delta\Omega[\{c_i^\infty = 0\}] \quad (24)$$

$$= \Omega - \Omega_{\text{sol}} - \Omega_{\text{electrolyte}}, \quad (25)$$

641 where the respective terms are computed as the total free energy in the electrolyte solu-
 642 tion, $\{c_i^\infty\}$, the total free energy in pure solvent, $\{c_i^\infty = 0\}$, and the total free energy of the
 643 pure electrolyte.

644 2.2.2 Fitting Potentials for Classical Molecular Dynamics

645 The development of sufficiently accurate interatomic potentials for a specific chemistry is
 646 quite challenging. Interatomic potentials are traditionally based on mathematical functions
 647 that have been parameterised using experimental and/or electronic structure methods de-
 648 rived data.^{109,140} There are a limited number of codes available with the explicit purpose or
 649 functionality for fitting potentials. Here, we present several available codes and discuss the
 650 complexities and considerations involved in deriving accurate interatomic potentials.

651 **GULP**,¹⁴¹ the General Utility Lattice Program, is a widely used code for performing
 652 a variety of simulation types on materials using boundary conditions.¹¹⁴ Within this code,
 653 there is the functionality to fit interatomic potentials to either experimental measurements
 654 or electronic structure methods data.¹⁴² GULP is capable of simultaneous fitting to multiple
 655 structures and can also handle core-shell models (which capture polarisation of atoms).

656 **Atomicrex**,¹⁴³ **dftfit**,¹⁴⁴ and **potfit**^{145,146} are codes designed to fit potentials to elec-
 657 tronic structure methods data. Each of these codes have different levels of flexibility and

658 their own unique features, however, a joint limitation is the ability to fit empirical potentials
659 is limited to rigid ions and cannot fit a core-shell model.

660 During the process of developing potentials for $\text{Li}(\text{Ni}_x\text{Mn}_y\text{Co}_z)\text{O}_2$ (NMC), and its ternary
661 system LiNiO_2 , it was found that none of these codes are able to accurately produce poten-
662 tials for these materials. The complex nature of Ni chemistry in a layered oxide material
663 is challenging, and to the best of our knowledge, no interatomic potentials exist for Ni^{3+} .
664 Oxide systems are widely described using a Buckingham potential form, as given in equa-
665 tion 16, and for layered structures, including NMC and its ternary systems, variations of the
666 Buckingham potentials are presented. Some use rigid ion models,^{147–150} others use core-shell
667 models,^{147,151–156} and a mixture of formal and partial charges have been implemented. With
668 literature in disagreement over which variation of the Buckingham potential is the most
669 accurate for representing the system, a code capable of fitting different permutations of the
670 Buckingham potential is needed.

671 Structure and composition of a material are crucial to determine the functional form
672 of the potential. For example, for a layered structure such as NMC-811, it is crucial to
673 consider polarisability. Polarisability is described in classical (potentials-based) MD using
674 a core-shell model. There are predominately two types of core-shell models: the relaxed
675 (massless shells) model¹⁵⁷ and the dynamic (adiabatic shells) model.¹⁵⁸ The adiabatic shell
676 model is more widely used in literature, including all core-shell related cited works in this
677 section,^{147,151–156} for calculating long trajectories, as it is less computationally taxing. In the
678 adiabatic shell model, a fraction of the atomic mass is assigned to the shell. There is no
679 defined fraction size; however, placing 10 % of the atomic mass on the shell is considered
680 common practice.^{112,113} An additional consideration for using a core-shell model is the sepa-
681 ration of the formal atomic charge across the core and shell. However, determined numerical
682 values of the core-shell charge separation are inconsistent.^{156,159–162} In some systems, where
683 there is high polarisability, such as in LMO, the short-range interactions are overwhelmed
684 by the longer-range coulombic term. In these cases, the system charges can be scaled to

increase the influence of the short-range interactions, and are termed partial charges. The scaling factor is system dependent therefore no specific value is ideal in all cases, however 60 % formal charge is commonly adopted.¹⁶³

POtential Parameter Optimisation for Force-Fields (PopOff),¹⁶⁴ a code developed within the Faraday institution, was specifically created for fitting different permutations of the Buckingham potential. It is unique in its ability to consider all the factors discussed above (rigid ion/core-shell/charge separation/charge scaling) in a modular design, allowing flexible fitting to suit individual systems. The code has been developed in Python, using a training set consisting of DFT derived data (DFT) and utilising the Large-scale Atomic/Molecular Massively Parallel Simulator (LAMMPS).¹¹³ The potential is fitted by minimising the mean squared error (χ^2) between the DFT forces, F^{DFT} , and stress tensors, σ^{DFT} , and those produced using the fitted interatomic potential (F^{IP} , σ^{IP}), defined as:

$$\chi^2 = \sum_{i,\alpha}^N \frac{(F_{i,\alpha}^{DFT} - F_{i,\alpha}^{IP})^2}{N_i} + \sum_{\beta} \frac{(\sigma_{\beta}^{DFT} - \sigma_{\beta}^{IP})^2}{6} \quad (26)$$

This modular design allows the construction of a Buckingham potential able to accommodate the considerations and complexities of different systems. PopOff also allows for individual parameters to be fixed/excluded from the fit, lowering the fit dimensionality and computational cost. This is particularly useful for excluding dispersion terms, which are known to be zero or close to, for a range of elements.^{161,165}

2.3 Calculating observable properties

2.3.1 Equilibrium voltage

The equilibrium cell voltage, $E(x)$, where $0 < x < 1$ denotes the fraction of sites occupied by lithium in the intercalation host, is a fundamental thermodynamic quantity related to the energy density of a cell.^{9,166,167} $E(x)$ can be probed through experimental measurements of the open circuit voltage (OCV), that is, the voltage between the cathode and anode

708 terminals under zero current flow, assuming that the system has been given sufficient time
 709 for the OCV to relax to the value of $E(x)$. Computationally, the equilibrium cell voltage can
 710 be modelled through DFT calculations at $T = 0$ K;^{9,166,167} the effect of thermal fluctuations
 711 can be included by modelling using Monte Carlo (MC) calculations.^{89,90}

712 There is a fundamental relationship between the Gibbs free energy of lithium dissolution
 713 into the host, $G(x)$, the chemical potential of Li intercalation in the host, $\mu(x)$, and the cell
 714 voltage $E(x)$. Knowledge of $G(x)$ also provides information about the evolution of the phase
 715 behaviour dependent on the fraction of intercalated Li,^{9,76,167,168} enabling the construction
 716 of phase diagrams from DFT. The relationships are represented schematically in Figure 6.
 717 In essence: the tangent to the free energy curve, $G(x)$, allows $\mu(x)$ and hence the cell voltage
 718 to be obtained. Alternatively, integration of $\mu(x)$ can be used to derive free energy curves.

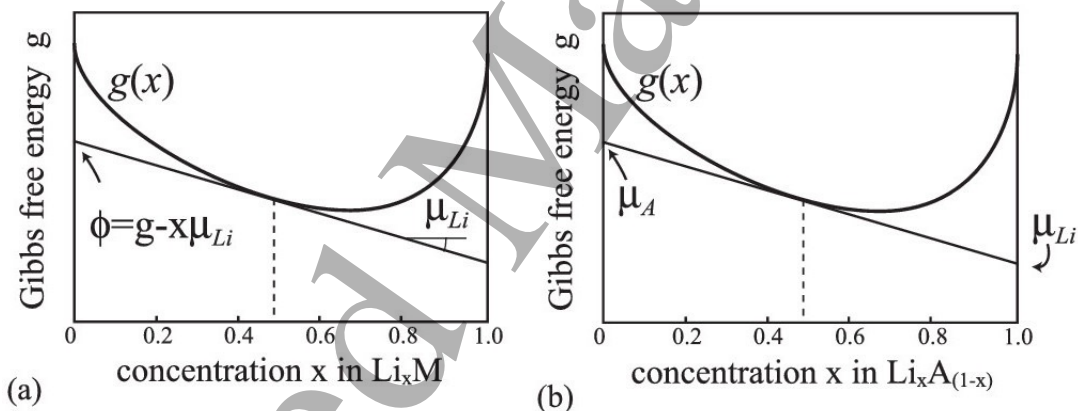


Figure 6: Representation of the connection between the Gibbs free energy, $G(x)$, the lithium chemical potential $\mu(x)$ in (a) an intercalation electrode and (b) an alloy electrode. Reprinted with permission from Ref. 9. Copyright 2020 American Chemical Society.

719 In the case of a Li-ion cell, the equilibrium cell voltage, $\phi(x)$, and the chemical potential
 720 of intercalated Li, $\mu(x)$, are related by:

$$\phi(x) = -\frac{\mu(x) - \mu_{\text{Li}}^{\text{ref}}}{nF}, \quad (27)$$

721 where $\mu_{\text{Li}}^{\text{ref}}$ is the chemical potential of the reference electrode, n is the number of electrons
 722 transferred per formula unit of intercalation host ($n = 1$ for Li-ion cells), and F is the Faraday

constant. The most convenient reference potential, both from the point of view of simulations and for comparison with experimental measurements of Li-ion half cells, is the bcc metallic Li anode. With a suitable choice of units for all potentials (μ expressed in eV per formula unit of intercalation host), equation 27 can be written much more simply as:¹⁶⁷

$$\phi(x) = -\mu(x) \quad (28)$$

The intercalated Li chemical potential is defined by:

$$\mu(x) = \left(\frac{\partial G(x)}{\partial N_{Li}} \right)_{p,T,N_{host}} = \left(\frac{\partial G(x)}{\partial x} \right)_{p,T,N_{host}}, \quad (29)$$

where G is the absolute (i.e. extensive) Gibbs free energy of Li dissolution into the host, p is pressure, T is the absolute temperature, and N_{host} and N_{Li} are the number of host and lithium atoms in the system, respectively. The subscripts p , T , and N_{host} will be implicitly assumed to be constant from now on and dropped, to simplify notation.

Similarly, it is well known that:

$$\frac{\partial G(x)}{\partial x} = \frac{\partial H(x)}{\partial x} - T \frac{\partial S(x)}{\partial x}, \quad (30)$$

where $H(x)$ and $S(x)$ are the enthalpy and entropy, respectively, per formula unit of host material.

We can use equations 28, 29, and 30 to get $\partial G/\partial x = -E_{OCV}$, then, taking the derivative of the OCV with respect to T and using the chain rule, we obtain:

$$\frac{\partial S(x)}{\partial x} = \frac{\partial E_{OCV}(x)}{\partial T} \quad (31)$$

and so:

$$\frac{\partial H(x)}{\partial x} = T \frac{\partial E_{OCV}(x)}{\partial T} - E_{OCV}(x) \quad (32)$$

Due to the units of electron Volts (eV) per formula unit for the potentials $H(x)$ and $TS(x)$, i.e. as in the conversion between equations 27 and 28, the usual factors of F have been omitted. In this way it is possible to simulate not only the equilibrium voltage, but split its contributions into enthalpy and entropy components. Both components can be experimentally measured^{91,93,100,169,170} and modelled through MC or mean field methods,^{89,91–93} providing additional properties for model validation purposes and to check the temperature dependence of those properties is modelled accurately. A good thermodynamic basis can then be used to derive dynamic properties, as outlined in the subsequent sections.

2.3.2 Activity coefficients of electrolytes

The activity coefficients of electrolytes (γ_j , $j = 1 \dots p$) describe the thermodynamics of non-ideal solutions.¹⁷¹ The activity coefficient of electrolytes can be computed from DFT+P-BE models, as described in section 2.2.1, by computing the electrolyte effect on solvation energies, $\Delta\Delta\Omega$:^{130,135}

$$\ln \gamma_j = \frac{\Delta\Delta\Omega_j[\{c_i^\infty\}]}{k_B T}, \quad j = 1 \dots p \quad (33)$$

For an electrolyte dissociating into p species, the mean activity coefficient can be calculated as:

$$\ln \gamma_{\text{mean}} = \frac{1}{p} \sum_{j=1}^p \ln \gamma_j \quad (34)$$

2.3.3 Diffusion coefficients

The *diffusion coefficient* is a term used to describe the rate of ion transport within a system. This term, however, has been used in literature to express several forms of diffusion, which characterise diffusion in a material in different ways. Here, we describe several commonly used forms of *diffusion coefficient*, in context of where they are used, focusing on bulk diffusion. Heitjans and Kärger gives a detailed description of diffusion along grain boundaries

1
2
3 and along surfaces (chapters 7 and 8).¹⁷²

4
5 760 Ionic transport within the electrodes and electrolyte plays a vital role in the kinetics of
6
7 761 a battery. It can be described fundamentally with flux expressions that relate ion fluxes to
8
9 762 chemical or electrochemical potential gradients. This is related by Fick's first law, where the
10
11 763 diffusion flux, \mathbf{j} , is described using the gradient of the concentration, c , via:

$$\mathbf{j} = -\mathcal{D}\nabla c, \quad (35)$$

12
13
14
15
16
17
18 764 where \mathcal{D} is denoted as the diffusion coefficient tensor or diffusivity tensor and implies
19
20 765 that \mathcal{D} varies with direction. In general, the diffusion flux and concentration gradient are
21
22 766 not always antiparallel. They are antiparallel for isotropic mediums. Heitjans and Kärger
23
24 767 discusses this in more detail.¹⁷²

25
26 768 Steady state methods for measuring diffusion coefficients, like the permeation method, are
27
28 769 directly based on Fick's first law.¹⁷³ In non-steady states, the diffusion flux and concentration
29
30 770 vary with time, t , and position x , and a balanced equation is necessary. For particles which
31
32 771 undergo no reaction this become the continuity equation:

$$\frac{\partial c}{\partial t} + \nabla \cdot \mathbf{j} = 0 \quad (36)$$

33
34
35
36
37
38
39 772 Combining equations 35 and 36 leads to Fick's second law, also called the diffusion
40
41 773 equation, which predicts how diffusion causes the concentration to change with time:

$$\frac{\partial c}{\partial t} = \nabla \cdot (\mathcal{D}\nabla c) \quad (37)$$

42
43
44
45
46
47
48 774 In diffusion studies with trace elements the material composition does not practically
49
50 775 change and \mathcal{D} is independent of the tracer concentration, presenting a concentration-independent
51
52 776 diffusion coefficient. For diffusion in multiple dimensions Fick's second law becomes:¹⁷⁴

$$\frac{\partial c}{\partial t} = \mathcal{D}\nabla^2 c \quad (38)$$

1
2
3
4 777 The temperature dependence of the diffusion coefficient is often described empirically by
5
6 778 an Arrhenius relation:

$$9 \quad \mathcal{D} = \mathcal{D}_0 \cdot \exp\left(-\frac{E_A}{k_B T}\right), \quad (39)$$

11
12 779 where E_A is the activation energy for the mass transport, D_0^T is the pre-exponential
13
14 780 factor, k_B is the Boltzmann constant, and T is the temperature.

15
16 781 From the microscopic point of view, the tracer diffusion coefficient can be defined by the
17
18 782 Einstein-Smoluchowski relation:^{175,176}

$$19 \quad \mathcal{D} = \lim_{t \rightarrow \infty} \frac{\langle r^2(t) \rangle}{2dt}, \text{ where } \langle r^2(t) \rangle = \langle (x(t) - x_0)^2 \rangle, \quad (40)$$

21
22
23
24
25 783 where, $\langle r^2(t) \rangle$ is the mean square displacement (MSD) of the particles after time t and
26
27 784 d is the dimensionality of the movement. This is also known as the *self diffusion coefficient*
28
29 785 and is the main approach used to calculate the diffusion coefficient in kMC and MD from
30
31 786 the atom trajectories. Van der Ven et al. discusses in greater detail.⁹

32
33 787 In atomistic modelling, diffusion coefficients can also be calculated using other approaches,
34
35 788 such as Green-Kubo. The Green-Kubo approach is linked to the Einstein-Smoluchowski re-
36
37 789 lation approach, equation 40. Both approaches assume that particle dynamics can be well
38
39 790 approximated by Brownian motion. As described in equation 40, Brownian motion of inde-
40
41 791 pendent particles can be expressed by the MSD of a particle proportional to time. This can
42
43 792 also be termed as the integral of the velocity. The Green-Kubo approach is derived from the
44
45 793 integration of the velocity (or current) autocorrelation function. Assuming that dynamics
46
47 794 is ergodic, the diffusion coefficient can be calculated using a linear fit to the velocity auto-
48
49 795 correlation function. Averaging is applied to this, for example, a time average for a selected
50
51 796 particle type, a sample average, or an ensemble average.

797 2.3.4 Vibrational and Thermal Properties

798 While MD simulates the evolution of a chemical system over time, lattice dynamics is an
 799 approach that models the underlying vibrations. In crystalline solids, extended vibrations
 800 can be described as phonons with a characteristic frequency and wavevector, $\omega(q)$. A unit
 801 cell with N atoms contains $3N$ phonon modes. The theory of phonons provides a direct
 802 connection between microscopic atomic motion and macroscopic properties including specific
 803 heat capacity, IR and Raman spectra, and thermal expansion.^{177–179}

804 While assuming that phonons are harmonic simplifies the theoretical description, it is
 805 necessary to include anharmonic effects to describe phenomena such as heat transport. The
 806 lattice thermal conductivity, κ , depends on the lifetime of each phonon, i.e. how long it
 807 persists before decaying, which is an anharmonic process. Formally, the thermal conductivity
 808 given by the product of the modal heat capacity, (C_V), the group velocity, v , and the phonon
 809 mean free path, $v \times \tau$ (where τ is the phonon lifetime). The macroscopic κ is obtained by
 810 summing over band indices, v , averaging over wavevectors, q , and normalising by the unit
 811 cell volume:

$$\kappa = \frac{1}{NV_0} \sum_{qv} C_{V,qv} v_{qv} \otimes v_{qv} \tau_{qv}, \quad (41)$$

812 where N is the number of unit cells in the crystal (number of wavevectors in the Brillouin
 813 zone summation) and V_0 is the volume of the crystallographic unit cell.

814 The heat capacity and group velocity can be extracted from the harmonic phonons, which
 815 are readily accessible from calculations based on electronic structure methods or potentials-
 816 based potential methods. The lifetime of each phonon mode is more demanding to compute
 817 and is often performed within a many-body perturbation theory expansion of phonon-phonon
 818 interactions. One approximation is to consider only the leading term of three-phonon cre-
 819 ation and annihilation.¹⁸⁰ However, higher-order processes may limit the lifetimes, depending
 820 on the material and temperature. There are a range of packages available to compute the

821 terms in equation 41 including PHONO3PY¹⁸⁰ (recently applied to LiCoO₂ and NMC cath-
822 odes),^{181,182} ALAMODE,¹⁸³ and SHENGBTE.¹⁸⁴

823 3 Anodes

824 3.1 Introduction

825 Critical to the success of lithium-ion batteries (LiBs) was the development of graphite-based
826 anodes. Graphite proved to be ideal for this application, due to its low (de)-intercalation
827 potential, only slightly higher than that of metallic lithium, and high theoretical gravimetric
828 capacity of 372 mAh g⁻¹. However, many key degradation mechanisms in present-day LiBs
829 that lead to their eventual failure, including cracking/reformation of the solid-electrolyte
830 interphase (SEI) and lithium plating, are still intimately connected with graphite-based
831 anodes.^{185,186} The understanding of these mechanisms is still far from complete and leads
832 to complex, non-linear degradation behaviour that is difficult to predict,¹⁸⁷ motivating the
833 development of multiscale models with a descriptive and predictive capability. A critical
834 starting point for these models is a physically accurate atomistic description of the graphite
835 and its interface with organic electrolytes.

836 The possibility to form Li-graphite intercalation compounds (Li-GICs), also known as
837 “stages”, up to a stoichiometry of LiC₆, was known in 1975, albeit at that time it was only
838 possible to form them by heat treating powders.¹⁸⁸⁻¹⁹⁰ Initial attempts to electrochemi-
839 cally intercalate lithium into graphite resulted in co-intercalation of the organic solvent and
840 exfoliation of the graphite.¹⁹¹ In 1983, Yazami and Touzain reported the first successful
841 intercalation into graphite using a solid polymer electrolyte.¹⁹² Fong et al. found that re-
842 versible lithium intercalation could be achieved in liquid organic electrolytes using ethylene
843 carbonate (EC) as part of the solvent, which finally enabled the formation of a stable SEI on
844 the graphite surface.¹⁹³ Mixtures of EC and dimethyl carbonate (DMC) were developed by
845 Tarascon and Guyomard in 1993¹⁹⁴ and present-day graphite-based LiBs are still primarily

1
2
3
4 846 based on this electrolyte mixture. The key challenge was finding a solvent chemistry that
5
6 847 provided sufficient ionic conductivity, did not decompose significantly at the ~ 4 V cathode
7
8 848 potential, while also avoiding co-intercalation into the graphite and producing a stable SEI
9
10 849 on its surface. Further incremental improvements in performance have since been achieved
11
12 850 through additional additives and, more recently, the inclusion of small amounts of silicon in
13
14 851 the anode as a secondary material.

15 852 This section predominantly focuses on graphite, since it remains the primary anode elec-
16
17 853 trode material in the majority of commercial lithium ion (Li-ion) cells.¹⁴ Here, the experi-
18
19 854 mentally confirmed Li-graphite stages and the nomenclature necessary for atomistic models
20
21 855 of bulk behaviour are defined. Atomistic modelling in the graphite bulk is outlined, in-
22
23 856 cluding both thermodynamic and kinetic properties. The key graphite surfaces relevant
24
25 857 to understanding the initial intercalation are described, then moving to modelling at the
26
27 858 graphite edges and the interface with the electrolyte. Throughout, it is shown how these
28
29 859 models enable quantitative understanding of the physical mechanisms of Li intercalation
30
31 860 in the graphite bulk, the initial insertion at the graphite edges, and the interface between
32
33 861 graphite and the electrolyte. Along the way, the key experimentally observable parameters
34
35 862 are outlined, showing success stories of atomistic models to not only quantify and describe
36
37 863 those parameters but to also predict new behaviour. In some cases, quantitative disagree-
38
39 864 ment between model and experimental observations is also informative and can create new
40
41 865 research directions. Work linking atomistic and continuum models is presented in the case
42
43 866 of the technologically important SEI. Given the emerging importance of C/Si and C/SiO_x
44
45 867 composites in commercial anode materials, some of the challenges in atomistic modelling of
46
47 868 Si and related materials are summarised at the end. In the outlook, key remaining challenges
48
49 869 are presented for modelling not only graphite, but also next generation materials such as
50
51 870 silicides. Challenges related to metallic Li formation on graphite anodes, and the use of
52
53 871 metallic Li as an anode material, are also summarised in the outlook.

3.2 Bulk Properties

3.2.1 Graphite structure and Li-graphite stages

Graphite possesses a layered structure with carbon atoms forming a network of hexagons in each layer. The carbon atoms located within one layer are covalently bonded to each other, whereas the weak interlayer binding arises from the dispersion or van der Waals (vdW) interactions.^{76,188,189,189,195–197} The lowest energy stacking of the carbon layers is AB stacked (Figure 7b), but synthesised graphite structures also contain a small amount of rhombohedral (ABC-stacked) domains.¹⁹⁸

Li-graphite stages, also known as lithium-graphite intercalation compounds (Li-GICs), are lithium concentration-dependent structures of various stoichiometries.^{188,189,195,197,199} In Li-GICs, Li atoms form a 2D hexagonal ($\sqrt{3} \times \sqrt{3}$)R 30° superstructure, with Li atoms sitting directly above each other, as shown in Figure 7a. The stage number, n , denotes the number of graphene layers between each lithium-filled layer.^{188,195,197,200} The experimentally confirmed stages adopt different stackings in the carbon host lattice, as shown in Figure 7. The standard nomenclature for GICs¹⁸⁹ denotes the carbon stacking and Li occupancies: periodic carbon layer stackings along the [001] axis are designated by uppercase letters separated by Greek lowercase letters, if Li is intercalated between planes. For instance, fully lithiated Stage I LiC_6 ($x = 1$) adopts $A\alpha A\alpha A\alpha$ stacking.^{170,197,201} Here α denotes a lithium filled layer and x is the fraction of Li in Li_xC_6 ($0 \leq x \leq 1$).

Li-GICs vary not only in their lithium concentrations, but also in their carbon stackings. The current consensus of all known stages, including their carbon stackings and lithium stoichiometries, is tabulated in Table 1.

Experimental observation of these stages relies largely on probing the average interlayer carbon spacing through diffraction measurements. Probing the lithium orderings of Li-GICs through experimental techniques remains very difficult,^{71,91,197,207–209} but as shown in section 3.2.3, atomistic techniques shed light on these orderings.

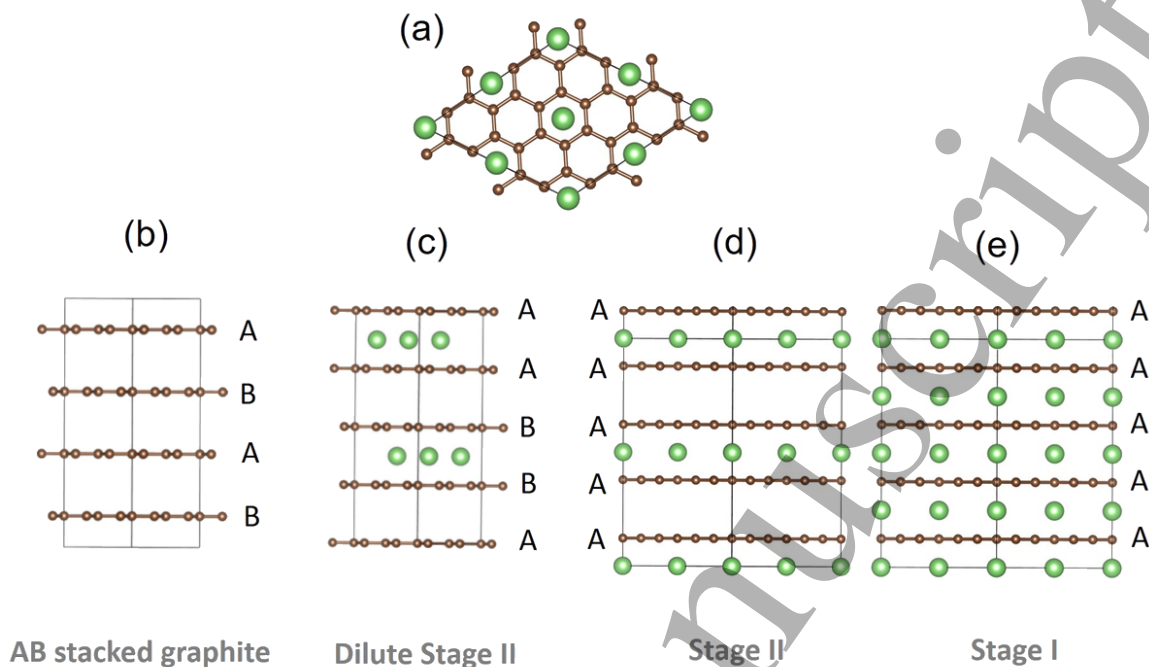


Figure 7: Structural representations of different carbon stackings in experimentally confirmed stages of graphite. (a) Top down view of carbon and lithium arrangements in Stages I and II. (b-e): side views, showing the layers occupied with Li and carbon stackings in (b) empty AB stacked graphite, (c) $A\alpha AB\beta B$ stacked dilute Stage II, with β indicating a lithium layer translated with respect to α , (d) $A\alpha AAA\alpha A$ Stage II and (e) $A\alpha$ stacked Stage I. Green represent Li atoms, while the brown indicate C atoms. Reproduced from Ref. 71 - Published by The Royal Society of Chemistry.

898 Thermodynamic and kinetic properties of Li-GICs have been studied by considering
 899 various structures of LiC_{6n} using Density Functional Theory (DFT),^{70,76,196,196,210–216} mean
 900 field,^{91,92,217} canonical and grand canonical Monte Carlo (MC),^{76,218,219} and kinetic Monte
 901 Carlo (kMC) simulation techniques.^{76,102,103,214,220} The rest of the section outlines electronic
 902 structure based studies of experimentally measurable bulk thermodynamic properties, before
 903 describing atomistic modelling of kinetic properties.

904 3.2.2 Equilibrium potential and measured open circuit voltage

905 Knowledge of the correct phase behaviour of an intercalation electrode is an important
 906 pre-requisite to building a dynamic model of the intercalation process. One of the most

Table 1: Overview of carbon stackings and stoichiometries of Li-graphite stages from the literature, where Latin characters denote carbon stackings and Greek characters denote Li-filled layers.^{188,189,195,197,200,202–206}

Stage	Stacking	x in Li_xC_6
Stage I	$A\alpha A\alpha$	$x = 1$ (LiC_6)
Stage II	$A\alpha AA\alpha A$	$x = 0.5$ (LiC_{12})
Dilute Stage II (IID)	$A\alpha AB\beta B$	$x \approx 0.33$ (LiC_{18})
Stage III	$A\alpha AB/A\alpha ABA\alpha AC$	$x \approx 0.22$ (LiC_{27})
Stage IV	Unknown	$x \approx 0.17$ (LiC_{36})
Dilute Stage I (ID)	AB	$x \approx 0.083$ (LiC_{72})
Graphite	AB	$x = 0$

directly measurable observables is the experimental open circuit voltage (OCV), which is related to the equilibrium potential determinable from atomistic methods (c.f. Methods section 2.3.1). The OCV is an important input parameter in continuum models and is also used in control models, for example, to determine the state of charge of a battery within a Battery Management System (BMS).²²¹ Inputting a polynomial fit to the experimental OCV at an arbitrary temperature without physical meaning could lead to incorrect predictions of temperature-dependent behaviour in these models. Therefore, to attain predictive, dynamic models on longer length scales, atomistic models of the OCV and equilibrium potential are important and can contribute to physically more robust and more predictive temperature dependence in continuum and control models.^{9,166}

In any intercalation electrode, ordered phases give rise to steps in the OCV. In the lithium-graphite system, the ordered stages described in section 3.2.1 therefore give rise to characteristic features in OCV versus x curves^{195,200} as shown in Figure 8. The influence of the Li-graphite stages on the measured OCV at $T \approx 25$ °C has been well characterised,^{195,199,200,207–209,222–224} although a more thorough study of the temperature dependence of the OCV has only been conducted more recently.⁷¹ Each OCV plateau represents a different two-phase equilibrium. At zero Kelvin, there is no contribution from configurational entropy and each step represents a sudden transition between two different two-phase equilibria. This is the behaviour that can be captured using DFT code. The cluster expansion

framework, described in more detail in the Methods section 2.1.4, allows the accuracy of DFT to be retained to explore configurational degrees of freedom. Thermal fluctuations can be included by determining effective cluster interactions (ECIs) from fitting DFT data and using these as parameters within an MC method (section 2.1.5). The entropy contribution at temperature, $T > 0$ K has the effect of smoothing out those steps,^{71,91,217,225} which is caused by some limited single phase solubility around the stoichiometric composition. This can be seen in experimentally measured OCV profiles at $T \approx 300$ K, such as the ones shown in Figure 8.

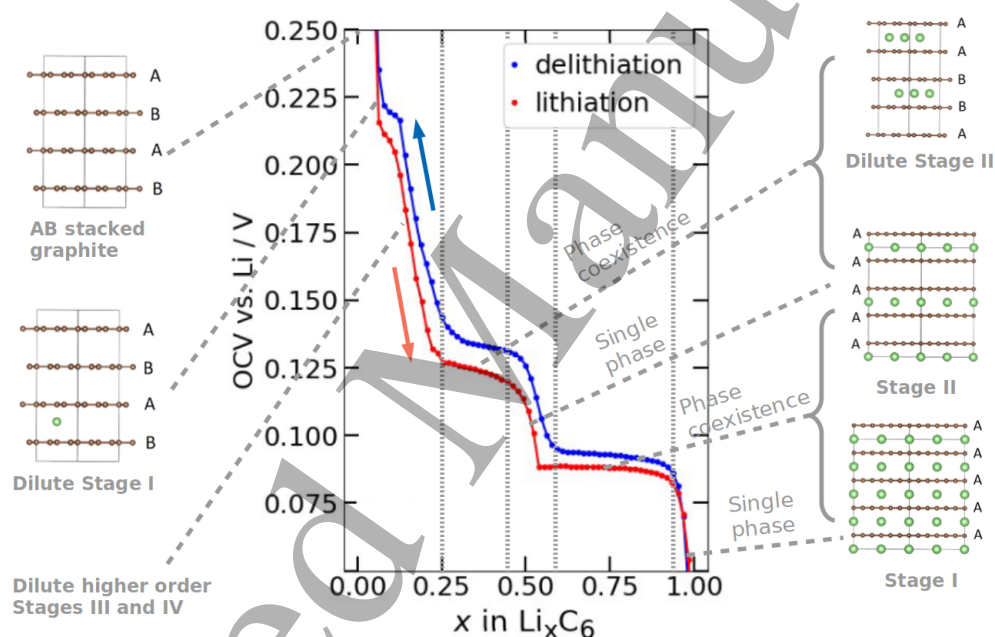


Figure 8: Illustration of OCV features of lithium in graphite using experimental data from ref. 91. Lithiation and delithiation behaviour is overlaid; labelled stages are linked to the lithiation profile, which is closer to the true equilibrium potential. Reproduced from Ref. 71 - Published by The Royal Society of Chemistry.

The equilibrium potential versus x can be modelled through atomistic techniques. For example, Li-graphite phase diagrams were constructed and the equilibrium potential was modelled by Persson et al.⁷⁶ They performed a cluster expansion of Li degrees of freedom from total energy DFT calculations, by fixing the carbon stacking degrees of freedom. Those degrees of freedom represent the host lattice stackings in the experimentally confirmed stages shown in Figure 7. Typically, different cluster expansions are performed in Li-vacancy lattices

1
2
3
4 940 of the respective hosts,^{71,76,196} to account for carbon stacking degrees of freedom with the
5
6 941 result from a more recent work⁷¹ represented in Figure 9a. Within this work, AA, AAB, B, and
7
8 942 AB stackings of the host lattice were considered, representing all stages of order up
9
10 943 to II (c.f. Figure 7). Reference states at $x = 0$ and $x = 1$ were used in AB and AA
11
12 944 stackings, respectively, to linearly correct the free energy and thus obtain the formation
13
14 945 energies at each lithium concentration. The convex hull over all stackings represents the
15
16 946 lowest energy structure for a given x value. A common tangent construction between the
17
18 947 different stackings represents two-phase coexistence. The slope of the resultant ground state
19
20 948 free energy profile, $dG(x)/dx$, (equation 29) equals the intercalated Li chemical potential,
21
22 949 μ , where $-\mu$ is equivalent to the equilibrium potential at $T = 0$ K, as represented more
23
24 950 generally in Figure 6 and the surrounding discussion in the Methods section.

25
26 951 The phase behaviour of the lithium-graphite system, and therefore the voltage profile,
27
28 952 is sensitive to the vdW interactions between the carbon planes.^{76,210,211} Conventional DFT
29
30 953 approaches without accounting for vdW interactions do not correctly reproduce the structure
31
32 954 and energetics of graphite and Li-GICs^{76,210,211} (Figure 9b). Therefore, vdW-corrected DFT
33
34 955 approaches, for example DFT-D2⁴⁵ and DFT-D3,⁴⁷ are important for correctly describing
35
36 956 the phase behaviour and dynamics of graphite and Li-GICs. Persson et al. considered the
37
38 957 vdW interaction as a constant.⁷⁶ This approximation can accurately describe the step height
39
40 958 at $x = 0.5$ (the height difference represents the difference between the chemical potentials
41
42 959 in the Stage I-Stage II and Stage II-Stage IID coexistence regions). The simulated voltage
43
44 960 profile Figure 9b (blue line), shows that the constant vdW interaction results in a systematic
45
46 961 error in the voltage scale.

47
48 962 Voltage profiles like the ones shown in Figure 9b represent the ground state behaviour,
49
50 963 at $T = 0$ K. As an additional step, cluster expansions can be used to parameterise an MC
51
52 964 simulation (section 2.1.5) and therefore include thermal fluctuations. The lithium-graphite
53
54 965 phase diagram, Figure 9c, has been constructed by performing a combination of canonical
55
56 966 and grand canonical MC simulations at different temperatures.⁷⁶

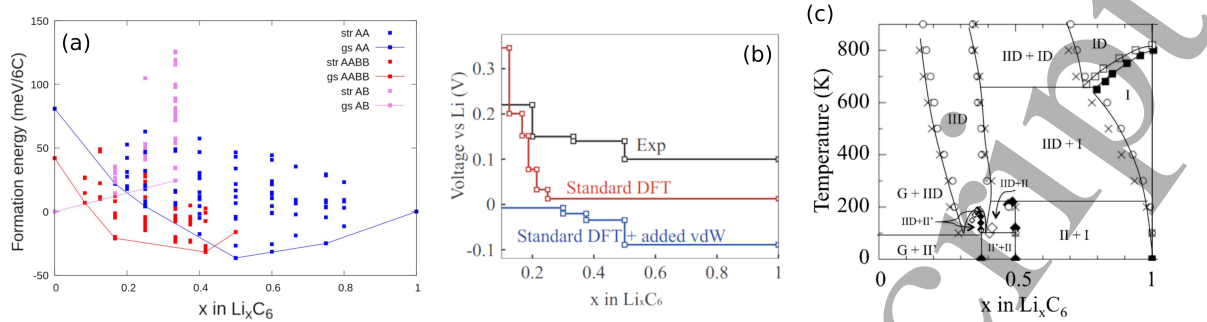


Figure 9: (a) Formation energies of lithium in graphite performed with different carbon stackings. All calculated structures are denoted “str” while the “gs” represent the ground state structures in each of the three carbon stackings: AB, AAB, AA. (b) Phase diagram of lithium in graphite, determined by performing Monte Carlo calculations parameterised by effective cluster interactions from Density Functional Theory calculations. (c) zero kelvin equilibrium potential profiles dependent on different levels of van der Waals corrections. (a) Reproduced from Ref. 71 - Published by The Royal Society of Chemistry; (b-c) Reprinted with permission from Ref. 76. Copyright 2010 American Chemical Society.

967 The experimental OCV and the theoretical equilibrium potential are often, erroneously,
 968 considered to be equivalent. However, the OCV refers to the measured cell voltage without
 969 any external current and drifts with time. With sufficient time, it is often assumed the
 970 OCV will eventually relax to the equilibrium potential, but meta-stable states can occur
 971 that show no variation over experimental time scales of hours or even days.^{71,226,227} The
 972 true equilibrium potential, as defined in equation 29, is a thermodynamic quantity and
 973 is not history-dependent.^{9,71} Experimentally, a hysteresis of the measurable OCV between
 974 lithiation and delithiation is observed for Li/graphite half cells^{71,170,195,200,206,207,223,228,229} as
 975 shown in Figure 8. Hysteresis is observed even after several hours of relaxation time and
 976 for $T > 298$ K, clearly demonstrating that the measured OCV is not a simple function
 977 of the thermodynamic ground state. Hysteresis therefore poses an interesting challenge to
 978 atomistic modellers.

979 It was recently shown that (de)-lithiation hysteresis in graphite is intimately connected
 980 with disorder in Stage II configurations and appears to be associated with a different carbon
 981 stacking pathway in each cycling direction.⁷¹ Notably, energetic barriers to translate between

ground state configurations, as determined through climbing image nudged elastic band (CI-NEB) calculations (Methods section 2.1.3), do not explain the hysteresis in graphite. Non-ground state configurations are involved in the delithiation direction. Understanding that behaviour requires the configurational entropy of Li/vacancy arrangements to be quantified, which is explained in more detail in the next section.

3.2.3 Entropy

The internal energy of intercalation electrodes arises largely from electrostatic interactions between the constituents. Those interactions can be well approximated by DFT. An atomistic description of the entropic behaviour of intercalation electrodes, $S(x)$, is also needed to correctly model thermal behaviour at $T > 0$ K. The partial molar entropy, $dS(x)/dx$, is an experimentally accessible quantity, which can be probed by monitoring how the OCV, described in the previous section, varies with temperature (equation 31, c.f. refs. 71,91,93,100, 169,170,230 for further details). $S(x)$ is a sum of configurational, vibrational, and electronic components.^{169,225} For lithium in graphite, the electronic component can be neglected and the vibrational component can be well approximated by assigning a Debye temperature to all of the vibrational modes,^{169,225} or by computing phonon spectra from electronic structure methods^{196,231} (c.f. section 2.3.4). The quantity that shows the greatest difference with lithium concentration, x , is the configurational entropy of Li/vacancy arrangements, S_{config} . Because of the staging phenomena described in section 3.2.1, S_{config} strongly deviates from ideal solid solution behaviour for Li in graphite.

The partial molar entropy $dS(x)/dx$ is difficult to interpret atomistically and so integration is required to get S_{config} :

$$\int_{x'=0}^{x'=x} \left(\frac{\partial S_{\text{config}}(x')}{\partial x'} \right) dx' = S_{\text{config}}(x) \approx S(x) - S_{\text{vib}}(x), \quad (42)$$

where S_{vib} is the vibrational entropy approximated by Debye temperatures.^{169,225} The integration constant is $S_{\text{config}} = 0$ at $x = 0$, because there can be no Li disorder in pure

1006 graphite.

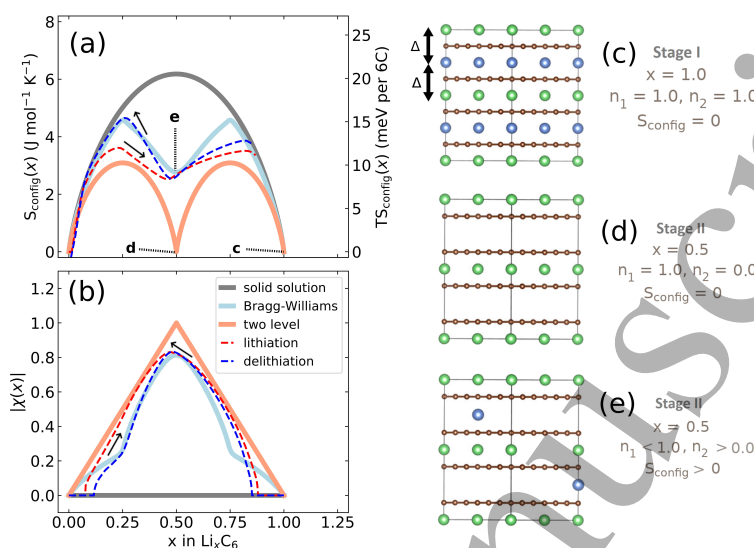


Figure 10: (a) Configurational entropy obtained at $T = 320$ K: *dark grey solid line*: ideal solid solution; *light blue solid line*: Bragg-Williams solution; *orange solid line*: sequential two level solid solution; *red dashed line*: experimental lithiation; *blue dashed line*: experimental delithiation. (b) Order parameter $|\chi|$, as described in the main text, labelled as in (a). In (a), select points (c-e) are indicated and schematic representations of the lattice occupations of Li in levels n_1 (green balls) and n_2 (blue balls) are shown on the right. Reproduced from Ref. 71 - Published by The Royal Society of Chemistry.

1007 Dashed lines in Figure 10a denote post-processed experimental data obtained during
 1008 lithiation and delithiation using equation 42 from ref. 71. Qualitatively, this shows more
 1009 configurational Li disorder, i.e. larger entropy, is obtained during delithiation than lithiation.
 1010 The lithium arrangements can be split into sublattice occupancies n_1 and n_2 arranged in
 1011 alternate planes, as shown visually in Figure 10c-e. Each sublattice occupancy is linked to
 1012 the degree of lithiation, x , via $x = (n_1 + n_2)/2$.

1013 Solid lines in Figure 10a-b indicate three hypothetical cases. The orange solid line denotes
 1014 solid solution (random) filling of Li into one of the sublattices for $x < 0.5$, followed by
 1015 solid solution filling of the other sublattice, resulting in two maxima. Note that S_{config}
 1016 is zero in Stage II at $x = 0.5$ (c.f. Figure 10d). The dark grey line shows the result
 1017 for an ideal solid solution, if Li were to fill all available sites at random, i.e. $n_1 = n_2$
 1018 for all x . The blue solid line is the solution to a Bragg-Williams model,^{91,217} assuming

1
2
3
4 1019 only nearest neighbour repulsive pairwise lithium interactions between planes of $\Delta = 75$
5
6 1020 meV and no in-plane interactions. That model allows a direct evaluation of the partition
7
8 1021 function (c.f. equation 10) by enumerating through all possible arrangements of Li atoms
9
10 1022 on the two sublattices for a given x within the canonical ensemble. The out-of-plane Li-
11
12 1023 Li interactions are treated within a mean field (non-local) approximation to simplify the
13
14 1024 computation (details and formulae in refs. 91,92,217).

15
16 1025 The Bragg-Williams model produces a behaviour in $S_{\text{config}}(x)$ between that expected
17
18 1026 for the solid solution and sequential two level filling. At $x = 1$, there is a net repulsion
19
20 1027 on each Li atom of 2Δ , as represented in Figure 10c. At $x = 0.5$, one of the sublattices
21
22 1028 becomes preferentially filled, as represented schematically in Figure 10e. In contrast, a
23
24 1029 perfect Stage II structure as predicted by sequential two level filling (Figure 10d), would
25
26 1030 result in $S_{\text{config}}(0.5) = 0$.

27
28 1031 These results can be understood within the framework of order parameters.⁸¹ The relevant
29
30 1032 staging order parameter, $\chi(x) = n_1 - n_2$, is shown in Figure 10b. Formally, $\chi(x)$ takes values
31
32 1033 between -1 and $+1$, but only the absolute value is meaningful in this case. If $|\chi(x)| = 1$,
33
34 1034 then only one layer is filled with Li, representing maximal staging order. If $\chi(x) = 0$, both
35
36 1035 sublattices are occupied with equal probability, maximising disorder and hence no staging
37
38 1036 order is observed.

39
40 1037 Greater interlayer Li disorder is observed during delithiation below $x = 0.5$. The Li
41
42 1038 ordering, as described by the order parameter, closely follows the Bragg-Williams model.
43
44 1039 This is expected if the host lattice remains in a metastable AA stacking. The lithiation
45
46 1040 behaviour shows a configurational entropy closer to solid solution filling of half the sites,
47
48 1041 which would be expected in AABB stacking, since only half the interlayers (i.e. those locally
49
50 1042 adopting AA or BB stacking) provide favourable Li insertion sites. As shown in Figure 9a,
51
52 1043 this is the ground state stacking configuration for $x < 0.5$.

53
54 1044 The wider implication of these results is that the transformations between the stackings in
55
56 1045 graphite, and possible stacking dynamics in other layered intercalation hosts, deserve more

1
2
3
4 1046 attention. These phase transformations not only create a challenge from a cell diagnosis
5
6 1047 point-of-view, they could also be partially responsible for mechanical degradation, fracture,
7
8 1048 unstable interfaces and loss of active material. Phase transformations should be described in
9
10 1049 a rigorous way in continuum models. It is not sufficient to approximate the guest ions as an
11
12 1050 ideal solid solution as, for instance, done in the popular Doyle-Fuller-Newman (DFN)-type
13
14 1051 models.

15
16 1052 It is worth noting that the host lattice ordering of graphite obtained in electrochemical
17
18 1053 conditions is difficult to access from experimental analysis. In-operando x-ray and neutron
19
20 1054 diffraction experiments allow the interlayer carbon separation to be obtained.^{189,195,200,204–206}
21
22 1055 However, it is extremely difficult to obtain the stacking displacements within each carbon
23
24 1056 layer, as the superstructure peaks associated with these displacements¹⁹⁷ are weak and ob-
25
26 1057 scured by peaks from the current collector.^{206,208,209} A reason as to why there is still some
27
28 1058 dispute in the literature regarding the Li-graphite stages of order greater than 2, as high-
29
30 1059 lighted earlier in 3.2.1, is that these in-plane displacements cannot be completely elucidated.
31
32 1060 These displacements influence the lithium ordering in each atomic layer, which is even harder
33
34 1061 to determine than the carbon ordering and is currently not feasible even in neutron diffraction
35
36 1062 experiments. It is also not possible to determine this information through local probes such
37
38 1063 as nuclear magnetic resonance (NMR) and Raman scattering.^{222,232} It is only through the
39
40 1064 combination of atomistic and statistical mechanical models, together with entropy profiling
41
42 1065 measurements, that the proportion of lithium in the different layers in Stage II configura-
43
44 1066 tions could be quantified.⁷¹ With regard to systems other than lithium-graphite, atomistic
45
46 1067 techniques could enable lithium guest orderings to be quantified by means of order parame-
47
48 1068 ters, which, for the reasons explained above, is information inaccessible through experiment
49
50 1069 alone. Synergies between models of host and guest ion orderings with appropriate exper-
51
52 1070 imental characterisation will enable a new generation of modelling tools that can predict
53
54 1071 these phenomena with greater accuracy.^{9,233}

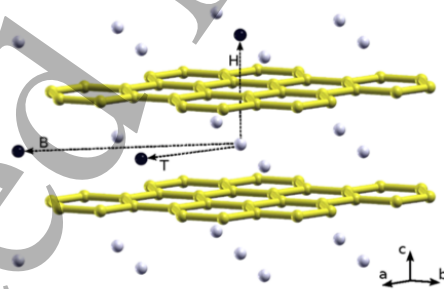
55 1072 As shown in the next section, orderings in Li-GICs have implications for the dynamics
56
57
58
59
60

1
2
3
4 1073 of Li intercalation as well.

5 6 7 1074 **3.2.4 Ion diffusion in Li-GIC**

8
9 1075 Having outlined the use of atomistic techniques to evaluate observable thermodynamic prop-
10 1076 erties of anodes and, in particular, graphite, this section focuses on the computation of bulk
11 1077 dynamic properties by DFT and kMC approaches.

12
13
14
15 1078 Li diffusivity is similar for stage I and stage II Li-GICs,⁷⁶ with the probable Li migration
16 1079 pathways for LiC_{6n} illustrated in Figure 11.²¹⁰ These pathways were determined from DFT
17 1080 calculations within a CI-NEB approach. Here, Li diffusion across the graphite layers through
18 1081 a carbon hexagon hollow (H) are denoted as the through-plane pathway. The in-plane or
19 1082 two-dimensional Li migration along the crystallographic *ab* plane occurs either by a bridge
20 1083 (B) migration pathway, where Li passes through a rectangle of carbon atoms of subsequent
21 1084 layers, or a top (T) migration pathway, where Li passes in between two congruent carbon
22 1085 atoms.



23
24
25
26
27
28
29
30
31
32
33
34
35
36
37
38
39
40
41
42
43
44
45
46
47
48
49
50
51
52
53
54
55
56
57
58
59
60
Figure 11: Li migration pathway in LiC_6 . In the through-plane pathway, lithium migrates through a carbon hexagon hollow (H) along the crystallographic *c* direction. The in-plane pathways are denoted as bridge (B) and top (T). Reprinted (adapted) with permission from Ref. 210. Copyright 2014 American Chemical Society.

1086 Diffusion proceeds in the aforementioned through-plane pathways and in-plane pathways
1087 via the Frenkel and vacancy mechanisms, respectively. Thinius et al. showed that Li diffu-
1088 sion along the crystallographic *c* direction is kinetically prohibited, due to a large activation

1
2
3
4 1089 energy barrier.²¹⁰ The calculated activation energy for this migration pathway is extremely
5
6 1090 high (8.00 – 8.23 eV), therefore, the Boltzmann probability for diffusion through pristine
7
8 1091 graphene planes is negligible at $T = 300$ K. It is therefore likely that diffusion in the c
9
10 1092 direction occurs via grain boundaries.²¹⁶ In contrast, the activation energy for Li diffusion
11
12 1093 in the crystallographic ab plane is much lower (0.42 – 0.52 eV), showing that in Li-GICs, Li
13
14 1094 diffuses mostly within the intercalation layers.²¹⁰ In the literature, DFT-based theoretical
15
16 1095 investigations provide the same qualitative trends for ion diffusion mechanisms in Li-GICs
17
18 1096 and the calculated activation barriers vary slightly, but are within the same order of magni-
19
20 1097 tude.^{215,216,234,235}

21
22 1098 In order to gain insights into the Li diffusion process in graphite, far from equilibrium and
23
24 1099 under fast charging conditions, Garcia et al. simulated a range of compositions between stage
25
26 1100 I and IV, i.e. dilute Stage I.²¹¹ Their study determined reduced activation barriers in the
27
28 1101 in-plane migration pathways (0.2 – 0.32 eV), which is attributed to the presence of a higher
29
30 1102 number of electrons compared to Li^+ ions, occurring at the very beginning of the lithiation
31
32 1103 cycle during fast charging conditions. This extra charge increases the interlayer spacing in
33
34 1104 the diffusion layer and adjacent channels, increasing the Li diffusivity.²¹¹ Ji et al. investigated
35
36 1105 the anisotropic strain effects on lithium diffusion in graphite anodes using DFT and kMC
37
38 1106 simulations.²¹⁴ According to their study, the activation energy for Li diffusion in unstrained
39
40 1107 Li_xC_{6n} is 0.48 eV. The tensile strain along the direction perpendicular to the graphite planes
41
42 1108 facilitates in-plane Li diffusion by reducing the energy barrier and vice versa.²¹⁴

43
44 1109 Gavilán-Arriazu et al. have recently simulated the dynamic properties of lithium inter-
45
46 1110 calation in graphite using kMC.^{102,103,220} These models considered exchange of Li with the
47
48 1111 solution on one side of a slab (Figure 12), with only interplanar Li transport allowed, based on
49
50 1112 the diffusion barrier arguments presented above. Energetic barriers for Li exchange into/out
51
52 1113 of the graphite were calculated assuming Butler-Volmer kinetics, based on experimental ex-
53
54 1114 change current density data. Interplanar diffusion barriers were computed using random
55
56 1115 walk theory, based on experimental data in the dilute limit. Respective barriers of 0.655 eV

1
2
3
4 1116 and 0.370 eV for exchange and interplanar diffusion were obtained. This approach enabled
5
6 1117 the simulation of several different dynamic properties dependent on lithium concentration,
7
8 1118 x ,^{102,102} sweep direction,¹⁰² and temperature,¹⁰³ with a few of these highlighted in Figure 13.
9
10 1119 Additionally, the importance of metastable Daumas-Hérold orderings in Stage II configura-
11
12 1120 tions²²⁰ and clogging of lithium at the interface¹⁰² leading to slow Li insertion kinetics were
13
14 1121 identified as important challenges limiting the kinetics of the lithium (de)insertion processes.

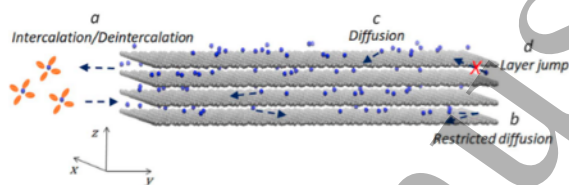


Figure 12: Representation of insertion and diffusion of lithium in graphite in a kinetic Monte Carlo model. Reproduced from Ref. 103 - Published by the Journal of The Electrochemical Society.

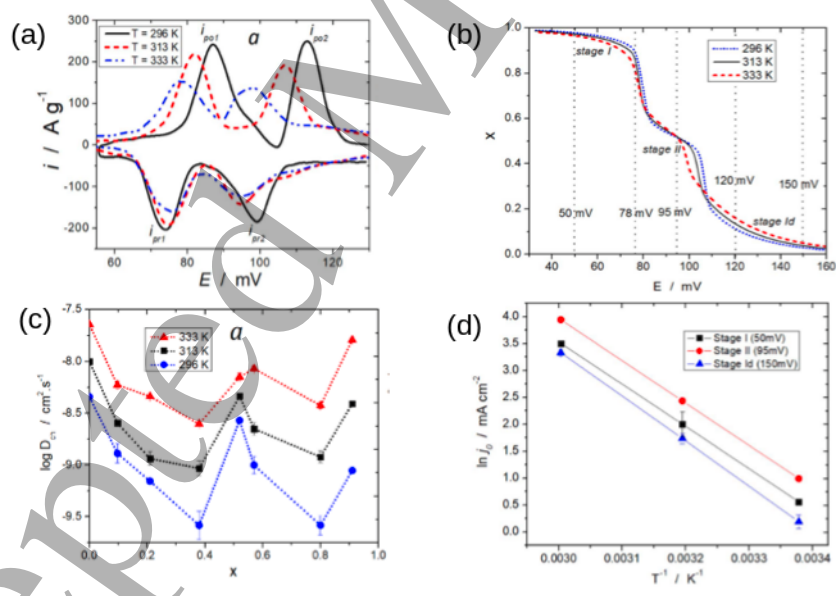


Figure 13: Effect of temperature on the dynamic behaviour of lithium insertion in graphite. (a) voltammograms (b) voltage profiles (isotherms) (c) diffusion coefficients, (d) exchange current density, insertion and diffusion of lithium in graphite in kMC model. Reproduced from Ref. 103 - Published by the Journal of The Electrochemical Society.

1122 Having described modelling of the thermodynamics and bulk Li diffusion in graphite, the
1123 following section will focus on another important aspect for a multiscale model: the structure

1124 and dynamics of the graphite edges.

1125 3.3 Graphite Surfaces and Interfaces

1126 3.3.1 Possible graphite surfaces and their stability

1127 As discussed above, investigating the bulk properties of lithium is key to understanding Li
 1128 intercalation kinetics and (dis)charging rates in graphite. However, Li exchange occurs be-
 1129 tween the graphite surfaces and the electrolyte, hence a multiscale model needs to include
 1130 these phenomena. Addressing the surface properties of graphite would improve the under-
 1131 standing of (dis)charging behaviours at graphite anodes and possibly suggest how to enhance
 1132 the (dis)charging rates.

1133 As shown in Figure 14 and section 3.2, graphite consists of multiple stacked graphene
 1134 layers. One of the exposed surfaces is the basal plane or the (001) surface, which has been
 1135 widely investigated in both the theoretical and experimental studies.^{76,210,235–237} In contrast,
 1136 the non-basal planes attract less attention, due to their complicated edge morphology. Re-
 1137 cently, experimental studies characterised the SEI formation and growth along the graphite
 1138 edges as opposed to the basal plane,^{238,239} indicating the importance of the graphite non-
 1139 basal plane for facilitating Li intercalation.

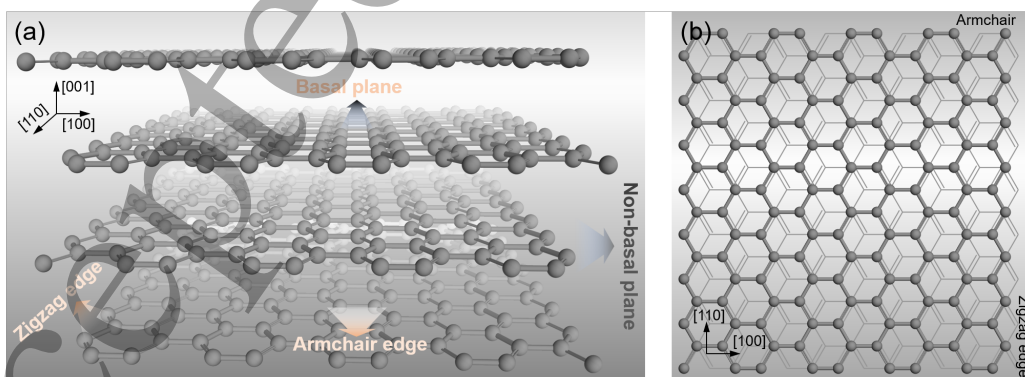


Figure 14: (a) structures of the basal plane and the non-basal plane of graphite. The latter plane consists of different edges of graphites, such as armchair edge and zigzag edge. (b) topological geometries of graphite edges.

1140 Thinius et al. investigated the stability of various low index graphite surface planes in-

cluding the (001), (110), and (100) planes. The calculations were performed using dispersion corrected DFT approaches.^{46,48} The surface energies of these planes were found to go in the order (001) < (110) < (100),²⁴⁰ indicating that the (001) surface (the basal plane) is the most energetically favourable. However, this plane does not favour Li intercalation, due to the high diffusion barrier required for Li to go through the carbon hexagon,^{76,210} as highlighted in the previous section on ion diffusion in Li-GICs (sec 3.2.4. Li intercalation of graphite particles must therefore proceed either via defects in the (001) plane or via the non-basal planes.

The (100) surface consists of nanoribbons with a zigzag edge, whereas the (110) surface adopts an armchair conformation. The relatively unstable surface planes, such as the (100) plane, can be stabilised by various procedures, including chemisorption of oxygen atoms.²⁴¹ It was found that the oxygen functional groups not only stabilise the graphite edges, but are also critical for the formation of the SEI layer near the edge, thereby preventing graphite exfoliation.²⁴² Investigating those non-basal planes and their effects on Li intercalation are therefore important and are addressed in the following section.

3.3.2 Surface Effect on Intercalation Energy

Understanding the nature of Li intercalation in graphite is important for optimisation of the anode material. As described above, Li intercalation in the bulk of graphite has been widely investigated.^{76,210,235,236,243} Experimental Li diffusivities in graphite have been reported, ranging from $10^{-6} - 10^{-14} \text{ cm}^2 \text{ s}^{-1}$.^{235,244-246} However, DFT calculations⁷⁶ based on bulk graphite indicate that Li diffusion coefficients based on the AABB and AA stacked graphite are around $10^{-7} \text{ cm}^2 \text{ s}^{-1}$ and decrease slightly with increasing Li concentration.⁷⁶ The variability between reported experimental diffusion coefficients arises from a combination of the staging dynamics and the anisotropy of Li diffusion (through versus into the basal plane). There is also a difference between the surface morphologies of different types of graphite, i.e. the proportion of zigzag and armchair edges and their surface chemical terminations, implying

possible differences between the electronic behaviour and charge transfer kinetics dependent on edge morphology and termination. Therefore, investigation beyond the bulk properties of graphite is necessary to optimise the overall rate performance of graphite electrodes. As described in section 3.3, the basal plane is relatively inert towards Li intercalation.²¹⁶ The non-basal plane, consisting of different edge morphology, attracts more attention due to observations of Li intercalation and SEI growth.^{238,239} Uthaisar and Barone studied the Li adsorption and diffusion on the edged graphene system using DFT.²⁴⁷ The graphene edges were found to affect not only Li adsorption but also the diffusion coefficient. Narrower graphite nanoribbons showed faster delithiation behaviour than the larger sized graphene, due to the topological effect of graphene edges. This highlights that an in-depth knowledge of interface effects is needed to understand Li intercalation rate and enable rational optimisation of the battery performance.

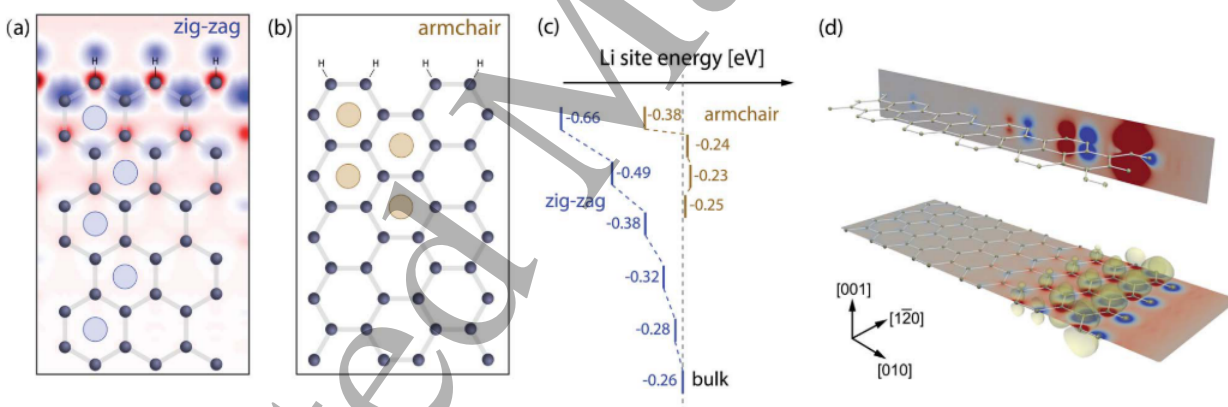


Figure 15: Structures of the zigzag-edged graphite (a) and the armchair-edged graphite (b). (c) shows the energy profile of Li adsorption in edged graphite. (d) is the spin densities of zigzag-edged graphite. The iso-surface value is $0.0002 \text{ e } \text{\AA}^{-3}$. Reproduced from Ref. 70 with permission from The Royal Society of Chemistry.

From an atomistic perspective, the surface and edge morphology of anode materials were found to have a strong impact on Li binding energies.^{247,248} Through investigating Si nano-structures, Chan and Chelikowsky found that Li has higher binding energies at the bulk site compared to the edge, requiring a higher energy cost of Li migration from the bulk towards the edge.²⁴⁹ In graphite anode materials, however, Leggesse et al. reported

1
2
3
4 1184 that the edged graphite systems showed remarkably enhanced Li binding energies and high
5
6 1185 Li mobility along graphite edges.²⁴⁸ Peng et al. recently quantified the edge effects on Li
7
8 1186 intercalation in graphite.⁷⁰ In their work, different edged graphites at dilute Li concentration
9
10 1187 were comprehensively investigated using DFT calculations. Interestingly, they found the
11
12 1188 unique topological electronic structures near the edges, particularly near the zigzag edge,
13
14 1189 induced distinct intercalation energies of Li in graphite. Figure 15c shows the Li adsorption
15
16 1190 energies at the armchair-edged and the zigzag-edged graphite, respectively. The adsorption
17
18 1191 energy, E_{ads} , is expressed as:

$$E_{\text{ads}} = E_{\text{Li|Graphite}} - E_{\text{Graphite}} - E_{\text{Li}}, \quad (43)$$

19
20
21
22
23
24 1192 where $E_{\text{Li|Graphite}}$, E_{Graphite} , and E_{Li} are the energies of Li adsorption in graphite, the
25
26 1193 pristine graphite, and one Li in body-centred cubic (bcc) Li metal, respectively. At the
27
28 1194 armchair edge, from the energy profile (c.f. Figure 15), the adsorption energy of Li is the
29
30 1195 lowest at the edge site (-0.38 eV). With Li penetrating into the bulk, the adsorption energy
31
32 1196 decreases rapidly to -0.24 eV at the sub-surface site and becomes -0.26 eV at the bulk
33
34 1197 site. The topological geometry of the armchair edge promotes Li adsorption relative to the
35
36 1198 graphite bulk.

37
38 1199 At the zigzag edge, the edge effect becomes even stronger, due to the existence of the
39
40 1200 surface state which consists of $C - p_z$ orbitals emerging from the zigzag edge.^{250,251} Figure
41
42 1201 15c shows that Li achieves a much lower adsorption energy of -0.66 eV at the zigzag edge
43
44 1202 site, indicating the strong binding of Li at the edge. The edge effect in the zigzag system
45
46 1203 is much stronger than that at the armchair edge and additionally penetrates into the bulk,
47
48 1204 indicated by the gradual decrease in magnitude of the Li adsorption energy from the edge
49
50 1205 to the bulk.

51
52 1206 The zigzag edge displays completely different spin densities contributed by the p_z orbitals
53
54 1207 perpendicular to the graphene planes, as shown in Figure 15a-b.^{70,248,250,251} These spin den-
55
56 1208 sities consist of the unpaired electrons accumulating on the edged carbons. The amplitude

1
2
3
4 1209 of this topological surface state gradually diminishes over a few bond distances beneath the
5
6 1210 surface. It is this surface state that interacts with Li at the zigzag edge and favours its
7
8 1211 adsorption. In summary, the graphite edges show stronger interactions with Li than those
9
10 1212 in the bulk. The effect is especially pronounced at the zigzag edge, strongly stabilising Li
11
12 1213 binding due to the topological surface states.

1214 **3.3.3 The Surface Effect on Li Diffusion**

1215 As Li obtains higher binding energies at the graphite edge, due to the specific topological
1216 structure of graphite edges,^{70,248} it's worth examining the impact of those edges on Li diffu-
1217 sion. In bulk graphite, the diffusion barrier of Li jumping from one site to another is around
1218 0.4 eV at the dilute limit.²¹⁰ Li, however, exhibits completely different diffusion kinetics at
1219 graphite edges in contrast to those in the bulk.^{70,248}

1220 Peng et al. show the energy profile of Li diffusion from the graphite edge towards the bulk
1221 at dilute Li concentration, Figure 16. In the armchair-edged graphite, Li has to overcome
1222 an energy barrier of 0.43 eV to move from site 1 to site 2 and a 0.42 eV barrier to further
1223 move from site 2 to site 3. The direct jump from site 1 to site 3 has to overcome an energy
1224 barrier of 0.58 eV and is therefore less favourable. In contrast, for bulk diffusion, Li needs to
1225 overcome a ~ 0.43 eV barrier to move to either adjacent site. The higher diffusion barrier at
1226 the armchair edge is caused by the compensation of Li adsorption energy at the edge site.
1227 At the zigzag edge, Li obtains two different diffusion pathways. Li diffusion from the edge
1228 (site 1) to the subsurface (site 3), where the diffusion barrier is 0.48 eV. In contrast, there is
1229 only a 0.21 eV activation barrier for Li diffusion along the edge sites (site 1 to site 2), which
1230 is much lower. This indicates that Li is extremely mobile at the zigzag edge, which can be
1231 verified by the stronger flux connecting the edge sites compared to diffusion towards the bulk
1232 (c.f. Figure 16). Due to the surface effect identified at the zigzag edge, Li favours diffusion
1233 along the edge direction within the first sub-surface sites, as the diffusion barrier (0.41 eV)
1234 is still lower than the barrier to moving Li into the bulk (0.49 eV). Markov chain analysis

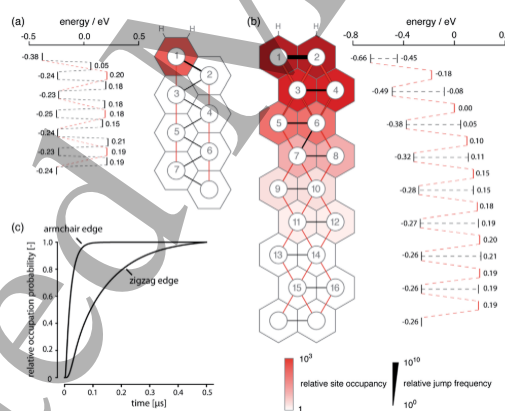
1
2
3 1235 was conducted in Peng et al.'s study to examine Li diffusion from the armchair edge and the
4
5 1236 zigzag edge to a bulk site 20 Å below the edge surface (see Figure 16c). They demonstrated
6
7 1237 that Li diffusion from the armchair edge to the bulk site is around one order of magnitude
8
9 1238 faster than its diffusion from the zigzag edge to the bulk, due to the strong binding of Li at
10
11 1239 the zigzag edge that generates a deep potential well for Li.⁷⁰

12
13 1240 On the basis of these studies, it was shown that the graphite edges have strong ef-
14
15 1241 fects not only on the Li intercalation energies but also on its diffusion kinetics close to
16
17 1242 the edge.^{70,248} The effect is pronounced at the zigzag edge.^{242,252,253} Thus much more slug-
18
19 1243 gish (de)intercalation kinetics are expected at that edge, compared to the armchair edge.
20
21 1244 Strategies including promoting growth of armchair edge over zigzag edge during synthesis of
22
23 1245 graphite nanomaterials,²⁴² and tuning the edge properties by chemical doping to improve Li
24
25 1246 diffusion rate towards the bulk could be useful to enhance Li (dis)charging rate for graphite
26
27 1247 anodes.^{254–256}

28
29 1248 Designing edge-controlled graphite for validating the electronic and electrochemical prop-
30
31 1249 erties predicted by DFT is still state-of-the-art. Commercial graphite powders contain a
32
33 1250 distribution of sizes, the proportion of edge types on each particle is dependent on particle
34
35 1251 size, and it is currently not possible to form graphite with only one type of edge. This makes
36
37 1252 systematic experimental characterisation to determine the influence of edges difficult.²⁵⁷ To
38
39 1253 try to understand these effects Bernardo et al. studied the effect of hydrogen and oxygen
40
41 1254 gas etching on graphite materials with a higher incidence of zigzag or armchair edge orienta-
42
43 1255 tions.²⁴² The proportion of each edge was quantified by high resolution transmission electron
44
45 1256 microscopy (HR-TEM), with the authors finding that a higher proportion of zigzag edges
46
47 1257 leads to a less stable SEI. Velický et al. studied the local electron transfer rate, double layer
48
49 1258 capacitance, and local density of states of the edge versus the basal plane of graphite in
50
51 1259 a microdroplet electrochemical cell.²⁵² This study was feasible owing to the vastly different
52
53 1260 electronic structure and electron transfer rate constant of the basal plane versus the graphite
54
55 1261 edges. It has yet to be determined if it is currently feasible to distinguish these properties

1
2
3
4 1262 for the zigzag and armchair edge, in a real electrochemical environment, through such an
5
6 1263 approach. Even so, the finding that the surface state from the zigzag edge could be a major
7
8 1264 bottleneck to the Li intercalation rate is a triumph for atomistic modelling that could direct
9
10 1265 future materials design strategies and experimental characterisation for anodes.^{70,258} More-
11
12 1266 over, the interplay between edge orientation and nitrogen/boron doping warrants further
13
14 1267 systematic exploration from both experiment and theory.

15 1268 These studies can also offer some universal insights for investigating the interface effects of
16
17 1269 other materials such as the cathode. Prior to Li intercalation into graphite, the Li desolvation
18
19 1270 process is also an important step affecting the overall (dis)charging rate. However, due to
20
21 1271 the complicated solid-liquid interface, addressing the graphite interaction with the electrolyte
22
23 1272 is an extremely challenging aspect for both modelling and experiment, as discussed in the
24
25 1273 following sections. We discuss the effect of that interface on Li plating and aspects related
26
27 1274 to the SEI in the following sections.



43 Figure 16: Li diffusion at (a) the armchair-edged and (b) the zigzag-edged graphite. The
44 hexagons indicate lattice sites and the colours show occupancy probability relative to that
45 in the bulk. The width of the lines connecting sites implies the jump frequencies. (c) shows
46 the occupation probability for Li to occupy a site approximately 20 Å below the graphite
47 edge, relative to the steady-state value after being introduced at time zero at the edge.
48 Reproduced from Ref. 70 with permission from The Royal Society of Chemistry.
49
50
51
52
53
54
55
56
57
58
59
60

1275 3.3.4 Li deposition on graphite anodes

1276 Apart from intercalation of Li ions into the graphite anode, Li ions can also deposit on surface
1277 of graphite in the form of metallic Li dendrites, which can grow during battery operation and
1278 cause internal short-circuits. Several situations for the deposition of Li metal on the graphite
1279 anode have been identified, as shown schematically in Figure 17.²⁵⁹ A “normal” intercalation
1280 mechanism is shown in Figure 17a. When the voltage of the graphite electrode drops below
1281 0 V with respect to Li/Li⁺, deposition of Li⁺ ions on the graphite surface, as metallic Li,
1282 becomes thermodynamically possible, as shown in Figure 17b. The thermodynamic criterion
1283 can be satisfied when the overpotential, η_{int} , is larger than the equilibrium voltage of the
1284 stage II to stage I phase transition (~ 85 mV). Deposition becomes kinetically feasible when
1285 the overpotential for the intercalation reaction (η_{int}) becomes larger than the intercalation
1286 voltage (~ 85 mV), so that the graphite voltage drops below 0 V with respect to Li/Li⁺.
1287 The overpotential originates from mass transfer limitations in the electrolyte region near the
1288 graphite edge, as shown schematically in Figure 17c. Li plating can be triggered upon local
1289 salt depletion in the electrolyte, $c_l \rightarrow 0$, if liquid diffusion is slow compared to intercalation.
1290 Solid-state diffusion between the graphite edge and the bulk, as shown schematically in
1291 Figure 17d, also contributes to this overpotential. Li plating can occur when intercalated
1292 Li⁺ ions saturate the graphite edge ($c \rightarrow 1$) and block further insertion, if diffusion from
1293 surface to the bulk is slow compared to Li insertion at the edge. A combination of both
1294 effects can result in Li deposition on the graphite surface.

1295 A recent DFT study by Peng et al. has shown that in a vacuum environment: (1) Li
1296 deposition is more favourable near the graphite edges rather on the basal plane, (2) the energy
1297 barrier for Li deposition at the zigzag edge (only) increases with the degree of lithiation of
1298 the graphite, (3) chemical doping of nitrogen can increase the energy barrier and can possibly
1299 suppress the Li deposition on graphite anode on the zigzag edge.²⁵⁸ More advanced models
1300 for DFT simulations in the presence of an electrolyte under applied potential (cf. (sec. 2.2.1
1301 and Ref. 260)), have the potential to shed more light on the Li deposition phenomenon in

1302 experimental conditions.

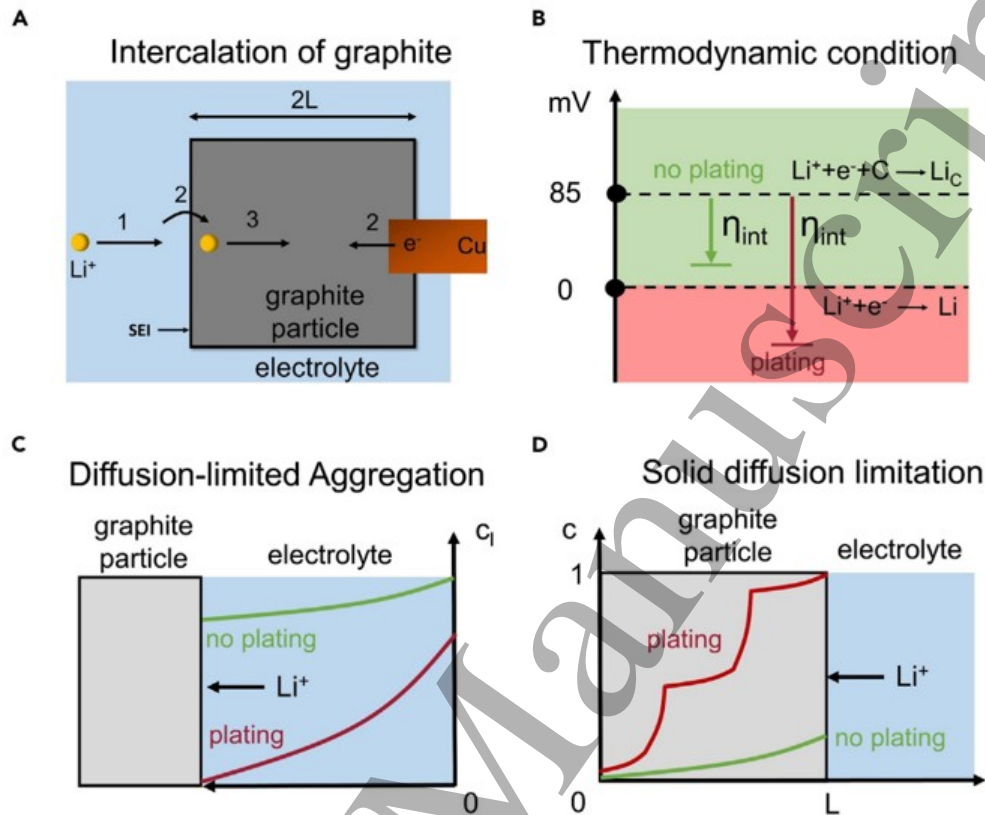


Figure 17: (a) 2D schematic of intercalation of a graphite particle. Three sequential steps take place during charging at the graphite anode: (1) Li^+ transport in electrolyte toward the reaction site; (2) Li^+ intercalation into a graphite particle (including de-solvation and migration through the SEI); and (3) Li^+ solid diffusion within the graphite particle. (b) Thermodynamic criterion for Li plating (cell voltage, $U < 0$ V versus Li/Li^+). The green and red arrows illustrate the required overpotentials to drive the insertion reaction at small current/fast insertion kinetics and large current/slow insertion kinetics. (c) 1D schematic of diffusion-limited aggregation resulting from electrolyte transport limitations. The green and red curves illustrate the Li^+ salt concentration profile in the electrolyte. (d) 1D schematic of solid diffusion-limitation mechanism. The green and red curves illustrate the Li^+ concentration profile in the graphite particle. Reprinted from Ref. 259, with permission from Elsevier.

1303 3.3.5 Solid-Electrolyte Interphase

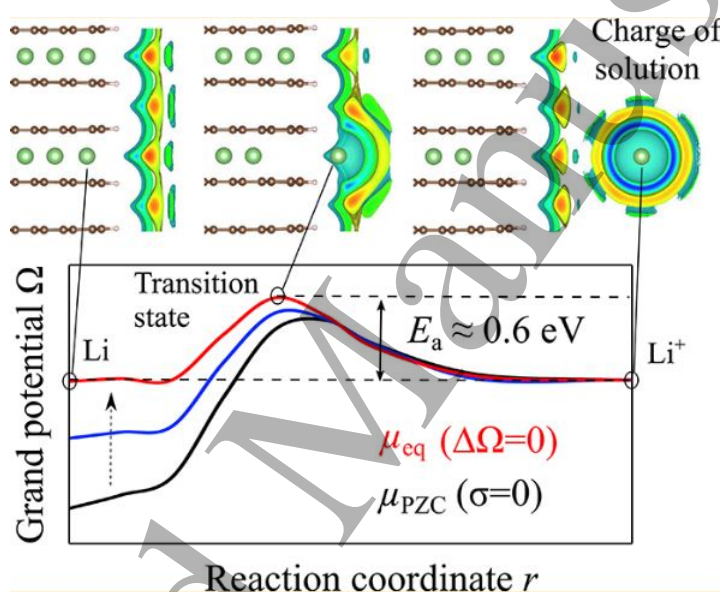
1304 The SEI is an important component of the rechargeable Li-ion battery and is formed from
 1305 deposition of the decomposition products of the electrolyte and solvent on the anode surface.
 1306 The SEI allows transport of Li^+ ions but blocks the transfer of electrons, thereby stopping

1
2
3 1307 further electrolyte decomposition reactions.^{261,262} Here we discuss aspects of the SEI related
4
5 1308 to our discussion of Li-ion diffusion energy barrier in bulk and graphite surfaces. A recent
6
7 1309 comprehensive review on the atomistic modelling of the SEI describes several other aspects
8
9 1310 of the SEI in detail:¹⁶

- 11 1311 • Electrolyte and solvent reduction mechanisms, including: prediction of the reduction
12
13 1312 voltage for each solvent and electrolyte species, the effect of the electrolyte solvation
14
15 1313 structure, the effect of anode surface termination, and the dynamic buildup of the
16
17 1314 nanometer thick SEI layer.
- 18
19
20 1315 • Modification of the SEI by electrolyte additives and prediction of new electrolyte ad-
21
22 1316 ditives.
- 23
24
25 1317 • Correlation of the SEI properties with battery performance, including: the electron
26
27 1318 insulating properties of the inorganic components in the SEI, the ionic conductivity
28
29 1319 of the SEI components, Li-ion desolvation at the SEI/electrolyte interface, chemical
30
31 1320 stability of the SEI components, and mechanisms of SEI growth and battery aging.
- 32
33
34 1321 • The use of coatings to artificially design the SEI.

35
36 1322 One way to describe the SEI is via the implicit continuum models described in sec. 2.2.1.
37
38 1323 Applying their DFT + implicit electrolyte model on an armchair edge of 1634-atom graphite
39
40 1324 slab in contact with a 0.5 M LiPF₆ in EC solution, Dziejczak et al. calculated that a Li atom
41
42 1325 is 2.34 eV more stable at the graphite edge than in the electrolyte solution.¹³⁵ Similarly,
43
44 1326 Haruyama et al. found favourable energetics for Li intercalation from the electrolyte solu-
45
46 1327 tion into the graphite edge.²⁶³ They also studied the variation in energy as a function of
47
48 1328 Li distance from the graphite edge, as shown in figure 18. In Haruyama et al.'s model, Li
49
50 1329 intercalation is accompanied by an electron gain from the external circuit. This was imple-
51
52 1330 mented using a grand canonical version of electronic DFT, where the number of electrons in
53
54 1331 the electrode can change subject to fixed electrode potential. Correspondingly, the appropri-
55
56 1332 ate thermodynamic quantity to represent this ensemble is the grand potential, $\Omega = A - \mu_e N_e$,

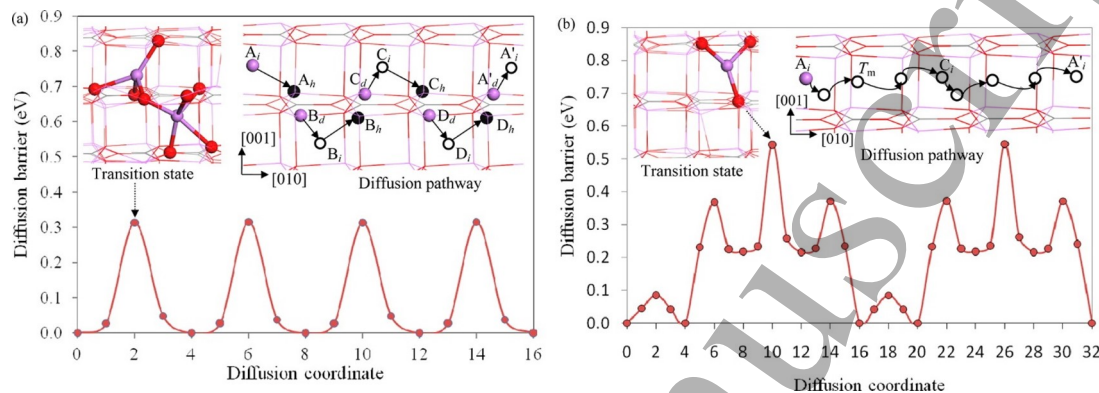
1
2
3
4 1333 which is plotted on the y axis for several different constant chemical potentials of electrons,
5
6 1334 μ_e . Two illustrative cases include: (a) the potential of zero charge (PZC), which is the
7
8 1335 electrochemical potential of a charge-neutral Li-graphite system, and (b) the equilibrium
9
10 1336 potential (c.f. sections 2.3.1 and 3.2.2), where the net change in the grand potential for
11
12 1337 the intercalation reaction becomes zero. Haruyama et al.'s simulations estimate an energy
13
14 1338 barrier of around 0.6 eV for Li intercalation into the graphite edge, which is close to the
15
16 1339 experimental measurements from impedance spectroscopy.²⁶⁴



17
18
19
20
21
22
23
24
25
26
27
28
29
30
31
32
33
34
35
36
37
38
39
40
41
42
43
44
45
46
47
48
49
50
51
52
53
54
55
56
57
58
59
60
Figure 18: Profiles of grand potential Ω as a function of the Li-position during Li-intercalation process at the interface between graphite edge and an implicit electrolyte solution. The simulation is performed at conditions of constant chemical potential of electrons μ_e (constant electrode potentials similar to experiments). Reprinted with permission from Ref. 263. Copyright 2018 American Chemical Society.

1340 Another way to describe the SEI is via explicit consideration of SEI components. Shi et al.
1341 performed a direct calculation of Li-ion transport in the Li_2CO_3 component of the SEI,²⁶⁵
1342 via DFT-based CI-NEB calculations (section 2.1.3). Two mechanisms for Li^+ diffusion were
1343 considered, namely, the knock-off and direct hopping mechanisms, which were found to
1344 have energy barriers of 0.31 eV and 0.54 eV respectively, as shown in Figure 19. The Li
1345 self-diffusion coefficient was calculated to be $1.1 \times 10^{-7} \text{ cm}^2 \text{ s}^{-1}$ and $8.4 \times 10^{-12} \text{ cm}^2 \text{ s}^{-1}$
1346 respectively. Estimating the formation energy of corresponding defects in the lattice of

1
2
3
4 1347 Li_2CO_3 as a function of voltage, the total activation energy barrier for Li-ion diffusion was
5
6 1348 predicted to be in the 0.67–1.07 eV range for the knock-off mechanism and in the 0.92–1.32
7
8 1349 eV range for the direct-hopping mechanism.



9
10
11
12
13
14
15
16
17
18
19
20
21
22 Figure 19: Energy barrier for Li-ion transport in the SEI via (a) knock-off and (b) direct
23 hopping mechanisms. Reprinted with permission from Ref. 265. Copyright 2012 American
24 Chemical Society.
25

26
27
28 1350 The predicted values of the Li-ion diffusion energy barrier by both the implicit and the
29
30 1351 explicit models described above are significantly higher than that in the bulk of graphite,
31
32 1352 which is reported to be between 0.2-0.5 eV (c.f. section 3.2.4).^{76,210,211} This indicates a
33
34 1353 limiting role of the SEI in determining overall kinetics of Li-ion diffusion and the overall
35
36 1354 rate-capability of Li-ion batteries.

39 1355 3.4 C/Si composites

40
41
42 1356 Use of anode materials capable of electrochemically alloying with lithium could allow higher
43
44 1357 energy densities than are possible with graphite. In particular, silicon, due to its high
45
46 1358 gravimetric capacity of 4200 mAh g⁻¹, has achieved tremendous attention as an anode
47
48 1359 material.²⁶⁶ Si has a low electrochemical potential 0.37–0.45 V vs. Li/Li⁺, which is only
49
50 1360 ~0.27 V higher than graphite.²⁶⁷ Si is highly abundant, cost effective and non-toxic.^{267–269}
51
52 1361 While pure Si anode materials are not presently viable, present day anode materials combine
53
54 1362 a small atomic fraction (typically 5-10 at %) of silicon with graphite to boost the gravimetric
55
56 1363 capacity of the anode.¹⁴ However, there are certain challenges in understanding the behaviour
57
58
59
60

1
2
3
4 1364 of Si and C/Si composites that are summarised in this section.

5
6 1365 The phase diagram of lithium and silicon shows five crystalline intermetallic Zintl-like
7
8 1366 phases: $\text{Li}_{21}\text{Si}_5$, $\text{Li}_{13}\text{Si}_4$, Li_7Si_3 , $\text{Li}_{12}\text{Si}_7$, and LiSi .²⁷⁰ However, LiSi is not accessible under
9
10 1367 electrochemical conditions, since it is synthesised under high pressure, and the stoichiometry
11
12 1368 of $\text{Li}_{21}\text{Si}_5$ is disputed, with a mixed $\text{Li}_{21}\text{Si}_5/\text{Li}_{22}\text{Si}_5$ phase also proposed.²⁷¹ Under electro-
13
14 1369 chemical conditions, metastable phases with compositions $\text{Li}_{15}\text{Si}_4$ ²⁷² and amorphous Li_xSi_y
15
16 1370 can be formed.²⁷³ It has been proposed that a different reaction pathway between these
17
18 1371 phases during lithiation and delithiation contributes to the observed charge/discharge hys-
19
20 1372 teresis in lithium silicides and C/Si composites.²⁷² In particular, Jiang et al. found that the
21
22 1373 crystalline phase $\text{Li}_{15}\text{Si}_4$ is accessed during lithiation, but the lattice undergoes an amor-
23
24 1374 phisation process during delithiation, with the latter step being rate determining.²⁷² This
25
26 1375 limits the utility of ground state DFT calculations for understanding the Li-Si system under
27
28 1376 operating battery conditions, and is therefore a challenge for multiscale modelling.

29
30 1377 An additional challenge is the volume expansion. Upon full lithiation, the volume of Si
31
32 1378 can expand to more than three times its original volume, which means the Si electrodes do
33
34 1379 not retain their morphology during prolonged cycling or, even worse, some particles become
35
36 1380 detached from the electrode assembly.^{267,269,274} This volume expansion/contraction during
37
38 1381 cycling also leads to severe cracking and degradation of the SEI. It is for mainly these
39
40 1382 reasons that pure Si anodes are not currently commercially viable and must be combined
41
42 1383 with graphite. Several strategies have been proposed to change the morphology to miti-
43
44 1384 gate these issues, including development of different Si robust nanostructures (0D or hollow
45
46 1385 nanoparticles, 1D nanowires, 2D film-like Si, and 3D Si structures),²⁶⁷ and the development
47
48 1386 of composites (Si/carbon composites, Si/polymer composites, Si alloys, and Si/metal oxide
49
50 1387 composites).¹⁴ While modelling the complex nature of the degradation pathways of the Si,
51
52 1388 Si-composites and their SEIs is presently out of reach of atomistic methods, these techniques
53
54 1389 nonetheless emerge as natural tools for high-throughput screening of different promising an-
55
56 1390 ode materials.²⁷⁵ These approaches can also tell experimentalists the most promising part

1
2
3
4 1391 of the parameter space in which to perform more extensive, time consuming, and sometimes
5
6 1392 costly characterisation.

7 1393 A more comprehensive overview of the application of mesoscale models to challenging
8
9 1394 composite systems is presented by Franco et al., with the volume averaging approach high-
10
11 1395 lighted perhaps being particularly applicable to Si and C/Si systems.²³³ Particularly for
12
13 1396 carbon anodes in combination with Si or silicon suboxide (SiO_x), collectively referred to as
14
15 1397 C/Si or C/SiO_x, it may presently be necessary to sacrifice some details of the atomic level de-
16
17 1398 scription to enable these systems to be tractably modelled at either mesoscale or continuum
18
19 1399 levels. Regarding the dynamic and metastable behaviour described above, kMC would be a
20
21 1400 natural technique to bridge length scales and include different time scale dynamic events, as
22
23 1401 explained in a recent review dedicated to this technique.¹⁰⁴

27 1402 **3.5 Outlook and challenges for anodes**

28
29
30 1403 Graphite remains the predominant anode material in most Li-ion cells, due to its suitably
31
32 1404 high capacity of 372 mAh g⁻¹, an operating potential close to 0 V vs. Li/Li⁺, and its
33
34 1405 compatibility with liquid organic electrolytes. Alternative materials that form solid solutions
35
36 1406 with lithium (including silicides) presently do not have sufficient long term structural stability
37
38 1407 to be used as the primary anode material, requiring them to be composites with graphite.
39
40 1408 The development of graphite-based anodes has relied upon not only understanding staging
41
42 1409 formation in bulk, but also upon the development and understanding of a stable SEI and its
43
44 1410 implications of that SEI for cell longevity and (de)intercalation rate behaviour.

45
46 1411 Advancements in developing all solid-state batteries (ASSBs) have resulted in additional
47
48 1412 research of Li metal anodes, as reviewed by Fang et al.,²⁷⁶ and Li et al..²⁷⁷ In this section,
49
50 1413 we have summarised the safety and degradation challenges caused by lithium plating on
51
52 1414 graphite anodes. The use of Li metal as the anode for LiBs and ASSBs still face similar issues
53
54 1415 regarding redeposition of metallic Li as dendrites and consumption of cyclable lithium.^{276,277}

55
56 1416 Many aspects of modelling the bulk behaviour of lithium (de)insertion graphite are well

1
2
3 1417 understood. As shown in this section, challenging aspects like quantifying the Li ion ordering
4
5 1418 with lithiation fraction can only be obtained by combining experimental observations with
6
7 1419 atomistic models. However, there are challenges with atomistic modelling in anodes that
8
9 1420 hinder improvements in capacity, rate performance, safety and durability of the anode itself
10
11 1421 and, consequently, full Li-ion cells. In addition, there are challenges with transferring insights
12
13 1422 from atomistic modelling in a scalable form to models on different length and time scales,
14
15 1423 while maintaining physical integrity. These outstanding challenges are:

- 18 1424 • The role of metastable phases in the kinetics of staging behaviour. New theoretic-
19
20 1425 cal frameworks should be developed to understand the connectivity between different
21
22 1426 phases and the effect of this on the path dependency of measurable behaviour like the
23
24 1427 OCV. These distinct pathways also have implications for mechanical degradation and
25
26 1428 fracture. A promising approach in this direction is the semi-grand canonical framework
27
28 1429 developed by Van der Ven et al., Van der Ven et al. describing layered transitions in
29
30 1430 cathodes^{9,231,278,279} that could also be applicable to graphite anodes and other candi-
31
32 1431 date materials like silicides.
- 35 1432 • The role of the configurational, vibrational and electronic entropy of lithium insertion.
36
37 1433 Longer length scales, i.e. continuum models, still assume that the entropy follows
38
39 1434 an ideal solid solution behaviour. The importance of configurational entropy to the
40
41 1435 phase transitions of lithium in graphite was highlighted in previous sections.^{71,91,225} One
42
43 1436 promising extension would be to use the results from MC calculations to parameterise
44
45 1437 a phase field model, such as those developed by Bazant,⁹⁵ Guo et al.⁹⁶ and Bai et al.,⁹⁷
46
47 1438 with a more realistic Hamiltonian and thus include entropy effects in a rigorous way.
- 50 1439 • Regarding dynamics, kMC approaches with an empirical Hamiltonian show promise,^{102–104,220}
51
52 1440 but are limited by the length and time scale of the properties that can currently be
53
54 1441 modelled. A possible solution would be to develop an effective cluster interaction
55
56 1442 Hamiltonian linking with a linear scaling DFT code, such as ONETEP. Parellelisation

1
2
3
4 1443 of the kMC calculations could be achieved by exploiting recently developed graphical
5 1444 processing unit (GPU) architectures.
6
7

8 1445 Superior models of surface and interface effects are needed. This includes development
9
10 1446 of a physically rigorous version of the Butler-Volmer equation, which is valid for electron
11
12 1447 transfer but is conventionally assumed to be valid too for ionic transfer in Li-ion batteries.
13
14 1448 The current models of the interface are too simplistic or represent an ideal situation instead of
15
16 1449 dealing with the complex reality of the SEI. A systematic coarse-graining approach involving
17
18 1450 multi-length- and multi-time-scale physics can help in understanding the complex nature of
19
20 1451 the SEI and its influence on performance of Li-ion batteries. Controlling and improving the
21
22 1452 properties of SEI is crucial to improve the overall rate capability of Li-ion batteries, as that
23
24 1453 interface is the bottleneck for Li-ion diffusion.
25

26 1454 Regarding graphite, atomistic modelling can be used to predict systematic modifications
27
28 1455 to the edge morphology or the use of dopants on the graphite edge,^{70,254,255} or tuning of
29
30 1456 the interlayer carbon spacing²¹⁴ to enable systematic tuning of the rate performance. This
31
32 1457 approach has the potential to lead to more robust interfaces and strategies to tune the anode
33
34 1458 voltage and dynamics, thus tuning nucleation barriers and mitigating the risk of lithium
35
36 1459 plating.²⁵⁸ In this regard, it should be pointed out that decoupling the rate performance of
37
38 1460 different graphite edges is still a great challenge from experiment and therefore this finding
39
40 1461 represents a success for atomistic modelling.
41

42 1462 We highlight that there are still outstanding challenges regarding modelling metastable
43
44 1463 behaviour, volume expansion and degradation in solid solution materials such as silicides.
45
46 1464 So far, high-throughput atomistic modelling techniques have provided a predictive tool to
47
48 1465 suggest anode materials that are promising for more extensive experimental characterisation.
49
50 1466 However, composite materials such as C/Si and C/SiO_x, which are increasingly being used in
51
52 1467 commercial anodes, are presently challenging to model on the atomistic scale. In this regard,
53
54 1468 an extension to mesoscale modelling, such as a volume averaged approach as suggested by
55
56 1469 Franco et al., could be a promising way to model challenging materials such as composites,
57
58
59
60

1
2
3 1470 in which each component experiences different degrees of volume expansion.²³³
4
5
6
7

8 1471 4 Electrolytes

11 1472 4.1 Introduction

14 1473 Electrolytes are a medium for the transport of charged ionic species, i.e. Li^+ , between the
15 1474 electrodes.^{280,281} While the electrons flow through the outer circuit, an equal ionic current
16 1475 flows through the electrolyte to balance the charge. Electrolytes can be categorised into two
17 1476 groups: liquid and solid, both of which have their benefits and drawbacks. Liquid electrolytes
18 1477 are currently used in commercial lithium-ion batteries (LiBs) and offer high conductivities,
19 1478 but have safety concerns.^{282–284} Solid electrolytes are a safer alternative that are approaching
20 1479 commercialisation and can potentially reach higher energy densities.²⁸⁵ There are several
21 1480 key aspects to the design of either liquid or solid electrolytes in LiBs: their electrochemical
22 1481 stability window,^{2,286} ionic conductivity,^{287,288} electric double layers,^{280,289} solid-electrolyte
23 1482 interphase (SEI),^{290,291} and safety, which are all discussed in the following sections.^{292,293}
24
25
26
27
28
29
30
31
32
33

34 1483 **Electrochemical stability window** An electrolyte can be safely used within its elec-
35 1484 trochemical stability window, which defines the voltage range outside of which it can be
36 1485 oxidised or reduced.² The electrochemical stability window is schematically depicted in Fig-
37 1486 ure 20, showing the electronic energy levels in the electrodes and electrolyte of a battery
38 1487 cell. If the anode electrochemical potential, μ_A , is above the lowest unoccupied molecu-
39 1488 lar orbital (LUMO) of the electrolyte, the electrolyte will be reduced. Conversely, if the
40 1489 cathode electrochemical potential, μ_C , is below the highest occupied MO (HOMO) of the
41 1490 electrolyte, the electrolyte will be oxidised. Therefore, the electrochemical potentials, μ_A
42 1491 and μ_C , should lie within the energy gap, E_g , between the LUMO and the HOMO of the
43 1492 electrolyte, constraining the open circuit voltage (OCV), V_{oc} , of a battery cell, such that:²
44
45
46
47
48
49
50
51
52
53
54

$$55 \quad eV_{oc} = \mu_A - \mu_C \leq E_g, \quad (44)$$

1493 where e is the elementary charge, i.e. the magnitude of the charge on an electron.

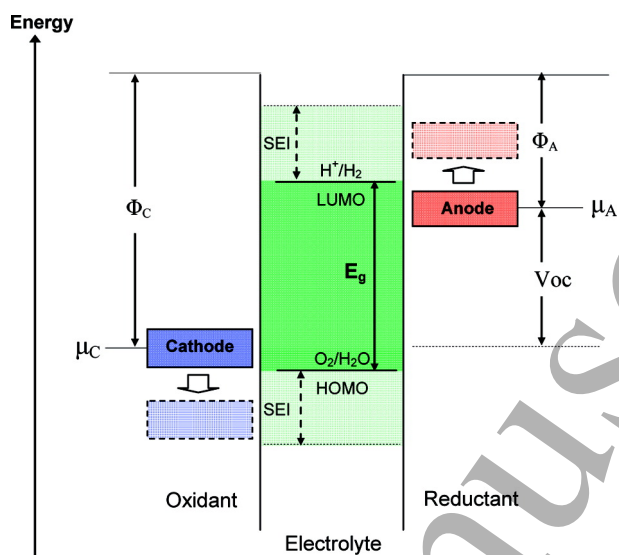


Figure 20: Schematic open circuit energy diagram of an aqueous electrolyte. Φ_A and Φ_C are the anode and cathode work functions. E_g is the electrochemical stability window of the electrolyte. If $\mu_A >$ lowest unoccupied molecular orbital (LUMO) and/or $\mu_C <$ highest occupied MO (HOMO), the electrolyte would be thermodynamically unstable and its usage would require kinetic stability through the formation of a solid-electrolyte interphase (SEI) layer. Reprinted with permission from Ref. 2. Copyright 2010 American Chemical Society.

1494 The energy gap, E_g , for an aqueous electrolyte is ~ 1.3 eV, severely limiting the OCV,
 1495 V_{oc} . In order to obtain a higher OCV, non-aqueous electrolytes with larger E_g have been used
 1496 in LiBs.^{2,292} A good summary of electrochemical stability windows of different classes of non-
 1497 aqueous electrolytes including (organic and inorganic) liquids, solids, ionic liquids, polymers
 1498 and their combinations is presented by Goodenough and Kim.² Commonly used organic
 1499 liquid electrolytes, such as 1 M LiPF_6 in 1:1 ethylene carbonate (EC) : dimethyl carbonate
 1500 (DMC), have stability windows between ~ 1.3 -5.0 V, while ionic liquids have stability window
 1501 between ~ 1.0 -5.3 V. A desirable property of solid electrolytes is their larger electrochemical
 1502 stability window (~ 0.0 -8.0 V), compared to liquid electrolytes,² allowing them to operate
 1503 within a larger voltage window and thus increase the energy density of the battery.

1504 **Ionic conductivity** High ionic conductivity ($> 10^{-4}$ S cm^2) in the electrolyte (liquid
 1505 or solid) and across the electrode-electrolyte interphase enables a high rate-capability of the
 1506 overall Li-ion battery.^{2,287,288} Generally, the ionic conductivity of liquid electrolytes is higher

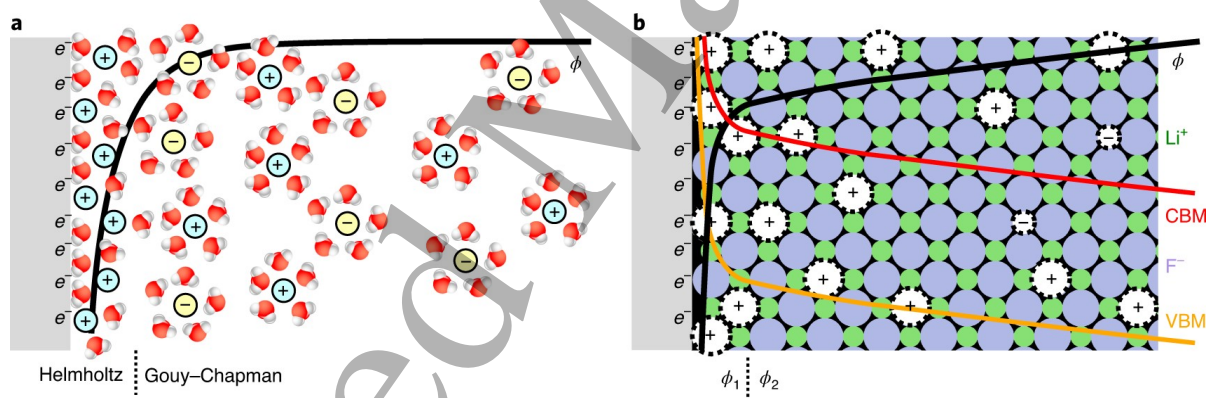
1
2
3
4 1507 than that of solid electrolytes. However, new classes of solid materials have been found with
5
6 1508 ionic conductivity surpassing that of liquids (cf. section 4.3), known as superionic conductors.
7
8 1509 The ionic conductivity of commonly used liquid electrolytes is several orders of magnitude
9
10 1510 higher than that in the bulk of electrodes and the electrode-electrolyte interphase.²⁸⁷

11 **Electric double layer** During the charging of an electrode in contact with a liquid elec-
12
13 1512 trolyte, excess charge develops at the electrode surfaces. This triggers the rearrangement of
14
15 1513 electrolyte ions in the electrolyte solution, such that counter-electrolyte charges accumulate
16
17 1514 near the electrode-electrolyte interface, forming an interfacial charge density perturbation, to
18
19 1515 achieve local electroneutrality at the interface. In the classical system of dilute electrolytes,
20
21 1516 electroneutrality is achieved by the formation of a monotonically decaying ‘double layer’.²⁸⁰
22
23 1517 The double layers in solid electrolytes cannot be directly observed experimentally, so mod-
24
25 1518 elling can be used to rationalise their effects. Several models of the electric double layer in
26
27 1519 electrochemistry exist, such as Helmholtz, Gouy-Chapman, and Gouy-Chapman-Stern.²⁸¹
28
29 1520 Early models were limited in sophistication: the Helmholtz double layer model suggested
30
31 1521 charge screening by a plane of counter-charged electrolyte ions near the electrode surface,
32
33 1522 resembling a capacitor. In contrast, the Gouy-Chapman model screens charge via a diffuse
34
35 1523 layer of electrolyte ions, decaying monotonically to their bulk concentration value, where the
36
37 1524 electric potential will fall to zero. The Gouy-Chapman-Stern model accounted for discrepan-
38
39 1525 cies encountered by including both a Helmholtz layer of counter charge, as well as a diffuse
40
41 1526 layer of electrolyte ions, as shown schematically in figure 21(a). These continuum models of
42
43 1527 electrolyte ions are also being integrated with quantum mechanical methods, such as Density
44
45 1528 Functional Theory (DFT) (c.f. section 2.2.1). Bhandari et al. recently implemented such
46
47 1529 a hybrid quantum-continuum model to achieve electroneutrality in simulations of charged
48
49 1530 electrochemical interfaces, based on a modified Poisson-Boltzmann equation (PBE).⁶⁶

51 1531 At the interface between solid electrolytes and electrodes, a similar decay in charge is
52
53 1532 observed. However, in this case, the charge carrier is the charge vacancy. Maier discuss the
54
55 1533 theory of this decay in detail²⁹⁴ and new continuum models continue to be developed for
56
57
58
59
60

1
2
3
4 1534 solid electrolytes.^{295–298} Swift et al. present a model for formation of the double layer in solid-
5
6 1535 solid electrochemical interfaces, based on the Poisson-Fermi-Dirac equation. The resulting
7
8 1536 space charge layer of point defects in a solid electrolyte material is shown schematically in
9
10 1537 figure 21(b). However, this study only accounts for the effect of correlations between ions
11
12 1538 by limiting the concentration of defects in the interfacial layer to be below a certain value.

13
14 1539 At higher concentrations, screening of electrodes changes markedly in liquids, with a new
15
16 1540 regime emerging when the Debye screening length is of roughly equal value to the ionic
17
18 1541 diameter. In this regime, charge is screened by means of exponentially damped oscillations
19
20 1542 of counter-ions and co-ions, in an ordered interfacial structure known as overscreening;²⁹⁹
21
22 1543 a structure that has previously been observed experimentally for liquids.^{300–303} In 2021,
23
24 1544 Dean et al. became the first to propose the existence of a similar oscillatory decay at solid
25
26 1545 electrolyte grain boundaries.³⁰⁴



27
28
29
30
31
32
33
34
35
36
37
38
39
40
41
42
43
44
45
46
47
48
49
50
51
52
53
54
55
56
57
58
59
60
Figure 21: Schematic comparing the double layer formed at the solid-liquid and solid-solid electrochemical interfaces. (a) For the solid-liquid interface, excess electrons on the electrode are balanced by increased density of solvated positive ions in the liquid electrolyte. ϕ is the electrostatic potential and is mediated by the Helmholtz layer, followed by exponential decay in the diffuse layer (described by Gouy-Chapman theory). (b) For the solid-solid interface, excess electrons on the electrode are balanced by increased density of positive point defects in the solid electrolyte. Electronic band bending occurs in the solid electrolyte. ϕ_1 and ϕ_2 are the electrostatic potentials next to and further from the interface. Electronic band-bending is shown via the valence-band maximum (VBM), also known as the highest occupied molecular orbital (HOMO), and conduction-band minimum (CBM), also known as the lowest unoccupied molecular orbital (LUMO). Reproduced with permission from Springer Nature: Ref. 289, Copyright 2021.

1546 **Solid-electrolyte interphase** The “interface” described above is basically a two-dimensional

1
2
3 1547 surface between the electrode and electrolyte. In LiBs, the electrolyte reacts irreversibly and
4
5 1548 decomposes on the electrode surfaces, leading to the formation of a distinct phase, several
6
7 1549 nanometres thick, between the electrode and the electrolyte, known as the SEI.²⁹⁰ The ability
8
9 1550 to form a stable interphase, which is both ionically conducting and electronically insulating,
10
11 1551 is an important criterion for the selection of an electrolyte material. The electron insulating
12
13 1552 property of the SEI is important, to stop further decomposition of the electrolyte on the
14
15 1553 electrode.^{2,292} High ionic conductivity through the SEI is important, otherwise this can form
16
17 1554 a bottleneck for the overall rate capability of LiBs.^{16,293} While the SEI was originally discov-
18
19 1555 ered in liquid electrolytes, its rate-limiting behaviour is now also observed in all-solid-state
20
21 1556 batteries (ASSBs).²⁹¹

22
23 1557 The two major classes of electrolyte materials, solid and liquid electrolytes, are discussed
24
25 1558 separately. We focus on the atomistic modelling of different types of liquid and solid elec-
26
27 1559 trolytes and their battery related properties. For the liquid electrolyte section, this includes
28
29 1560 the bulk structure, diffusion properties, solvation energies, and activity coefficients of dif-
30
31 1561 ferent solvents. For the solid electrolyte section, there is a particular emphasis on the ion
32
33 1562 transport mechanisms, material stability, and the electrode-electrolyte interfaces. Finally,
34
35 1563 we discuss the individual challenges and outlook for future atomistic modelling of both liquid
36
37 1564 and solid electrolytes.

41 1565 **4.2 Liquid Electrolytes**

42 43 1566 **4.2.1 Introduction to liquid electrolyte materials**

44
45
46 1567 The most widely used liquid electrolyte in Li-ion batteries is LiPF_6 in a solvent, which
47
48 1568 is typically a mix of two or more solvents, for example EC, DMC, propylene carbonate
49
50 1569 (PC), or ethyl methyl carbonate (EMC), in order to achieve the competing objectives of
51
52 1570 dissolution of a high concentration of salt, low viscosity, and high dielectric constant at
53
54 1571 typical operational temperatures.^{22,194,292,293,305} Cyclic carbonates (EC, PC) have a higher
55
56 1572 dielectric constant but also high viscosity, while “linear” carbonates (DMC, EMC) have

1
2
3 1573 low viscosity but also a low dielectric constant. For that reason, mixtures of solvents are
4
5 1574 often used to optimise performance in a specific application.^{22,194,306} However, in the last
6
7 1575 two decades there has been continued innovation in electrolyte mixtures, including ionic
8
9 1576 liquids³⁰⁷ and salt in water-based systems.³⁰⁸ This section will touch on both traditional
10
11 1577 and emergent electrolyte solvents.

14 15 1578 **4.2.2 An introduction to modelling liquid electrolytes**

16
17 1579 The modelling of liquid electrolytes for conventional batteries is a broad and diverse field.
18
19 1580 Over the past 20-30 years, atomistic modelling has helped to shape the fundamental physics
20
21 1581 of liquids, determining a new physical basis and validating decades-old pen and paper theories
22
23 1582 of concentrated electrolytes.^{309–312} Here, we focus on the development of liquid electrolyte
24
25 1583 models and the considerations needed when modelling these materials, before moving on to
26
27 1584 their applications in measuring different properties.

28
29 1585 Atomistic modelling of liquid electrolytes can be broadly separated into *ab initio* and
30
31 1586 classical (potentials-based) Molecular Dynamics (MD) modelling (c.f. section 2.1.6). These
32
33 1587 are complementary techniques which can be used to aid each other. For example, *ab initio*
34
35 1588 calculations are able to provide information on the electron distribution, required for param-
36
37 1589 eterising the non-bonded components of force fields used in classical MD. Classical MD can
38
39 1590 also be used to provide the starting conditions for DFT calculations. *Ab initio* and classical
40
41 1591 methods can also be combined in quantum mechanics/molecular mechanics (QM/MM) stud-
42
43 1592 ies, where the larger system is treated classically with a smaller sub-region being modelled
44
45 1593 using *ab initio* methods. For example, a study by Fujie et al. used the “Red Moon” method
46
47 1594 to investigate the formation of the SEI at the metallic electrode.³¹³

48
49 1595 In this section, we first discuss the separate design and use of *ab initio* and classical MD
50
51 1596 methods, followed by their application to determine properties in the bulk liquid electrolyte.
52
53 1597 Finally, we discuss the application of atomistic methods to SEI investigations, from the
54
55 1598 perspective of the liquid electrolyte (complementary to the solid-focused SEI discussion given

1
2
3
4
5
6
7
8
9
10
11
12
13
14
15
16
17
18
19
20
21
22
23
24
25
26
27
28
29
30
31
32
33
34
35
36
37
38
39
40
41
42
43
44
45
46
47
48
49
50
51
52
53
54
55
56
57
58
59
60

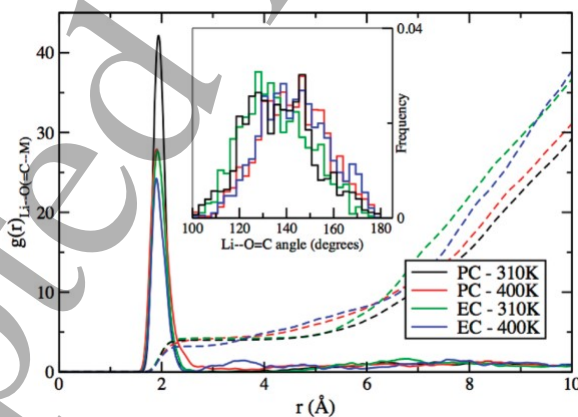
1599 in section 3.3.5).

1600 **4.2.3 *Ab initio* modelling of liquid electrolytes**

1601 *Ab initio* calculations on liquid electrolytes provide critical information that has been used
1602 to explain their behaviour in experimental applications. For many years, DFT calculations
1603 (c.f. section 2.1.1) have been used to provide information on the electrochemical stability
1604 of solvents.³¹⁴ Modelling the electrochemical stability allows more complex effects to be
1605 decoupled, which is not possible through experimental techniques, and these models have
1606 aided the understanding of the functional form of the LUMO and HOMO, opening routes
1607 to raise the stability window by design. Computational models were further developed in
1608 2011 when Ong et al. used a combined MD and DFT approach to model the electrochemical
1609 stability window of several ionic liquids with a higher degree of accuracy than previously
1610 seen.³¹⁵ This methodology has since been widely used in studying the stability of various
1611 ions in solution, with many key studies being based on the initial work of Vuilleumier and
1612 Sprik.³¹⁶ Here, the authors modelled the ionisation of sodium and silver using *ab initio* MD
1613 (AIMD), which was later extended to model fluctuations in the coordination shells,³¹⁷ and
1614 then to model copper³¹⁸ ions and the redox of molecular species.³¹⁹ However, the applicability
1615 of any such method is somewhat dependent on the solvent. This point was made clear by
1616 Lynden-Bell on the subject of the difficulties of applying Marcus theory to ionic liquids,
1617 where long range electrostatic interactions may become important.³²⁰ This type of modelling
1618 is important, as single atom events cannot easily be viewed in isolation experimentally, with
1619 a temporally and spatially averaged perspective of the system being obtained using most
1620 experimental probes. In explicit atomistic simulations, behaviour can be observed at an
1621 atomic scale, as shown in further detail in section 4.2.5.

1622 *Ab initio* modelling using DFT provides a parameter-free approach to simulating the
1623 properties of liquid electrolytes. For example, Ganesh et al. demonstrated the use of AIMD of
1624 liquid electrolytes, using the PBE-generalised gradient approximation (PBE-GGA) exchange-

1
 2
 3
 4 1625 correlation functional to calculate the statistical and dynamic properties.³²¹ They performed
 5
 6 1626 simulations of LiPF_6 at 310 K and 400 K in EC and PC at densities comparable with typical
 7
 8 1627 experimental compositions. They observed a spontaneous decomposition of LiPF_6 into Li^+
 9
 10 1628 and PF_6^- and a coordination number of 4 for solvated Li^+ , similar to experimental observa-
 11
 12 1629 tions. The plots of the radial distribution function (RDF) of Li-ion with the carbonyl oxygen
 13
 14 1630 of EC and PC are shown in Figure 22. The Li-O (carbonyl) near-neighbour distance in PC
 15
 16 1631 is found to be ~ 1.94 Å at 310 K and ~ 1.90 Å at 400 K, quite close to the experimentally
 17
 18 1632 measured distance of ~ 2.04 Å by time of flight neutron scattering experiments.³²² The Li-O
 19
 20 1633 (carbonyl) peak for EC is ~ 1.92 Å at 310 K and ~ 1.90 Å at 400 K, which is quite close to
 21
 22 1634 that for PC. Comparatively, a classical MD simulation predicted a Li-O (carbonyl) peak at
 23
 24 1635 ~ 1.70 Å.³²³ The Li-O=C bond angle distribution is shown in the inset of Figure 22. The
 25
 26 1636 center of the distribution for PC is at 140° which is in agreement with the experimentally
 27
 28 1637 measured value of 138° .³²² Here, the distribution for EC is predicted to be similar to that
 29
 30 1638 for PC. Calculations using classical MD simulation also predict EC and PC to have similar
 31
 32 1639 distributions, though at a much higher Li-O=C angle $\sim 160^\circ$ for both solvents.³²³



47 Figure 22: Partial radial distribution function of Li-ion with the carbonyl oxygen of EC and
 48 PC along with the partial-density weighted integral (dashed lines) which equals the Li-ion
 49 coordination number. In both electrolytes, the Li-O (carbonyl) distance is ~ 2 Å and the
 50 first-solvation shell of Li-ion has 4 EC or PC molecules, consistent with the experiments.
 51 The inset shows the histogram of the Li-O=C angle. Reprinted with permission from Ref.
 52 321. Copyright 2011 American Chemical Society.

56 1640 Perhaps the most enticing possibility regarding *ab initio* methods at interfaces is to study

1
2
3 1641 the liquid-electrode interfacial behavior. The physics of such a study are, however, complex
4
5 1642 and therefore trade-offs in functional choice and solvent model may need to be made, in order
6
7 1643 to make calculations feasible. Lespes and Filhol used an implicit solvent model to study the
8
9 1644 interfacial electrochemistry of lithium EC solutions.³²⁴

10
11 1645 While AIMD is free from the effects of arbitrary parameters and is highly accurate, a
12
13 1646 major limitation of this approach is the high computational cost, restricting the reachable
14
15 1647 time- and length-scales to just tens of pico-seconds and between hundreds (conventional
16
17 1648 DFT) and thousands of atoms (linear-scaling DFT approaches, c.f. section 2.1.2), resulting
18
19 1649 in inaccuracies and irregularities in the calculations.

20
21 1650 When considering the impacts of small length scales, the critical issue is the introduc-
22
23 1651 tion of spurious long- to medium-range correlations of atoms and molecules. As liquids do
24
25 1652 not exhibit long-range order, the presence of periodic images that are located at exactly a
26
27 1653 cell's width in all directions introduces an unphysical correlation. This is observed in the
28
29 1654 modelling of systematically disordered solids in smaller cells.³²⁵ For example, Zhao et al.
30
31 1655 recently revealed that there is a distribution of different, low-symmetry, local motifs in cubic
32
33 1656 halide perovskites, such as tilting and rotations, which are only observed if you allow for
34
35 1657 a larger-than-minimal cell size.³²⁶ Beyond truncating the RDF to a shorter distance than
36
37 1658 is optimal (i.e. half the shortest distance between periodic images), this effect will also in-
38
39 1659 troduce (normally small) inaccuracies in thermodynamic and dynamic quantities.^{85,327-329}
40
41 1660 These inaccuracies are of a particular concern in liquid electrolytes, as the electrostatic in-
42
43 1661 teractions between ions gives rise to longer range interactions, even when the Debye length
44
45 1662 is far smaller than the system size.³³⁰

46
47 1663 The short time scales of *ab initio* simulations can, particularly for more viscous liquids,
48
49 1664 lead to highly non-ergodic (fully-sampled) simulations. When snapshots throughout the
50
51 1665 whole trajectory are highly correlated,³³¹ this can lead to problems for both dynamic and
52
53 1666 equilibrium studies.

54
55 1667 Often, neither time correlation nor finite size have a significant detrimental effect on
56
57
58
59
60

1
2
3 1668 the reproducibility of experimental results in *ab initio* studies. However, in specific studies
4
5 1669 where they need to be avoided, or where a quantum description of a liquid electrolyte pro-
6
7 1670 vides no significant advantage over a classical description, it is beneficial to turn towards
8
9 1671 far less computationally expensive potentials-based simulations, allowing larger and longer
10
11 1672 simulations.

14 15 1673 **4.2.4 Classical modelling of liquid electrolytes**

16
17 1674 Classical simulation of liquid electrolytes includes classical force field-based MD (c.f. sec-
18
19 1675 tion 2.1.6) and the related field of classical Monte Carlo (MC) (c.f. section 2.1.5). Classical
20
21 1676 MD, also known in solid-state communities as potentials-based MD, is a broad field which
22
23 1677 uses many different types of force fields for different studies. The development of force fields
24
25 1678 for ionic solids is described in section 2.2.2, whereas here we evaluate the force fields used
26
27 1679 for liquid electrolytes and the considerations for developing them. Historically, force fields
28
29 1680 for different electrolyte systems have developed at similar paces. Here, we use the example
30
31 1681 of the development of force fields for ionic liquids.

32
33 1682 Electrolyte solvents, from water to molecular solvents and ionic liquids, pose a challenge
34
35 1683 that is not normally present in the solid-state, specifically the need to model covalent bond-
36
37 1684 ing. This is achieved by splitting the potential acting on each atom into bonding and non-
38
39 1685 bonding contributions. The non-bonding component accounts for the effects of electrostatics,
40
41 1686 dispersion, and degeneracy pressure; and the bonding component accounts for the effects of
42
43 1687 covalent bonding. In classical modelling of liquid electrolytes, we are mainly interested in
44
45 1688 the behaviour within the electrolyte's electrochemical stability window (c.f. section 4.1).
46
47 1689 Therefore, the vast majority of classical studies model bonds with unbreakable, harmonic
48
49 1690 potentials. There are four distinct types of bonded potential: ^{331,332} bonds, angles, dihedrals,
50
51 1691 and improper dihedrals. These can be traced back to the parameterisation of force fields,
52
53 1692 such as OPLSA-AA, ^{333,334} and are often parameterised from spectroscopic force constants.
54
55 1693 There are many ways of defining bonded potential types in available codes, ^{113,332} though

1
2
3 1694 their discussion is beyond the scope of this review. Atoms which are subject to a bonded
4
5 1695 potential are often wholly, or partially, excluded from non-bonded interactions, though in
6
7 1696 large molecules, non-bonded intramolecular interactions are important. Alternatively, bonds
8
9 1697 can be kept rigid using a constraint algorithm.^{335–337}

10
11 1698 When developing force fields, generally, it is the non-bonded force field components, in
12
13 1699 particular the partial charges on atoms, which are more frequently varied. A common model
14
15 1700 for liquid electrolytes is the OPLS-AA force field.³³⁴ This is a Lennard-Jones potential-
16
17 1701 based force field with an additional coulombic term.^{338–341} Further developments can be
18
19 1702 made from this base force field, such as the CP&P force field,^{333,342–344} describing a wide
20
21 1703 range of ionic liquid cations and anions. Some non-bonded parameters, particularly charges,
22
23 1704 were varied from OPLS-AA. The charges on the individual molecules are obtained from DFT
24
25 1705 calculations, in this case by use of the charge mapping algorithm CHelpG³³³ (though other
26
27 1706 algorithms may also be used.^{345–347})

28
29 1707 Electrostatic interactions are important when modelling charged electrolytes, as are the
30
31 1708 effects of polarisability. Often it is advantageous in a non-polarisable force field to scale the
32
33 1709 charge on each ion down from a value of $1e$.^{348–350} This accounts for the effect of polarisability
34
35 1710 on the strength of electrostatic interactions between ions, which is particularly important
36
37 1711 for transport properties. However, other force fields have been defined to account directly
38
39 1712 for polarisability.³⁴⁹ As described in section 2.2.2, polarisability can be introduced to a force
40
41 1713 field by the employment of Drude Oscillators (core shell model).^{332,348,349} This approach is
42
43 1714 computationally cheap and is core to the polarisable ionic liquid force field developed from
44
45 1715 CL&P by Schröder.³⁴⁸ A more advanced representation of polarisability can be provided
46
47 1716 by intrinsically polarisable force fields, normally based on the Fumi-Tosi potential.³⁵¹ This
48
49 1717 method has been used for molten salts,³⁵² ionic liquids,^{349,353} and lithium salts in molecular
50
51 1718 solvents.^{354–356} This provides the best description of polarisability in a classical force field,
52
53 1719 however, there is an associated higher computational cost, and a particular code, such as
54
55 1720 metalwalls,³⁵⁷) is often required to implement it.

1
2
3
4 1721 The development of force fields for metal cations has seen an equal level of discussion
5
6 1722 and interest. These cations can be slightly easier to model, owing to their relative non-
7
8 1723 polarisability.^{349,358,359} They are frequently modeled as Lennard-Jones spheres to match the
9
10 1724 potential in the prevailing solvent models (SPC and OPLS-AA). For alkali and alkali earth
11
12 1725 metal cations, a wide range of values of σ (excluded volume) and ϵ (interaction strength)
13
14 1726 can be used, as the basic energetics associated with one of these force fields can be recovered
15
16 1727 for many pairs of sigma and epsilon values. The choice of which pair of parameters to use is
17
18 1728 normally driven by which property requires the highest degree of accuracy for the targeted
19
20 1729 study.³⁵⁸ It is worth noting that many force fields used to modeled the electrolytes of specific
21
22 1730 interest to us here, were parameterised for aqueous solutions.³⁵⁸

23 24 25 1731 **4.2.5 Bulk Structure and Landscaping**

26
27 1732 For structural analysis of liquid electrolytes, analysis of the RDF is the mostly widely used
28
29 1733 approach. Modelling of structural properties in this capacity provide more information-rich
30
31 1734 data compared to scattering, especially in complex systems, and is less labour intensive.
32
33 1735 RDFs can be converted to structure factors by a simple Fourier transform into reciprocal
34
35 1736 space, allowing for easy comparison with experimental structure factors,^{350,360-362} subject
36
37 1737 to re-scaling for the specific intensities associated with different atoms. This method has
38
39 1738 been used frequently for a broad array of electrolytes and has seen particular utility for ionic
40
41 1739 liquids, where the large, inhomogenous ion surface can lead to complex patterns, for which
42
43 1740 MD can provide explanation. Modelling of this sort of behaviour has been performed for
44
45 1741 aprotic³⁶³ solvate ionic liquids,³⁵⁰ imidazolium salts,³⁶¹ lithium carbonate solutions,³⁶⁴ and
46
47 1742 highly concentrated aqueous solvents.³⁶⁰

48
49 1743 The RDF is closely related to potential of mean force acting on a particle, however, the
50
51 1744 physical relevance of RDFs goes further than this. The mean force describes the changing
52
53 1745 potential landscape acting between particles as they approach one another.³³¹ Information
54
55 1746 on the potential of mean force is exceptionally challenging to obtain experimentally, which is

1
2
3 1747 why modelling techniques are frequently used in colloidal systems, as outlined below, where
4
5 1748 this information is also of interest.^{330,365–370}
6

7 1749 The form and gradient of the decay of the RDF towards an asymptote is crucial when
8
9 1750 studying the charge screening properties of an electrolyte. These charge screening properties
10
11 1751 have a particularly prominent effect on electrolyte behaviour when confined²⁹⁹, for instance,
12
13 1752 in a nanoporous electrode.³⁷¹ Surface force experiments³⁶⁵ and fluorescence³⁶⁶ based methods
14
15 1753 do provide an indirect experimental probe of charge screening. However the form of the decay
16
17 1754 in the correlations between charges, which can be either damped oscillatory or monotonic,
18
19 1755 cannot be observed, and both methods are restrictive in the systems that can be studied.
20
21 1756 Atomistic studies of this decay are able to resolve the form of this decay with a great deal
22
23 1757 of precision, allowing direct calculation of many body correlations.^{330,367,368} This provides
24
25 1758 validation to integral equation theories, which can describe confined electrolytes with greater
26
27 1759 accuracy.^{369,370}
28

29 1760 As well as being generated from an RDF, the potential of mean force can be obtained by
30
31 1761 direct calculation by use of centre of mass pulling, umbrella sampling,³³² or running multi-
32
33 1762 ple calculations with ions frozen an exact distance apart from one another. When modelling
34
35 1763 liquid electrolytes, this method is also used to study the approach of ions to an electrode,
36
37 1764 where the energetics associated with decoordination from the solvent and coordination to
38
39 1765 the electrode can be modelled. Such information about the energetics of ion approach is not
40
41 1766 directly accessible experimentally and therefore this allows us to understand the liquid elec-
42
43 1767 trode interface more intimately. For instance, in the solvate ionic liquid $[G4(Li)]_+[TFSI]_-$,
44
45 1768 a lithium sulfur electrolyte, this sort of analysis gives an understanding of the interplay
46
47 1769 between dechelation and approach to electrode which would not have been observable exper-
48
49 1770 imentally, nor explainable with mean field theory.^{372,373} In another example, Sergeev et al.
50
51 1771 looked at the approach of oxygen and lithium based species towards electrodes.³⁷⁴ Here, the
52
53 1772 authors performed MD simulations of the electrode/electrolyte interfaces of a Li-O₂ cathode
54
55 1773 with an experimentally relevant potential in 1 M dimethyl sulfoxide (DMSO) solution of
56
57
58
59
60

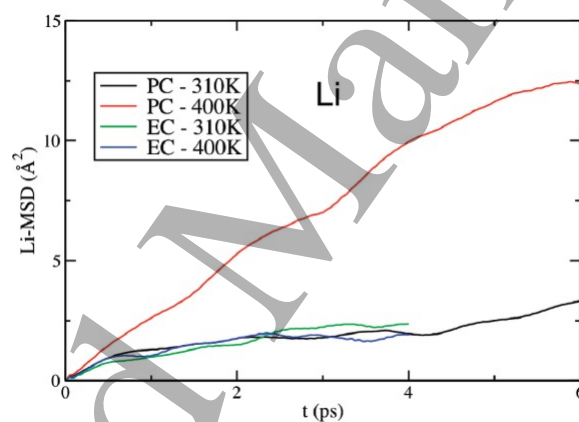
1
2
3 1774 LiPF₆ salt. They found that oxygen anions are effectively pushed out of the reaction layer,
4
5 1775 making the second reduction of superoxide anion improbable, indicating the main cause of
6
7 1776 the electrode surface passivation is the presence of lithium superoxide near the electrode
8
9 1777 surface. This mechanistic result could not be obtained experimentally due to the number of
10
11 1778 side reactions; however, the ability of atomistic modelling to simplify the problem allowed for
12
13 1779 the mechanism to be elucidated. Sergeev et al. proposes a way to suppress the passivation
14
15 1780 by shifting the equilibrium $\dot{O}_2 + Li^+ \rightleftharpoons LiO_2$ to the side of separately solvated ions, for
16
17 1781 example, by using solvents resulting in lower free energy of the ions.³⁷⁴

1782 4.2.6 Li-ion Diffusion

1783 Diffusion (c.f. section 2.3.3) plays a critical role in the operation of liquid electrolytes through
1784 its impact on conductivity. However, in liquid electrolytes its impact goes deeper, as the
1785 dielectric constant of liquids consists of both dipolar and ionic contributions. These two con-
1786 tributions can be obtained by analysis of the dipole orientation and current auto-correlation
1787 functions using the Einstein-Helfand method. For example, Coles et al. performed this
1788 analysis on four liquid electrolytes (three in aqueous solvent and one in a common organic
1789 solvent mixture): aqueous solutions of LiCl, NaI, and lithium bistriflimide (LiTFSI), as well
1790 as the same LiTFSI salt solvated in an equimolar mixture of dimethoxyethane (DME) and
1791 1,3-dioxolane (DOL).³³⁰ Here, it was shown that for polar solvents, the dipolar contribution
1792 is nearly always dominant, with the current making a small corrective contribution which
1793 could feasibly be neglected (particularly for more dilute systems). For ionic liquids, which
1794 contain ionic species that can exhibit a net dipole, such as TFSI, both dipolar and ionic
1795 contributions would be observed. The effect of molecular ions having simultaneous charges
1796 and dipoles was explored by Schröder, who showed that even more thorough treatment may
1797 be required to observed the impacts of their interplay.³⁷⁶ These contributing factors cannot
1798 be easily/feasibly disentangled experimentally.

1799 The self-diffusion coefficient can be calculated from the slope of the mean-squared dis-

1
2
3
4 1800 placement, according to the Stokes-Einstein relation. For example, Ganesh et al. calculated
5
6 1801 the mean-squared displacement of solvated Li-ion in EC and PC solvents from AIMD, as
7
8 1802 shown in Figure 23. For PC, the self-diffusion coefficient is calculated to be $\sim 0.7 \times 10^{-9}$
9
10 1803 $\text{m}^2 \text{s}^{-1}$ at 310 K while the experimentally measured value of self-diffusion coefficient at 303
11
12 1804 K is $\sim 0.16 \times 10^{-9} \text{m}^2 \text{s}^{-1}$.³⁷⁷ For EC, it is calculated to be $\sim 1.0 \times 10^{-9} \text{m}^2 \text{s}^{-1}$ at 310 K,
13
14 1805 while the experimentally measured value of self-diffusion coefficient at 313 K is $\sim 0.21 \times 10^{-9}$
15
16 1806 $\text{m}^2 \text{s}^{-1}$.³⁷⁷ At 400 K, the calculated diffusion coefficient for PC increases to $\sim 3.7 \times 10^{-9}$
17
18 1807 $\text{m}^2 \text{s}^{-1}$, while it remains the same for EC. It is notable here that the Li-ion diffusion in the
19
20 1808 electrolyte solution is 4-5 orders of magnitude higher than that in the bulk of electrodes, e.g.
21
22 1809 in the graphite anode (cf. section 3.2.4).



23
24
25
26
27
28
29
30
31
32
33
34
35
36
37
38 Figure 23: Mean-squared displacement of solvated Li-ion in EC and PC. Reprinted with
39 permission from Ref. 321. Copyright 2011 American Chemical Society.
40
41

42 1810 Investigation of the diffusion of different ions subject to a field gives a sense of the
43
44 1811 diffusion rate of specific ions and also an idea of exchange rates of solvent molecules. This
45
46 1812 information can be obtained using nuclear magnetic resonance (NMR), however, atomistic
47
48 1813 models can provide more detailed data, as outlined here. For instance, strongly coordinated
49
50 1814 solvents will have diffusion coefficients closer to the ions they are coordinated to, whereas less
51
52 1815 strongly coordinated ligands will have diffusion coefficients dissimilar from the coordinating
53
54 1816 ion.^{350,354,378-380} Examples of this behaviour can be found in the MD studies of Borodin
55
56 1817 et al., which looked at diffusion in lithium solutions of both the common carbonate³⁵⁴ and
57
58
59
60

1
2
3
4 1818 ethylene glycol oligomer solvents.³⁷⁹ For the common carbonate, MD predictions of the
5
6 1819 ion and solvent self-diffusion coefficients and conductivity were in good agreement with
7
8 1820 experiments, with approximately half of the charge transported by charged ion aggregates
9
10 1821 with the other half carried by free ions.³⁵⁴ The self-diffusion coefficients and conductivity
11
12 1822 predicted by MD for the ethylene glycol oligomer solvents were also found to be in good
13
14 1823 agreement with experimental data. Li^+ transport was found to primarily occur through
15
16 1824 exchange of TFSI⁻ anions in the first coordination shell.³⁷⁹ The 2015 study of Shimizu
17
18 1825 et al. investigated a number of different lithium glyme solvate ionic liquids.³⁵⁰ Here, the
19
20 1826 authors found that although MD was unable to yield quantitative information about the
21
22 1827 dynamics of the system, it could provide two important pieces of information: the auto-
23
24 1828 diffusion coefficients of glyme molecules in pure glyme are much larger than those of glyme
25
26 1829 molecules in glyme equimolar mixtures at the same temperature; the decrease in the glyme
27
28 1830 diffusion coefficients is more pronounced in the $\text{Li}[\text{Ntf}_2] + \text{glyme}$ system than in the $\text{Li}[\text{NO}_3]$
29
30 1831 $+ \text{glyme}$ mixture.³⁵⁰ The study of Lesch et al. used MD to investigate lithium salts dissolved
31
32 1832 in aprotic ionic liquids.³⁷⁸ The authors found that the exchange of TFSI anions in and out
33
34 1833 of the first coordination shell of Li^+ was faster in pyr₁₃-based systems, compared to emim-
35
36 1834 based systems, and that the Li^+ ion transference number was higher.³⁷⁸ The atomic scale
37
38 1835 context provided by atomistic simulation allows for the specific dynamics and atomic scale
39
40 1836 effects, such as dynamic (de)coordination, which govern diffusion to be observed directly.
41
42 1837 These behaviours cannot be observed directly in a spatially and globally averaged NMR
43
44 1838 measurement.³⁵⁰

45
46 1839 In more complex solvents, such as ionic liquids, the nature of the solvent plays an important
47
48 1840 role too, for instance Borodin and Smith showed the effect of fluorination of ionic liquid
49
50 1841 cations on diffusion behaviour.³⁸⁰ This sort of study can be directly compared with pulsed
51
52 1842 field gradient NMR experiments of battery materials. This was done, for example, when
53
54 1843 Shimizu et al. studied a LiTFSI-based solvate ionic liquid, which had been proposed as
55
56 1844 a solvent for Lithium Sulfur batteries.³⁵⁰ The authors found the molecular behaviour of
57
58
59
60

1
2
3 1845 solvate ionic liquids to be probed effectively using a combination of MD trajectories and
4
5 1846 structural/aggregation analysis techniques.
6

7 1847 Atomistic simulations are also providing new understanding of the fundamental physics
8
9 1848 behind non-linear relationships between the electric field and the electrolyte conductivity,
10
11 1849 known as Onsager's Wein effect.³⁸¹ In a recent study of dilute electrolytes and molten salts³⁸²
12
13 1850 Lesnicki et al. performed a direct study of this half century old conundrum, by directly
14
15 1851 observing the interplay between external fields as well as the correlations between, and
16
17 1852 clustering of, ions using atomistic modelling and innovative statistical mechanical analysis.
18
19 1853 This direct observation of liquid structure and dynamics could only be obtained through
20
21 1854 simulation. Such studies are likely to expand into the study of battery electrolytes in the
22
23 1855 coming years where this sort of behaviour has a direct effect on conductivity and function.
24
25 1856 In the above examples of diffusion studies, ion pairing plays a contributing role; in general,
26
27 1857 any phenomenon originating from ion pairing can benefit from investigation by atomistic
28
29 1858 simulation.
30

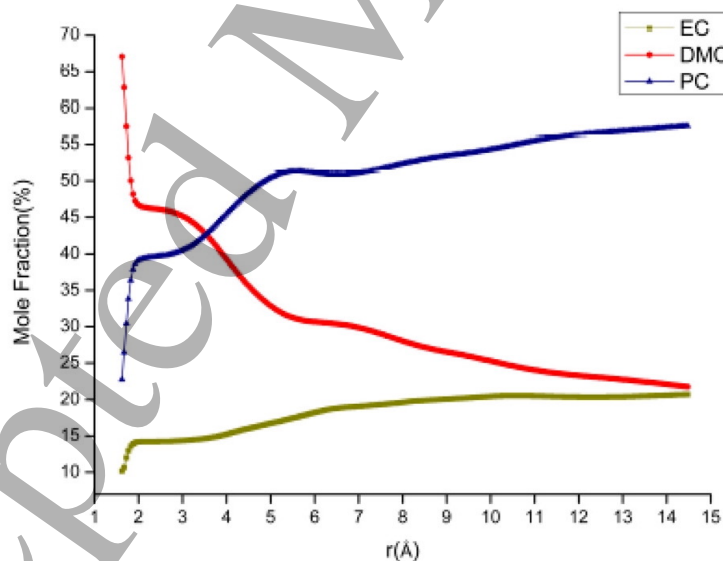
31 1859 Shimizu et al.'s work highlights a key advantage of molecular simulation. While the
32
33 1860 authors utilised both scattering and NMR based experimental probes, neither could provide
34
35 1861 the same unambiguous detail of the nature and dynamics of ion pairing, on the single atom
36
37 1862 scale in the liquid, that can be obtained from simulation.³⁵⁰ More recently, the richness
38
39 1863 of simulated data sets has allowed for the analysis of liquid structures with deep learning
40
41 1864 based approaches, providing a more complete picture of electrolytes, their disorder, and
42
43 1865 complexity.³⁸³
44
45

46 1866 **4.2.7 Solvation Energies**

47
48
49 1867 Solvation energies in electrolytes have been widely studied and, though research focus has
50
51 1868 been on aqueous solvation of biomolecules, these techniques can also be used to look at
52
53 1869 solvation of metal ions with organic solvents. Dependent on the exact thermodynamics
54
55 1870 of the system, the solvation energies of ions may be obtained by a number of methods.
56
57
58
59
60

1
2
3
4 1871 Skarmoutsos et al. combined DFT and MD methods to look at the solvation structures of
5
6 1872 lithium salts in ternary mixtures of different carbonate solvents and showed that different
7
8 1873 solvents were found to dominate at different distances from a central lithium cation, observing
9
10 1874 a particular preference for solvation of lithium by DMC ions over PC and EC, as shown in
11
12 1875 Figure 24. Takeuchi et al. looked even deeper at the energetics behind the direct contact
13
14 1876 between cations and anions in solution.³⁸⁵ The relative stabilities of the mono-, bi-, and tri-
15
16 1877 dentate coordination structures were assessed with and without solvent, where water, PC,
17
18 1878 and DMC were found to favour the ion pair (CIP)–solvent contact. Vacant sites of Li^+ cation
19
20 1879 in CIP are solvated with three carbonyl oxygen atoms of PC and DMC solvent molecules,
21
22 1880 and the solvation is stronger for the monodentate CIP than for the multidentate.³⁸⁵ Such
23
24 1881 detailed analysis is not possible to resolve through experimental techniques.

25
26 1882 These are just a few notable studies on solvation energies in liquid electrolytes. A com-
27
28 1883 pelling theoretical description of solvation is given by Lazaridis.³⁸⁶



48 Figure 24: Local mole fractions (%) of ethylene carbonate, propylene carbonate, and
49 dimethyl carbonate as a function of the distance from the lithium cation in the ternary
50 mixture. Reprinted with permission from Ref. 384. Copyright 2015 American Chemical
51 Society.
52
53
54
55
56
57
58
59
60

1884 4.2.8 Activity coefficients of electrolytes

1885 The activity coefficients describe the deviation of actual electrolytes from an ideal mixture
1886 of substances¹⁷¹ and can be calculated using DFT+PBE simulations (c.f. section 2.1.1) of
1887 solutes in electrolyte solutions, as described in sec 2.3.2. The experimental value of bulk
1888 permittivity of EC is ($\epsilon^\infty = 90.7$)³⁸⁷ and its surface tension is (0.0506 N m^{-1}).³⁸⁸ These
1889 values were used by Dziedzic et al. to calculate the activity coefficient of LiPF_6 in EC.¹³⁵
1890 The solvent radius was set to $R_k^{\text{solvent}} = 10.5 a_0$, to approximate the size of an EC molecule,
1891 and the isovalue of solute electronic density, (ρ_e^λ), is varied to match the experimental activity
1892 coefficients. A plot of the computed activity coefficients as a function of the square root of
1893 electrolyte concentration is given in Figure 25, along with experimental values from Stewart
1894 and Newman.³⁸⁹ Here, we see a good agreement for $\rho_e^\lambda = 0.002 e/a_0^3$. Trends are also plotted
1895 from the linearised approximation of PBE, where the solvent radius is reduced to resemble
1896 the prediction for point charges from the Debye-Hückel theory.³⁹⁰ The thermodynamic factor
1897 can be obtained from numerically differentiating these curves. This is a novel technique of
1898 calculating activity coefficients and thermodynamic factors from hybrid atomistic-continuum
1899 methods.

1900 4.2.9 Interfacial Nanostructure of Electrolytes

1901 In sections 3.3 and 5.4, the interfaces between solids and liquids from the perspective of the
1902 solid have been discussed. However, the interface from the perspective of the liquid is also of
1903 interest. The structure of liquid electrolytes at metallic³⁹¹ and charged dielectric³⁶⁵ interfaces
1904 will normally extend away from the interfacial region and can be observed prominently for
1905 tens of nanometers and, dependent on concentration of the liquid, can either be monotonic
1906 or oscillatory, as described in section 4.2. Spectroscopic and surface methods used to study
1907 the liquid-solid interface are often indirect and require specific conditions for analysis (e.g.
1908 transparency and smoothness)³⁹²⁻³⁹⁴, which often constrains the interfaces we can study as
1909 well as the detail and conclusiveness of the data obtained. Computational modelling provides

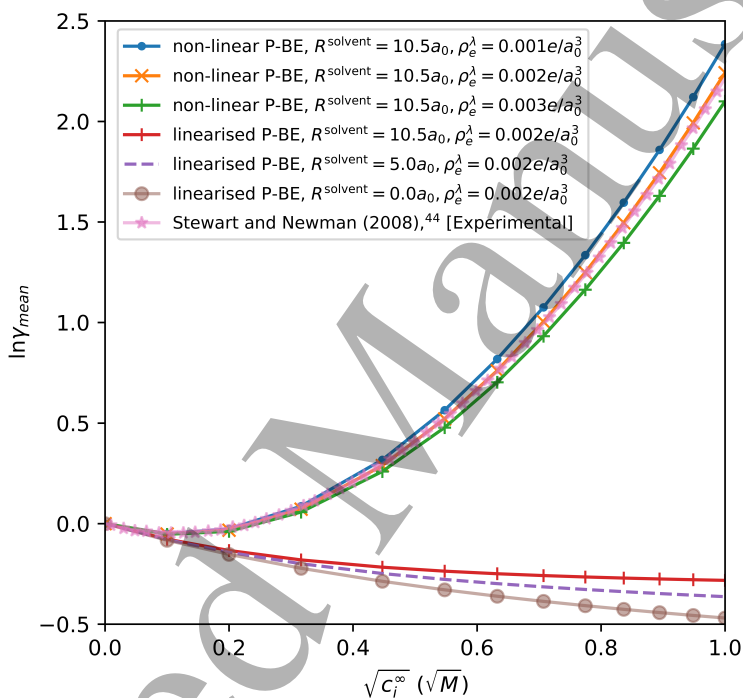


Figure 25: Mean activity coefficients for LiPF_6 in ethylene carbonate at $T = 308$ K as a function of concentration and for different values of the atomic electronic density isovalue parameter which determines the extent of the accessibility function. Calculations with the linearised approximation to P-BE are also shown. Reprinted with permission from Ref. 135. Copyright 2020 American Chemical Society.

1
2
3
4 1910 a route to direct and data rich understanding of the liquid solid interface. This section will
5
6 1911 highlight some particular areas of study.

7 1912 Concentrated electrolytes and ionic liquids both adopt the characteristic overscreening
8
9 1913 structure at charged interfaces, including electrodes. This structure, comprising oscillations
10
11 1914 of charge decaying into the bulk, is commonly observed.^{373,391} Modelling these systems re-
12
13 1915 quires an appropriate electrode model. While interesting information can be gained from
14
15 1916 simulating ions at an electrode with a fixed charge, for example in a high throughput study
16
17 1917 looking at structural changes with electrode surface charge,³⁷³ fixed potential boundary con-
18
19 1918 ditions will provide a more accurate description of the capacitance,^{391,395} interfacial struc-
20
21 1919 turing of a liquid electrolyte,^{373,396,397} and the decoordination and dechelation dynamics of
22
23 1920 coordinated ions.³⁹⁸ Though we note that, in light of a recent study by Scalfi et al., this
24
25 1921 field continues to evolve as more nuanced classical electrode models are employed, such as
26
27 1922 the Thomas-Fermi based model proposed by Scalfi et al..³⁹⁵

28
29 1923 A wide variety of different electrolytes have been studied using fixed potential electrolytes,
30
31 1924 from ionic liquids to concentrated electrolyte. Both nanoporous^{371,396,398,399} and nanoscopi-
32
33 1925 cally rough electrode surfaces have been heavily used.⁴⁰⁰ A specific example of interest is the
34
35 1926 work of Borodin and Bedrov, where MD simulations were performed on dilithium ethylene
36
37 1927 dicarbonate (Li_2EDC) and dilithium butylene dicarbonate (Li_2BDC), in contact with mixed
38
39 1928 solvent electrolyte (EC:DMC) doped with LiPF_6 .⁴⁰¹ In this study, the authors examined the
40
41 1929 SEI–electrolyte interface and found an increase of EC and PF_6^- molecules and a decrease of
42
43 1930 DMC at the interfacial layer next to the SEI surface, compared to bulk electrolyte concen-
44
45 1931 trations. The activation energies for the Li^+ solvation–desolvation reaction were estimated
46
47 1932 to be 0.42–0.46 eV for the Li_2EDC –electrolyte and Li_2BDC –electrolyte interfaces.

48
49 1933 While the context provided by these methods is useful, more generally the capacitance
50
51 1934 curves generated by atomistic studies of fixed potential electrodes have frequently been able
52
53 1935 to replicate experimental results when mean field theory cannot. For instance, Simoncelli
54
55 1936 et al. were able to replicate the experimental behaviour, in particular the double layer ca-

1
2
3 1937 capacitance, of a nanoporous brine based capacitor, where a variety of mean field models
4
5 1938 were unsuccessful.⁴⁰² Li et al. were able to show the exact rearrangements of the molecules
6
7 1939 and ions at a metallic interface which gave rise to the nature of the experimentally and
8
9 1940 computationally observed relationship between capacitance and voltage of a water in salt
10
11 1941 electrolyte.³⁹⁷
12
13

14 1942 **4.2.10 Outlook and challenges**

15
16
17 1943 Liquid electrolytes will likely remain the most prominent form of commercialised electrolyte
18
19 1944 for battery applications in the near future. This is partly due to their monopoly in the
20
21 1945 market and partly due to their low cost, which will continue to drive popularity. Despite
22
23 1946 the overwhelming success of commercial liquid electrolytes, there is still room for further
24
25 1947 performance improvements, with several key issues as limiting factors. Liquid electrolytes
26
27 1948 are known to be limited by narrow electrochemical windows, solvent toxicity, and material
28
29 1949 flammability/safety concerns. There are two potential avenues for solving these issues:
30
31

32 1950 • Resolving these limitations within the confines of liquid electrolytes: ionic liquids have
33
34 1951 a large electrochemical window and high thermal stability, and their conductivities
35
36 1952 are similar to those of conventional organic solvent solutions.³⁰⁷ However, they are
37
38 1953 expensive and there are associated safety concerns.^{282,283} A liquid electrolyte alternative
39
40 1954 to this could be in water-in-salt electrolytes. Water-in-salt electrolytes are a novel
41
42 1955 class of electrolytes, which inverts the conventional idea of a salt being dissolved in
43
44 1956 a solvent, with a small amount of water being dissolved in a hygroscopic lithium salt
45
46 1957 to the point where a liquid is obtained,^{403,404} analogous to the high concentration
47
48 1958 organic electrolyte solutions described by Yamada et al..³⁰⁶ These liquids have the
49
50 1959 advantage of being comprised solely of a lithium salt and water, which decreases cost
51
52 1960 and eliminates the toxicity and risk of flammability and thermal runaway traditionally
53
54 1961 associated with organic solvents. The high concentration of salt also leads to a greatly
55
56 1962 expanded electrochemical window of 3 V³⁰⁸ from the 1.23 V value for dilute aqueous
57
58
59
60

1
2
3
4 1963 solutions. However, the highly concentrated solutions in these electrolytes lead to re-
5
6 1964 crystallisation of the lithium salt and low conductivity, due to the high viscosity of the
7
8 1965 liquid.^{404,405}

- 9
10 1966 • Replacing liquid electrolytes with solid or soft matter alternatives: despite the suc-
11
12 1967 cess of liquid electrolytes in LiBs, a number of issues have arisen that may prove
13
14 1968 impractical to address within the grouping of liquids. Organic liquid electrolytes are
15
16 1969 highly flammable, leading to safety issues, such as thermal runaway, when deployed
17
18 1970 in portable electronic devices and EVs.^{17,18,406} These safety issues may have a low fre-
19
20 1971 quency of occurrence, but when used often by a large number of people, they become
21
22 1972 nearly inevitable events, as evidenced by EV and portable device explosions making
23
24 1973 the news headlines.

25
26 1974 The use of liquid electrolytes also limits the compatibility with electrode materials and
27
28 1975 thereby limits the maximum energy density of a battery.¹⁹ For example, higher energy
29
30 1976 density lithium sulfur (Li-S) batteries are unstable, due to interactions between the
31
32 1977 liquid electrolyte and the electrodes.⁴⁰⁷ Similarly, Li metal anodes cannot be used with
33
34 1978 organic liquid electrolyte solvents without additives,⁴⁰⁸ because of dendrite formation
35
36 1979 and capacity loss.^{409,410} Due to these concerns, research in recent years has shifted
37
38 1980 to looking at alternatives, such as solid and soft matter-based electrolytes.²⁶ Solid
39
40 1981 electrolytes are discussed in detail in the next section (c.f. section 4.3) and soft matter
41
42 1982 electrolytes are discussed in detail by Hallinan Jr and Balsara and Popovic.^{411,412}

43
44
45 1983 The design of the electrode-electrolyte interfaces affects the capacity and rate capabil-
46
47 1984 ity in LiBs.^{290,293} Further work to design better interfaces that are compatible with the
48
49 1985 electrodes, thermodynamically stable, kinetically fast for Li-ion transfer, electronically in-
50
51 1986 sulating, and which lead to minimal loss in performance, will be crucial to progress LiB
52
53 1987 performance.^{2,291,292} Atomistic modelling can help in this area by analysing the chemical re-
54
55 1988 actions leading to SEI formation and predicting new materials which form a well-structured

1
2
3 1989 SEI, conducive to ion transmission.¹⁶ Further details of the formation and function of the
4
5 1990 SEI at the graphite anode are summarised in section 3.3.5.
6

7 1991 Liquid electrolytes are complex substances and are therefore difficult to fully capture
8
9 1992 in atomistic models. In recent years, computational capacity has expanded, allowing more
10
11 1993 complex models to be studied. Alongside this, new computational methods have been de-
12
13 1994 veloped under the open source license, allowing research of these materials to become more
14
15 1995 accessible.^{357,371,401,402} Future advances in computational ability, combined with improved
16
17 1996 experimental studies, provide a framework for high throughput screening of electrolyte ma-
18
19 1997 terials.
20

21 1998 Developments in expanding the achievable time and length scales of AIMD will allow
22
23 1999 more complex models to be developed. However, it is still implausible that AIMD will be
24
25 2000 able to simulate whole electrodes/interfaces/battery cells for long enough time and length
26
27 2001 periods to achieve full ergodicity (statistical convergence). Therefore, methods which can
28
29 2002 provide long scale simulations are still needed. In particular, the emerging fields of fitting
30
31 2003 machine learnt potentials for liquid electrolytes,⁴¹³⁻⁴¹⁵ and more complex classical models
32
33 2004 which incorporate polarisability^{349,357} or bond breaking dynamics.^{416,417} This would enable
34
35 2005 simulations of electron transfer, bond formation, and the effect of ion and solvent polaris-
36
37 2006 ability at larger scales and in greater detail.
38

39 2007 Atomistic modelling of liquid electrolytes does not necessarily require more computational
40
41 2008 expense to advance. Exploitation of underused physical methods to model liquid systems at
42
43 2009 far lower cost has been explored. One such method, classical DFT, has already been applied
44
45 2010 to model aqueous capacitors³⁶⁹ and confined ionic liquids.⁴¹⁸ This has the potential to be
46
47 2011 coupled with electronic DFT (c.f. section 2.1.1) to model electron transfer.⁴¹⁹
48

49 2012 It should be emphasised that, for practical use, the interfaces between the liquid elec-
50
51 2013 trolyte and the electrodes are the major limiting factors in terms of performance, stability,
52
53 2014 and safety. Therefore, advancement through electrolyte design is crucial, where the critical
54
55 2015 obstacles discussed here could be resolved by the use of novel, solvents, salts, or electrolyte
56
57
58
59
60

2016 salts. Several articles discuss the challenges of this topic in greater detail.^{420–422}

2017 **4.3 Solid Electrolytes**

2018 **4.3.1 Introduction**

2019 Solid electrolytes have attracted considerable attention as an alternative to highly-flammable
2020 liquid electrolytes, as they significantly improve device safety and have the potential to im-
2021 prove energy and power densities, while also reducing the cost of synthesis.^{285,423–426} An
2022 ideal solid electrolyte material should possess high electronic resistance, high ionic conduc-
2023 tivity, outstanding thermal stability, strong electrochemical stability, excellent mechanical
2024 strength, and reduced interfacial resistance.^{427,428} There are three different categories of solid
2025 electrolytes used in rechargeable batteries:⁴²⁶ (1) inorganic ceramic electrolytes, (2) organic
2026 polymer electrolytes, and (3) composite electrolytes.

2027 Solid electrolytes were discovered by Michael Faraday in the early 1830s through research
2028 on the conduction properties of heated solid silver sulfide (Ag_2S) and lead fluoride (PbF_2).⁴²⁹
2029 The use of a ceramic-based β -alumina ($\text{Na}_2\text{O}\cdot 11\text{Al}_2\text{O}_3$) in high-temperature sodium-sulfur
2030 (Na-S) batteries in the 1960s was considered as a milestone in the development of batteries,
2031 enabled by solid electrolytes.⁴³⁰ In the 1980s, the Zeolite Battery Research Africa (ZEBRA)
2032 group developed the “ZEBRA” batteries using $\text{Na}_2\text{O}\cdot 11\text{Al}_2\text{O}_3$ as the solid electrolyte.⁴³¹ So
2033 far, the Na-S battery has been commercialised in Japan,⁴³² whereas the ZEBRA battery is
2034 currently being developed by the General Electric Corporation in the United States.⁴³³

2035 In 1990, the Oak Ridge National Laboratory synthesised a lithium phosphorus oxynitride
2036 (LiPON) material,^{434,435} opening up the use of inorganic solid-state electrolytes in LiBs.
2037 Since then, a huge number of inorganic, lithium-ion conductive ceramic materials have been
2038 developed, including perovskite-type,⁴³⁶ garnet-type oxides,^{437,438} garnet-type sulfides,⁴³⁹
2039 lithium super ionic conductor (LISICON),⁴⁴⁰ sodium super ionic conductor (NASICON)-
2040 like materials,⁴⁴¹ lithium-argyrodite materials,⁴⁴² and Li-rich anti-perovskites.^{443,444}

2041 Despite recent advancements in crystalline inorganic electrolytes, they are still brit-

1
2
3
4 2042 tle and therefore difficult to fit into different battery shapes. Solid-state polymer elec-
5
6 2043 trolytes (SSPEs), due to their high flexibility, can fit into any battery shape and present
7
8 2044 improved safety and stability features compared to crystalline inorganic electrolytes.⁴²⁶
9
10 2045 Since 1980, various high molecular weight, dielectric polymer hosts were investigated for
11
12 2046 LiBs as high conductivity electrolytes, such as poly(ethylene oxide) (PEO),⁴⁴⁵ polyacry-
13
14 2047 lonitrile (PAN),^{446,447} poly(vinylidene fluoride) (PVDF),^{448–450} poly(methyl methacrylate)
15
16 2048 (PMMA),^{451,452} and poly(vinylidene fluoride-hexa-fluoropropylene) (PVDF-HFP).^{453–455}

17
18 2049 The ionic conductivities of most polymer electrolytes are significantly lower than those of
19
20 2050 both oxide solid electrolytes and liquid electrolytes.⁴⁵⁶ A possible solution to this limitation is
21
22 2051 to create composites by integrating nanoscale, highly conductive, inorganic, particulate fillers
23
24 2052 into the polymer electrolyte material.⁴²⁶ This enhances the ionic conductivity and improves
25
26 2053 the mechanical strength and stability of the SSPEs, including the interfacial stability.⁴⁵⁷
27
28 2054 Here, heterogeneous doping increases the ionic conductivity as a result of increasing inter-
29
30 2055 facial regions between an inert solid phase, such as silica, alumina, or boron oxide particles,
31
32 2056 and an electrolyte.⁴⁵⁸ A wide range of inorganic solid composite electrolytes have previously
33
34 2057 been studied, based on oxides ($\text{Li}_2\text{O}:\text{Al}_2\text{O}_3$,⁴⁵⁹ $\text{Li}_2\text{O}:\text{B}_2\text{O}_3$,^{460–462}) hydrides ($\text{LiBH}_4:\text{SiO}_2$,⁴⁶³)
35
36 2058 halides ($\text{LiI}:\text{Al}_2\text{O}_3$,⁴⁶⁴ $\text{LiI}:\text{SiO}_2$,⁴⁶⁵ $\text{LiF}:\text{Al}_2\text{O}_3$,⁴⁶⁶) and sulfides ($\text{Li}_2\text{S}:\text{SiS}_2$.⁴⁶⁷)

37
38 2059 Over the last decade, a limited number of candidates with high ionic conductivities (>1
39
40 2060 mS cm^{-1}) have arisen as potential competitors to liquid electrolytes.^{468–476} Figure 26 presents
41
42 2061 the ionic conductivities of most currently known solid electrolytes.²⁶

43
44 2062 In this section, we review atomistic modelling investigations into the structure-property
45
46 2063 relationships in selected solid-state electrolytes: $\text{Li}_{10}\text{GeP}_2\text{S}_{12}$ (LGPS), lithium argyrodites,
47
48 2064 and $\text{Li}_7\text{La}_3\text{Zr}_2\text{O}_{12}$ (LLZO), belonging to the inorganic solid ceramic electrolyte type, and
49
50 2065 $\text{Li}_2\text{O}:\text{B}_2\text{O}_3$ materials, belonging to the oxide-based solid composite type. A particular focus
51
52 2066 is given to the ion transport mechanism in those materials, which is important for reaching
53
54 2067 high conductivities, a key property of battery materials. Finally, we take a more detailed
55
56 2068 look at the interface of solid electrolytes with the electrodes, and discuss the challenges and

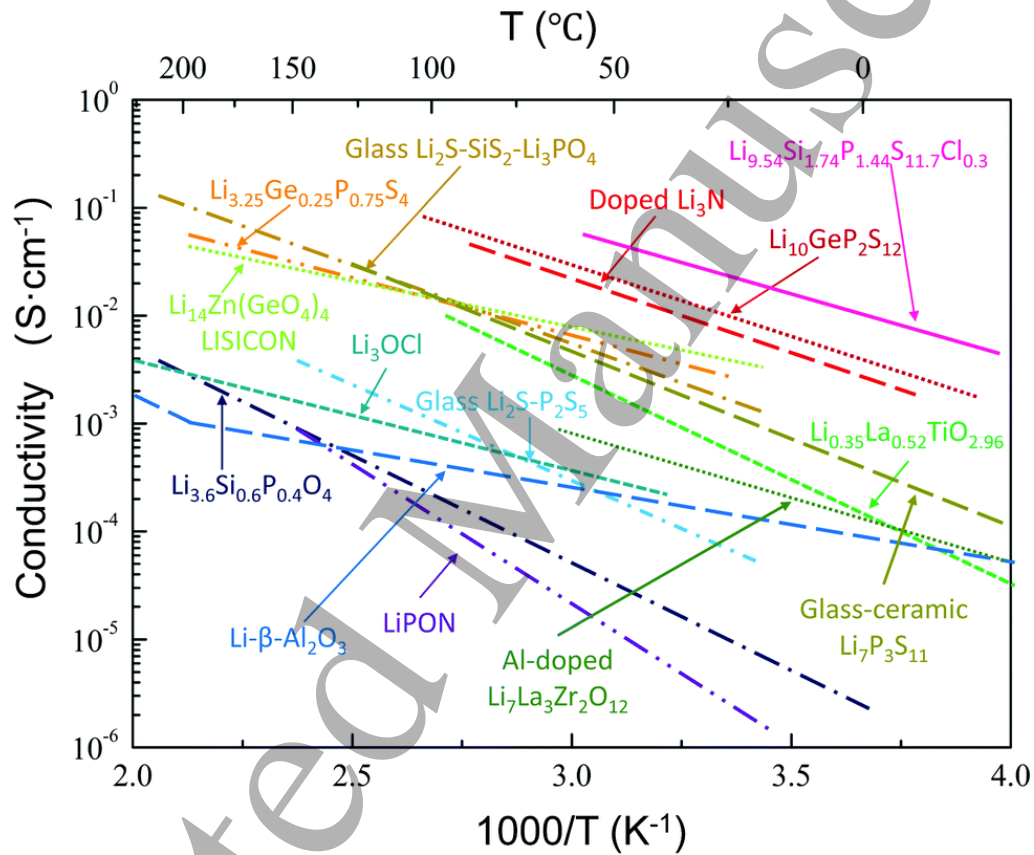


Figure 26: Ion conductivity of several well-known solid lithium ion conductors, including glass and crystalline conductors. Reproduced from Ref. 26 - Published by The Royal Society of Chemistry.

2069 outlook for future atomistic modelling investigations.

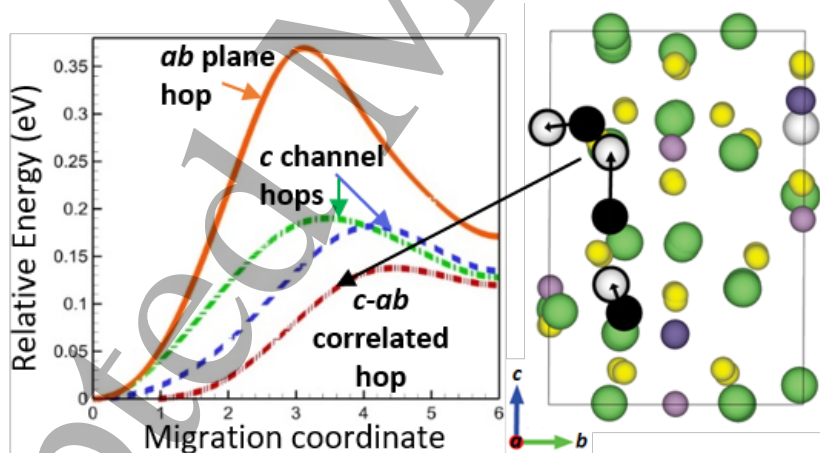
2070 4.3.2 Sulfides

2071 There are a substantial number of computational studies of sulfides which largely relate
2072 to a recent emergence of newly discovered crystalline sulfide superionic conductors. Sul-
2073 fides also tend to have comparatively lower intrinsic electrochemical and chemical stability,
2074 which has stimulated interest in understanding the interfacial interactions within batteries.²⁸
2075 The sulfide group encompasses a range of sulfide-based solid electrolytes, including glass
2076 ceramics,⁴⁷⁷ argyrodites,⁴⁷⁸ and thio-LISICONs.⁴⁷⁹ Some of the most promising solid elec-
2077 trolytes to emerge in recent years include LGPS,^{288,480,481} and the Li-argyrodite ($\text{Li}_6\text{PS}_5\text{X}$,
2078 $\text{X}=\text{Cl,Br,I}$)^{442,482-486} families of superionic conductors.

2079 **LGPS** A study by Kamaya et al. reports that LGPS can reach high room temperature
2080 ionic conductivities of 12 mS cm^{-1} , comparable to that of commercial liquid electrolytes (\sim
2081 10 mS cm^{-1}).²⁸⁸ The authors also determined that diffusion in LGPS is anisotropic, where
2082 c directional motion is predominant over the ab plane, with an overall energy barrier for Li
2083 diffusion being 0.24 eV , with later reports measuring 0.22 eV .⁴⁸⁷ Using AIMD, Mo et al. later
2084 determined the average direction energy barriers of 0.17 eV along the c channel and 0.28 eV
2085 in the cross channel (ab plane),⁴⁸¹ with Xu et al. showing the Li migration mechanism is
2086 through cooperative motion, instead of the initially determined single hop mechanism.⁴⁸⁸
2087 More recently, Adams and Prasada Rao predicted the presence of additional Li sites using
2088 MD, which would allow diffusion along the ab plane.⁴⁸⁹ These sites could change not only
2089 the Li occupancies in the c channel, but also provide a diffusion mechanism involving the ab
2090 plane, opening up the possibility of cross-channel diffusion. The presence of these additional
2091 sites were later confirmed experimentally using single crystal X-ray Diffraction (XRD).⁴⁹⁰

2092 More recently, Bhandari and Bhattacharya also investigated the lithium diffusion dimen-
2093 sionality in LGPS by performing a DFT study of the lithium diffusion energy barrier, using
2094 the nudged elastic band (NEB) method.⁴⁸⁰ In this study, the authors took into account

2095 the fractional occupancies leading to variable c channel Li populations, variable chemical
 2096 environments surrounding Li, and all possible migration mechanisms. The authors found
 2097 that lithium diffusion is neither purely c directional nor purely along the ab plane, but there
 2098 exists a correlated mechanism of motion along $c - ab$ which critically controls the degree
 2099 of anisotropy of Li diffusion in LGPS. The energy barriers for different mechanisms of Li-
 2100 diffusion, shown in Figure 27, suggest that correlated hopping has the lowest energy barrier.
 2101 Bhandari and Bhattacharya further performed a statistical average of all diffusion energy
 2102 barriers, taking into account the formation energy of various Li configurations and predicting
 2103 an overall energy barrier of 239 meV,⁴⁸⁰ which is in close agreement with experiments.²⁸⁸
 2104 Thus, the DFT approach not only explained the overall diffusivities and energy barriers,
 2105 but also gave insight into the underlying mechanism behind the fast Li diffusion in LGPS,
 2106 resolving the discrepancy about the anisotropy of Li diffusion in this compound, which was
 2107 insight not possible to obtain only from experiments.



45 Figure 27: Energy barrier for Li-ion diffusion in the solid electrolyte, $\text{Li}_{10}\text{GeP}_2\text{S}_{12}$ (LGPS),
 46 calculated using the nudged elastic band (NEB) method. Reprinted with permission from
 47 Ref. 480. Copyright 2016 American Chemical Society.

2108 **Lithium argyrodites**, $\text{Li}_6\text{PS}_5\text{X}$ ($X = \text{Cl}, \text{Br}, \text{I}$), can reportedly reach ionic conductivities
 2109 of up to $10^{-2} \text{ S cm}^{-1}$.⁴⁸³ While $\text{Li}_6\text{PS}_5\text{Cl}$ and $\text{Li}_6\text{PS}_5\text{Br}$ exhibit high ionic conductivities of
 2110 $10^{-3} \text{ S cm}^{-1}$ at room temperature, $\text{Li}_6\text{PS}_5\text{I}$ has considerably lower conductivities of 10^{-6}
 2111 S cm^{-1} .⁴⁹¹ The difference of three orders of magnitude is surprising, as the identical crystal

2112 structures suggest the same Li diffusion pathways exist in all systems. Another intriguing
2113 aspect is that the conductivity trend runs counter to other families of solid electrolytes,
2114 such as LGPS, where larger, more polarisable and less electronegative anions are linked with
2115 increased ionic conductivities.⁴⁹²

2116 Understanding which properties and mechanisms influence the conductivity is essential
2117 to obtaining higher ionic conductivities and improving battery performance. Material stoi-
2118 chiometry, anion/cation disorder, and doping, have all been shown to influence conductivity.
2119 Modification of the lithium stoichiometry has been achieved through aliovalent cation substi-
2120 tution on the P sites^{482,493–495} and through anion substitution on the S^{2-}/X^- sites.^{486,496,497}
2121 For example, Ge substitution on the P site to give $Li_{6+x}P_{1-x}Ge_xS_5I$ is able to reach conduc-
2122 tivities of up to 5.4 mS cm^{-1} .^{482,495} The underlying reasons for increased ionic conductivity
2123 through cation/anion doping in lithium argyrodites are not clear, with two competing ex-
2124 planations proposed in the literature. 1) Doping increases anion disorder, resulting in perco-
2125 lating networks of lithium diffusion pathways.⁴⁹⁸ 2) Doping increases lithium stoichiometry.
2126 The additional lithium is accommodated as “interstitials” which switches on a low-energy
2127 concerted diffusion mechanism.

2128 The effects of interrelated factors on ionic conductivity is challenging to resolve purely
2129 from experiment. In doped Li-argyrodites there are always *both* changes to the host-framework
2130 (e.g. disorder on anion sites and/or substitution and disorder on the P sites) and a change
2131 in lithium stoichiometry. This is where computational analysis can provide vital insight,
2132 allowing deconvolution of coupled properties by modelling non-charge-balanced hypothetical
2133 systems to better understand how each of these factors affect ionic conductivity, which is
2134 not feasible in experimental systems.

2135 A particularly interesting aspect of the Li-argyrodites is the diffusion topology, comprising
2136 of interconnected Li_6S cages, with anions arranged at $4a$, $4c$, and $16e$ Wyckoff positions and Li
2137 arranged over a tetrahedra, with sites labelled as types 1-5.⁴⁹⁹ Lithium mainly occupies type
2138 5 tetrahedral sites in $x(Li)=6$ argyrodites, with occupation of non-type 5 sites only recently

2139 observed experimentally.^{493,500} Computational studies, however, have previously predicted
 2140 occupation of non-type 5 sites, showing lithium distributed over tetrahedral types 5, 2, and
 2141 4.^{483,498,501}

2142 Li hopping within these cages, while effectively barrierless, does not contribute to long-
 2143 range diffusion. In fact, a combination of inter-cage and intra-cage hopping is needed, with
 2144 occupation of non-type 5 sites and transitions between all adjacent site types, to achieve
 2145 long-range diffusion. This is shown schematically in Figure 28, showing the connectivity
 2146 between the Li tetrahedral sites. AIMD simulations have shown that cation and anion
 2147 substitution,^{442,493} anion site disorder,^{498,500} and lithium concentration^{502–504} all influence
 2148 the ionic conductivity.

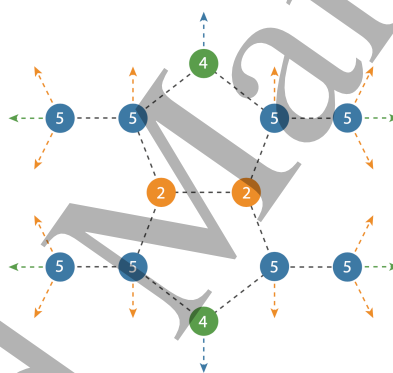


Figure 28: (a) Possible Li diffusion pathways in Li-argyrodites, involving type 2, 4, and 5 tetrahedra for long-range diffusion. Reprinted with permission from Ref. 498. Copyright 2020 American Chemical Society.

2149 The influence of anion substituent concentration on conductivity is currently uncertain,
 2150 with research by De Klerk et al. determining excess Cl in $\text{Li}_5\text{PS}_4\text{Cl}_2$, resulting in similar con-
 2151 ductivities to $\text{Li}_6\text{PS}_5\text{Cl}$,⁴⁴² in contrast to research by Yu et al. and Feng et al., who concluded
 2152 that excess Cl improved Li conductivity.^{504,505} Yu et al. determined the highest conductivity
 2153 was produced by $\text{Li}_{5.7}\text{PS}_{4.7}\text{Cl}_{1.3}$ (6.4 mS cm^{-1}),^{503,505} while Feng et al. determined this to
 2154 be $\text{Li}_{5.3}\text{PS}_{4.3}\text{Cl}_{1.7}$ (17 mS cm^{-1}).⁵⁰⁴ Feng et al., however, presented alternative, or coupled,
 2155 reasoning for this increased conductivity. Drawing from previous studies,^{486,496} they pro-
 2156 posed that the increased Cl content amplified the anion disorder in the system, which is the

2157 underpinning cause of the higher conductivities.

2158 4.3.3 Oxides

2159 **LLZO** Cubic $\text{Li}_7\text{La}_3\text{Zr}_2\text{O}_{12}$ (c-LLZO) has a high Li-ion conductivity of $10^{-4} \text{ S cm}^{-1}$,⁵⁰⁶ a
2160 high shear modulus of 59 GPa,⁵⁰⁷ and the largest thermodynamic stability window with
2161 reference to lithium metal^{24,508,509} of current solid electrolyte materials (c.f. section 4.3.4).
2162 However, at low temperatures ($< 150^\circ\text{C}$), c-LLZO is not stable and transitions to the less
2163 conductive tetragonal LLZO (t-LLZO) phase.⁵¹⁰ Attempts have been made to retain the
2164 more desirable c-LLZO by Al doping on lithium sites, with some success.^{510,511}

2165 Lithium dendrite growth has been shown to be a challenge in solid-electrolytes. For
2166 LLZO, dendrite growth has caused short circuits in the cells after relatively short peri-
2167 ods.^{512,513} Cheng et al. observed this growth directly and found that the process occurs
2168 mostly through grain boundaries.⁵¹⁴ Recently, Kim et al. confirmed these observations and
2169 investigated the use of an interlayer buffer, to restrict Li propagation through grain bound-
2170 aries.⁵¹⁵

2171 There has been a wide effort to understand dendrite formation through modelling.^{516–518}
2172 For example, Tian et al. used DFT to investigate dendrite growth through analysis of c-LLZO
2173 and t-LLZO bulk and slab surface energies, via the total density of states (TDOS).⁵¹⁷ The
2174 authors found that t-LLZO forms at the surface of bulk c-LLZO, even with Al-doping,^{519,520}
2175 and that extra states appear in the band gap for the slab structures, which do not appear
2176 in the bulk, potentially allowing electrons to be trapped on the surface of LLZO. Electrons
2177 localised primarily around Li^+ and La^{3+} ions on the surface lead to the nucleation of lithium
2178 metal, which can result in lithium growth through grain boundaries and pores in the LLZO,
2179 eventually forming dendrites,⁵¹² as shown in Figure 29. This analysis was also conducted on
2180 LiPON, where no electron trapping was found to occur, indicating that LiPON could be a
2181 suitable coating to prevent dendrite and t-LLZO formation (c.f. section 4.3.4).

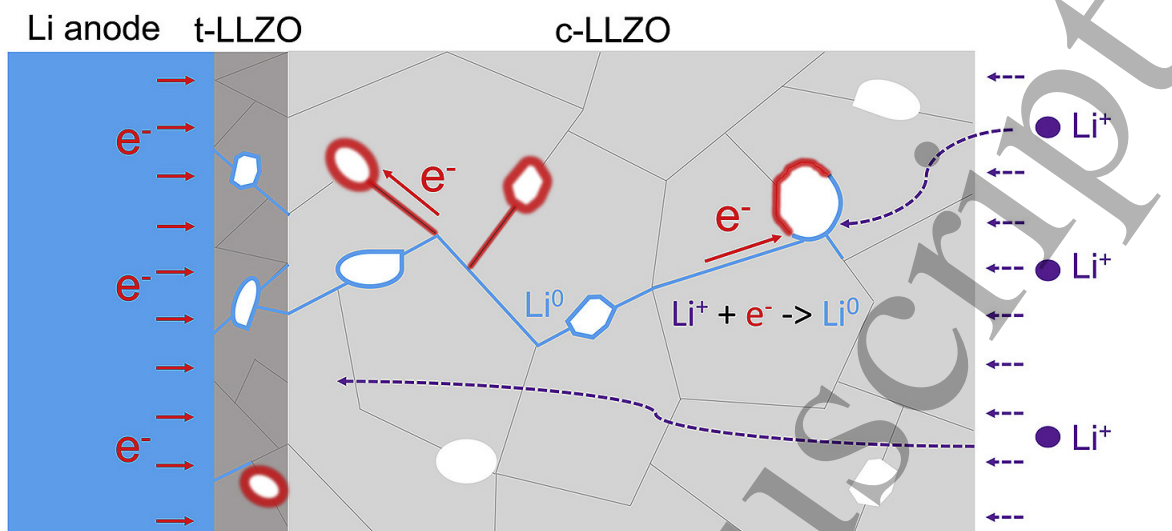


Figure 29: Schematic showing Li metal formation (blue) along grain boundaries and pores, due to electron accumulation (red) combining with Li^+ as they move through the electrolyte. Reprinted from Ref. 517, Copyright 2018, with permission from Elsevier.

2182 Gao et al. attributed the dendrite growth mechanism to the under-coordination of Zr
 2183 present on some of the stable interfaces of LLZO with Li,⁵¹⁸ leading to inhomogenous Li
 2184 depletion, which has been linked to Li metal deposition and dendrite formation.^{521–525} It
 2185 is unclear whether the suggested cause by Gao et al. is complementary evidence of Tian
 2186 et al.'s electron trapping theory or a separate cause of interface dendrite growth. However,
 2187 the papers do differ on their choice of surface. Tian et al. used Li and La rich surfaces,
 2188 which were determined to be more stable by Thompson et al., who used DFT to investigate
 2189 6 different LLZO slabs for the (100) and (110) planes.⁵²⁶ By contrast, Gao et al. drew upon
 2190 results presented in several methods^{516,526,527} and performed DFT calculations on a wider
 2191 range of surfaces, finding (100) and (001) surfaces to be the most stable. The findings of these
 2192 studies agree that Li and La rich surfaces are the most stable. However, Gao et al. calculated
 2193 the interface formation energies of the Li-LLZO interfaces using the CALYPSO interface
 2194 structure prediction method⁵²⁸ and determined the Zr-rich surfaces to be the most stable
 2195 at this interface.⁵²⁹ Experimental observations corroborate these findings, also determining
 2196 that the formation of Zr-rich surfaces to be a cause of interfacial degradation.⁵²⁴

2197 Experimental measurements have suggested a non-uniform distribution of current on the

1
2
3
4 2198 surfaces as a possible cause of dendrite growth.^{522,530} Non-uniform current distribution pro-
5
6 2199 duces random, local spikes in current density for short periods of time, leading to a reduction
7
8 2200 of Li at these sites. Squires et al. used DFT to model the electronic conductivity in LLZO to
9
10 2201 probe the importance of the surface current to dendrite formation.⁵³¹ The authors determined
11
12 2202 that at room temperature, bulk c-LLZO was found to have negligible electron/electron-hole
13
14 2203 concentrations, indicating that bulk defects are not a significant factor in dendrite growth.
15
16 2204 However, these models did not account for other forms of defects, such as grain boundary
17
18 2205 and surface effects.

19
20 2206 Understanding Li-ion migration is key to improving battery conductivity. Xu et al.
21
22 2207 analysed the Li-ion migration path through LLZO using DFT with the NEB method (c.f.
23
24 2208 section 2.1.3).⁵³² Two migration paths were observed, depending on Li concentration. Low
25
26 2209 Li_x ($\text{Li}_5\text{La}_3\text{Zr}_2\text{O}_{12}$) led to a higher energy, single hop migration path, whereas higher Li_x
27
28 2210 ($\text{Li}_7\text{La}_3\text{Zr}_2\text{O}_{12}$) led to a lower energy, two hop migration path. Using potentials-based MD
29
30 2211 (c.f. section 2.1.6), Burbano et al. further investigated the Li-ion transport mechanisms by
31
32 2212 comparing ionic conductivity in t-LLZO and c-LLZO.⁵³³ The authors found that the longer
33
34 2213 time scale of potentials-based MD allowed the observation of a large sample of diffusion
35
36 2214 events in both LLZO structural forms. Diffusion events in t-LLZO were less common and
37
38 2215 involved exactly 8 Li ions, which corresponds to the cyclic movement of Li ions around the
39
40 2216 12 octahedral and tetrahedral ring sites in t-LLZO. This cyclic mechanism results in no
41
42 2217 net long-range diffusion of Li and hampers the ability of t-LLZO to conduct ions. AIMD
43
44 2218 (c.f. section 2.1.6) investigations of the transport mechanism in LLZO have also been con-
45
46 2219 ducted. However, the shorter time scale led to some key disagreements about the transport
47
48 2220 mechanism in c-LLZO.⁵³³⁻⁵³⁵

49
50 2221 DFT calculations have determined that Al doping reduces the energy barrier for Li-ions to
51
52 2222 move between octahedral and tetrahedral sites, increasing the ionic conductivity.^{536,537} More
53
54 2223 recent work by Bonilla et al., using potentials-based MD, supports this conclusion, finding
55
56 2224 increased conductivity in t-LLZO, due to the Al forcing Li ions into previously inaccessible

1
2
3 2225 tetrahedral sites.⁵³⁸ The authors also found that Al doping in c-LLZO led to a slight decrease
4
5 2226 in conductivity. They attributed this to the tendency for Al to “trap” Li ions close to the
6
7 2227 dopant. Resolving Li-ion migration through LLZO experimental measurement is challenging
8
9 2228 due to the complexity of the system coupled with the need to observe the processes dur-
10
11 2229 ing active (dis)charge. While high-level experimental measurements regarding conductivity
12
13 2230 can be made, which provide spatially-averaged information,⁵³⁹ techniques such as X-ray and
14
15 2231 neutron diffraction struggle to probe at the atomistic level required for investigating Li-ion
16
17 2232 migration pathways, due to low ⁷Li scattering intensities.⁵³⁴ Other experimental techniques,
18
19 2233 such as pulsed-gradient NMR, require high-temperature measurements⁵⁴⁰ and electrochem-
20
21 2234 ical impedance spectroscopy (EIS) often includes non-Li charge carriers such as protons or
22
23 2235 electrons.⁵⁴¹ Brugge et al. used an ion exchange method with focused ion beam secondary ion
24
25 2236 mass spectrometry (FIB-SIMS) to directly observe ion transport occurring through LLZO.⁵⁴¹
26
27 2237 The authors noted that the sensitivity of LLZO surfaces to carbon contaminants from the
28
29 2238 air is problematic and leads to large interfacial resistances.^{541,542} Atomistic modelling does
30
31 2239 not have the same hindrances stated above and was able to provide a mechanistic pathway
32
33 2240 to explain the reduced ionic-conductivity of t-LLZO and a thermodynamic description of the
34
35 2241 effect of Al-doping on ionic conductivity.

36
37 2242 **Oxide Nanocomposites** Due to attractive mechanical, electrical, optical, and mag-
38
39 2243 netic properties, nanocomposite oxide materials represent a new generation of advanced
40
41 2244 materials.^{458,460} They often show enhanced conductivity, compared to single-phase ceramic
42
43 2245 oxides, making them suitable candidates as electrolytes for future ASSBs. For example,
44
45 2246 $\text{Li}_2\text{O}:\text{B}_2\text{O}_3$ ^{460–462} and $\text{Li}_2\text{O}:\text{Al}_2\text{O}_3$ nanocomposites⁴⁵⁹ have higher ionic conductivities than
46
47 2247 nanocrystalline Li_2O , although B_2O_3 and Al_2O_3 are insulators. The ionic conductivity shows
48
49 2248 a maximum at about 50 % of $\text{B}_2\text{O}_3/\text{Al}_2\text{O}_3$ content. This surprising behaviour was attributed
50
51 2249 to the increased fraction of structurally disordered interfacial regions and the enhanced sur-
52
53 2250 face area of the nanosized particles.⁴⁶⁰ The oxide nanocomposites contain three types of in-
54
55 2251 terfaces, as presented in Figure 30 (a): interfaces between the ionic conductor grains (green

lines), between the insulator grains (black lines), and between the ionic conductor and the insulator grains (red lines). The latter can lead to surprising effects in the conductivity of composite materials. In this case, the highly conducting interface region can act as a bridge between two Li_2O grains not in direct contact with each other, opening up additional paths for Li ions. The conductivity enhancement in the interfacial regions may have different origins, e.g. the formation of space charge layers, an enhanced concentration of dislocations, or defects, or the formation of new phases.

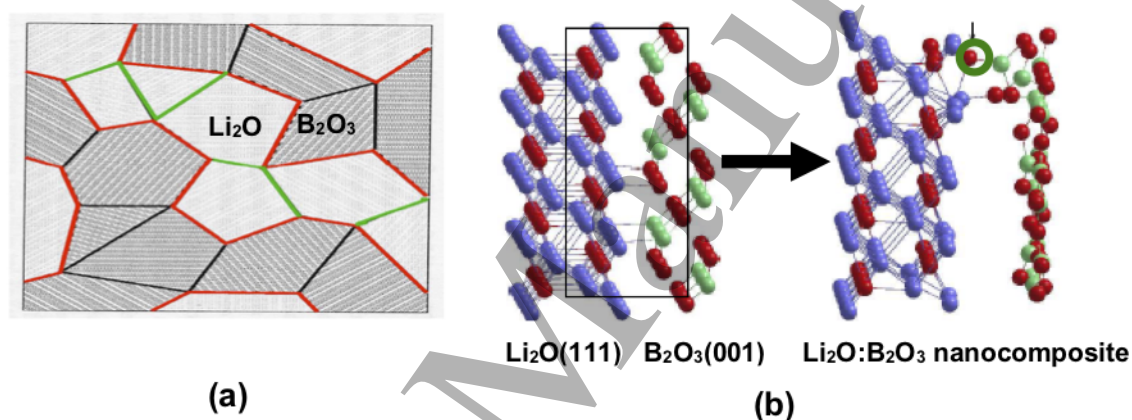


Figure 30: (a) Schematic diagram of Li_2O and B_2O_3 interface (b) Atomistic model of $\text{Li}_2\text{O}:\text{B}_2\text{O}_3$ nanocomposite. Reproduced with permission from Ref. 543 Copyright IOP Publishing. All rights reserved.

Islam et al. studied the interface of $\text{Li}_2\text{O}:\text{B}_2\text{O}_3$ nanocomposite, by modelling a combination of two favorable surfaces of Li_2O and B_2O_3 using HF/DFT Hybrid approach.^{543,544} After full structural optimisation, it was observed that Li–O bonds are weakened, while B–O bonds are formed simultaneously at the boundary between the two surfaces, Figure 30 (b). An oxygen atom from the Li_2O surface (marked by a green circle) is pulled from the surface layer towards a neighbouring boron atom of the B_2O_3 surface. This preference of oxygen bonding with B (or Al in $\text{Li}_2\text{O}:\text{Al}_2\text{O}_3$) plays a key role in generating low-coordinated Li. As a consequence of this dislocation, the coordination of a Li atom in the second layer is reduced from four to three.

1
2
3
4 2268 The defect properties were investigated in the interface region. It was observed that the
5
6 2269 removal of surface oxygen from Li_2O is responsible for the increased vacancy defect concentra-
7
8 2270 tion in $\text{Li}_2\text{O}:\text{B}_2\text{O}_3$ (or $\text{Li}_2\text{O}:\text{Al}_2\text{O}_3$) nanocomposite materials. Therefore, the nanocomposites
9
10 2271 of ionic compounds (containing weakly bound and therefore mobile cations) with highly co-
11
12 2272 valent compounds (with strong metal- or nonmetal-oxygen bonds) are promising candidates
13
14 2273 for high ionic conductivity. The model calculations showed that the most likely mechanism
15
16 2274 for Li^+ migration was in a zigzag pathway, rather than in a straight line along a direction
17
18 2275 parallel to the interface plane.

19
20 2276 The average calculated activation energy for Li^+ migration in the $\text{Li}_2\text{O}:\text{B}_2\text{O}_3$ interface
21
22 2277 (0.28 eV)^{543,544} is similar to the experimental values of bulk Li_2O (0.31 eV),⁴⁶⁰ $\text{Li}_2\text{O}:\text{B}_2\text{O}_3$
23
24 2278 ($0.34 \pm 0.04 \text{ eV}$),⁴⁶² and $\text{Li}_2\text{O}:\text{Al}_2\text{O}_3$ ($0.30 \pm 0.02 \text{ eV}$)⁴⁵⁹ nanocomposites. According to
25
26 2279 the defect formation energies, the interface region of $\text{Li}_2\text{O}:\text{B}_2\text{O}_3$ nanocomposites contains
27
28 2280 higher concentrations of both Li vacancies and Frenkel defects than bulk Li_2O and Li_2O sur-
29
30 2281 faces.^{543,544} Therefore, the experimentally observed enhanced Li mobility in the $\text{Li}_2\text{O}:\text{B}_2\text{O}_3$
31
32 2282 interface region is thermodynamically and not kinetically controlled. The models proposed in
33
34 2283 this study allowed a direct simulation of the defect formation and ion mobility at the atomic
35
36 2284 scale, without any experimental input. They provide a deep insight into the local bonding
37
38 2285 situation at the interface of oxide nanocomposites, which is difficult to obtain from experi-
39
40 2286 ments. State-of-the-art synchrotron techniques, like hard x-ray photoelectron spectroscopy
41
42 2287 (HAXPES), could possibly shed light on this challenge.^{545,546}

44 2288 **4.3.4 Interface stability**

45
46
47 2289 Experimental investigations of solid electrolyte interfaces are often challenging, making atom-
48
49 2290 istic modelling a vital tool.²⁹ The interfacial stability properties of solid electrolyte materials
50
51 2291 in contact with an electrode are best described by the electrochemical stability window, de-
52
53 2292 fined by Zhu et al. as the range of voltages under which the interface configuration, a mixture
54
55 2293 of electrode (Li) and the solid electrolyte, does not undergo a decomposition reaction.⁵⁰⁸

Atomistic simulation was able to resolve the characterisation of the electrochemical stability window for a number of SSEs. Cyclic voltammetry experiments had reported no significant SSE degradation in contact with a Li anode for a large (>5 V) voltage range.^{288,547,548} For example, Kamaya et al. used cyclic voltammetry to probe the stability of the LGPS/Li interface for a voltage range of -0.5 to 5 V.²⁸⁸ The authors found no evidence of electrolyte decomposition using this technique, and thus concluded that LGPS has a high electrochemical stability. However, a DFT based investigation by Mo et al. predicted an electrochemical stability window of 3.6 V for LGPS by simply calculating the band gap of the SSE, rendering an electrochemical stability window > 5 V, as indicated by the cyclic voltammetry results, to be unlikely.⁴⁸¹ A more recent DFT study by Zhu et al., posits the formation of an interphase layer, and determining the electrochemical stability window for LGPS to be 0.43 V (Figure 31).²⁴ The authors attribute the apparent contradictory interpretation of the cyclic voltammetry results to the slow kinetics of degradation that occur at SSE/Li interfaces, forming the interphase layer, i.e. there is a large kinetic overpotential for the oxidation and reduction reactions calculated by Zhu et al..²⁴ Cyclic voltammetry is also only able to detect electrochemical degradation processes, in which electrons are transferred. These experiments are unable to detect purely chemical processes (i.e. no electron transfer), which may also occur in parallel with electrochemical processes and lead to erroneous conclusions of “stability” of solid electrolytes through cyclic voltammetry.⁵⁰⁸

A smaller thermodynamic window increases the importance of the interphase layer formation. Zhu et al. determined that a range of solid electrolytes are unstable with respect to Li metal at low and high voltages, with the exception of LLZO, which appears to be kinetically stabilised at low voltages, due to an unfavourable reduction energy of -0.02 eV per atom. Any potential outside of the thermodynamic stability window results in decomposition into lithium binary compounds, unless otherwise kinetically stabilised. This is problematic for germanium- and titanium-containing compounds, as they form electronically conductive alloys upon decomposition.²⁴ This renders the passivation process, proposed by Mo et al.,^{481,549}

2321 as the cause of cyclic voltammetry overestimates, unlikely as this degradation process would
 2322 be sustained throughout the bulk cycling, severely limiting the efficacy of these materials
 2323 as electrolytes.²⁴ Such degradation can also increase interfacial resistance.^{550,551} Other solid
 2324 electrolytes face different problems. As explained in section 4.3.3, LLZO forms the far less
 2325 ionically conductive tetragonal LLZO at the surface. The Li-LiPON and Li-argyrodite inter-
 2326 faces were reported to degrade favourably, forming an ionically conductive and electronically
 2327 insulating interphase consisting of Li_2O , Li_2S , Li_3P , Li_3N , and LiI .²⁴

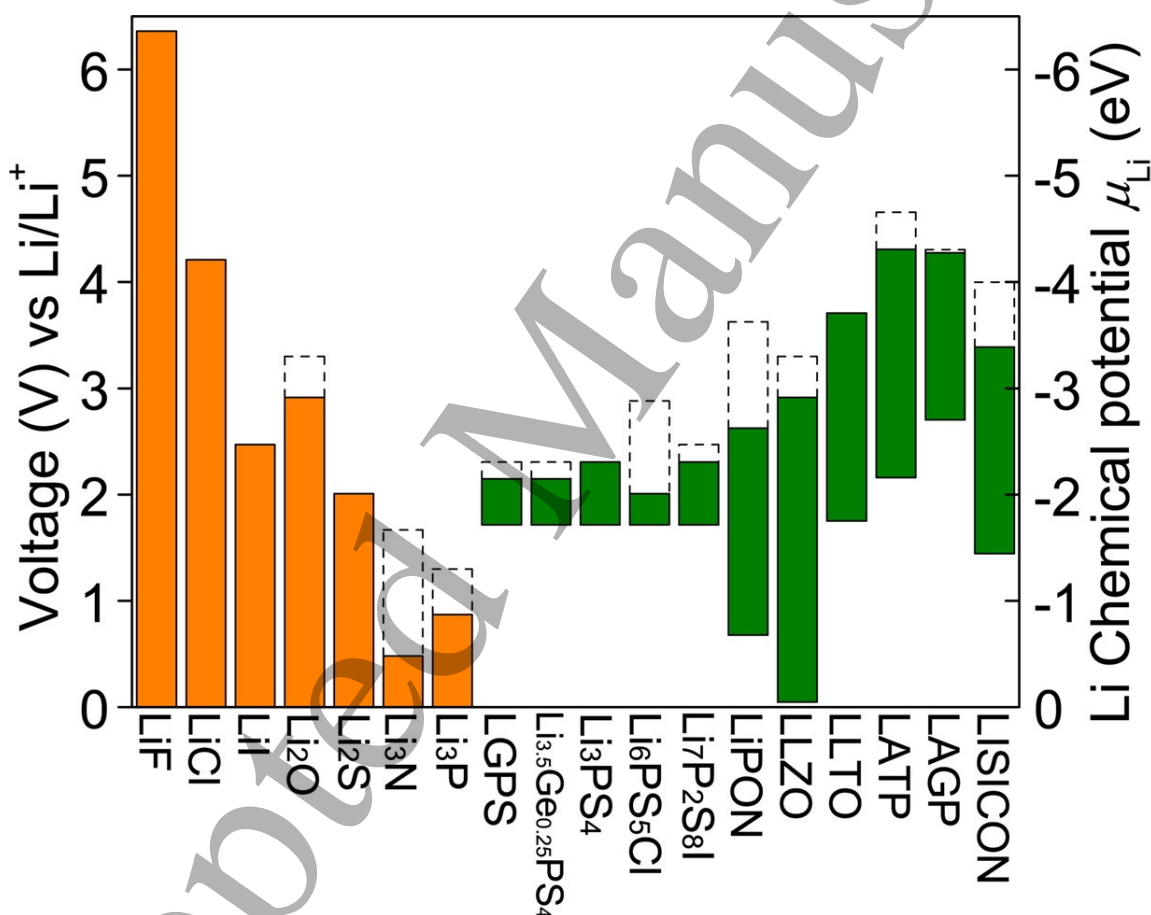


Figure 31: A comparison of the voltage stability windows for a selection of solid electrolytes (green) and the binary compounds that often form upon decomposition of the solid electrolyte (orange). The dashed line represents the oxidation potential to fully delithiate the material. Reprinted with permission from Ref. 24. Copyright 2015 American Chemical Society.

2328 Further study by Zhu et al. sought to investigate the mechanism behind the degrada-
 2329 tion/instability at the surface.⁵⁰⁸ In order to probe these mechanisms, the authors calculated

1
2
3 2330 the chemical and electrochemical stability of several solid electrolytes (LGPS, LLZO, LiPON,
4 2331 NASICON-type, lithium lanthanum titanate oxide (LLTO)) as well as the equilibrium con-
5
6 2332 ditions at the interfaces. Examining the cathode-electrolyte interface, using lithium cobalt
7
8 2333 oxide (LCO) as the cathode, a similar pattern emerged: oxides were found to be far more
9
10 2334 stable than their sulfide counterparts. However, LLTO and lithium aluminum titanium
11
12 2335 phosphate (LATP) had the best electrochemical stability against LCO.

13
14
15 2336 Studies looking into the interfacial resistance have been conducted,^{30,552-554} with the
16
17 2337 main source of resistance attributed to the electric double layer, which, in liquid electrolytes,
18
19 2338 consists of a capacitance and diffusion layer (c.f. section 4.1).³⁰ Tateyama et al. used the
20
21 2339 CALYPSO method^{528,529} to find low-energy surfaces to probe the interface. The lithium
22
23 2340 chemical potential of these stable interfaces in the Helmholtz layer, corresponding to the
24
25 2341 negative of the Li ion vacancy formation energy, was determined. These energies correspond
26
27 2342 to lithium moving from the electrode to the electrolyte, with the vacant lithium sites becom-
28
29 2343 ing a potential source of interfacial resistance. Okuno et al. use DFT calculations to compare
30
31 2344 the interfacial resistances of sulfide and oxide based solid electrolytes with LCO cathodes.⁵⁵²
32
33 2345 The Li vacancy formation energy and ion exchange across various interfaces were calculated.
34
35 2346 It was found that sulfide-based electrolytes had a higher interfacial resistance, due to the
36
37 2347 presence of more sites with a low vacancy formation energy on the surface. The authors also
38
39 2348 found the interfacial resistance to be dependent on the orientation of the crystals at the inter-
40
41 2349 face. Interfacial resistance is a major impediment to the commercialisation of ASSBs. The
42
43 2350 cause of this phenomenon has been elucidated through atomistic simulation of the interface
44
45 2351 and has provided direction to future SSE development.

46
47 2352 A study by Lepley and Holzwarth used DFT to investigate the interface energies between
48
49 2353 the Li electrode and the compounds that make up the interphase layer of the electrolyte.⁵⁵⁵
50
51 2354 They defined the interface energy as:

$$\gamma_{ab}(\Omega) = \frac{E_{ab}(\Omega, A, n_a, n_b) - n_a E_a - n_b E_b}{A}, \quad (45)$$

1
2
3
4 2355 where Ω is the interface configuration of atoms, E_{ab} is the energy of the complete system,
5
6 2356 E_x is the bulk energy per formula unit and A is the surface energy. Because the interface
7
8 2357 energy is intensive, calculating larger systems will give a converging value for γ_{ab} ,
9

$$\lim_{\Omega_s \rightarrow \Omega} [\gamma_{ab}(\Omega_s)] = \gamma_{ab}(\Omega), \quad (46)$$

10
11
12
13
14 2358 where Ω_s is the atomic configuration in a sample of the interface volume. Because the
15
16 2359 exact matching of lattice constants between interfaces is unlikely, a semi-coherent interface is
17
18 2360 considered, meaning lattice strain needed to be taken into account. Using the lowest overall
19
20 2361 lattice energy structure and explicitly accounting for the lattice strain, the most probable
21
22 2362 interfaces could be found. The Li/Li₃PO₄, Li/Li₂O and Li/Li₂S interfaces were found to be
23
24 2363 stable and the Li/Li₃PS₄ interface was found to be unstable.⁵⁵⁵

25
26 2364 In response to the apparent poor stability of most solid electrolytes, many studies have
27
28 2365 attempted to simulate the effect of coating the electrolyte with an oxide layer.^{517,556,557} As
29
30 2366 discussed in section 4.3.3, Tian et al. identified LiPON as a suitable coating material for
31
32 2367 LLZO, by comparing the bulk and surface density of states.⁵¹⁷ The authors found no extra
33
34 2368 states on the surface structure, so concluded that no electron trapping would occur (the pri-
35
36 2369 mary mechanism that they attributed to dendrite formation). Recently, Sang et al. proposed
37
38 2370 an artificial interphase layer between the Li anode and the solid electrolyte, composed of a
39
40 2371 Li_{3a_b}N_aX_b compound, where X is a halide.⁵⁵⁸ This material was investigated computation-
41
42 2372 ally by screening stable and metastable structures using the USPEX structure prediction
43
44 2373 software.^{559,560} The dynamic stability of the stable structures was found by analysing the
45
46 2374 phonon frequency spectrum by using PHONO3PY.^{180,561,562} The temperature-dependant ionic
47
48 2375 transport properties were found using AIMD (c.f. section 2.1.6).
49

50 2376 Phase diagrams for various atomic configurations were then constructed using cluster
51
52 2377 expansion, implemented through the Alloy Theoretic Automated Toolkit (AT-AT) (c.f. sec-
53
54 2378 tion 2.1.4).^{80,563} Through these various computational techniques, Sang et al. found that
55
56 2379 Li₆NCl₃ has the most favourable properties for use with sulfide-based solid electrolytes, such

1
2
3 2380 as LGPS.⁵⁵⁸ Authors such as Tian et al. and Sang et al. have leveraged the knowledge of
4
5 2381 the electronic structure and thermodynamic stability gained through atomistic simulation
6
7 2382 to predict viable coatings for the SSE. The versatility of computational methods allows for
8
9 2383 a greater variety of these materials to be analysed and could provide a means to screen
10
11 2384 potential SSE coating materials before performing costly and time-consuming experimental
12
13 2385 investigations.⁵⁶⁴
14
15

16 2386 **4.3.5 Outlook and challenges**

17
18
19 2387 The drive for the development of commercialised ASSBs has been intense, with the EV indus-
20
21 2388 try at the forefront of promoting this.²³ Although ASSBs can offer high gravimetric energy
22
23 2389 density (250 Wh kg⁻¹) and volumetric energy density (700 Wh L⁻¹), along with improved
24
25 2390 safety over conventional liquid electrolytes, the slow ionic diffusion can impair fast discharge
26
27 2391 and charge performance. With solid electrolytes intended to replace both the separator and
28
29 2392 liquid electrolyte in conventional LiBs,⁵⁶⁵ there are still multiple challenges which need to
30
31 2393 be overcome for this to be viable. In recent years, there have been breakthroughs in the
32
33 2394 discovery of new solid electrolytes, such as Li_{9.54}Si_{1.74}P_{1.44}S_{11.7}Cl_{0.3},⁵⁶⁶ which exhibit ionic
34
35 2395 conductivity competitive with that of organic liquid electrolytes. The improved performance
36
37 2396 of these materials is enabled by interfacial coatings or buffer layers and micro-structure
38
39 2397 engineering solutions at the electrode/electrolyte interfaces.⁵⁶⁷
40

41 2398 ASSBs are currently not capable of reliable cycling at current densities > 0.6 mA cm⁻².^{424,568}

42
43 2399 The current density and stability is limited by: poor electrode/electrolyte physical contact,
44
45 2400 leading to particle cracking and interface delamination, formation and propagation of Li
46
47 2401 dendrites, chemical and electrochemical stability, and high interfacial resistance.⁴²⁴ There
48
49 2402 are several critical issues related to the pairing of solid electrolytes with cathode and anode
50
51 2403 materials, which need to be addressed for long-term battery operation:

- 52
53
54 2404 • The limited system sizes of atomistic modelling are not sufficient to capture lattice
55
56 2405 relaxation, which would allow a coherent (completely matched) interface to form. This

1
2
3
4 2406 amplifies the effects of lattice strain in the model, particularly in cases where periodic
5
6 2407 boundary conditions are used.⁵⁵⁵ The lattice strain energy can be calculated and fac-
7
8 2408 tored into bulk scale calculations, but it is not as accurate as explicitly calculating
9
10 2409 dislocation defects that naturally relieve lattice strain.^{569,570}

- 11
12 2410 • Dendrite formation has been a notable problem for even the most physically robust elec-
13
14 2411 trolytes (c.f. section 4.3.3). Modelling of dendrite formation mechanisms has yielded
15
16 2412 some contradictory results, due to incomplete models of the interface.^{516–518} However,
17
18 2413 a more detailed understanding requires modelling of larger systems, encompassing the
19
20 2414 interface and bulk regions of both materials. This incurs a high computational cost
21
22 2415 not currently reachable through electronic structure methods methods. Further de-
23
24 2416 velopment of the linear-scaling DFT approach (c.f. section 2.1.2) may allow a more
25
26 2417 complete, multiscale approach.
- 27
28
29 2418 • The system size limitations in DFT modelling also hinder the modelling of the full
30
31 2419 electric double layer, which is also applicable to liquid electrolytes. Comparatively, in
32
33 2420 solid electrolytes the double layer is less understood. For example, Tateyama et al. were
34
35 2421 only able to successfully model the initial capacitance layer at the interface (Helmholtz
36
37 2422 layer).³⁰
- 38
39 2423 • Interfacial resistance presents an interesting challenge, as it can be introduced through
40
41 2424 multiple mechanisms:⁵⁵⁴ electric double layer,³⁰ surface crystal orientation,⁵⁵² and pro-
42
43 2425 duction issues, such as poor wettability.⁵⁵³ Strong collaboration between theorists and
44
45 2426 experimentalists will be needed, in order to make informed improvements to current
46
47 2427 interfacial structures.

48
49
50 2428 The interface is the primary source of dendrite formation, lattice mismatch, and inter-
51
52 2429 facial resistance in solid electrolytes. The interface also presents opportunities for atomistic
53
54 2430 modelling, with the growing popularity of coatings that try to address the shortcomings of
55
56 2431 popular solid electrolytes.^{29,515,571–584} For example, Tian et al.'s solution to dendrite growth

1
2
3 2432 in LLZO by utilising a LiPON coating⁵¹⁷ (c.f. section 4.3.3). Understanding how effective
4
5 2433 coatings are at addressing the aforementioned issues is essential.^{517,556,557} A very recent re-
6
7 2434 view by Kim et al. presents a detailed insight into the challenges and future prospects of
8
9 2435 solid-state Li-metal batteries, which we have touched upon here.⁵⁶⁷
10
11
12

13 2436 5 Cathodes

14 2437 5.1 Introduction

15
16
17 2438 As mentioned in our Introduction (section 1), lithium-ion batteries (LiBs) became promising
18
19 2439 applications in 1979 when Goodenough and Mizushima successfully demonstrated LiCoO_2
20
21 2440 as a cathode.⁵⁸⁵ Since then, LiBs have become instrumental in portable electronics, such
22
23 2441 as mobile phones, and electric vehicles,^{586–590} largely attributed to their high energy den-
24
25 2442 sity.^{287,425,430,591–599} Due to the high abundance and low material cost, sodium-ion batteries
26
27 2443 have also received increased attention, especially for grid storage applications.^{600–604} Re-
28
29 2444 gardless of the application, the discovery of new materials and the optimisation of current
30
31 2445 chemistries for improved performance is crucial for the next generation of rechargeable bat-
32
33 2446 teries. With that in mind, it is known that the energy density of the cathode material is the
34
35 2447 limiting factor in improving battery performance, thus current research is largely focused
36
37 2448 on exploring cathode chemistries. These include layered oxides (LiMO_2 , $M=\text{Co,Mn,Ni}$),
38
39 2449 spinel oxides (LiM_2O_4), olivine phosphates (LiFePO_4), disordered rock-salts, ($\text{Li}_2\text{MnO}_2\text{F}$),
40
41 2450 and other compounds, such as silicates.^{605,606}
42
43
44

45
46 2451 Layered transition metal (TM) oxides (LiMO_2 , $M=\text{Co,Mn,Ni,etc.}$) are commonly con-
47
48 2452 sidered to be the first generation of cathode materials in commercial LiBs. These materials
49
50 2453 possess a theoretical specific capacity of 270 mAh g^{-1} . However, their practical capacity is
51
52 2454 generally limited to below 200 mAh g^{-1} .⁶⁰⁷ LiCoO_2 held high capacities but the material was
53
54 2455 problematic due to capacity fading, low abundance, and the high cost of cobalt and geopolit-
55
56 2456 ical issues, including ethical concerns, making large scale applications impractical.⁶⁰⁸ There
57
58
59
60

1
2
3
2457 is also considerable instability in the LiCoO_2 structure, caused by the extraction of Li during
4
5
2458 cycling, which results in undesirable phase transitions from O3-type to O6-type Li_xCoO_2 and
6
7
2459 O1-type CoO_2 .^{609,610} Other layered oxides also pose their own challenges, such as Li_xNiO_2
8
9
2460 presenting capacity fade and poor safety,⁶¹¹ and $\text{Li}_x\text{Mn}_2\text{O}_4$ presenting low capacity.⁶¹² An
10
11
2461 emerging alternative to solve some of these challenges is using a combination of the TMs. In
12
13
2462 2000, Paulsen et al. presented $\text{Li}_{2/3}[\text{Ni}_{1/3}\text{Mn}_{2/3}]\text{O}_2$,^{613,614} with $\text{Li}[\text{Ni}_x\text{Mn}_{1-2x}\text{Co}_z]\text{O}_2$ (NMC)
14
15
2463 presented by the authors in 2001.⁶¹⁵ Partially replacing Co in LiCoO_2 with Ni and Mn to
16
17
2464 obtain layered $\text{Li}[\text{Ni}_x\text{Mn}_y\text{Co}_z]\text{O}_2$,⁵⁸⁶ where $x + y + z = 1$, shows improved electrochemical
18
19
2465 performance, while also reducing material cost and improving stability.⁶¹⁶ These layered ox-
20
21
2466 ides are commonly termed as NMC, with the subsequent numbering relating to the ratio
22
23
2467 between the cations.

24
25
2468 A huge benefit of combining these TMs is the ability to tune the TM composition to
26
27
2469 optimise aspects including capacity, (dis)charging rate, electrochemical stability, and lifetime,
28
29
2470 with the potential of reaching capacities $> 220 \text{ mAh g}^{-1}$.⁶¹⁷ Some NMC compositions are
30
31
2471 already used commercially, with industry focus shifting from NMC111 to higher Ni containing
32
33
2472 compositions including NMC442, NMC532, and NMC622.⁶¹⁸ These compositions, however,
34
35
2473 still contain 20 % or more Co. A great deal of research is working towards reducing the Co
36
37
2474 content even further, with compositions such as NMC811 ($\text{Li}[\text{Ni}_{0.8}\text{Mn}_{0.1}\text{Co}_{0.1}]\text{O}_2$) showing
38
39
2475 promise as future commercial materials for applications, such as in long-range electric vehicles
40
41
2476 (EVs).⁶¹⁹ These Ni-rich NMC compositions are also considered to be the cathode of choice
42
43
2477 for future all-solid-state LiBs.⁶⁰⁷

44
45
2478 Recently, research into further improving the capacity of these materials by inserting
46
47
2479 lithium into the TM cation sites has attracted considerable attention. This has lead to
48
49
2480 a new generation of cathode materials termed “Li-rich” or lithium excess. The increased
50
51
2481 capacities of these materials arises from invoking redox chemistry on both the TM and oxide
52
53
2482 ions, as opposed to just TM ions in traditional oxide-based intercalation compounds.^{620–628}

54
55
2483 These Li-rich cathodes, including $\text{Li}_{1+x}\text{Ni}_y\text{Co}_z\text{Mn}_{(1-x-y-z)}\text{O}_2$ layered oxide, can reach high

2484 capacities of $> 300 \text{ mAh g}^{-1}$. However, synthesis of these materials has proven to be difficult
2485 and work is ongoing to improve synthesis techniques.⁶²⁹

2486 There has also been growing interest in disordered intercalation structures, especially
2487 disordered rock-salt structures. They were initially disregarded as cathodes, as their struc-
2488 ture appeared to limit lithium diffusion. However, recent research has shown that lithium
2489 diffusion can be facile in some disordered materials, provided that there is enough of a
2490 lithium excess to allow the formation of an uninterrupted percolating network of channels
2491 involving no face-sharing TM ions.^{621,630,631} There have been several examples reported,
2492 including $\text{Li}_{1.2}\text{Ni}_{0.33}\text{Ti}_{0.33}\text{Mo}_{0.13}\text{O}_2$,⁶³¹ $\text{Li}_{1.2}\text{Ti}_{0.4}\text{Mn}_{0.4}\text{O}_2$,⁶³² $\text{Li}_4\text{Mn}_2\text{O}_5$,⁶³³⁻⁶³⁵ Li_3NbO_4 -based
2493 systems,⁶³⁶⁻⁶³⁸ and oxyfluorides, where some of the anion sites are occupied by F^- rather than
2494 O^{2-} , such as $\text{Li}_2\text{MnO}_2\text{F}$,⁶³⁹⁻⁶⁴¹ $\text{Li}_2\text{VO}_2\text{F}$,⁶⁴²⁻⁶⁴⁸ and $\text{Li}_2\text{Mn}_{2/3}\text{Nb}_{1/3}\text{O}_2\text{F}$.⁶⁴⁹ These materials
2495 can be difficult to synthesise, however, as Mn-rich 3D TM compounds tend to form ordered
2496 phases, such as LiMnO_2 or Li_2MnO_3 , high energy mechano-chemical ball-milling methods
2497 have been utilised to counter this.^{633,640,650} These materials are able to reach very high en-
2498 ergy storage capacities of 300 mAh g^{-1} ,⁶⁵¹ which is attributed to the ability to perform both
2499 cationic and anionic redox.^{648,651,652} These materials typically show less first cycle hysteresis
2500 than other Li-rich compounds, thought to be because the structure already resembles that
2501 of the Li-rich materials after they undergo cation disorder on cycling.

2502 Knowledge of the broad structural and electrochemical properties of cathode materials
2503 can be obtained from various experimental methods. However, detailed insight into, for
2504 example, TM configurations, vibrational and thermal properties, and atomistic diffusion
2505 mechanisms, is challenging and, in some cases, not resolvable using experimental techniques.
2506 This is where atomistic modelling can provide greater insight. In this section, we explore
2507 a range of cathode material properties, using several Li-ion materials, to highlight different
2508 properties and the considerations needed to gain the most desirable electrochemical perfor-
2509 mance. We describe which atomistic modelling methods are used to investigate the discussed
2510 properties and the importance of modelling in this context. Using a range of promising cath-

ode materials (layered oxides, spinel oxides, polyanions, and disordered rock-salt oxides and oxyfluorides) to aid in the discussion, we first look at the different cathode crystal structures and the effects of micro-structuring. We then discuss some of the bulk material properties, including ion diffusion, redox and electronic properties, TM ordering, and vibration and thermal properties. Finally, we consider the surfaces and interfaces of these cathode materials, with an outlook to current and future challenges in the atomistic modelling of cathodes.

5.2 Bulk Properties

5.2.1 Crystal Structure and Micro-Structure

Crystal structure. Cathode materials consist of a range of different crystal structures, with some of the most promising LiCoO₂ based materials adopting the α -NaFeO₂ structure, with alternating layers of [CoO₂]⁻ and Li⁺. In LiBs, the cathode is a limiting factor, as the amount of lithium that can be reversibly extracted and re-inserted (cycled) directly influences the battery capacity, with the Fermi energy linked to the cell voltage.⁶⁰⁶ Thermo-chemical stability and high energy density are also important considerations, with several promising candidates for future battery materials. These include mixed-metal layered oxides (NMC), spinel oxides (LiMn₂O₄), polyanion materials (LiFePO₄,^{425,587,591,599} Li₂FeSiO₄,⁶⁵³⁻⁶⁵⁵ LiFeSO₄F⁶⁵⁶), and disordered rock-salt oxides and oxyfluorides (Li₂MnO₂F^{639,648,651,652,657}). The crystal structures of these cathode materials are presented in Figures 32 and 33, where these materials are described in more detail.

Some TM oxides are stable in various structural forms, such as lithium manganese oxide (LMO), which has been synthesised with layered,⁶⁵⁸ spinel,⁶⁵⁹ and rock-salt structures.⁶⁶⁰ For intercalation-type cathodes used in LiBs, the structural framework is expected to remain relatively unchanged, with only small changes from lattice expansion/contraction. However, phase transitions can occur during the cycling process. For example, during cycling, a phase transition can occur from the LiMn₂O₄ spinel structure to the LiMnO₂ rock-salt structure, partially due to oxygen evolution.⁶⁶¹ Phase transitions between layered and spinel struc-

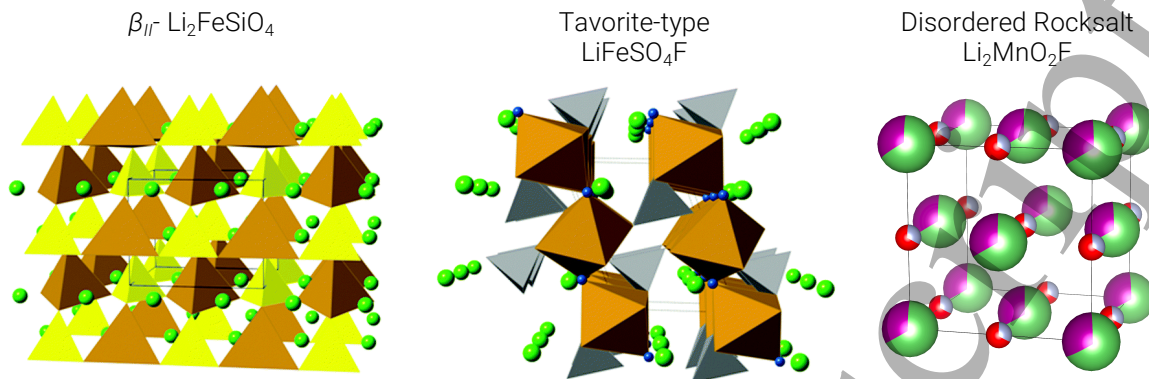


Figure 32: Representative crystal structures of β_{II} - $\text{Li}_2\text{FeSiO}_4$, tavorite-type LiFeSO_4F , and disordered rock-salt $\text{Li}_2\text{MnO}_2\text{F}$ cathode materials for lithium-ion batteries. Li^+ ions are shown in green spheres, O in red, Mn in mauve, and F in grey. Fe-O polyhedra are shown in brown, SiO_4 tetrahedra in yellow, and SO_4 tetrahedra in grey.

tures are also widely observed.⁶⁶² For example, Reed et al. investigated the layered to spinel phase transitions in Li_xMnO_2 using Density Functional Theory (DFT) modelling (c.f. section 2.1.1).⁶⁶³ Their investigation determined that partially lithiated layered Li_xMnO_2 transitions to spinel in a two-stage process. Firstly, a large percent of Mn and Li ions quickly occupy tetrahedral sites, to form a meta-stable intermediate. Then, a more complex, coordinated rearrangement of Mn and Li occurs to form spinel. Interestingly, this behaviour is in contrast to Li_xCoO_2 and understanding the reasons for this could prove useful for creating Mn-based cathode materials.

Micro-Structuring. It is clear that control over bulk structure has an impact on the material's performance, as many properties are dependent on shape and size.⁶⁶⁴ The structural and micro-structural properties of a material are also vital to the cycling stability of a cathode. For example, reducing the particle size of LiFePO_4 to the nanometre scale is shown to increase the electrochemical performance, compared to equivalent, but larger, particles, by reducing transport path lengths.⁶⁶⁵⁻⁶⁶⁷ Selective structuring can also provide mechanical benefits, for example, where forces acting on the functional cathode during cycling, as the lattice expands and contracts with lithium intercalation, can cause plastic deformation and extinguish desirable activities. Ledwaba et al. modelled diffusion-induced stress in layered-spinel

1
2
3 2554 LMO composites, revealing structural resilience, enabled by flexing of a porous structure.⁶⁶⁸
4
5 2555 In this study, Ledwaba et al. found the yield stress of the bulk material was 11.35 GPa,
6
7 2556 whilst the nanoporous material subjected to an equivalent strain experienced a stress of 4.32
8
9 2557 GPa. In fact, it has been proposed that a β -MnO₂ host should be symmetrically porous and
10
11 2558 heavily twinned to maximise the cathode's electrochemical properties.⁶⁶⁹ Further to this, in-
12
13 2559 tergrowing structures of two polymorphs of MnO₂, β -MnO₂ and Ramsdellite-MnO₂,⁶⁷⁰ has
14
15 2560 been shown to enhance cell performance,⁶⁷¹ due to reduction in stresses and facile diffusion
16
17 2561 in more open structure of Ramsdellite-MnO₂.

20 21 2562 **5.2.2 Lithium-ion Diffusion**

22
23 2563 As discussed in section 2.3.3, Li-ion diffusion coefficients can be calculated using multiple
24
25 2564 techniques, including *ab initio* Molecular Dynamics (MD), classical (potentials-based) MD,
26
27 2565 and Monte Carlo (MC). Diffusion coefficients, although important experimentally and for
28
29 2566 parameterising continuum models, are not the only ion transport property of interest on
30
31 2567 the atomistic scale. Properties such as atomistic diffusion mechanisms, hopping frequencies,
32
33 2568 and activation energy barriers are all vital to understanding Li-ion transport and (dis)charge
34
35 2569 rate behaviour. This is of particular interest for investigating the effects of grain-boundaries
36
37 2570 and interfaces on the migration routes and mechanisms. For example, in LiCoO₂, Moriwake
38
39 2571 et al. determined that the activation energy, E_a , for Li migration *along* a twin boundary is
40
41 2572 0.20 eV, smaller than that in the bulk, while the E_a *across* a twin boundary is 0.4 eV.⁶⁷²
42
43 2573 This demonstrates the influence of grain-boundaries on the kinetic properties.

44
45 2574 Computational techniques can provide information regarding a material's diffusion be-
46
47 2575 haviour, which cannot be fully understood through experiments alone. For example, Dixit
48
49 2576 et al. compared Li and Na diffusion in Li_{0.25}FePO₄ and Na_{0.25}FePO₄, respectively, by calcu-
50
51 2577 lating the potential and free energy diffusion barriers and determining the nuclear quantum
52
53 2578 effects (NQEs) of the Li ions.⁶⁷³ Their calculations found that Li diffusion was faster than
54
55 2579 Na diffusion, which is in agreement with experiments. However, the authors also determined

2580 that the NQEs for Li-ions were higher than those for Na-ions and that the quantum be-
 2581 haviour of the Li-ions was unusual. This information would not be possible to resolve using
 2582 current experimental methods.

Dimensionality of the Li⁺ ion transport

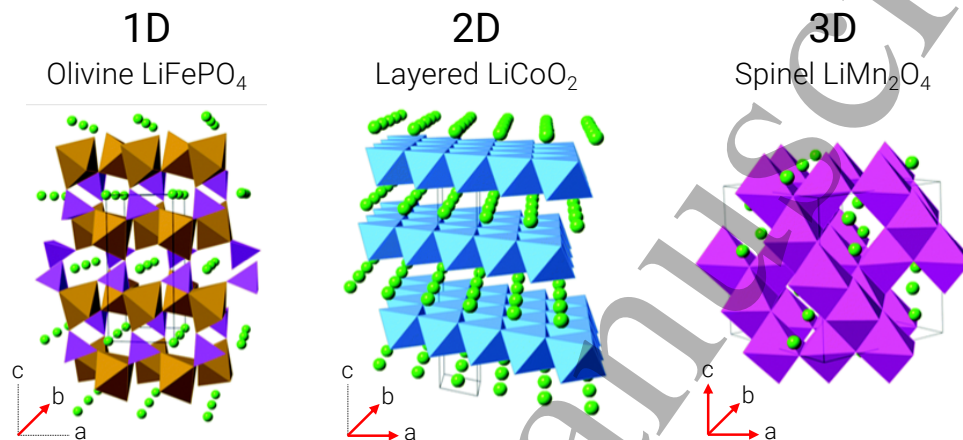


Figure 33: Dimensionality of the Li⁺ ion diffusion in LiFePO₄, LiCoO₂, and LiMn₂O₄. Figure edited and reproduced with permission from Ref. 606 - Published by The Royal Society of Chemistry.

2583 The cathode crystal structure determines the available diffusion pathways in the material.
 2584 DFT calculations^{674,675} and classical MD using a core-shell model⁶⁷⁶ show Li_{*x*}FePO₄ is an
 2585 olivine based structure which hosts Li over an interstitial network that has one-dimensional
 2586 connectivity, i.e. 1-D diffusion, along the *b* lattice vector of the orthorhombic cell.⁶⁷⁷ Li_{*x*}CoO₂
 2587 is a layered compound that accommodates Li ions within octahedral sites forming two-
 2588 dimensional triangular lattices, resulting in 2-D diffusion, along the *b* and *c* lattice vector
 2589 of the orthorhombic cell.⁶⁷⁸ The spinel form of Li_{*x*}Mn₂O₄ has both tetrahedrally and octa-
 2590 hedrally coordinated Li interstitial sites, forming a three-dimensional network and resulting
 2591 in 3-D diffusion, along all lattice vectors.^{679,680} These different diffusion pathways can be
 2592 seen in Figure 33. The 1-D diffusion pathways in Li_{*x*}FePO₄ are not actually exactly one
 2593 dimensional. Although they travel solely along the *b* lattice vector, the pathways themselves
 2594 are curved, as shown in Figure 34, as originally predicted by Islam et al. using atomistic
 2595 modelling,⁶⁷⁶ before later being observed experimentally.⁶⁸¹

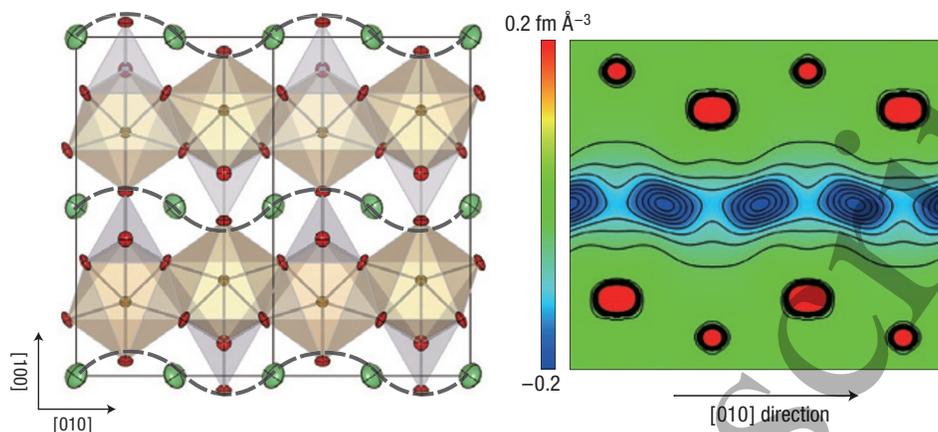


Figure 34: Anisotropic harmonic lithium vibration in LiFePO₄. Expected curved one-dimensional continuous chains of lithium motion are drawn as dashed lines to show how the motions of Li atoms evolve from vibrations to diffusion. Two-dimensional contour map sliced on the (001) plane at $z = 0.5$; lithium delocalises along the curved one-dimensional chain along the [010] direction, whereas Fe, P, and O remain near their original positions. Adapted by permission from Springer Nature: Ref. 681, Copyright 2008.

2596 Chemical diffusion coefficient of Li in an intercalation compound often has a strong
 2597 dependence on Li concentration and crystal structure. The combination of DFT cluster
 2598 expansion Hamiltonians with kinetic Monte Carlo (kMC) simulations, as described in sections
 2599 2.1.4 and 2.1.5 revealed that the Li diffusion coefficients of TM oxides (and sulfides) are
 2600 very sensitive to the Li concentration and also to the degree of cation ordering.^{77,682–685} For
 2601 example, Van der Ven et al. shows the calculated Li diffusion coefficients for the layered (2D)
 2602 and spinel (3D) forms of Li_xTiS₂ as a function of Li concentration.^{9,682,683,685} This is presented
 2603 in Figure 35, along with the structural images and vacancy mechanisms highlighted. Here it
 2604 can be seen that not only do the Li diffusion coefficients differ by orders of magnitude, but
 2605 the shape of the diffusion/Li concentration relation is very different. This shows how the
 2606 crystal structure, and thus the active diffusion pathways, plays a crucial role in determining
 2607 the concentration dependence of the diffusion coefficients in these materials.

2608 We have already eluded that diffusion is sensitive to the Li-ion concentration. However,
 2609 the exact relation is through the activation barriers. Early DFT studies^{678,686} of Li_xCoO₂
 2610 systems showed that the lithium diffusion was predominately through a divacancy mecha-

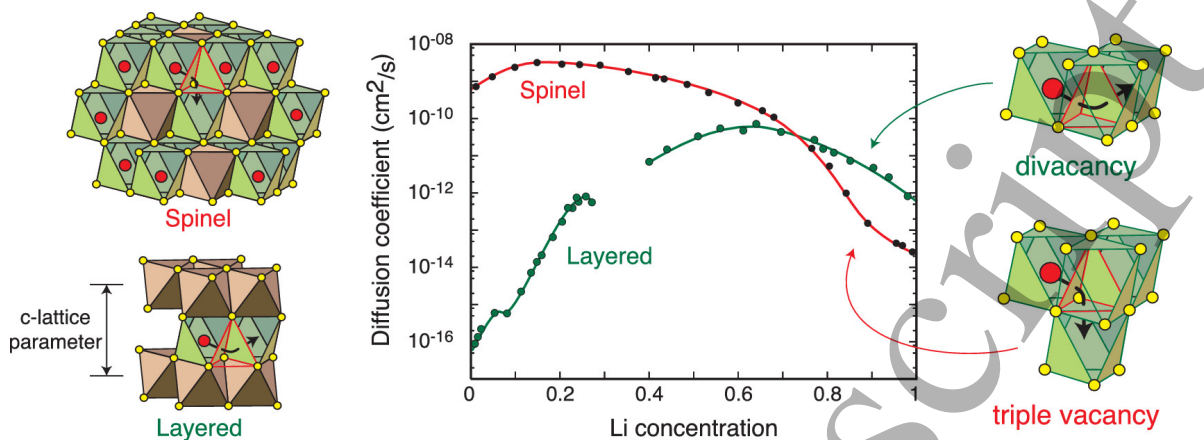


Figure 35: Chemical diffusion coefficient of Li in an intercalation compound often has a strong dependence on Li concentration and crystal structure. Reprinted with permission from Ref. 9. Copyright 2020 American Chemical Society.

2611 nism, when $0 \leq x < 1$. However, at infinite vacancy dilutions diffusion is through a single
 2612 vacancy mechanism.⁶⁰⁶ There are two hopping mechanisms at play here; oxygen dumbbell
 2613 hops and tetrahedral site hops. Oxygen dumbbell hopping occurs when there is a single
 2614 vacancy and a Li-ion has to travel between two occupied adjacent lithium sites to reach the
 2615 vacant lithium site. Tetrahedral site hopping occurs when there are divacant or trivacant
 2616 sites, i.e. when one or both of the adjacent lithium sites are vacant.⁶⁸⁶ Oxygen dumbbell
 2617 hopping has a significantly lower migration barrier energy compared to tetrahedral site hop-
 2618 ping, which highlights the sensitivity of the activation barrier to the lithium concentration.
 2619 Experimental studies of mixed-TM layered oxides, such as $\text{Li}(\text{Ni}_{0.5}\text{Mn}_{0.5})\text{O}_2$, have reported
 2620 site exchange between Li and Ni ($\sim 8\text{-}12\%$).⁶⁸⁷ DFT has been used to aid in understanding
 2621 the effects of site-exchange on Li-ion mobility.^{688,689} (De)intercalation of lithium in the ma-
 2622 terial changes the distances between the layers. As Li is removed from the structure, there
 2623 is a reduced “barrier” between the oxygen layers which start to repel one another. By calcu-
 2624 lating the activation energy as a function of the distance between the O layers on either side
 2625 of the Li layers, a trend between increased O layer separation and lower activation energy is
 2626 seen.^{688,689}

2627 In addition to the crystal structure and available diffusion pathways, doping the cathode

material can also influence the material properties, including ion diffusion. NMC cathodes are effectively LiCoO_2 doped with Ni and Mn. As previously mentioned in section 5.1, introducing Ni and Mn into the system to form a mixed-TM layered oxide increases the diffusion/conductivity and electrochemical performance. There are very few detailed computational studies of mixed-TM oxides due to their complexities. An illustration of this is the complexities which arise from TMs, such as Fe, Ni, Co, and Mn, which exhibit localised oxidation states. This can be further complicated, or influenced by, TM ordering. For instance, Lee and Persson investigated the effects of TM disorder on the electrochemical properties of $\text{Li}_x\text{Ni}_{0.5}\text{Mn}_{1.5}\text{O}_4$ using cluster expansion and MC methods (c.f. sections 2.1.4 and 2.1.5). The authors determined a correlation between Li vacancy ordering and TM ordering.⁶⁹⁰ Hao et al. found similar evidence for $\text{Li}_x(\text{Mn}_y\text{Ni}_{1-y})_2\text{O}_4$.⁶⁹¹ These also have an effect on the diffusion properties of the material. TM ordering in NMC cathodes is discussed in more detail in section 5.2.4. Using experimental techniques, Capsoni et al. found that doping the cationic sublattice of spinel LiMn_2O_4 with as low as 1 % Ga^{3+} significantly modifies the temperature of the conductivity drop associated with Jahn-Teller (JT) distortion, preventing the transition observed near room temperature.⁶⁹² This allows for a wider temperature window for the higher conductivity phase. DFT using generalised gradient approximation (GGA) or its variant GGA+U (c.f. section 2.1.1), was also employed to analyse the effect of doping LiMn_2O_4 on the JT distortion. In this study, Singh et al. found that doping with Cr and Mg also suppressed the JT distortion and thus the associated temperature of the conductivity drop.⁶⁹³

5.2.3 Redox and Electronic Properties

The cathode operates by the deintercalation of Li^+ on charging, and the reinsertion of Li^+ on discharging. The charge is balanced by the oxidation and reduction of the TM ion, e.g. $\text{LiCo}^{3+}\text{O}_2 \rightleftharpoons \text{Li}_{1-x}\text{Co}^{4+}\text{O}_2 + x\text{Li}^+ + xe^-$. The role of TM redox in LiBs has been well known since the first publications by Goodenough on LiCoO_2 as an intercalation electrode

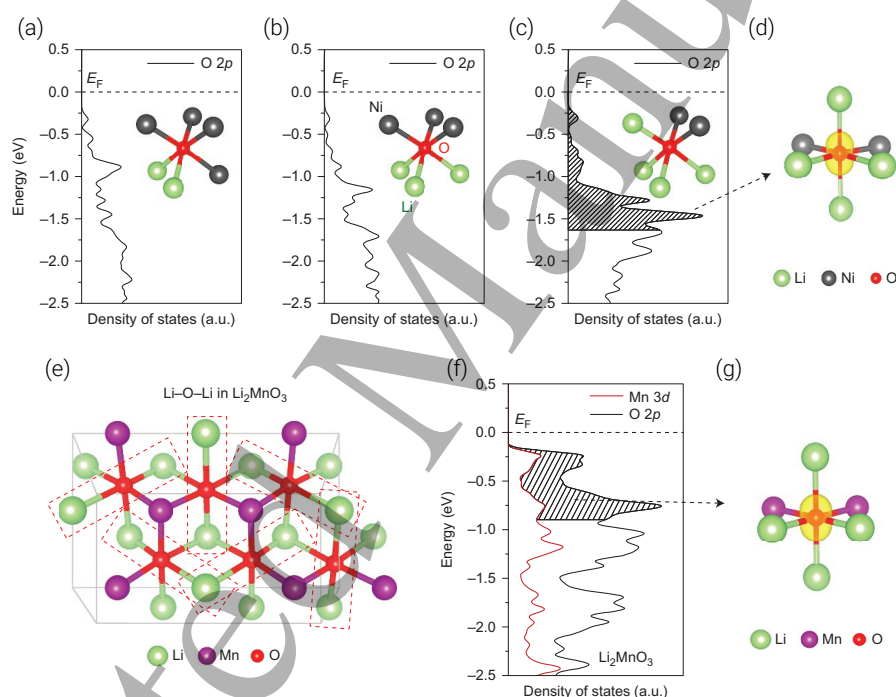
1
2
3 2654 in 1980.⁵⁸⁵ Although various classes of compounds have been investigated over the years, the
4
5 2655 overall mechanism of TM redox is broadly similar. The three major classes of oxide cathodes,
6
7 2656 (layered,⁵⁸⁵ polyanion,⁶⁹⁴ and spinel⁶⁹⁵) all function via a TM redox couple. The specific
8
9 2657 capacity of most LiB cathode materials is limited by the number of electrons per TM cation
10
11 2658 that can participate in the redox reaction. However, the recent discovery of oxygen redox
12
13 2659 reactivity, $O^{2-} \rightarrow (O_2)^{n-}$, in Li-excess cathode materials^{620,622-627,629,639,696-710} has prompted
14
15 2660 further investigation.

16
17 2661 DFT has been pivotal in shedding light on this phenomenon, in conjunction with a range
18
19 2662 of experimental techniques. DFT can be used to analyse the atomic charge and electronic
20
21 2663 structure of each ground state, enabling the charge compensation during delithiation to be
22
23 2664 correctly attributed during simulated charging. Yao et al. were able to propose a sequence
24
25 2665 of redox events for delithiation of $Li_xMn_2O_5$;⁶³⁴ first, cationic redox, Mn^{3+}/Mn^{4+} , dominates
26
27 2666 for $Li_xMn_2O_5$, when $4 \geq x > 2$. Then anionic redox, O^{2-}/O^{1-} , dominates for $Li_xMn_2O_5$,
28
29 2667 when $2 \geq x > 1$. Finally, mixed cationic (Mn^{4+}/Mn^{5+}) and anionic (O^{2-}/O^{1-}) redox for
30
31 2668 $Li_xMn_2O_5$, when $1 \geq x \geq 0$. Meanwhile, fluorinated materials such as $Li_2Mn_{2/3}Nb_{1/3}O_2F$ ⁶⁴⁹
32
33 2669 and Li_2MnO_2F ⁶³⁹ were found to exhibit some overlap between the redox processes, suggest-
34
35 2670 ing that the substitution of O by F favours lower Mn oxidation states, therefore leading
36
37 2671 to more redox overlap with oxygen. DFT has also been used to establish the band struc-
38
39 2672 ture for cathode materials, determining which TM orbitals hybridise more with the O(2p)
40
41 2673 orbitals^{699,711} and to identify hole states.^{704,712}

42
43 2674 In a combined experimental and computational study, Gent et al. observed a strong
44
45 2675 correlation between anion redox, cation migration, and open circuit voltage (OCV) hysteresis
46
47 2676 in Li-rich layered oxides.⁶²⁴ Hong et al. offered an explanation for the strong coupling between
48
49 2677 anion redox and structural disordering in Li rich layered oxides; they found local stabilisation
50
51 2678 of short ~ 1.8 Å metal-oxygen π bonds and ~ 1.4 Å O-O dimers during oxygen redox.⁷¹³

52
53 2679 Seo et al. showed that anion redox chemistry is heavily dependent on the anion nearest-
54
55 2680 neighbour coordination environment.⁶²³ In particular, they described how more Li-O-Li con-

2681 configurations lead to more potentially labile oxygen electrons, resulting in enhanced O redox
 2682 chemistry, as shown in Figure 36. A similar result was found with $\text{Li}_2\text{MnO}_2\text{F}$; those oxygens
 2683 coordinated to at least five Li (e.g. OLi_5Mn) in the fully lithiated state were the first to oxi-
 2684 dise, whereas those coordinated to three or fewer (e.g. OLi_3Mn_3) did not undergo oxidation
 2685 at all. This showcased a more continuous variation in the O-redox potential, dependent on
 2686 the number of Li coordinated to a given O^{2-} ion.⁶³⁹ Recent computational screening work on
 2687 layered oxide cathodes using hybrid DFT has reported trends in O-redox activity associated
 2688 with the electrostatic (Madelung) energy at oxygen sites.⁷¹⁴



42 Figure 36: Effect of local atomic environments on the electronic states of O ions in (a-d)
 43 cation-mixed layered LiNiO_2 and (e-g) Li_2MnO_3 . Cation mixing introduces various local
 44 environments around oxygen. Projected density of states (pDOS) of the O 2p orbitals of
 45 O atoms in cation-mixed layered LiNiO_2 coordinated by (a) two Li and four Ni, (b)
 46 three Li and three Ni, and (c) four Li and two Ni. (d) gives the isosurface of the charge
 47 density (yellow) around the oxygen coordinated by four Li and two Ni, in the energy range of 0
 48 to -1.64 eV. (e) gives an illustration of Li-O-Li configurations in Li_2MnO_3 , with (f) giving
 49 the related pDOS of the O 2p orbitals and Mn 3d orbitals, and (g) giving the isosurface of
 50 the charge density (yellow) around the oxygen, in the energy range of 0 to -0.9 eV. Adapted by
 51 permission from Springer Nature: Ref. 623, Copyright 2016.

2689 Chen and Islam investigated delithiation and kinetic processes in Li_2MnO_3 using hybrid

1
2
3
4 2690 DFT and found that Li extraction is charge-compensated by oxidation of the oxide anion,
5
6 2691 so that the overall delithiation reaction involves lattice oxygen loss.⁷⁰¹ Localised holes on
7
8 2692 oxygen (O^-) are formed at the first step but, due to their instability, lead to oxygen dimers
9
10 2693 ($O-O$ is approximately 1.3 Å) and eventually to the formation of molecular O_2 . This then
11
12 2694 facilitates Mn migration to the octahedral site in the vacant Li layer, leading to a spinel-like
13
14 2695 structure. DFT has also been used to show the formation of O_2 at high states of charge in
15
16 2696 Li_2MnO_2F ⁶³⁹ and $Li_{1.2}Ni_{0.13}Co_{0.13}Mn_{0.54}O_2$,⁶²⁸ agreeing with experimental resonant inelastic
17
18 2697 X-ray scattering (RIXS) data, and to report superoxide formation in Li_2VO_2F , in agreement
19
20 2698 with electron paramagnetic resonance (EPR) spectroscopy studies.⁶⁴⁸

21 22 23 2699 **5.2.4 TM Ordering in NMC Layered Oxides**

24
25 2700 Cation/anion ordering also plays a vital role in the properties/activity of a material, such
26
27 2701 as the physical and electrochemical properties. A topical illustration of this is the NMC
28
29 2702 cathode materials, where recent experimental studies show that spin interaction of the TM
30
31 2703 ions is a major challenge.^{617,715} The varying compositions, charge distributions, and elec-
32
33 2704 tronegativities of the TMs lead to a mixture of valence states, where Ni can exist as Ni^{2+} ,
34
35 2705 Ni^{3+} , and Ni^{4+} , Co can exist as Co^{3+} and Co^{4+} , and Mn exists as Mn^{4+} .⁷¹⁵ The interac-
36
37 2706 tions between these mixed valence states poses a challenge to the identification of ground
38
39 2707 states. As NMC materials, such as NMC811, emerge as front runners for commercialisation,
40
41 2708 research into their specific chemistry has become of great interest. Recently, several compu-
42
43 2709 tational studies have been performed to analyse the influence of TM valence states on the
44
45 2710 stability and structure-property relationships of NMC materials, which are challenging to
46
47 2711 resolve experimentally.⁷¹⁶⁻⁷¹⁹ For example, Sun and Zhao analysed 81 NMC compositions
48
49 2712 using DFT, observing that random arrangements of TMs present similar thermodynamic
50
51 2713 states.⁷¹⁶ Clusters of random geometries and population were seen, which confirmed that
52
53 2714 no specific ordering exists at the superlattice scale. This is consistent with previous experi-
54
55 2715 ment analysis using X-ray and neutron diffraction characterization on a specific composition

1
2
3
4 2716 of NMC, $\text{Li}_{2/3}[\text{Co}_x\text{Ni}_{1/3-x}\text{Mn}_{2/3}]\text{O}_2$, demonstrating that Co suppresses the superlattice or-
5
6 2717 dering when $x > 1/6$.⁷²⁰ The authors also demonstrated, through intensive computational
7
8 2718 screening, that no long-range ordering exists in the TM layer of NMC. These DFT studies
9
10 2719 provide fundamental understanding of the physicochemical properties at the intrinsic level
11
12 2720 of electronic structures and will offer important insight in the selection of NMC materials
13
14 2721 for enhanced electrochemical performance. It would not be tractable to analyse so many
15
16 2722 compositions of NMC through experiments.

18 19 2723 **5.2.5 Vibrational and Thermal Properties**

20
21 2724 An important contribution to the thermodynamic properties at finite temperature is the
22
23 2725 vibrational partition function, which can be evaluated by calculating the material's normal
24
25 2726 modes of lattice vibrations. A number of researchers have theoretically addressed the vibra-
26
27 2727 tional contribution to the material thermodynamic properties in LiBs, especially in NMC
28
29 2728 cathodes.^{181,182,721} There are several works studying cathode materials beyond NMC. Shang
30
31 2729 et al. employed DFT phonon calculations with a mixed-space approach to probe the lattice
32
33 2730 dynamics and finite-temperature thermodynamic properties of olivine structure LiMPO_4 (M
34
35 2731 = Mo, Fe, Co, Ni).⁷²² The authors reported that LiMPO_4 structures from Mn, Fe, Co, to
36
37 2732 Ni show increasing zero-point vibrational energy, but a diminishing vibrational contribution
38
39 2733 to the Gibbs energy, due to the decreasing phonon densities of state at the low frequency re-
40
41 2734 gion of LiMPO_4 . Recently, lattice dynamics studies have been expanded to solid electrolytes,
42
43 2735 aiding in the discovery of lithium fast-ion conductors.⁷²³

44
45 2736 Two major approaches have been developed to compute lattice thermal conductivity;
46
47 2737 by solving the Boltzmann transport equation (BTE) using anharmonic lattice dynamics
48
49 2738 and through MD simulations. Puligheddu et al. compared lattice thermal conductivity
50
51 2739 values from these two methods and found a satisfactory agreement.⁷²⁴ The comparison used
52
53 2740 empirical potentials and took into account the effects of both fourth order phonon scattering
54
55 2741 and temperature-dependent phonon frequencies, reporting the different effects of quantum

1
2
3
4 2742 and classical statistics.

5 2743 Using BTE within the relaxation-time approximation, Mattila and Karttunen reported
6
7 2744 the highly anisotropic lattice thermal conductivities in isotopic LiCoO_2 , close to the values
8
9 2745 in Yang et al.'s work,^{181,182} and illustrated the effect of the alkali metal atom by replacing
10
11 2746 Li by Na.⁷²⁵ The authors explained this through the significantly shorter phonon lifetimes
12
13 2747 in LiCoO_2 . They found that in-plane lattice thermal conductivities in NaCoO_2 are ~ 0.7
14
15 2748 times larger than that in LiCoO_2 at room temperature, since the former has significantly
16
17 2749 longer phonon life times. While Feng et al. report much lower thermal conductivity values
18
19 2750 by including four-phonon scattering, using a different functional, the local density approxi-
20
21 2751 mation (LDA), for exchange and correlation.⁷²⁶ They also investigated the thermal transport
22
23 2752 reduction during delithiation (charging) due to reduced phonon velocities and increasing an-
24
25 2753 harmonicity. Furthermore, grain-boundary effects reduced thermal transport and suppressed
26
27 2754 thermal conductivities in polycrystals are well reproduced when grain sizes were reduced down
28
29 2755 to several nm in either BTE or MD simulations.¹⁵⁵

30
31 2756 The thermal conductivity investigation can be also performed on anodes and many other
32
33 2757 materials.^{727,728} Recently, a high-throughput study was reported for 37 binary rock-salt and
34
35 2758 zinc blende material systems, in which the authors highlight the importance of high-order
36
37 2759 phonon-phonon interactions based on harmonic calculations.⁷²⁹ Modelling heat transport
38
39 2760 using DFT calculations is complex but essential due to the difficulties inherent in preparing
40
41 2761 high-quality samples for experimental measurements.

42 43 44 45 2762 **5.3 Surfaces**

46
47
48 2763 Surface structures and morphologies of cathode particles can be difficult to determine using
49
50 2764 experimental microscopy and spectroscopy methods alone and thus computational investiga-
51
52 2765 tions can provide vital insights.⁷³⁰ Due to their synthesis conditions, experimental cathode
53
54 2766 materials comprise different surface facets, defects, and particle sizes. It is therefore neces-
55
56 2767 sary to use model systems to determine which of these effects is more important by studying

1
2
3
4 2768 them in isolation, separating the effects, which is not possible using experimental materi-
5
6 2769 als. Both *ab initio* and potentials-based MD have been extensively used to investigate the
7
8 2770 surfaces and morphologies of layered oxides, spinel oxides, and olivine phosphates, which
9
10 2771 will be briefly discussed here. These techniques have also been used to investigate cathode
11
12 2772 materials in sodium-ion batteries, which is covered in more detail in Ref. 606.

13 2773 With oxides at the forefront of the battery revolution, it is unsurprising that there have
14
15 2774 been many DFT and potentials-based MD studies into layered LiCoO_2 , LiMn_2O_4 spinel,
16
17 2775 MnO_2 -type and related materials, looking at properties including the surfaces, nanostruc-
18
19 2776 tures, and morphologies.^{731–738} Surface energies for low-index layered LiCoO_2 surfaces, as a
20
21 2777 function of external Li and O chemical potentials, revealed the (0001) and (10 $\bar{1}$ 4) surfaces
22
23 2778 were present for all reasonable values of Li and O chemical potentials, whereas the (01 $\bar{1}$ 2)
24
25 2779 surface was only stable under oxidising conditions.⁷³¹ Studies into the low-index surface
26
27 2780 facets of LiMn_2O_4 determine the (111) surface to be the most stable. This is due to the site
28
29 2781 exchange of under-coordinated Mn on the surface, which exhibit a cubo-octahedral type, pre-
30
31 2782 dominately comprising {111} surfaces.⁷³⁶ Other studies show that the Mn-terminated (111)
32
33 2783 surfaces undergo surface reconstruction, indicating instead that the Li-terminated (001) sur-
34
35 2784 face has the lowest energy.⁷³⁵

36
37 2785 It has also been shown that electronic spin state transitions occur on the surfaces of sto-
38
39 2786 ichiometric LiCoO_2 . Here Qian et al. found that the trivalent Co ions at the surface adopt
40
41 2787 an intermediate spin state if they are square-pyramidally coordinated and a high spin state
42
43 2788 if they are pseudo-tetrahedrally coordinated. This highlighted the effect of low-coordinated
44
45 2789 geometries at the particle surface on the Co^{3+} – Co^{4+} redox potential.⁷³⁹ Hong et al. investi-
46
47 2790 gated the surface properties of LiCoO_2 nanoplatelets and their chemical modifications with
48
49 2791 Al^{3+} , using combined experimental and theoretical approaches.⁷⁴⁰ Their models also showed
50
51 2792 the electronic structures of several LiCoO_2 surface facets are different from those of the bulk,
52
53 2793 attributing this to the altered spin states of surface Co^{3+} atoms. The authors found splitting
54
55 2794 of the Co 3d–O 2p states, which were linked with high-spin-state Co^{3+} at the surface. Partial
56
57
58
59
60

1
2
3 substitution of Co^{3+} by Al^{3+} was found to increase the ratio of low-spin-state Co^{3+} at the
4
5 surface, resulting in a distinct change in the intensity ratio of the split Co 3d–O 2p states.
6

7
8 When exposed to certain environmental conditions, LiCoO_2 releases Co cations, a known
9
10 toxicant. Abbaspour-Tamijani et al. has applied DFT (with different functionals) and ther-
11
12 modynamics modelling to study the LiCoO_2 surface transformations.⁷⁴¹ They assessed how
13
14 the calculated predictions for ion release depend on aspects of the structural surface model.
15
16 Here, the authors propose a generalised scheme for predicting a threshold pH at which Co
17
18 release becomes favourable, providing information that could be used to inform macroscopic
19
20 contaminant fate models. More recently, these authors have furthered this investigation in
21
22 cation dissolution at the LiCoO_2 surface, finding that at a pH of 7, 16 % of surface Co
23
24 undergoes dissolution.⁷⁴¹

25
26 Phase transitions in cathode materials can have negative effects on the desirable proper-
27
28 ties. However, there are circumstances where use of different structural phases are beneficial.
29
30 For example, post-modification of Li-rich layered material surfaces to form a spinel LiMn_2O_4
31
32 membrane, i.e. encapsulating the layered particle, has shown enhanced related rate capabil-
33
34 ity and cycling stability.^{148,742,743} More significantly, insertion of a spinel component⁷⁴⁴ or the
35
36 formation of platelets⁷⁴⁵ on layered-layered composites of NMC cathodes, yields a high spe-
37
38 cific capacity ($\sim 250 \text{ mAh g}^{-1}$) and can partly correct for voltage fade.¹⁴⁸ Phase transitions
39
40 can also be a negative consequence of particle surface stress. Warburton et al. investigated
41
42 the particle fracturing in LiMn_2O_4 caused by stress through the delithiation process.⁷⁴⁶ Using
43
44 DFT, the authors provide a good understanding of the stress buildup at the surface during
45
46 delithiation, demonstrating that the delithiation of near-surface layers contribute towards
47
48 the buildup, leading to a $\text{LiMn}_2\text{O}_4/\text{Li}_{0.5}\text{Mn}_2\text{O}_4$ low-voltage phase transition, Figure 37. The
49
50 authors also investigate if there is an orientation preference, concluding that cracks due to
51
52 tensile stress buildup are not likely to orient preferentially in the [001] direction, because the
53
54 stresses act in the plane of the (001) surface.⁷⁴⁶ This shows that an in-depth understanding of
55
56 the electrochemical processes of cathode materials, at the atomistic scale, is urgently needed,
57
58
59
60

2822 especially for more complex chemistries like NMC. A recent study on the NMC surfaces by
 2823 Liang et al. looked at the surface segregation and anisotropy using DFT+U calculations.⁷⁴⁷
 2824 In this study, the authors looked at surface stability, morphology, and elastic anisotropy, all
 2825 related to the degradation of Li-ion batteries. Ni surface segregation predominantly occurs
 2826 on the (100), (110), and (104) nonpolar surfaces, showing a tendency to form a rock-salt
 2827 NiO domain on the surface, due to severe Li-Ni exchange. The findings of this study showed
 2828 that an uneven deformation is more likely to form in particles which have been synthesised
 2829 under low oxygen conditions, leading to crack generation and propagation.⁷⁴⁷

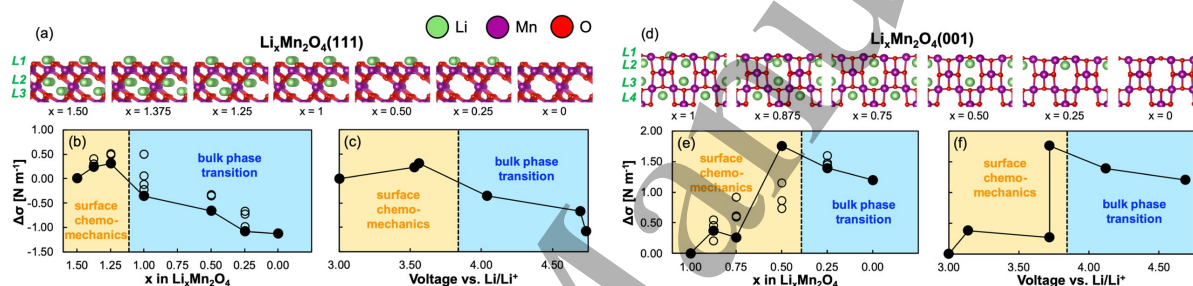


Figure 37: Surface stress evolution upon delithiation of lithium manganese oxide (LMO) surfaces. Low energy structures of the (a) LMO(111) and (d) LMO(001) surfaces at different Li^+ contents. Differential surface stresses of (b) LMO(111) and (e) LMO(001) as a function of the Li^+ content for various Li^+ configurations. The filled circles in (b,e) represent the most energetically stable structures for a given stoichiometry. The unfilled circles in (b,e) denote metastable lithium configurations. Differential surface stresses of (c) LMO(111) and (f) LMO(001) as a function of the cell voltage. The dashed lines correspond to the calculated equilibrium potential of 3.84 V vs Li/Li^+ between LMO and $\text{L}_{0.5}\text{MO}$. The yellow-shaded regions correspond to surface-dominated mechanics from the near-surface delithiation. The blue-shaded regions correspond to surface phases that are thermodynamically inaccessible because they become stable only at voltages above the equilibrium potential. Reprinted with permission from Ref 746. Copyright 2020 American Chemical Society.

2830 The surface structures of LiFePO_4 exhibit a complex and uneven topology due to the
 2831 size difference of Li^+ , Fe^{2+} , and PO_4^{3-} . The majority of terminating surfaces undergo
 2832 fairly considerable relaxation, which makes predictions based on rigid terminations unre-
 2833 liable. Although LiFePO_4 can be synthesised in multiple morphologies exposing different
 2834 surfaces,^{666,748} studies on the (010) surfaces are particularly interesting. This surface is nor-
 2835 mal to the most facile pathway for lithium ion conduction,⁷⁴⁹ reducing the diffusion path

1
2
3 2836 lengths for lithium at the surface, enhancing the electrochemical performance of the cath-
4
5 2837 ode. DFT calculation of the diffusion pattern and energy landscape of lithium in LiFePO_4
6
7 2838 showed that the energy barrier for the Li diffusion along (010) is lower than along the other
8
9 2839 directions, e.g. (100), indicating that the Li diffusion in LiFePO_4 is one dimensional.⁷⁵⁰
10
11 2840 Understanding processes such as the lithium (de)intercalation on the LiFePO_4 (010) surface
12
13 2841 is important for developing effective approaches for further improving the material's rate
14
15 2842 performance. Using DFT calculations, Xu et al. found that the extraction of Li from the
16
17 2843 surface layer has a significant effect on the work function of the LiFePO_4 (010) surface, pro-
18
19 2844 viding evidence for whether Li atoms are present in the outermost layer of LiFePO_4 (010)
20
21 2845 surface or not.⁷⁵¹ Here, the authors also calculate the redox potential and formation energies
22
23 2846 for extracting Li from different (010) surface layers. They find that extracting lithium from
24
25 2847 the outer surface layers has the lowest redox potential and formation energy, indicating that
26
27 2848 it is energetically favorable to extract Li first from the surface layer. Xu et al. propose a
28
29 2849 new method that surface work functions can be used for providing insight into the lithium
30
31 2850 (de)intercalation on the LiFePO_4 (010) surface.⁷⁵¹

32
33 2851 Zhang et al. used a combined experimental and computational (DFT) approach to inves-
34
35 2852 tigate the preferential cation doping on the surface of LiFePO_4 and its effect on properties.⁷⁵²
36
37 2853 The authors found that, for all chosen dopants, there were increased ratios of $\text{Fe}^{3+}/\text{Fe}^{2+}$ ox-
38
39 2854 idation on the particle surfaces, while the core atoms remained closer to that of the pristine,
40
41 2855 undoped material. This indicates that the dopants are predominantly pushed to the particle
42
43 2856 surfaces during phase formation. This disparity in distribution of dopant across the core and
44
45 2857 surface results in improved conductivities.⁷⁵² *ab initio* MD simulations with X-ray Diffrac-
46
47 2858 tion (XRD) and microscopy experiments on the LiFePO_4 cathode show Li-ions migrating
48
49 2859 along the surface, facilitated by solvent molecules.⁷⁵³ This work establishes fluid-enhanced
50
51 2860 surface diffusion as a key factor in tuning phase transformation in anisotropic solids.

2861 5.4 Interfaces

2862 Although the cathode-electrolyte interphase (CEI) is thinner than the SEI at the anode,
2863 it is still quite complex in structure and composition.^{115,754} DFT-based simulations can
2864 provide insight into adsorption trends,⁷⁵⁵ reaction pathways and energetics,^{756,757} and mi-
2865 gration barriers for Li-ion transfer,⁷⁵⁸ etc. The electrolyte in a Li-ion battery is typically a
2866 Li salt, for example LiPF_6 in an organic carbonate solvent, such as ethylene carbonate (EC),
2867 propylene carbonate (PC), diethyl carbonate (DEC) or dimethyl carbonate (DMC). The
2868 LiPF_6 electrolyte reacts with trace amounts of moisture to form hydrofluoric acid (HF),⁷⁵⁶
2869 which is highly corrosive and reacts with the cathode surface to form fluoride-based prod-
2870 ucts.⁷⁵⁷ The organic carbonate solvent also reacts with the cathode surface to form a series
2871 of decomposition products.⁷⁵⁹ The adsorption of solvent-decomposition and fluoride-based
2872 products is the first step in the series of reactions that lead to the formation of the CEI.
2873 The decomposition reaction of cyclic organic carbonate solvents proceeds via ring opening,
2874 having an energy barrier predicted via climbing image nudged elastic band (CI-NEB) calcu-
2875 lations (sections 2.1.1 and 2.1.3) to be around 0.62 eV on (100) LiMn_2O_4 surfaces,⁷³⁷ over
2876 1 eV on (101 $\bar{4}$) LiCoO_2 surfaces,⁷⁵⁹ and around 0.29 eV on (101 $\bar{4}$) $\text{Li}(\text{Ni},\text{Mn},\text{Co})\text{O}_2$ sur-
2877 faces.⁷⁶⁰ While experimental studies on the composition of the CEI have shown the presence
2878 of both solvent-decomposition and fluoride-based products on most oxide cathodes, such as
2879 LiMn_2O_4 , LiNiO_2 , LiCoO_2 and $\text{LiNi}_{0.8}\text{Co}_{0.2}\text{O}_2$, no solvent reaction or solvent decomposition
2880 products are detected on LiFePO_4 .^{754,761} Recent calculations of adsorption energies based
2881 on DFT have shown that adsorption preference of HF over EC leads to the entire LiFePO_4
2882 nano-particle being covered by fluoride-based products, further leading to their dominant
2883 presence in the CEI.⁷⁵⁵ DFT simulations have also been used to design suitable coatings in
2884 order to prevent cathode degradation.⁷⁵⁷ These calculations can shortlist effective candidate
2885 materials to guide experiments. Thus, atomistic methods can not only provide the neces-
2886 sary insights needed in order to explain experimental observations, but also suggest novel
2887 solutions for mitigating cathode degradation.

1
2
3
4 2888 Apart from the complexity of structure of the CEI, another challenge is understanding
5
6 2889 Li-ion migration at the CEI, impacting the rate capability of LiBs. Li-ion conductivity in
7
8 2890 bulk electrolyte is around 1 S cm^{-1} (c.f. section 4) which is several orders of magnitude
9
10 2891 higher than that in bulk electrode materials (c.f. sections 3.2.4 and 5.2.2) (around 10^{-7} –
11
12 2892 $10^{-2} \text{ S cm}^{-1}$).^{287,685} However, the complex structure of the CEI and uncertainty about the
13
14 2893 mechanism of Li-ion transfer across it has hindered the understanding of kinetics at the in-
15
16 2894 terface. Recent NEB calculations on the LiFePO_4 cathode have estimated an energy barrier
17
18 2895 of 756 meV, for Li to move from a near-surface solvated cluster to a sub-surface vacancy
19
20 2896 in the LiFePO_4 cathode material.⁷⁵⁸ Due to preferential adsorption of fluoride on LiFePO_4
21
22 2897 surfaces,^{754,755} the energy barrier has been found to decrease to 410 meV in the presence
23
24 2898 of fluoride. Nevertheless, the interfacial energy barrier is higher than that in bulk cathode
25
26 2899 material, which is estimated to be around 270–290 meV.^{674,762} This highlights a rate-limiting
27
28 2900 behaviour of the interface in the overall Li-ion diffusion process in LiBs. This study moti-
29
30 2901 vates further investigation on other cathode electrolyte interfaces, especially with recently
31
32 2902 developed advanced methods for characterising the interface, as described in section 2.2.1.

35 2903 5.5 Outlook and challenges for cathodes

36
37
38 2904 Lowering the cost, increasing capacity, and improving the sustainability of battery materials
39
40 2905 is becoming more critical, as we move towards large-scale deployment of LiBs for applications
41
42 2906 such as EVs.⁵⁸⁸ Here, we highlight some of the outstanding challenges for cathodes and how
43
44 2907 atomistic modelling can provide insights and suggest solutions.

45
46 2908 Ni-rich NMC layered oxides are favorite candidates for cathode materials, due to their
47
48 2909 high gravimetric and volumetric energy densities.⁷⁶³ However, these materials have three
49
50 2910 critical challenges: cycle instability, thermal instability, and air instability. These are all
51
52 2911 linked with the instability of Ni^{3+} and Ni^{4+} at the surface/interface. Other cathode materials,
53
54 2912 such as oxyfluorides, have worked towards solving some of these issues, however, there are
55
56 2913 still outstanding surface and interfacial challenges, for which atomistic modelling is vital:

- 1
2
3
4 2914 • In Ni-rich NMC, the unstable Ni^{3+} and Ni^{4+} react aggressively with the electrolyte
5 2915 to form thick CEI layers and cause Ni and Mn dissolution. The dissolve TMs then
6 2916 migrate to the anode and cause electrolyte decomposition, leading to thick SEI layers
7 2917 which limit the battery cyclability.^{764,765} CEI and SEI formation are crucial challenges
8 2918 to be overcome for both conventional and solid-state batteries. Although electrochemi-
9 2919 cal spectroscopic techniques have been used to obtain molecular scale information, fur-
10 2920 ther detail, which cannot be resolved using current experimental techniques, is needed
11 2921 to gain more reliable information.⁷⁶⁶ For example, deconvoluting impedance compo-
12 2922 nents in two-terminal electrochemical impedance spectroscopy (EIS) data for materials
13 2923 that have similar time constants, such as solid-state lithium charge transfer in a cell
14 2924 with a graphitized carbon anode and LiCoO_2 cathode, is challenging.⁷⁶⁷ Half-cell mea-
15 2925 surements can be used to study the impedance of the two electrodes separately, but
16 2926 these measurements do not fully reflect the processes occurring in a full-cell battery
17 2927 at different states of (dis)charge.⁷⁶⁸ Three-electrode cell configurations present a way
18 2928 to potentially disentangle the impedance components from the anode and cathode.⁷⁶⁷
19 2929 However, these measurements are fraught with uncertainties, as the insertion of the
20 2930 reference electrode can fundamentally change the electrochemistry.^{769,770} This is where
21 2931 atomistic modelling is well suited to provide the fundamental understanding of the lim-
22 2932 iting rate constants in electrochemistry, that can be used to guide further experiments.
23 2933 As available experimental techniques are unable to provide significant insight into the
24 2934 atomistic mechanism of Li-ion transfer at the cathode-electrolyte interface, atomistic
25 2935 modelling is ideally suited to shed light in this area. For example, Bhandari et al. used
26 2936 DFT to investigate the interfacial Li-ion transfer mechanism at an atomic level, from
27 2937 bulk ethylene carbonate (EC)/ LiPF_6 electrolyte into a LiFePO_4 cathode, and provide
28 2938 an estimate on the corresponding energy barrier.⁷⁵⁸
- 29 2939 • Phase transitions at the surface of cathode materials occur at a high state of charge
30 2940 and affect the surface reactivity, resulting in increased TM dissolution and CEI/SEI

1
2
3
4 2941 formation. The effect of this is rapid capacity fading during cycling.⁷⁷¹ Co-free Li-
5 2942 rich layered oxides, such as $\text{Li}[\text{Li}_{0.2}\text{Mn}_{0.6}\text{Ni}_{0.2}]\text{O}_2$, are appealing due to their low cost
6
7 2943 and high capacities (300 mAh g^{-1}).^{772,773} However, these materials undergo layered to
8
9 2944 spinel transitions due to low octahedral site stability of Mn^{3+} , leading to voltage decay
10
11 2945 during cycling and Mn dissolution,⁷⁷⁴ making these materials challenging to employ
12
13 2946 as a practical cathode. Atomistic insight into the mechanisms involved in these phase
14
15 2947 transitions, gained through *ab initio* and potentials-based MD methods, can provide
16
17 2948 the detail and understanding needed to prevent these phase transitions from occurring.

19
20 2949 • Some cathode materials show reversible O-redox, with lower voltage hysteresis and,
21
22 2950 where O_2 is formed, it reincorporates into the lattice.⁶³⁹ In contrast, other materials
23
24 2951 show irreversible O-redox, with O_2 lost from the surface,^{628,701,775} leading to unwanted
25
26 2952 side reactions with the electrolyte. The formation and potential loss of molecular O_2
27
28 2953 is likely to be heavily dependent on local structure. In the case of $\text{Li}_2\text{MnO}_2\text{F}$, DFT
29
30 2954 showed that O_2 is formed only in O-Li rich areas, not in O-Mn rich areas.⁶³⁹ Meanwhile,
31
32 2955 other oxyfluorides, such as $\text{Li}_2\text{VO}_2\text{F}$, do not show molecular O_2 formation at all, but
33
34 2956 instead form superoxides on charging.⁶⁴⁸

35
36 2957 It is challenging to model disordered systems as, by their very nature, they can have
37
38 2958 an almost infinite arrangement of atoms. Use of computational techniques, such as cluster
39
40 2959 expansion, to generate low energy structures of disordered rock-salts, is a promising route
41
42 2960 to more realistic DFT studies.⁶⁴¹

43
44 2961 As discussed in sections 2.2.2 and 4.2.4, more careful considerations of the factors/parameters
45
46 2962 to include when fitting interatomic potentials for a system is key to improving the quality
47
48 2963 of research conducted through potentials-based modelling. It is commonplace to reuse po-
49
50 2964 tentials from literature sources, without determining how they were fitted, which can lead
51
52 2965 to inaccuracies in the calculations performed. For example, if the potentials for a cathode
53
54 2966 material were fitted only to lattice parameters, elastic constants, and the bulk modulus, then
55
56 2967 the potential would not be accurately representative of the cathode redox properties. If prop-

erties such as the dielectric constant were included, then redox chemistry would be better represented. In effect, interatomic potentials in literature are not necessarily transferable to different types of study. It is not feasible to fit to every material property, however, a broader range of properties, most relevant to the study being conducted, is required. There are tools in development^{142,143,145,164} aiming to make this potential fitting process more accessible to atomistic modellers, with the ability to fit to a larger range of parameters. However, there is still a need for improved transparency in the publication of studies using interatomic potentials. Use of machine learning to develop potentials has also shown to be a promising avenue. Deringer et al. recently published a progress update, showing how machine learning is improving interatomic potentials by “learning” from electronic-structure data, giving increased accuracy in approximating material properties.⁷⁷⁶

In-depth insight into the elemental distribution, electronic structure, and crystalline structure under electrochemical conditions is challenging to achieve experimentally. Atomistic techniques, including DFT and MD, are well suited to provide the insight needed for these properties. However, future research and development of cathode materials will require collaborative efforts, involving the disciplines of chemistry, physics, material science, nanoscience/nanotechnology, and computational modelling/simulation.¹¹⁶

6 Outlook

In this review, we have introduced the key methods deployed in battery modelling at the atomistic scale (section 2.1) in lithium-ion batteries (LiBs) and solid-state batteries (ASSBs), which are collectively called lithium batteries. We have summarised progress in this field, covering models for anodes, liquid and solid electrolytes, and cathodes. Outlooks specific to these components are summarised as follows: anodes, in section 3.5; liquid electrolytes, in section 4.2.10; solid electrolytes, in section 4.3.5; and cathodes, in section 5.5.

There are several notable developments in atomistic methods for lithium batteries which

1
2
3
4 2993 need to be addressed. These include development of a semi-grand canonical framework, incor-
5
6 2994 porating order parameters, with initial promising work developed by Van der Ven et al.,^{9,231}
7
8 2995 the expansion of the linear scaling Density Functional Theory (DFT) codes,^{58,62,65} to link up
9
10 2996 with kinetic Monte Carlo (kMC), the inclusion of entropy effects by parameterising a phase
11
12 2997 field model (such as those developed by Bazant)⁹⁵⁻⁹⁷ using results obtained from Monte Carlo
13
14 2998 (MC) calculations, development of more accurate force field potentials, and parallelisation
15
16 2999 to speed up MC calculations on longer length scales.

17
18 3000 Alongside deepening our understanding of atomic structure and processes, atomistic mod-
19
20 3001 els can be used to aid the design of new materials with improved capacity, rate capability,
21
22 3002 and stability. Atomistic modelling approaches have been shown to be strong tools to de-
23
24 3003 velop novel nanostructures and composites, understand dynamics and phase behaviour, and
25
26 3004 could identify novel interfaces to accommodate volume expansion in solid solution materials,
27
28 3005 such as silicides. Promising areas for future work include tuning the morphology and com-
29
30 3006 position of graphite edges^{70,254,255} and interlayer spacings²¹⁴ to aid intercalation, improved
31
32 3007 understanding of the phase behaviour and dynamics of silicides as anode materials,²⁷² and
33
34 3008 investigation of the emerging class of Li-rich cathode materials.^{626,627,629}

35
36 3009 We have identified several outstanding challenges for further work. For example, certain
37
38 3010 anode and cathode materials show pronounced hysteresis between charge and discharge cy-
39
40 3011 cles.^{71,226,272,777-779} This results in a difference between expected equilibrium potentials from
41
42 3012 atomic-scale calculations and the experimentally measurable open circuit voltage (OCV),
43
44 3013 which creates ambiguity when using the measured OCV in longer length scale models, like
45
46 3014 control models for battery management systems. Future kinetic models must therefore ac-
47
48 3015 count for metastable behaviour that can persist over experimental time scales of hours or
49
50 3016 even days.²²⁶ The next generation of models should consider the connectivity between differ-
51
52 3017 ent phase transformations, with the framework developed by Van der Ven et al. highlighted
53
54 3018 above being one promising solution that is potentially transferable to a variety of material
55
56 3019 types.

1
2
3
4 3020 Flammable liquid electrolyte materials currently dominate the commercial market. De-
5
6 3021 velopment of safer, non-flammable, electrolyte materials is key to addressing safety concerns
7
8 3022 and accidents resulting from attempts to confine increasing energy densities into smaller
9
10 3023 volumes and into geometries that are challenging to thermally manage. More work is needed
11
12 3024 to investigate potential avenues for resolving these issues, including alternative liquid elec-
13
14 3025 trolytes,^{17,18,406} such as water-in-salt electrolytes,^{403,404} and replacing liquid electrolytes with
15
16 3026 solid or soft matter alternatives.^{23,567} Advancements in electrolyte design are crucial, where
17
18 3027 critical obstacles could be resolved through new novel electrolyte salts and solvents. De-
19
20 3028 velopment and open source accessibility of atomistic scale models, combined with improved
21
22 3029 experimental studies, provide a framework for high throughput screening of electrolyte ma-
23
24 3030 terials.^{357,371,401,402}

25
26 3031 More work is needed to incorporate heterogeneities formed during material synthesis and
27
28 3032 battery degradation,^{780–782} such as point defects^{89,93,289,531,718} and grain boundaries,^{304,515,783}
29
30 3033 into atomistic models and to determine their effect on battery performance. Modelling of
31
32 3034 the complex behaviour at interfaces, such as the solid-electrolyte interphase (SEI) in LiBs
33
34 3035 and lattice mismatch in ASSBs, is a prominent challenge which requires further investiga-
35
36 3036 tion. Atomistic models have already provided insight into particular aspects of degradation,
37
38 3037 leading to design of more robust materials, but the development of a universal framework
39
40 3038 for simulating degradation mechanisms and their interactions would be of great benefit and
41
42 3039 is still beyond current capabilities. In order for such a framework to be truly multiscale,
43
44 3040 significant work is needed to connect the modelling scales, linking atomistic to continuum
45
46 3041 modelling and on to longer length scales, such as control models, as well as forming closer
47
48 3042 links with experiments at all scales.

49
50 3043 As we have seen throughout this review, different atomistic modelling approaches can be
51
52 3044 used individually to gain insight into different aspects and properties of LiB materials, across
53
54 3045 the wide range of time and length scales encompassing atomistic modelling. When combined
55
56 3046 into multiscale modelling (MSM) approaches, these techniques can provide a more complete

1
2
3 3047 interpretation of the material(s).^{10,11,233} A popular approach has been to combine DFT cal-
4
5 3048 culations of activation energies of different events, which are then used to implement kMC
6
7 3049 simulations.¹⁰⁴ DFT calculations of the migration mechanisms and activation barriers of Li-
8
9 3050 ions have also been combined with classical MD studies of Li-ion diffusion to gain a more
10
11 3051 complete analysis of the dynamic properties in LiB materials.^{784,785} Quantum mechanical
12
13 3052 techniques, such as DFT, are also increasing being used to parameterise larger scale tech-
14
15 3053 niques, for example classical MD.^{143-145,164,776} The key consideration when designing MSM
16
17 3054 approaches is to reproduce the phenomena that dictate the natural behaviour and evolution
18
19 3055 of the material in given conditions. Thorough reviews, which focus more on the MSM aspect
20
21 3056 of LiB research, have recently been published by Franco et al.²³³ and Shi et al.¹⁰ kMC
22
23 3057 in particular has been highlighted as a natural technique to bridge length scales, naturally
24
25 3058 including different time scale dynamic events.¹⁰⁴ In this review, we have instead focused on
26
27 3059 the individual contributions of atomistic techniques, the understanding of which is key to
28
29 3060 building MSM approaches. However, the full complexity of composite materials, such as
30
31 3061 C/Si, may only be accessible by bridging atomistic techniques to MSM such as via phase
32
33 3062 field methods, volume-averaged approaches, or mesostructurally-resolved models.^{10,11,95,233}

35 3063 This review has focused almost entirely on lithium batteries, given that they currently
36
37 3064 comprise the most technologically advanced rechargeable battery systems that are commer-
38
39 3065 cialised at scale. However, atomistic modelling applied to LiBs also improves understanding
40
41 3066 of batteries that could be based on more environmentally-friendly or Earth-abundant ma-
42
43 3067 terials, such as sodium. Solid state models of intercalation, applied to LiBs, are directly
44
45 3068 transferable to other intercalation chemistries. The understanding of interfaces in batteries
46
47 3069 with other chemistries is even less developed than in LiBs. However, the modelling frame-
48
49 3070 works highlighted in this review, such as the linear-scaling DFT framework, could also be
50
51 3071 applied to improve understanding of these interfaces.

Acknowledgement

The authors thank the Faraday Institution (<https://faraday.ac.uk/>; EP/S003053/1), grant number FIRG003, for funding, and Dr. Maxim Zyskin for his discussions. We also thank Mr. Amir Kosha Amiri for his graphical design expertise in constructing and formatting the figures, as well as Dr. Felix Hanke and Dr. Victor Milman from BIOVIA for their comments and suggestions.

References

- (1) Zeng, X.; Li, M.; Abd El-Hady, D.; Alshitari, W.; Al-Bogami, A. S.; Lu, J.; Amine, K. Commercialization of lithium battery technologies for electric vehicles. *Advanced Energy Materials* **2019**, *9*, 1900161.
- (2) Goodenough, J. B.; Kim, Y. Challenges for rechargeable Li batteries. *Chemistry of Materials* **2010**, *22*, 587–603.
- (3) Kubiak, P.; Cen, Z.; López, C. M.; Belharouak, I. Calendar aging of a 250 kW/500 kWh Li-ion battery deployed for the grid storage application. *Journal of Power Sources* **2017**, *372*, 16–23.
- (4) Doyle, M.; Fuller, T. F.; Newman, J. Modeling of galvanostatic charge and discharge of the lithium/polymer/insertion cell. *Journal of the Electrochemical society* **1993**, *140*, 1526.
- (5) Fuller, T. F.; Doyle, M.; Newman, J. Simulation and optimization of the dual lithium ion insertion cell. *Journal of the Electrochemical Society* **1994**, *141*, 1.
- (6) Fuller, T. F.; Doyle, M.; Newman, J. S. Relaxation Phenomena in Lithium-Ion-Insertion Cells. *Journal of The Electrochemical Society* **1994**, *141*, 982.

- 1
2
3
4 3094 (7) Doyle, M.; Newman, J. The use of mathematical modeling in the design of
5 3095 lithium/polymer battery systems. *Electrochimica Acta* **1995**, *40*, 2191–2196.
6
7
8 3096 (8) Newman, J.; Thomas-Alyea, K. E. *Electrochemical Systems*; Wiley-Interscience, 2004;
9
10 3097 Vol. 3; pp 1–647.
11
12
13 3098 (9) Van der Ven, A.; Deng, Z.; Banerjee, S.; Ong, S. P. Rechargeable Alkali-Ion Battery
14
15 3099 Materials: Theory and Computation. *Chemical Reviews* **2020**, *120*, 6977–7019.
16
17
18 3100 (10) Shi, S.; Gao, J.; Liu, Y.; Zhao, Y.; Wu, Q.; Ju, W.; Ouyang, C.; Xiao, R. Multi-
19
20 3101 scale computation methods: Their applications in lithium-ion battery research and
21
22 3102 development. *Chinese Physics B* **2016**, *25*, 018212.
23
24
25 3103 (11) Franco, A. A. Multiscale modelling and numerical simulation of rechargeable lithium
26
27 3104 ion batteries: concepts, methods and challenges. *Rsc Advances* **2013**, *3*, 13027–13058.
28
29
30 3105 (12) Herbert, J. M. Dielectric continuum methods for quantum chemistry. *Wiley Interdis-*
31
32 3106 *ciplinary Reviews: Computational Molecular Science* **2021**, 1–73.
33
34
35 3107 (13) Scrosati, B. Lithium Rocking Chair Batteries: An Old Concept? *Journal of The*
36
37 3108 *Electrochemical Society* **1992**, *139*, 2776–2781.
38
39
40 3109 (14) Asenbauer, J.; Eisenmann, T.; Kuenzel, M.; Kazzazi, A.; Chen, Z.; Bresser, D. The
41
42 3110 success story of graphite as a lithium-ion anode material – fundamentals, remaining
43
44 3111 challenges, and recent developments including silicon (oxide) composites. *Sustainable*
45
46 3112 *Energy & Fuels* **2020**, 10.1039.D0SE00175A.
47
48
49 3113 (15) Zhang, H.; Yang, Y.; Ren, D.; Wang, L.; He, X. Graphite as anode materials: Fun-
50
51 3114 damental mechanism, recent progress and advances. *Energy Storage Materials* **2021**,
52
53 3115 *36*, 147–170.
54
55 3116 (16) Wang, A.; Kadam, S.; Li, H.; Shi, S.; Qi, Y. Review on modeling of the anode solid
56
57
58
59
60

- 1
2
3
4 3117 electrolyte interphase (SEI) for lithium-ion batteries. *npj Computational Materials*
5 3118 **2018**, *4*.
- 6
7
8 3119 (17) Shepherd, K.; Siddiqui, F. A driverless Tesla crashed and burned for four hours, police
9 said, killing two passengers in Texas. *Washington Post*
- 10 3120
11
12 3121 (18) Pfrang, A.; Kriston, A.; Ruiz, V.; Lebedeva, N.; di Persio, F. *Emerging Nanotechnolo-*
13 *gies in Rechargeable Energy Storage Systems*; Elsevier Inc., 2017; pp 253–290.
14 3122
- 15
16 3123 (19) Liu, L.; Xu, J.; Wang, S.; Wu, F.; Li, H.; Chen, L. Practical evaluation of energy
17 densities for sulfide solid-state batteries. *eTransportation* **2019**, *1*, 100010.
18 3124
- 19
20 3125 (20) Galiński, M.; Lewandowski, A.; Stepniak, I. Ionic liquids as electrolytes. *Electrochimica*
21 *acta* **2006**, *51*, 5567–5580.
22 3126
- 23
24 3127 (21) Wang, Y.; Meng, X.; Sun, J.; Liu, Y.; Hou, L. Recent Progress in “Water-in-Salt”
25 Electrolytes Toward Non-lithium Based Rechargeable Batteries. *Frontiers in Chem-*
26 *istry* **2020**, *8*.
27 3128
- 28
29 3129 (22) Logan, E.; Dahn, J. Electrolyte Design for Fast-Charging Li-Ion Batteries. *Trends in*
30 *Chemistry* **2020**, *2*, 354–366.
31 3130
- 32
33 3131 (23) Woods, L. Technological Advancements in Solid State Batteries for Electric Vehicles,
34 2020 Report - Toyota is the Pioneer of Solid-state Battery Research and Development
35 with a Lion’s Share of Patent Ownership. 2021.
36 3132
- 37
38 3133 (24) Zhu, Y.; He, X.; Mo, Y. Origin of Outstanding Stability in the Lithium Solid Elec-
39 trolyte Materials: Insights from Thermodynamic Analyses Based on First-Principles
40 Calculations. *ACS Applied Materials & Interfaces* **2015**, *7*, 23685–23693.
41 3134
- 42
43 3135 (25) Zhang, Q.; Cao, D.; Ma, Y.; Natan, A.; Aurora, P.; Zhu, H. Sulfide-Based Solid-State
44 Electrolytes: Synthesis, Stability, and Potential for All-Solid-State Batteries. *Advanced*
45 *Materials* **2019**, *31*, 1901131.
46 3136
47 3137
48 3138
49 3139
50 3140

- 1
2
3 3141 (26) Zhang, Z.; Shao, Y.; Lotsch, B.; Hu, Y. S.; Li, H.; Janek, J.; Nazar, L. F.; Nan, C. W.;
4
5 3142 Maier, J.; Armand, M.; Chen, L. New horizons for inorganic solid state ion conductors.
6
7 3143 *Energy & Environmental Science* **2018**, *11*, 1945–1976.
8
9
10 3144 (27) Gurung, A.; Pokharel, J.; Baniya, A.; Pathak, R.; Chen, K.; Lamsal, B. S.;
11
12 3145 Ghimire, N.; Zhang, W.-H.; Zhou, Y.; Qiao, Q. A review on strategies addressing
13
14 3146 interface incompatibilities in inorganic all-solid-state lithium batteries. *Sustainable*
15
16 3147 *Energy & Fuels* **2019**, *3*, 3279–3309.
17
18
19 3148 (28) Xiao, Y.; Wang, Y.; Bo, S. H.; Kim, J. C.; Miara, L. J.; Ceder, G. Understanding
20
21 3149 interface stability in solid-state batteries. *Nature Reviews Materials* **2020**, *5*, 105–126.
22
23
24 3150 (29) Xu, L.; Tang, S.; Cheng, Y.; Wang, K.; Liang, J.; Liu, C.; Cao, Y.-C.; Wei, F.; Mai, L.
25
26 3151 Interfaces in Solid-State Lithium Batteries. *Joule* **2018**, *2*, 1991–2015.
27
28
29 3152 (30) Tateyama, Y.; Gao, B.; Jalem, R.; Haruyama, J. Theoretical picture of positive elec-
30
31 3153 trode–solid electrolyte interface in all-solid-state battery from electrochemistry and
32
33 3154 semiconductor physics viewpoints. *Current Opinion in Electrochemistry* **2019**, *17*,
34
35 3155 149–157.
36
37
38 3156 (31) Ceder, G.; Ong, S. P.; Wang, Y. Predictive modeling and design rules for solid elec-
39
40 3157 trolytes. *MRS Bulletin* **2018**, *43*, 782–788.
41
42
43 3158 (32) Ma, Y. Computer simulation of cathode materials for lithium ion and lithium batteries:
44
45 3159 A review. *Energy & Environmental Materials* **2018**, *1*, 148–173.
46
47
48 3160 (33) Yan, L.-M.; Su, J.-M.; Sun, C.; Yue, B.-H. Review of the first principles calculations
49
50 3161 and the design of cathode materials for Li-ion batteries. *Advances in Manufacturing*
51
52 3162 **2014**, *2*, 358–368.
53
54 3163 (34) Wang, L.; Chen, B.; Ma, J.; Cui, G.; Chen, L. Reviving lithium cobalt oxide-based
55
56
57
58
59
60

- 1
2
3
4 3164 lithium secondary batteries-toward a higher energy density. *Chemical Society Reviews*
5 3165 **2018**, *47*, 6505–6602.
6
7
8 3166 (35) Maleki Kheimeh Sari, H.; Li, X. Controllable cathode–electrolyte interface of
9
10 3167 $\text{Li}[\text{Ni}_{0.8}\text{Co}_{0.1}\text{Mn}_{0.1}]\text{O}_2$ for lithium ion batteries: a review. *Advanced Energy Materi-*
11
12 3168 *als* **2019**, *9*, 1901597.
13
14
15 3169 (36) Parr, R. G.; Yang, W. *Density-Functional Theory of Atoms and Molecules (Interna-*
16
17 3170 *tional Series of Monographs on Chemistry)*; Oxford University Press, USA, 1994.
18
19
20 3171 (37) Hohenberg, P.; Kohn, W. Inhomogeneous Electron Gas. *Phys. Rev.* **1964**, *136*, B864–
21
22 3172 B871.
23
24 3173 (38) Kohn, W.; Sham, L. J. Self-Consistent Equations Including Exchange and Correlation
25
26 3174 Effects. *Phys. Rev.* **1965**, *140*, A1133–A1138.
27
28
29 3175 (39) Dirac, P. A. M. Note on Exchange Phenomena in the Thomas Atom. *Mathematical*
30
31 3176 *Proceedings of the Cambridge Philosophical Society* **1930**, *26*, 376–385.
32
33
34 3177 (40) Perdew, J. P.; Wang, Y. Accurate and simple analytic representation of the electron-
35
36 3178 gas correlation energy. *Phys. Rev. B* **1992**, *45*, 13244–13249.
37
38 3179 (41) Perdew, J. P.; Burke, K.; Ernzerhof, M. Generalized Gradient Approximation Made
39
40 3180 Simple. *Phys. Rev. Lett.* **1996**, *77*, 3865–3868.
41
42
43 3181 (42) Becke, A. D. Density-functional exchange-energy approximation with correct asymp-
44
45 3182 totic behavior. *Phys. Rev. A* **1988**, *38*, 3098–3100.
46
47
48 3183 (43) Lee, C.; Yang, W.; Parr, R. G. Development of the Colle-Salvetti correlation-energy
49
50 3184 formula into a functional of the electron density. *Phys. Rev. B* **1988**, *37*, 785–789.
51
52
53 3185 (44) Perdew, J. P.; Kurth, S.; Zupan, A.; Blaha, P. Accurate density functional with correct
54
55 3186 formal properties: A step beyond the generalized gradient approximation. *Physical*
56
57 3187 *review letters* **1999**, *82*, 2544.
58
59
60

- 1
2
3 3188 (45) Grimme, S. Semiempirical GGA-type density functional constructed with a long-range
4 dispersion correction. *Journal of Computational Chemistry* **2006**, *27*, 1787–1799.
5 3189
6
7
8 3190 (46) Grimme, S.; Antony, J.; Ehrlich, S.; Krieg, H. A consistent and accurate ab initio
9 parametrization of density functional dispersion correction (DFT-D) for the 94 ele-
10 3191 ments H-Pu. *The Journal of Chemical Physics* **2010**, *132*, 154104.
11 3192
12
13
14
15 3193 (47) Caldeweyher, E.; Bannwarth, C.; Grimme, S. Extension of the D3 dispersion coefficient
16 3194 model. *The Journal of Chemical Physics* **2017**, *147*, 034112.
17
18
19
20 3195 (48) Grimme, S.; Ehrlich, S.; Goerigk, L. Effect of the damping function in dispersion
21 3196 corrected density functional theory. *Journal of Computational Chemistry* **2011**, *32*,
22 1456–1465.
23 3197
24
25
26 3198 (49) Johnson, E. R.; Becke, A. D. A post-Hartree-Fock model of intermolecular interactions:
27 Inclusion of higher-order corrections. *The Journal of Chemical Physics* **2006**, *124*,
28 3199 174104.
29 3200
30
31
32
33 3201 (50) Becke, A. D. Density-functional thermochemistry. III. The role of exact exchange. *The*
34 3202 *Journal of Chemical Physics* **1993**, *98*, 5648–5652.
35
36
37
38 3203 (51) Cramer, C. J. *Essentials of computational chemistry: theories and models*; John Wiley
39 & Sons, 2013.
40 3204
41
42
43 3205 (52) Bredow, T.; Gerson, A. R. Effect of exchange and correlation on bulk properties of
44 MgO, NiO, and CoO. *Phys. Rev. B* **2000**, *61*, 5194–5201.
45 3206
46
47
48 3207 (53) Islam, M. M.; Bredow, T.; Gerson, A. Electronic properties of oxygen-deficient and
49 3208 aluminum-doped rutile TiO₂ from first principles. *Phys. Rev. B* **2007**, *76*, 045217.
50
51
52
53 3209 (54) Heyd, J.; Scuseria, G. E.; Ernzerhof, M. Hybrid functionals based on a screened
54 3210 Coulomb potential. *The Journal of Chemical Physics* **2003**, *118*, 8207–8215.
55
56
57
58
59
60

- 1
2
3 3211 (55) Dudarev, S. L.; Botton, G. A.; Savrasov, S. Y.; Humphreys, C. J.; Sutton, A. P.
4
5 3212 Electron-energy-loss spectra and the structural stability of nickel oxide: An LSDA+U
6
7 3213 study. *Phys. Rev. B* **1998**, *57*, 1505–1509.
8
9
10 3214 (56) Dudarev, S. L.; Liechtenstein, A. I.; Castell, M. R.; Briggs, G. A. D.; Sutton, A. P.
11
12 3215 Surface states on NiO (100) and the origin of the contrast reversal in atomically
13
14 3216 resolved scanning tunneling microscope images. *Phys. Rev. B* **1997**, *56*, 4900–4908.
15
16
17 3217 (57) Anisimov, V. I.; Aryasetiawan, F.; Liechtenstein, A. I. First-principles calculations
18
19 3218 of the electronic structure and spectra of strongly correlated systems: the LDA+U
20
21 3219 method. *Journal of Physics: Condensed Matter* **1997**, *9*, 767–808.
22
23
24 3220 (58) Goedecker, S. Linear scaling electronic structure methods. *Reviews of Modern Physics*
25
26 3221 **1999**, *71*, 1085–1123.
27
28
29 3222 (59) Prodan, E.; Kohn, W. Nearsightedness of electronic matter. *Proceedings of the Na-*
30
31 3223 *tional Academy of Sciences* **2005**, *102*, 11635–11638.
32
33
34 3224 (60) Galli, G.; Parrinello, M. Large scale electronic structure calculations. *Phys. Rev. Lett.*
35
36 3225 **1992**, *69*, 3547–3550.
37
38
39 3226 (61) Hernández, E.; Gillan, M. J. Self-consistent first-principles technique with linear scal-
40
41 3227 ing. *Phys. Rev. B* **1995**, *51*, 10157–10160.
42
43
44 3228 (62) Skylaris, C. K.; Haynes, P. D.; Mostofi, A. A.; Payne, M. C. Introducing ONETEP:
45
46 3229 Linear-scaling density functional simulations on parallel computers. *Journal of Chem-*
47
48 3230 *ical Physics* **2005**, *122*, 1–10.
49
50
51 3231 (63) Gillan, M. J.; Bowler, D. R.; Torralba, A. S.; Miyazaki, T. Order-N first-principles
52
53 3232 calculations with the conquest code. *Computer Physics Communications* **2007**, *177*,
54
55 3233 14–18.
56
57
58
59
60

- 1
2
3 3234 (64) Mohr, S.; Ratcliff, L. E.; Genovese, L.; Caliste, D.; Boulanger, P.; Goedecker, S.;
4
5 3235 Deutsch, T. Accurate and efficient linear scaling DFT calculations with universal ap-
6
7 3236 plicability. *Physical Chemistry Chemical Physics* **2015**, *17*, 31360–31370.
8
9
10 3237 (65) A., P. J. C. The ONETEP linear-scaling density functional theory program. *J. Chem.*
11
12 3238 *Phys.* **2020**, *152*, 174111.
13
14
15 3239 (66) Bhandari, A.; Anton, L.; Dziejczak, J.; Peng, C.; Kramer, D.; Skylaris, C.-K. Electronic
16
17 3240 structure calculations in electrolyte solutions: Methods for neutralization of extended
18
19 3241 charged interfaces. *The Journal of Chemical Physics* **2020**, *153*, 124101.
20
21
22 3242 (67) Jónsson, H.; Mills, G.; Jacobsen, K. W. Nudged elastic band method for finding
23
24 3243 minimum energy paths of transitions. *Classical and Quantum Dynamics in Condensed*
25
26 3244 *Phase Simulations* **1998**, 385–404.
27
28
29 3245 (68) Henkelman, G.; Uberuaga, B. P.; Jónsson, H. A climbing image nudged elastic band
30
31 3246 method for finding saddle points and minimum energy paths. *The Journal of chemical*
32
33 3247 *physics* **2000**, *113*, 9901–9904.
34
35
36 3248 (69) Henkelman, G.; Jónsson, H. Improved tangent estimate in the nudged elastic band
37
38 3249 method for finding minimum energy paths and saddle points. *The Journal of chemical*
39
40 3250 *physics* **2000**, *113*, 9978–9985.
41
42
43 3251 (70) Peng, C.; Mercer, M. P.; Skylaris, C.-K.; Kramer, D. Lithium intercalation edge effects
44
45 3252 and doping implications for graphite anodes. *Journal of Materials Chemistry A* **2020**,
46
47 3253 *8*, 7947–7955.
48
49 3254 (71) Mercer, M. P.; Peng, C.; Soares, C.; Hoster, H. E.; Kramer, D. Voltage hysteresis
50
51 3255 during lithiation/delithiation of graphite associated with meta-stable carbon stackings.
52
53 3256 *J. Mater. Chem. A* **2021**, *9*, 492–504.
54
55
56
57
58
59
60

- 1
2
3 3257 (72) Sanchez, J. M.; Ducastelle, F.; Gratias, D. Generalized cluster description of multi-
4
5 3258 component systems. *Physica A: Statistical Mechanics and its Applications* **1984**, *128*,
6
7 3259 334–350.
8
9
10 3260 (73) De Fontaine, D. Cluster approach to order-disorder transformations in alloys. *Solid*
11
12 3261 *state physics* **1994**, *47*, 33–176.
13
14
15 3262 (74) Blum, V.; Zunger, A. Mixed-basis cluster expansion for thermodynamics of bcc alloys.
16
17 3263 *Physical Review B* **2004**, *70*, 155108.
18
19
20 3264 (75) Gallavotti, G. *Statistical mechanics: A short treatise*; Springer Science & Business
21
22 3265 Media, 2013.
23
24 3266 (76) Persson, K.; Hinuma, Y.; Meng, Y. S.; Van der Ven, A.; Ceder, G. Thermodynamic
25
26 3267 and kinetic properties of the Li-graphite system from first-principles calculations. *Phys.*
27
28 3268 *Rev. B* **2010**, *82*, 125416.
29
30
31 3269 (77) Van der Ven, A.; Ceder, G.; Asta, M.; Tepesch, P. D. First-principles theory of ionic
32
33 3270 diffusion with nondilute carriers. *Phys. Rev. B* **2001**, *64*, 184307.
34
35
36 3271 (78) van de Walle, A. Multicomponent multisublattice alloys, nonconfigurational entropy
37
38 3272 and other additions to the Alloy Theoretic Automated Toolkit. *Calphad* **2009**, *33*,
39
40 3273 266–278.
41
42
43 3274 (79) van de Walle, A.; Asta, M. D.; Ceder, G. The Alloy Theoretic Automated Toolkit: A
44
45 3275 User Guide. *Calphad* **2002**, *26*, 539–553.
46
47
48 3276 (80) van de Walle, A.; Ceder, G. Automating first-principles phase diagram calculations.
49
50 3277 *Journal of Phase Equilibria* **2002**, *23*, 348–359.
51
52
53 3278 (81) Natarajan, A. R.; Thomas, J. C.; Puchala, B.; Van der Ven, A. Symmetry-adapted or-
54
55 3279 der parameters and free energies for solids undergoing order-disorder phase transitions.
56
57 3280 *Phys. Rev. B* **2017**, *96*, 134204.
58
59
60

- 1
2
3 3281 (82) Pickard, C. J.; Needs, R. J. Ab initio random structure searching. *Journal of Physics:*
4
5 3282 *Condensed Matter* **2011**, *23*, 053201.
6
7
8 3283 (83) Ångqvist, M.; Muñoz, W. A.; Rahm, J. M.; Fransson, E.; Durniak, C.; Rozyczko, P.;
9
10 3284 Rod, T. H.; Erhart, P. ICET – A Python Library for Constructing and Sampling Alloy
11
12 3285 Cluster Expansions. *Advanced Theory and Simulations* **2019**, *2*, 1900015.
13
14
15 3286 (84) Chang, J. H.; Kleiven, D.; Melander, M.; Akola, J.; Garcia-Lastra, J. M.; Vegge, T.
16
17 3287 CLEANSE: a versatile and user-friendly implementation of cluster expansion method.
18
19 3288 *Journal of Physics: Condensed Matter* **2019**, *31*, 325901.
20
21
22 3289 (85) Binder, K.; Landau, D. P. *A Guide to Monte-Carlo Simulations in Statistical Physics,*
23
24 3290 *Third Edition*; Cambridge University Press: Cambridge, UK, 2009.
25
26
27 3291 (86) Lee, T. D.; Yang, C. N. Statistical Theory of Equations of State and Phase Transitions.
28
29 3292 II. Lattice Gas and Ising Model. *Phys. Rev.* **1952**, *87*, 410–419.
30
31
32 3293 (87) Mercer, M. P.; Hoster, H. E. Ultrahigh vacuum and electrocatalysis - The powers of
33
34 3294 quantitative surface imaging. *Nano Energy* **2016**, *29*, 394–413.
35
36
37 3295 (88) Oviedo, O.; Reinaudi, L.; Garcia, S.; Leiva, E. *Underpotential Deposition: From Fun-*
38
39 3296 *damentals and Theory to Applications at the Nanoscale*; Monographs in Electrochem-
40
41 3297 istry; Springer International Publishing, 2015.
42
43
44 3298 (89) Mercer, M. P.; Finnigan, S.; Kramer, D.; Richards, D.; Hoster, H. E. The influence
45
46 3299 of point defects on the entropy profiles of Lithium Ion Battery cathodes: a lattice-gas
47
48 3300 Monte Carlo study. *Electrochimica Acta* **2017**, *241*, 141–152.
49
50
51 3301 (90) Kim, S.-W.; Pyun, S.-I. Thermodynamic and kinetic approaches to lithium intercala-
52
53 3302 tion into a $\text{Li}_{1-\delta}\text{Mn}_2\text{O}_4$ electrode using Monte Carlo simulation. *Electrochimica Acta*
54
55 3303 **2001**, *46*, 987–997.
56
57
58
59
60

- 1
2
3 3304 (91) Mercer, M. P.; Otero, M.; Ferrer-Huerta, M.; Sigal, A.; Barraco, D. E.; Hoster, H. E.;
4
5 3305 Leiva, E. P. Transitions of lithium occupation in graphite: A physically informed
6
7 3306 model in the dilute lithium occupation limit supported by electrochemical and ther-
8
9 3307 modynamic measurements. *Electrochimica Acta* **2019**, *324*, 134774.
- 11
12 3308 (92) Leiva, E. P. M.; Perassi, E.; Barraco, D. Shedding Light on the Entropy Change Found
13
14 3309 for the Transition Stage II \rightarrow Stage I of Li-Ion Storage in Graphite. *Journal of The*
15
16 3310 *Electrochemical Society* **2017**, *164*, A6154–A6157.
- 18
19 3311 (93) Schlueter, S.; Genieser, R.; Richards, D.; Hoster, H. E.; Mercer, M. P. Quantifying
20
21 3312 structure dependent responses in Li-ion cells with excess Li spinel cathodes: matching
22
23 3313 voltage and entropy profiles through mean field models. *Physical Chemistry Chemical*
24
25 3314 *Physics* **2018**, *20*, 21417–21429.
- 27
28 3315 (94) Haftbaradaran, H.; Song, J.; Curtin, W.; Gao, H. Continuum and atomistic models of
29
30 3316 strongly coupled diffusion, stress, and solute concentration. *Journal of Power Sources*
31
32 3317 **2011**, *196*, 361–370.
- 34
35 3318 (95) Bazant, M. Z. Thermodynamic stability of driven open systems and control of phase
36
37 3319 separation by electro-autocatalysis. *Faraday Discussions* **2017**, *199*, 423–463.
- 39
40 3320 (96) Guo, Y.; Smith, R. B.; Yu, Z.; Efetov, D. K.; Wang, J.; Kim, P.; Bazant, M. Z.;
41
42 3321 Brus, L. E. Li Intercalation into Graphite: Direct Optical Imaging and Cahn–Hilliard
43
44 3322 Reaction Dynamics. *The Journal of Physical Chemistry Letters* **2016**, *7*, 2151–2156.
- 46
47 3323 (97) Bai, P.; Cogswell, D. A.; Bazant, M. Z. Suppression of Phase Separation in LiFePO₄
48
49 3324 Nanoparticles During Battery Discharge. *Nano Letters* **2011**, *11*, 4890–4896.
- 51
52 3325 (98) Metropolis, N.; Rosenbluth, A. W.; Rosenbluth, M. N.; Teller, A. H.; Teller, E. Equa-
53
54 3326 tion of State Calculations by Fast Computing Machines. *The Journal of Chemical*
55
56 3327 *Physics* **1953**, *21*, 1087–1092.

- 1
2
3 3328 (99) Darling, R.; Newman, J. Dynamic Monte Carlo Simulations of Diffusion in $\text{Li}_y\text{Mn}_2\text{O}_4$,
4
5 3329 *Journal of The Electrochemical Society* **1999**, *146*, 3765–3772.
6
7
8 3330 (100) Thomas, K. E.; Newman, J. Heats of mixing and of entropy in porous insertion elec-
9
10 3331 trodes. *Journal of Power Sources* **2003**, *119-121*, 844 – 849.
11
12
13 3332 (101) Zhang, X.-F.; Zhao, Y.; Patel, Y.; Zhang, T.; Liu, W.-M.; Chen, M.; Offer, G. J.;
14
15 3333 Yan, Y. Potentiometric measurement of entropy change for lithium batteries. *Phys.*
16
17 3334 *Chem. Chem. Phys.* **2017**, *19*, 9833–9842.
18
19
20 3335 (102) Gavilán-Arriazu, E.; Pinto, O.; López de Mishima, B.; Barraco, D.; Oviedo, O.;
21
22 3336 Leiva, E. Kinetic Monte Carlo applied to the electrochemical study of the Li-ion
23
24 3337 graphite system. *Electrochimica Acta* **2020**, *331*, 135439.
25
26
27 3338 (103) Gavilán-Arriazu, E. M.; Mercer, M. P.; Pinto, O. A.; Oviedo, O. A.; Barraco, D. E.;
28
29 3339 Hoster, H. E.; Leiva, E. P. M. Effect of Temperature on The Kinetics of Electrochemical
30
31 3340 Insertion of Li-Ions into a Graphite Electrode Studied by Kinetic Monte Carlo. *Journal*
32
33 3341 *of The Electrochemical Society* **2020**, *167*, 013533.
34
35
36 3342 (104) Gavilán-Arriazu, E. M.; Mercer, M. P.; Barraco, D. E.; Hoster, H. E.; Leiva, E. P. M.
37
38 3343 Kinetic Monte Carlo simulations applied to Li-ion and post Li-ion batteries: a key
39
40 3344 link in the multi-scale chain. *Progress in Energy* **2021**, *3*, 042001.
41
42
43 3345 (105) Car, R.; Parrinello, M. Unified Approach for Molecular Dynamics and Density-
44
45 3346 Functional Theory. *Physical Review Letters* **1985**, *55*, 2471–2474.
46
47
48 3347 (106) Tuckerman, M. E.; Parrinello, M. Integrating the Car–Parrinello equations. I. Basic
49
50 3348 integration techniques. *The Journal of Chemical Physics* **1994**, *101*, 1302–1315.
51
52
53 3349 (107) Grossman, J. C.; Schwegler, E.; Draeger, E. W.; Gygi, F.; Galli, G. Towards an
54
55 3350 assessment of the accuracy of density functional theory for first principles simulations
56
57 3351 of water. *The Journal of Chemical Physics* **2004**, *120*, 300–311.
58
59
60

- 1
2
3 3352 (108) Harding, J. H. Computer simulation of defects in ionic solids. *Reports on Progress in*
4
5 3353 *Physics* **1990**, *53*, 1403–1466.
6
7
8 3354 (109) Buckingham, R. A. The classical equation of state of gaseous helium, neon and argon.
9
10 3355 *Proceedings of the Royal Society of London. Series A. Mathematical and Physical*
11
12 3356 *Sciences* **1938**, *168*, 264–283.
13
14
15 3357 (110) Born, M.; Mayer, J. On the Lattice Theory of Ionic Crystals. *Zeitschrift für Physik*
16
17 3358 **1932**, *75*, 1–18.
18
19
20 3359 (111) Mayer, J. E. Dispersion and Polarizability and the Van der Waals Potential in the
21
22 3360 Alkali Halides. *The Journal of Chemical Physics* **1932**, *1*, 270.
23
24
25 3361 (112) Todorov, I. T.; Smith, W.; Trachenko, K.; Dove, M. T. DL_POLY_3: new dimen-
26
27 3362 sions in molecular dynamics simulations via massive parallelism. *Journal of Materials*
28
29 3363 *Chemistry* **2006**, *16*, 1911–1918.
30
31 3364 (113) Plimpton, S. Fast Parallel Algorithms for Short-Range Molecular Dynamics. *Journal*
32
33 3365 *of Computational Physics* **1995**, *117*, 1 – 19.
34
35
36 3366 (114) Gale, J. D. GULP: A computer program for the symmetry-adapted simulation of
37
38 3367 solids. *Journal of the Chemical Society, Faraday Transactions* **1997**, *93*, 629–637.
39
40
41 3368 (115) Gauthier, M.; Carney, T. J.; Grimaud, A.; Giordano, L.; Pour, N.; Chang, H.-H.;
42
43 3369 Fenning, D. P.; Lux, S. F.; Paschos, O.; Bauer, C.; Maglia, F.; Lupart, S.; Lamp, P.;
44
45 3370 Shao-Horn, Y. The Electrode-Electrolyte Interface in Li-ion Batteries: Current Under-
46
47 3371 standing and New Insights. *The Journal of Physical Chemistry Letters* **2015**, 4653—
48
49 3372 -4672.
50
51
52 3373 (116) Yu, X.; Manthiram, A. Electrode–electrolyte interfaces in lithium-based batteries.
53
54 3374 *Energy & Environmental Science* **2018**, *11*, 527–543.
55
56
57
58
59
60

- 1
2
3 3375 (117) Jinnouchi, R.; Kodama, K.; Morimoto, Y. Electronic structure calculations on elec-
4 trolyte–electrode interfaces: Successes and limitations. *Current Opinion in Electro-*
5 3376 *chemistry* **2018**, *8*, 103–109.
6
7 3377
8
9
10 3378 (118) Hansen, M. H.; Rossmeisl, J. PH in Grand Canonical Statistics of an Electrochemical
11 Interface. *Journal of Physical Chemistry C* **2016**, *120*, 29135–29143.
12 3379
13
14
15 3380 (119) Sakong, S.; Naderian, M.; Mathew, K.; Hennig, R. G.; Groß, A. Density functional
16 theory study of the electrochemical interface between a Pt electrode and an aqueous
17 3381 electrolyte using an implicit solvent method. *Journal of Chemical Physics* **2015**, *142*.
18 3382
19
20
21 3383 (120) Skyner, R. E.; McDonagh, J. L.; Groom, C. R.; Van Mourik, T.; Mitchell, J. B. A
22 review of methods for the calculation of solution free energies and the modelling of
23 3384 systems in solution. *Physical Chemistry Chemical Physics* **2015**, *17*, 6174–6191.
24
25 3385
26
27
28 3386 (121) Kang, J.; Wei, S. H.; Zhu, K.; Kim, Y. H. First-principles theory of electrochemical
29 capacitance of nanostructured materials: Dipole-assisted subsurface intercalation of
30 3387 lithium in pseudocapacitive TiO₂ anatase nanosheets. *Journal of Physical Chemistry*
31 *C* **2011**, *115*, 4909–4915.
32 3388
33 3389
34
35
36
37 3390 (122) Dufils, T.; Jeanmairet, G.; Rotenberg, B.; Sprik, M.; Salanne, M. Simulating Electro-
38 chemical Systems by Combining the Finite Field Method with a Constant Potential
39 3391 Electrode. *Physical Review Letters* **2019**, *123*, 195501.
40
41 3392
42
43
44 3393 (123) Jorn, R.; Kumar, R.; Abraham, D. P.; Voth, G. A. Atomistic modeling of the electrode-
45 electrolyte interface in Li-ion energy storage systems: Electrolyte structuring. *Journal*
46 3394 *of Physical Chemistry C* **2013**, *117*, 3747–3761.
47
48 3395
49
50
51 3396 (124) Zhang, C.; Sayer, T.; Hutter, J.; Sprik, M. Modelling electrochemical systems with
52 finite field molecular dynamics. *Journal of Physics: Energy* **2020**, 0–21.
53 3397
54
55
56
57
58
59
60

- 1
2
3 3398 (125) Cramer, C. J.; Truhlar, D. G. Implicit Solvation Models: Equilibria, Structure, Spec-
4
5 3399 tra, and Dynamics. *Chemical Reviews* **1999**, *99*, 2161–2200.
6
7
8 3400 (126) Tomasi, J.; Mennucci, B.; Cammi, R. Quantum mechanical continuum solvation mod-
9
10 3401 els. *Chemical Reviews* **2005**, *105*, 2999–3093.
11
12
13 3402 (127) Grochowski, P.; Trylska, J. Continuum molecular electrostatics, salt effects, and coun-
14
15 3403 terion binding – A review of the Poisson-Boltzmann theory and its modifications.
16
17 3404 *Biopolymers* **2008**, *89*, 93–113.
18
19
20 3405 (128) Jinnouchi, R.; Anderson, A. B. Electronic structure calculations of liquid-solid in-
21
22 3406 terfaces: Combination of density functional theory and modified Poisson-Boltzmann
23
24 3407 theory. *Phys. Rev. B* **2008**, *77*, 245417.
25
26
27 3408 (129) Gunceler, D.; Letchworth-Weaver, K.; Sundararaman, R.; Schwarz, K. A.; Arias, T. A.
28
29 3409 The importance of nonlinear fluid response in joint density-functional theory studies
30
31 3410 of battery systems. *Modelling and Simulation in Materials Science and Engineering*
32
33 3411 **2013**, *21*.
34
35
36 3412 (130) Ringe, S.; Oberhofer, H.; Hille, C.; Matera, S.; Reuter, K. Function-Space-Based
37
38 3413 Solution Scheme for the Size-Modified Poisson–Boltzmann Equation in Full-Potential
39
40 3414 DFT. *Journal of Chemical Theory and Computation* **2016**, *12*, 4052–4066.
41
42
43 3415 (131) Nattino, F.; Truscott, M.; Marzari, N.; Andreussi, O. Continuum models of the elec-
44
45 3416 trochemical diffuse layer in electronic-structure calculations. *The Journal of Chemical*
46
47 3417 *Physics* **2019**, *150*, 41722.
48
49
50 3418 (132) Melander, M. M.; Kuisma, M. J.; Christensen, T. E. K.; Honkala, K. Grand-canonical
51
52 3419 approach to density functional theory of electrocatalytic systems: Thermodynamics
53
54 3420 of solid-liquid interfaces at constant ion and electrode potentials. *Journal of Chemical*
55
56 3421 *Physics* **2019**, *150*, 041706.
57
58
59
60

- 1
2
3 3422 (133) Stein, C. J.; Herbert, J. M.; Head-Gordon, M. The Poisson-Boltzmann model for
4
5 3423 implicit solvation of electrolyte solutions: Quantum chemical implementation and
6
7 3424 assessment via Sechenov coefficients. *Journal of Chemical Physics* **2019**, *151*, 224111.
8
9
10 3425 (134) Womack, J. C.; Anton, L.; Dziedzic, J.; Hasnip, P. J.; Probert, M. I.; Skylaris, C. K.
11
12 3426 DL-MG: A Parallel Multigrid Poisson and Poisson-Boltzmann Solver for Electronic
13
14 3427 Structure Calculations in Vacuum and Solution. *Journal of Chemical Theory and*
15
16 3428 *Computation* **2018**, *14*, 1412–1432.
17
18
19 3429 (135) Dziedzic, J.; Bhandari, A.; Anton, L.; Peng, C.; Womack, J. C.; Famili, M.;
20
21 3430 Kramer, D.; Skylaris, C.-K. A Practical Approach to Large Scale Electronic Struc-
22
23 3431 ture Calculations in Electrolyte Solutions via Continuum-Embedded Linear-Scaling
24
25 3432 DFT. *The Journal of Physical Chemistry C* **2020**, *124*, 7860–7872.
26
27
28 3433 (136) Andreussi, O.; Dabo, I.; Marzari, N. Revised self-consistent continuum solvation in
29
30 3434 electronic-structure calculations. *Journal of Chemical Physics* **2012**, *136*, 064102.
31
32
33 3435 (137) Fisticaro, G.; Genovese, L.; Andreussi, O.; Mandal, S.; Nair, N. N.; Marzari, N.;
34
35 3436 Goedecker, S. Soft-Sphere Continuum Solvation in Electronic-Structure Calculations.
36
37 3437 *Journal of Chemical Theory and Computation* **2017**, *13*, 3829–3845.
38
39 3438 (138) Sundararaman, R.; Letchworth-Weaver, K.; Schwarz, K. A. Improving accuracy of
40
41 3439 electrochemical capacitance and solvation energetics in first-principles calculations.
42
43 3440 *Journal of Chemical Physics* **2018**, *148*, 144105.
44
45
46 3441 (139) Dziedzic, J.; Helal, H. H.; Skylaris, C. K.; Mostofi, A. A.; Payne, M. C. Minimal
47
48 3442 parameter implicit solvent model for ab initio electronic-structure calculations. *Epl*
49
50 3443 **2011**, *95*, 1–6.
51
52
53 3444 (140) Jones, J. E. On the determination of molecular fields. —II. From the equation of state
54
55 3445 of a gas. *Proceedings of the Royal Society of London. Series A, Containing Papers of*
56
57 3446 *a Mathematical and Physical Character* **1924**, *106*, 463–477.
58
59
60

- 1
2
3 3447 (141) Gale, J. D. GULP fitting. 1996; [https://gulp.curtin.edu.au/local/docs/gulp/](https://gulp.curtin.edu.au/local/docs/gulp/gulp_31_manual/gulpnode38.html)
4 3448 [gulp_31_manual/gulpnode38.html](https://gulp.curtin.edu.au/local/docs/gulp/gulp_31_manual/gulpnode38.html).
- 5
6
7
8 3449 (142) Gale, J. D. Empirical potential derivation for ionic materials. *Philosophical Magazine*
9 3450 *B* **1996**, *73*, 3–19.
- 10
11
12
13 3451 (143) Stukowski, A.; Fransson, E.; Mock, M.; Erhart, P. Atomicrex—a general purpose
14 3452 tool for the construction of atomic interaction models. *Modelling and Simulation in*
15 3453 *Materials Science and Engineering* **2017**, *25*, 055003.
- 16
17
18
19
20 3454 (144) Ostrouchov, C. dftfit. <https://chrisostrouchov.com/dftfit>.
- 21
22
23 3455 (145) Wen, M.; Li, J.; Brommer, P.; Elliott, R. S.; Sethna, J. P.; Tadmor, E. B. A KIM-
24 3456 compliant *potfit* for fitting sloppy interatomic potentials: application to the EDIP
25 3457 model for silicon. *Modelling and Simulation in Materials Science and Engineering*
26 3458 **2017**, *25*, 014001.
- 27
28
29
30
31 3459 (146) Wen, M.; Li, J.; Brommer, P.; Elliott, R. S.; Sethna, J. P.; Tadmor, E. B. potfit.
32 3460 <https://www.potfit.net/wiki/doku.php>.
- 33
34
35
36 3461 (147) Lewis, G. V.; Catlow, C. R. A. Potential models for ionic oxides. *Journal of Physics*
37 3462 *C: Solid State Physics* **1985**, *18*, 1149–1161.
- 38
39
40
41 3463 (148) Ledwaba, R. S.; Sayle, D. C.; Ngoepe, P. E. Atomistic Simulation and Characterization
42 3464 of Spinel $\text{Li}_{1+x}\text{Mn}_2\text{O}_4$ ($0 \leq x \leq 1$) Nanoparticles. *ACS Applied Energy Materials*
43 3465 **2020**, *3*, 1429–1438.
- 44
45
46
47
48 3466 (149) Sayle, T. X. T.; Catlow, C. R. A.; Maphanga, R. R.; Ngoepe, P. E.; Sayle, D. C. Gen-
49 3467 erating MnO_2 Nanoparticles Using Simulated Amorphization and Recrystallization.
50 3468 *Journal of the American Chemical Society* **2005**, *127*, 12828–12837.
- 51
52
53
54 3469 (150) Dawson, J. A.; Tanaka, I. Oxygen Vacancy Formation and Reduction Properties of
55
56
57
58
59
60

- 1
2
3
4 3470 β -MnO₂ Grain Boundaries and the Potential for High Electrochemical Performance.
5 3471 *ACS Applied Materials & Interfaces* **2014**, *6*, 17776–17784.
6
7
8 3472 (151) Hart, F. X.; Bates, J. B. Lattice model calculation of the strain energy density and
9
10 3473 other properties of crystalline LiCoO₂. *Journal of Applied Physics* **1998**, *83*, 7560–
11
12 3474 7566.
13
14
15 3475 (152) A. J. Fisher, C.; Saiful Islam, M.; Moriwake, H. Atomic Level Investigations of Lithium
16
17 3476 Ion Battery Cathode Materials. *Journal of the Physical Society of Japan* **2010**, *79*,
18
19 3477 59–64.
20
21
22 3478 (153) Ammundsen, B.; Burns, G. R.; Islam, M. S.; Kanoh, H.; Rozière, J. Lattice Dynamics
23
24 3479 and Vibrational Spectra of Lithium Manganese Oxides: A Computer Simulation and
25
26 3480 Spectroscopic Study. *The Journal of Physical Chemistry B* **1999**, *103*, 5175–5180.
27
28
29 3481 (154) Kerisit, S.; Chaka, A. M.; Droubay, T. C.; Ilton, E. S. Shell Model for Atomistic
30
31 3482 Simulation of Lithium Diffusion in Mixed Mn/Ti Oxides. *The Journal of Physical*
32
33 3483 *Chemistry C* **2014**, *118*, 24231–24239.
34
35
36 3484 (155) He, J.; Zhang, L.; Liu, L. Thermal transport in monocrystalline and polycrystalline
37
38 3485 lithium cobalt oxide. *Physical Chemistry Chemical Physics* **2019**, *21*, 12192–12200.
39
40
41 3486 (156) Lee, S.; Park, S. S. Atomistic simulation study of mixed-metal oxide
42
43 3487 (LiNi_{1/3}Co_{1/3}Mn_{1/3}O₂) cathode material for lithium ion battery. *The Journal of Phys-*
44
45 3488 *ical Chemistry C* **2012**, *116*, 6484–6489.
46
47
48 3489 (157) Lindan, P. J. D.; Gillan, M. J. Shell-model molecular dynamics simulation of superionic
49
50 3490 conduction in CaF₂. *Journal of Physics: Condensed Matter* **1993**, *5*, 1019–1030.
51
52
53 3491 (158) Mitchell, P. J.; Fincham, D. Shell model simulations by adiabatic dynamics. *Journal*
54
55 3492 *of Physics: Condensed Matter* **1993**, *5*, 1031–1038.
56
57
58
59
60

- 1
2
3 3493 (159) Wang, B.; Cormack, A. N. Molecular dynamics simulations of Mg-doped beta"-alumina
4 with potential models fitted for accurate structural response to thermal vibrations.
5 3494
6
7 3495 *Solid State Ionics* **2014**, *263*, 9–14.
8
9
10 3496 (160) Escribano, B.; Lozano, A.; Radivojević, T.; Fernández-Pendás, M.; Carrasco, J.;
11 3497 Akhmatskaya, E. Enhancing sampling in atomistic simulations of solid-state mate-
12 3498 rials for batteries: a focus on olivine NaFePO₄. *Theoretical Chemistry Accounts* **2017**,
13 3499 *136*, 43.
14
15
16
17
18 3500 (161) Lee, S.; Park, S. S. Lithium transition metal fluorophosphates (Li₂CoPO₄F and
19 3501 Li₂NiPO₄F) as cathode materials for lithium ion battery from atomistic simulation.
20
21 3502 *Journal of Solid State Chemistry* **2013**, *204*, 329 – 334.
22
23
24
25 3503 (162) Dai, J.; Chen, Q.; Glossmann, T.; Lai, W. Comparison of interatomic potential models
26 3504 on the molecular dynamics simulation of fast-ion conductors: A case study of a Li
27 garnet oxide Li₇La₃Zr₂O₁₂. *Computational Materials Science* **2019**, *162*, 333–339.
28
29 3505
30
31 3506 (163) Pedone, A.; Malavasi, G.; Menziani, M. C.; Cormack, A. N.; Segre, U. A New Self-
32 Consistent Empirical Interatomic Potential Model for Oxides, Silicates, and Silica-
33 3507 Based Glasses. *The Journal of Physical Chemistry B* **2006**, *110*, 11780–11795.
34
35 3508
36
37
38 3509 (164) Morgan, Lucy M. and Clarke, Matthew and Islam, M. Saiful and Morgan, Benjamin
39 3510 J., PopOff: POtential Parameter Optimisation for Force-Fields. 2021; [https://doi.](https://doi.org/10.5281/zenodo.4773795)
40 3511 [org/10.5281/zenodo.4773795](https://doi.org/10.5281/zenodo.4773795).
41
42
43
44
45 3512 (165) Fisher, C. A. J.; Hart Prieto, V. M.; Islam, M. S. Lithium Battery Materials LiMPO₄
46 3513 (M = Mn, Fe, Co, and Ni): Insights into Defect Association, Transport Mechanisms,
47 and Doping Behavior. *Chemistry of Materials* **2008**, *20*, 5907–5915.
48
49 3514
50
51 3515 (166) Urban, A.; Seo, D.-H.; Ceder, G. Computational understanding of Li-ion batteries.
52
53 3516 *npj Computational Materials* **2016**, *2*, 16002.
54
55
56
57
58
59
60

- 1
2
3 3517 (167) Ceder, G.; Van der Ven, A. Phase diagrams of lithium transition metal oxides: inves-
4
5 3518 tigation from first principles. *Electrochimica Acta* **1999**, *45*, 131 – 150.
6
7
8 3519 (168) Van Der Ven, A.; Marianetti, C.; Morgan, D.; Ceder, G. Phase transformations and
9
10 3520 volume changes in spinel $\text{Li}_x\text{Mn}_2\text{O}_4$. *Solid State Ionics* **2000**, *135*, 21–32.
11
12
13 3521 (169) Reynier, Y.; Graetz, J.; Swan-Wood, T.; Rez, P.; Yazami, R.; Fultz, B. Entropy of Li
14
15 3522 intercalation in Li_xCoO_2 . *Phys. Rev. B* **2004**, *70*, 174304.
16
17
18 3523 (170) Yazami, R.; Reynier, Y. Thermodynamics and crystal structure anomalies in lithium-
19
20 3524 intercalated graphite. *Journal of Power Sources* **2006**, *153*, 312–318.
21
22
23 3525 (171) Atkins, P. W.; De Paula, J. *Atkins' Physical chemistry, 9th Ed.*; 2014.
24
25
26 3526 (172) Heitjans, P.; Kärger, J. *Diffusion in condensed matter: methods, materials, models*;
27
28 3527 Springer Science & Business Media, 2006.
29
30 3528 (173) Heumann, T. *Diffusion in Metallen: Grundlagen, Theorie, Vorgänge in Reinmetallen*
31
32 3529 *und Legierungen*; Springer-Verlag, 2013; Vol. 10.
33
34
35 3530 (174) Crank, J. *The mathematics of diffusion*; Oxford university press, 1979.
36
37
38 3531 (175) Einstein, A. The presumed movement of suspended particles in static fluids. *Ann.*
39
40 3532 *Phys. Lpz* **1905**, *17*, 549–560.
41
42
43 3533 (176) Von Smoluchowski, M. Zur kinetischen theorie der brownschen molekularbewegung
44
45 3534 und der suspensionen. *Annalen der physik* **1906**, *326*, 756–780.
46
47
48 3535 (177) Ladd, A. J.; Moran, B.; Hoover, W. G. Lattice thermal conductivity: A comparison of
49
50 3536 molecular dynamics and anharmonic lattice dynamics. *Physical Review B* **1986**, *34*,
51
52 3537 5058.
53
54
55
56
57
58
59
60

- 1
2
3 3538 (178) Turney, J.; Landry, E.; McGaughey, A.; Amon, C. Predicting phonon properties and
4
5 3539 thermal conductivity from anharmonic lattice dynamics calculations and molecular
6
7 3540 dynamics simulations. *Physical Review B* **2009**, *79*, 064301.
8
9
10 3541 (179) Seko, A.; Togo, A.; Hayashi, H.; Tsuda, K.; Chaput, L.; Tanaka, I. Prediction of low-
11
12 3542 thermal-conductivity compounds with first-principles anharmonic lattice-dynamics
13
14 3543 calculations and Bayesian optimization. *Physical review letters* **2015**, *115*, 205901.
15
16
17 3544 (180) Togo, A.; Chaput, L.; Tanaka, I. Distributions of Phonon Lifetimes in Brillouin Zones.
18
19 3545 *Phys. Rev. B* **2015**, *91*, 094306.
20
21
22 3546 (181) Yang, H.; Yang, J.-y.; Savory, C. N.; Skelton, J. M.; Morgan, B. J.; Scanlon, D. O.;
23
24 3547 Walsh, A. Highly Anisotropic Thermal Transport in LiCoO₂. *The journal of physical*
25
26 3548 *chemistry letters* **2019**, *10*, 5552–5556.
27
28
29 3549 (182) Yang, H.; Savory, C. N.; Morgan, B. J.; Scanlon, D. O.; Skelton, J. M.; Walsh, A.
30
31 3550 Chemical Trends in the Lattice Thermal Conductivity of Li (Ni, Mn, Co) O₂ (NMC)
32
33 3551 Battery Cathodes. *Chemistry of Materials* **2020**, *32*, 7542–7550.
34
35
36 3552 (183) Tadano, T.; Gohda, Y.; Tsuneyuki, S. Anharmonic force constants extracted from
37
38 3553 first-principles molecular dynamics: applications to heat transfer simulations. *Journal*
39
40 3554 *of Physics: Condensed Matter* **2014**, *26*, 225402.
41
42
43 3555 (184) Li, W.; Carrete, J.; Katcho, N. A.; Mingo, N. ShengBTE: a solver of the Boltzmann
44
45 3556 transport equation for phonons. *Comp. Phys. Commun.* **2014**, *185*, 1747–1758.
46
47
48 3557 (185) Vetter, J.; Novák, P.; Wagner, M.; Veit, C.; Möller, K.-C.; Besenhard, J.; Winter, M.;
49
50 3558 Wohlfahrt-Mehrens, M.; Vogler, C.; Hammouche, A. Ageing mechanisms in lithium-
51
52 3559 ion batteries. *Journal of Power Sources* **2005**, *147*, 269 – 281.
53
54 3560 (186) Agubra, V.; Fergus, J. Lithium Ion Battery Anode Aging Mechanisms. *Materials*
55
56 3561 **2013**, *6*, 1310–1325.
57
58
59
60

- 1
2
3
4 3562 (187) Yang, X.-G.; Leng, Y.; Zhang, G.; Ge, S.; Wang, C.-Y. Modeling of lithium plating
5 3563 induced aging of lithium-ion batteries: Transition from linear to nonlinear aging.
6
7 3564 *Journal of Power Sources* **2017**, *360*, 28 – 40.
8
9
10 3565 (188) Guerard, D.; Herold, A. Intercalation of lithium into graphite and other carbons.
11
12 3566 *Carbon* **1975**, *13*, 337 – 345.
13
14
15 3567 (189) Woo, K. C.; Kamitakahara, W. A.; DiVincenzo, D. P.; Robinson, D. S.; Mertwoy, H.;
16 3568 Milliken, J. W.; Fischer, J. E. Effect of In-Plane Density on the Structural and Elastic
17
18 3569 Properties of Graphite Intercalation Compounds. *Phys. Rev. Lett.* **1983**, *50*, 182–185.
20
21
22 3570 (190) Basu, S.; Zeller, C.; Flanders, P.; Fuerst, C.; Johnson, W.; Fischer, J. Synthesis and
23
24 3571 properties of lithium-graphite intercalation compounds. *Materials Science and Engi-*
25
26 3572 *neering* **1979**, *38*, 275 – 283.
27
28
29 3573 (191) Besenhard, J. The electrochemical preparation and properties of ionic alkali metal-
30
31 3574 and NR₄-graphite intercalation compounds in organic electrolytes. *Carbon* **1976**, *14*,
32
33 3575 111–115.
34
35 3576 (192) Yazami, R.; Touzain, P. A reversible graphite-lithium negative electrode for electro-
36
37 3577 chemical generators. *Journal of Power Sources* **1983**, *9*, 365 – 371.
38
39
40 3578 (193) Fong, R.; von Sacken, U.; Dahn, J. R. Studies of Lithium Intercalation into Car-
41
42 3579 bons Using Nonaqueous Electrochemical Cells. *Journal of The Electrochemical Society*
43
44 3580 **1990**, *137*, 2009–2013.
45
46
47 3581 (194) Tarascon, J.; Guyomard, D. The Li_{1+x}Mn₂O₄/C rocking-chair system: a review. *Elec-*
48
49 3582 *trochimica Acta* **1993**, *38*, 1221 – 1231.
50
51
52 3583 (195) Dahn, J. R. Phase diagram of Li_xC₆. *Physical Review B* **1991**, *44*, 9170–9177.
53
54
55 3584 (196) Hazrati, E.; de Wijs, G. A.; Brocks, G. Li intercalation in graphite: A van der Waals
56
57 3585 density-functional study. *Physical Review B* **2014**, *90*, 155448.
58
59
60

- 1
2
3
4 3586 (197) Konar, S.; Häusserman, U.; Svensson, G. Intercalation compounds from LiH and
5
6 3587 graphite: Relative stability of metastable stages and thermodynamic stability of dilute
7
8 3588 stage Id. *Chemistry of Materials* **2015**, *27*, 2566–2575.
- 9
10 3589 (198) Shi, H.; Barker, J.; Saïdi, M. Y.; Koksang, R. Structure and Lithium Intercalation
11
12 3590 Properties of Synthetic and Natural Graphite. *Journal of The Electrochemical Society*
13
14 3591 **1996**, *143*, 3466–3472.
- 15
16
17 3592 (199) Sethuraman, V. A.; Hardwick, L. J.; Srinivasan, V.; Kostecki, R. Surface structural
18
19 3593 disordering in graphite upon lithium intercalation/deintercalation. *Journal of Power*
20
21 3594 *Sources* **2010**, *195*, 3655–3660.
- 22
23
24 3595 (200) Ohzuku, T. Formation of Lithium-Graphite Intercalation Compounds in Nonaqueous
25
26 3596 Electrolytes and Their Application as a Negative Electrode for a Lithium Ion (Shut-
27
28 3597 tlecock) Cell. *Journal of The Electrochemical Society* **1993**, *140*, 2490.
- 29
30
31 3598 (201) He, H.; Huang, C.; Luo, C.-W.; Liu, J.-J.; Chao, Z.-S. Dynamic study of Li intercala-
32
33 3599 tion into graphite by in situ high energy synchrotron XRD. *Electrochimica Acta* **2013**,
34
35 3600 *92*, 148–152.
- 36
37 3601 (202) Trucano, P.; Chen, R. Structure of graphite by neutron diffraction. *Nature* **1975**, *258*,
38
39 3602 136–137.
- 40
41
42 3603 (203) Okamoto, H. The C-Li (Carbon-Lithium) system. *Bulletin of Alloy Phase Diagrams*
43
44 3604 **1989**, *10*, 69–72.
- 45
46
47 3605 (204) Billaud, D.; Henry, F.; Lelaurain, M.; Willmann, P. Revisited structures of dense
48
49 3606 and dilute stage II lithium-graphite intercalation compounds. *Journal of Physics and*
50
51 3607 *Chemistry of Solids* **1996**, *57*, 775–781.
- 52
53
54 3608 (205) Billaud, D.; Henry, F. Structural studies of the stage III lithium-graphite intercalation
55
56 3609 compound. *Solid State Communications* **2002**, *124*, 299 – 304.

- 1
2
3 3610 (206) Didier, C.; Pang, W. K.; Guo, Z.; Schmid, S.; Peterson, V. K. Phase Evolution and
4 Intermittent Disorder in Electrochemically Lithiated Graphite Determined Using in
5 3611 Operando Neutron Diffraction. *Chemistry of Materials* **2020**, *32*, 2518–2531.
6
7 3612
8
9
10 3613 (207) Zheng, T.; Reimers, J. N.; Dahn, J. R. Effect of turbostratic disorder in graphitic
11 carbon hosts on the intercalation of lithium. *Physical Review B* **1995**, *51*, 734–741.
12 3614
13
14
15 3615 (208) Senyshyn, A.; Dolotko, O.; Muhlbauer, M. J.; Nikolowski, K.; Fuess, H.; Ehrenberg, H.
16 Lithium Intercalation into Graphitic Carbons Revisited: Experimental Evidence for
17 3616 Twisted Bilayer Behavior. *Journal of the Electrochemical Society* **2013**, *160*, A3198–
18 A3205.
19 3617
20 3618
21
22
23 3619 (209) Taminato, S. et al. Real-time observations of lithium battery reactions - Operando
24 neutron diffraction analysis during practical operation. *Scientific Reports* **2016**, *6*,
25 28843.
26 3620
27 3621
28
29
30 3622 (210) Thinius, S.; Islam, M. M.; Heitjans, P.; Bredow, T. Theoretical study of Li migration
31 in lithium–graphite intercalation compounds with dispersion-corrected DFT methods.
32 3623 *The Journal of Physical Chemistry C* **2014**, *118*, 2273–2280.
33
34 3624
35
36
37 3625 (211) Garcia, J. C.; Bloom, I.; Johnson, C.; Dees, D.; Iddir, H. Graphite Lithiation un-
38 der Fast Charging Conditions: Atomistic Modeling Insights. *The Journal of Physical*
39 3626 *Chemistry C* **2020**, *124*, 8162–8169.
40
41 3627
42
43
44 3628 (212) Olsson, E.; Cottom, J.; Au, H.; Guo, Z.; Jensen, A. C. S.; Alptekin, H.; Drew, A. J.;
45 Titirici, M.-M.; Cai, Q. Elucidating the Effect of Planar Graphitic Layers and Cylin-
46 3629 drical Pores on the Storage and Diffusion of Li, Na, and K in Carbon Materials.
47 *Advanced Functional Materials* **2020**, *30*, 1908209.
48 3630
49 3631
50
51
52 3632 (213) Lenchuk, O.; Adelhelm, P.; Mollenhauer, D. Comparative study of density functionals
53 for the description of lithium-graphite intercalation compounds. *Journal of Computa-*
54 3633 *tional Chemistry* **2019**, *40*, 2400–2412.
55
56 3634
57
58
59
60

- 1
2
3
4 3635 (214) Ji, X.; Wang, Y.; Zhang, J. Understanding the anisotropic strain effects on lithium
5 3636 diffusion in graphite anodes: A first-principles study. *Physica B: Condensed Matter*
6
7 3637 **2018**, *539*, 66 – 71.
8
9
10 3638 (215) Wang, Z.; Ratvik, A. P.; Grande, T.; Selbach, S. M. Diffusion of alkali metals in the
11
12 3639 first stage graphite intercalation compounds by vdW-DFT calculations. *RSC Adv.*
13
14 3640 **2015**, *5*, 15985–15992.
15
16
17 3641 (216) Persson, K.; Sethuraman, V. A.; Hardwick, L. J.; Hinuma, Y.; Meng, Y. S.; Van
18
19 3642 Der Ven, A.; Srinivasan, V.; Kostecki, R.; Ceder, G. Lithium diffusion in graphitic
20
21 3643 carbon. *The journal of physical chemistry letters* **2010**, *1*, 1176–1180.
22
23
24 3644 (217) Otero, M.; Sigal, A.; Perassi, E.; Barraco, D.; Leiva, E. Statistical mechanical modeling
25
26 3645 of the transition Stage II → Stage I of Li-ion storage in graphite. A priori vs induced
27
28 3646 heterogeneity. *Electrochimica Acta* **2017**, *245*, 569 – 574.
29
30
31 3647 (218) Gavilán-Arriazu, E. M.; Pinto, O. A.; de Mishima, B. A. L.; Leiva, E. P. M.;
32
33 3648 Oviedo, O. A. Grand Canonical Monte Carlo Study of Li Intercalation into Graphite.
34
35 3649 *Journal of The Electrochemical Society* **2018**, *165*, A2019–A2025.
36
37 3650 (219) Gavilán Arriazu, E. M.; López de Mishima, B. A.; Oviedo, O. A.; Leiva, E. P. M.;
38
39 3651 Pinto, O. A. Criticality of the phase transition on stage two in a lattice-gas model
40
41 3652 of a graphite anode in a lithium-ion battery. *Phys. Chem. Chem. Phys.* **2017**, *19*,
42
43 3653 23138–23145.
44
45
46 3654 (220) Gavilán-Arriazu, E.; Pinto, O.; López de Mishima, B.; Barraco, D.; Oviedo, O.;
47
48 3655 Leiva, E. The kinetic origin of the Daumas-Hérolde model for the Li-ion/graphite in-
49
50 3656 tercalation system. *Electrochemistry Communications* **2018**, *93*, 133 – 137.
51
52
53 3657 (221) Plett, G. L. Extended Kalman filtering for battery management systems of LiPB-based
54
55 3658 HEV battery packs: Part 2. Modeling and identification. *Journal of Power Sources*
56
57 3659 **2004**, *134*, 262 – 276.
58
59
60

- 1
2
3 3660 (222) Sole, C.; Drewett, N. E.; Hardwick, L. J. In situ Raman study of lithium-ion interca-
4
5 3661 lation into microcrystalline graphite. *Faraday Discussions* **2014**, *172*, 223–237.
6
7
8 3662 (223) Allart, D.; Montaru, M.; Gualous, H. Model of Lithium Intercalation into Graphite
9
10 3663 by Potentiometric Analysis with Equilibrium and Entropy Change Curves of Graphite
11
12 3664 Electrode. *Journal of The Electrochemical Society* **2018**, *165*, A380–A387.
13
14
15 3665 (224) Markevich, E.; Levi, M. D.; Aurbach, D. New Insight into Studies of the Cycling
16
17 3666 Performance of Li-Graphite Electrodes. *Journal of The Electrochemical Society* **2005**,
18
19 3667 *152*, A778.
20
21 3668 (225) Reynier, Y.; Yazami, R.; Fultz, B. The entropy and enthalpy of lithium intercalation
22
23 3669 into graphite. *Journal of Power Sources* **2003**, *119-121*, 850 – 855.
24
25
26 3670 (226) Liu, H.; Strobridge, F. C.; Borkiewicz, O. J.; Wiaderek, K. M.; Chapman, K. W.;
27
28 3671 Chupas, P. J.; Grey, C. P. Capturing metastable structures during high-rate cycling
29
30 3672 of LiFePO₄ nanoparticle electrodes. *Science* **2014**, *344*, 1252817–1–7.
31
32
33 3673 (227) Oriksa, Y.; Maeda, T.; Koyama, Y.; Murayama, H.; Fukuda, K.; Tanida, H.; Arai, H.;
34
35 3674 Matsubara, E.; Uchimoto, Y.; Ogumi, Z. Direct Observation of a Metastable Crystal
36
37 3675 Phase of Li_xFePO₄ under Electrochemical Phase Transition. *Journal of the American*
38
39 3676 *Chemical Society* **2013**, *135*, 5497–5500.
40
41
42 3677 (228) Gallagher, K. G.; Dees, D. W.; Jansen, A. N.; Abraham, D. P.; Kang, S.-H. A Vol-
43
44 3678 ume Averaged Approach to the Numerical Modeling of Phase-Transition Intercalation
45
46 3679 Electrodes Presented for Li_xC₆. *Journal of The Electrochemical Society* **2012**, *159*,
47
48 3680 A2029–A2037.
49
50
51 3681 (229) Grimsmann, F.; Gerbert, T.; Brauchle, F.; Gruhle, A.; Parisi, J.; Knipper, M. Hys-
52
53 3682 teresis and current dependence of the graphite anode color in a lithium-ion cell and
54
55 3683 analysis of lithium plating at the cell edge. *Journal of Energy Storage* **2018**, *15*, 17 –
56
57 3684 22.
58
59
60

- 1
2
3
4 3685 (230) Osswald, P. J.; del Rosario, M.; Garche, J.; Jossen, A.; Hoster, H. E. Fast and accurate
5 3686 measurement of entropy profiles of commercial lithium-ion cells. *Electrochimica Acta*
6
7 3687 **2015**, *177*, 270–276.
8
9
10 3688 (231) Van der Ven, A.; Thomas, J.; Puchala, B.; Natarajan, A. First-Principles Statistical
11
12 3689 Mechanics of Multicomponent Crystals. *Annual Review of Materials Research* **2018**,
13
14 3690 *48*, 27–55.
15
16
17 3691 (232) Lorie Lopez, J. L.; Grandinetti, P. J.; Co, A. C. Enhancing the real-time detec-
18
19 3692 tion of phase changes in lithium–graphite intercalated compounds through derivative
20
21 3693 operando (dOp) NMR cyclic voltammetry. *J. Mater. Chem. A* **2018**, *6*, 231–243.
22
23
24 3694 (233) Franco, A. A.; Rucci, A.; Brandell, D.; Frayret, C.; Gaberscek, M.; Jankowski, P.;
25
26 3695 Johansson, P. Boosting Rechargeable Batteries R&D by Multiscale Modeling: Myth
27
28 3696 or Reality? *Chemical Reviews* **2019**, *119*, 4569–4627.
29
30
31 3697 (234) Imai, Y.; Watanabe, A. Energetic evaluation of possible stacking structures of Li-
32
33 3698 intercalation in graphite using a first-principle pseudopotential calculation. *Journal of*
34
35 3699 *alloys and compounds* **2007**, *439*, 258–267.
36
37
38 3700 (235) Toyoura, K.; Koyama, Y.; Kuwabara, A.; Tanaka, I. Effects of off-stoichiometry of LiC_6
39
40 3701 on the lithium diffusion mechanism and diffusivity by first principles calculations. *The*
41
42 3702 *Journal of Physical Chemistry C* **2010**, *114*, 2375–2379.
43
44
45 3703 (236) Yao, F.; Gunes, F.; Ta, H. Q.; Lee, S. M.; Chae, S. J.; Sheem, K. Y.; Cojocar, C. S.;
46
47 3704 Xie, S. S.; Lee, Y. H. Diffusion mechanism of lithium ion through basal plane of layered
48
49 3705 graphene. *Journal of the American Chemical Society* **2012**, *134*, 8646–8654.
50
51
52 3706 (237) NuLi, Y.; Yang, J.; Jiang, Z. Intercalation of lithium ions into bulk and powder highly
53
54 3707 oriented pyrolytic graphite. *Journal of Physics and Chemistry of Solids* **2006**, *67*,
55 3708 882–886.
56
57
58
59
60

- 1
2
3 3709 (238) Liu, T.; Lin, L.; Bi, X.; Tian, L.; Yang, K.; Liu, J.; Li, M.; Chen, Z.; Lu, J.; Amine, K.,
4
5 3710 et al. In situ quantification of interphasial chemistry in Li-ion battery. *Nature nan-*
6
7 3711 *otechnology* **2019**, *14*, 50–56.
- 8
9
10 3712 (239) Zhang, Z.; Smith, K.; Jervis, R.; Shearing, P. R.; Miller, T. S.; Brett, D. J. Operando
11
12 3713 Electrochemical Atomic Force Microscopy of Solid–Electrolyte Interphase Formation
13
14 3714 on Graphite Anodes: The Evolution of SEI Morphology and Mechanical Properties.
15
16 3715 *ACS applied materials & interfaces* **2020**, *12*, 35132–35141.
- 17
18
19 3716 (240) Thinius, S.; Islam, M. M.; Bredow, T. Reconstruction of low-index graphite surfaces.
20
21 3717 *Surface Science* **2016**, *649*, 60–65.
- 22
23
24 3718 (241) Larciprete, R.; Lacovig, P.; Gardonio, S.; Baraldi, A.; Lizzit, S. Atomic Oxygen on
25
26 3719 Graphite: Chemical Characterization and Thermal Reduction. *The Journal of Physi-*
27
28 3720 *cal Chemistry C* **2012**, *116*, 9900–9908.
- 29
30 3721 (242) Bernardo, P.; Le Meins, J.-M.; Vidal, L.; Dentzer, J.; Gadiou, R.; Märkle, W.;
31
32 3722 Novák, P.; Spahr, M. E.; Vix-Guterl, C. Influence of graphite edge crystallographic
33
34 3723 orientation on the first lithium intercalation in Li-ion battery. *Carbon* **2015**, *91*, 458–
35
36 3724 467.
- 37
38
39 3725 (243) Toyoura, K.; Koyama, Y.; Kuwabara, A.; Oba, F.; Tanaka, I. First-principles approach
40
41 3726 to chemical diffusion of lithium atoms in a graphite intercalation compound. *Physical*
42
43 3727 *Review B* **2008**, *78*, 214303.
- 44
45
46 3728 (244) Takami, N.; Satoh, A.; Hara, M.; Ohsaki, T. Structural and kinetic characterization
47
48 3729 of lithium intercalation into carbon anodes for secondary lithium batteries. *Journal of*
49
50 3730 *the Electrochemical Society* **1995**, *142*, 371.
- 51
52
53 3731 (245) Yang, H.; Bang, H. J.; Prakash, J. Evaluation of electrochemical interface area and
54
55 3732 lithium diffusion coefficient for a composite graphite anode. *Journal of the Electro-*
56
57 3733 *chemical Society* **2004**, *151*, A1247.

- 1
2
3
4 3734 (246) Yu, P.; Popov, B. N.; Ritter, J. A.; White, R. E. Determination of the lithium ion
5 3735 diffusion coefficient in graphite. *Journal of The Electrochemical Society* **1999**, *146*, 8.
6
7
8 3736 (247) Uthaisar, C.; Barone, V. Edge effects on the characteristics of Li diffusion in graphene.
9 3737 *Nano letters* **2010**, *10*, 2838–2842.
10
11
12
13 3738 (248) Leggesse, E. G.; Chen, C.-L.; Jiang, J.-C. Lithium diffusion in graphene and graphite:
14 3739 Effect of edge morphology. *Carbon* **2016**, *103*, 209–216.
15
16
17
18 3740 (249) Chan, T.-L.; Chelikowsky, J. R. Controlling diffusion of lithium in silicon nanostruc-
19 3741 tures. *Nano letters* **2010**, *10*, 821–825.
20
21
22 3742 (250) Fujita, M.; Wakabayashi, K.; Nakada, K.; Kusakabe, K. Peculiar localized state at
23 3743 zigzag graphite edge. *Journal of the Physical Society of Japan* **1996**, *65*, 1920–1923.
24
25
26
27 3744 (251) Lee, H.; Son, Y.-W.; Park, N.; Han, S.; Yu, J. Magnetic ordering at the edges of
28 3745 graphitic fragments: Magnetic tail interactions between the edge-localized states.
29 3746 *Physical Review B* **2005**, *72*, 174431.
30
31
32
33
34 3747 (252) Velický, M.; Toth, P. S.; Woods, C. R.; Novoselov, K. S.; Dryfe, R. A. Electrochemistry
35 3748 of the Basal Plane versus Edge Plane of Graphite Revisited. *The Journal of Physical*
36 3749 *Chemistry C* **2019**, *123*, 11677–11685.
37
38
39
40
41 3750 (253) Gerischer, H. An interpretation of the double layer capacity of graphite electrodes in
42 3751 relation to the density of states at the Fermi level. *The Journal of Physical Chemistry*
43 3752 **1985**, *89*, 4249–4251.
44
45
46
47 3753 (254) Weydanz, W.; Way, B.; Van Buuren, T.; Dahn, J. Behavior of Nitrogen-Substituted
48 3754 Carbon (N_zC_{1-z}) in Li/Li (N_zC_{+1-z})₆ Cells. *Journal of the Electrochemical Society*
49 3755 **1994**, *141*, 900.
50
51
52
53
54 3756 (255) Way, B.; Dahn, J. The effect of boron substitution in carbon on the intercalation of
55 3757 lithium in $Li_x(B_zC_{1-z})_6$. *Journal of The Electrochemical Society* **1994**, *141*, 907.
56
57
58
59
60

- 1
2
3 3758 (256) Endo, M.; Hayashi, T.; Hong, S.-H.; Enoki, T.; Dresselhaus, M. S. Scanning tunneling
4 3759 microscope study of boron-doped highly oriented pyrolytic graphite. *Journal of Applied*
5 3760 *Physics* **2001**, *90*, 5670–5674.
- 6
7
8
9
10 3761 (257) Ishii, T.; Kaburagi, Y.; Yoshida, A.; Hishiyama, Y.; Oka, H.; Setoyama, N.; Ichi
11 3762 Ozaki, J.; Kyotani, T. Analyses of trace amounts of edge sites in natural graphite,
12 3763 synthetic graphite and high-temperature treated coke for the understanding of their
13 3764 carbon molecular structures. *Carbon* **2017**, *125*, 146–155.
- 14
15
16
17
18 3765 (258) Peng, C.; Bhandari, A.; Dziedzic, J.; Owen, J. R.; Skylaris, C.-K.; Kramer, D. Mech-
19 3766 anism of Li nucleation at graphite anodes and mitigation strategies. *J. Mater. Chem.*
20 3767 *A* **2021**, *9*, 16798–16804.
- 21
22
23
24
25 3768 (259) Gao, T.; Han, Y.; Fraggedakis, D.; Das, S.; Zhou, T.; Yeh, C. N.; Xu, S.; Chueh, W. C.;
26 3769 Li, J.; Bazant, M. Z. Interplay of Lithium Intercalation and Plating on a Single
27 3770 Graphite Particle. *Joule* **2021**, *5*, 393–414.
- 28
29
30
31
32 3771 (260) Bhandari, A.; Peng, C.; Dziedzic, J.; Anton, L.; Owen, J. R.; Kramer, D.; Sky-
33 3772 laris, C. K. Electrochemistry from first-principles in the grand canonical ensemble.
34 3773 *Journal of Chemical Physics* **2021**, *155*, 1–14.
- 35
36
37
38
39 3774 (261) Winter, M. The solid electrolyte interphase—the most important and the least under-
40 3775 stood solid electrolyte in rechargeable Li batteries. *Zeitschrift für physikalische Chemie*
41 3776 **2009**, *223*, 1395–1406.
- 42
43
44
45 3777 (262) Verma, P.; Maire, P.; Novák, P. A review of the features and analyses of the solid
46 3778 electrolyte interphase in Li-ion batteries. *Electrochimica Acta* **2010**, *55*, 6332 – 6341.
- 47
48
49
50 3779 (263) Haruyama, J.; Ikeshoji, T.; Otani, M. Analysis of lithium insertion/desorption reac-
51 3780 tion at interfaces between graphite electrodes and electrolyte solution using density
52 3781 functional+ implicit solvation theory. *The Journal of Physical Chemistry C* **2018**,
53 3782 *122*, 9804–9810.
- 54
55
56
57
58
59
60

- 1
2
3
4 3783 (264) Yamada, Y.; Iriyama, Y.; Abe, T.; Ogumi, Z. Kinetics of Lithium Ion Transfer at the
5
6 3784 Interface between Graphite and Liquid Electrolytes: Effects of Solvent and Surface
7
8 3785 Film. *Langmuir* **2009**, *25*, 12766–12770.
9
- 10 3786 (265) Shi, S.; Lu, P.; Liu, Z.; Qi, Y.; Hector, L. G.; Li, H.; Harris, S. J. Direct calculation of
11
12 3787 Li-ion transport in the solid electrolyte interphase. *Journal of the American Chemical*
13
14 3788 *Society* **2012**, *134*, 15476–15487.
15
- 16
17 3789 (266) Larcher, D.; Beattie, S.; Morcrette, M.; Edstroem, K.; Jumas, J.-C.; Tarascon, J.-M.
18
19 3790 Recent findings and prospects in the field of pure metals as negative electrodes for
20
21 3791 Li-ion batteries. *Journal of Materials Chemistry* **2007**, *17*, 3759–3772.
22
- 23
24 3792 (267) Feng, K.; Li, M.; Liu, W.; Kashkooli, A. G.; Xiao, X.; Cai, M.; Chen, Z. Silicon-based
25
26 3793 anodes for lithium-ion batteries: from fundamentals to practical applications. *Small*
27
28 3794 **2018**, *14*, 1702737.
29
- 30 3795 (268) Nitta, N.; Yushin, G. High-capacity anode materials for lithium-ion batteries: choice
31
32 3796 of elements and structures for active particles. *Particle & Particle Systems Charac-*
33
34 3797 *terization* **2014**, *31*, 317–336.
35
- 36
37 3798 (269) Wagner, N. P.; Tron, A.; Tolchard, J. R.; Noia, G.; Bellmann, M. P. Silicon anodes for
38
39 3799 lithium-ion batteries produced from recovered kerf powders. *Journal of Power Sources*
40
41 3800 **2019**, *414*, 486–494.
42
- 43
44 3801 (270) Okamoto, H. The Li-Si (Lithium-Silicon) system. *Bulletin of Alloy Phase Diagrams*
45
46 3802 **1990**, *11*, 306–312.
47
- 48
49 3803 (271) Gruber, T.; Thomas, D.; Röder, C.; Mertens, F.; Kortus, J. Raman spectroscopic
50
51 3804 studies of Li_xSi_y compounds. *Journal of Raman Spectroscopy* **2013**, *44*, 934–938.
52
- 53
54 3805 (272) Jiang, Y.; Offer, G.; Jiang, J.; Marinescu, M.; Wang, H. Voltage Hysteresis Model
55
56 3806 for Silicon Electrodes for Lithium Ion Batteries, Including Multi-Step Phase Transfor-

- 1
2
3 3807 mations, Crystallization and Amorphization. *Journal of The Electrochemical Society*
4
5 3808 **2020**, *167*, 130533.
6
7
8 3809 (273) Kuhn, A.; Sreeraj, P.; Pöttgen, R.; Wiemhöfer, H.-D.; Wilkening, M.; Heitjans, P.
9
10 3810 Li Ion Diffusion in the Anode Material $\text{Li}_{12}\text{Si}_7$: Ultrafast Quasi-1D Diffusion and
11
12 3811 Two Distinct Fast 3D Jump Processes Separately Revealed by ^7Li NMR Relaxometry.
13
14 3812 *Journal of the American Chemical Society* **2011**, *133*, 11018–11021.
15
16
17 3813 (274) Wang, D.; Gao, M.; Pan, H.; Wang, J.; Liu, Y. High performance amorphous-Si@
18
19 3814 SiO_x/C composite anode materials for Li-ion batteries derived from ball-milling and
20
21 3815 in situ carbonization. *Journal of Power Sources* **2014**, *256*, 190–199.
22
23
24 3816 (275) Kirklin, S.; Meredig, B.; Wolverton, C. High-Throughput Computational Screening of
25
26 3817 New Li-Ion Battery Anode Materials. *Advanced Energy Materials* **2013**, *3*, 252–262.
27
28
29 3818 (276) Fang, C.; Wang, X.; Meng, Y. S. Key issues hindering a practical lithium-metal anode.
30
31 3819 *Trends in Chemistry* **2019**, *1*, 152–158.
32
33
34 3820 (277) Li, S.; Jiang, M.; Xie, Y.; Xu, H.; Jia, J.; Li, J. Developing high-performance lithium
35
36 3821 metal anode in liquid electrolytes: challenges and progress. *Advanced Materials* **2018**,
37
38 3822 *30*, 1706375.
39
40
41 3823 (278) Radin, M. D.; Alvarado, J.; Meng, Y. S.; Van der Ven, A. Role of Crystal Symmetry in
42
43 3824 the Reversibility of Stacking-Sequence Changes in Layered Intercalation Electrodes.
44
45 3825 *Nano Letters* **2017**, *17*, 7789–7795.
46
47
48 3826 (279) Vinckevičiūtė, J.; Radin, M. D.; Van der Ven, A. Stacking-Sequence Changes and
49
50 3827 Na Ordering in Layered Intercalation Materials. *Chemistry of Materials* **2016**, *28*,
51
52 3828 8640–8650.
53
54 3829 (280) Schmickler, W.; Santos, E. *Interfacial electrochemistry*, 2nd ed.; Springer-Verlag Berlin
55
56 3830 Heidelberg, 2010; pp 1–272.
57
58
59
60

- 1
2
3
4 3831 (281) Bard, A. J.; Faulkner Larry R., *Electrochemical Methods: Fundamentals and Applica-*
5 3832 *tions*, 2nd ed.; John Wiley & Sons, Ltd, 2010; pp 1–864.
- 6
7
8 3833 (282) Kralisch, D.; Stark, A.; Körsten, S.; Kreisel, G.; Ondruschka, B. Energetic, environ-
9 3834 mental and economic balances: Spice up your ionic liquid research efficiency. *Green*
10 3835 *Chemistry* **2005**, *7*, 301–309.
- 11
12
13
14
15 3836 (283) Smiglak, M.; Reichert, W. M.; Holbrey, J. D.; Wilkes, J. S.; Sun, L.; Thrasher, J. S.;
16 3837 Kirichenko, K.; Singh, S.; Katritzky, A. R.; Rogers, R. D. Combustible ionic liquids
17 3838 by design: is laboratory safety another ionic liquid myth? *Chemical Communications*
18 3839 **2006**, 2554–2556.
- 19
20
21
22
23
24 3840 (284) Ding, F.; Xu, W.; Chen, X.; Zhang, J.; Engelhard, M. H.; Zhang, Y.; Johnson, B. R.;
25 3841 Crum, J. V.; Blake, T. A.; Liu, X., et al. Effects of carbonate solvents and lithium
26 3842 salts on morphology and coulombic efficiency of lithium electrode. *Journal of The*
27 3843 *Electrochemical Society* **2013**, *160*, A1894.
- 28
29
30
31
32 3844 (285) Janek, J.; Zeier, W. G. A solid future for battery development. *Nature Energy* **2016**,
33 3845 *1*, 16141.
- 34
35
36
37 3846 (286) Kazemiabnavi, S.; Zhang, Z.; Thornton, K.; Banerjee, S. Electrochemical stability
38 3847 window of imidazolium-based ionic liquids as electrolytes for lithium batteries. *The*
39 3848 *Journal of Physical Chemistry B* **2016**, *120*, 5691–5702.
- 40
41
42
43
44 3849 (287) Park, M.; Zhang, X.; Chung, M.; Less, G. B.; Sastry, A. M. A review of conduction
45 3850 phenomena in Li-ion batteries. *Journal of Power Sources* **2010**, *195*, 7904–7929.
- 46
47
48
49 3851 (288) Kamaya, N.; Homma, K.; Yamakawa, Y.; Hirayama, M.; Kanno, R.; Yonemura, M.;
50 3852 Kamiyama, T.; Kato, Y.; Hama, S.; Kawamoto, K.; Mitsui, A. A lithium superionic
51 3853 conductor. *Nature materials* **2011**, *10*, 682–6.

- 1
2
3 3854 (289) Swift, M. W.; Swift, J. W.; Qi, Y. Modeling the electrical double layer at solid-state
4
5 3855 electrochemical interfaces. *Nature Computational Science* **2021**, *1*, 212–220.
6
7
8 3856 (290) Xu, K.; von Cresce, A. Interfacing electrolytes with electrodes in Li ion batteries.
9
10 3857 *Journal of Materials Chemistry* **2011**, *21*, 9849.
11
12
13 3858 (291) Yu, C.; Ganapathy, S.; van Eck, E. R. H.; Wang, H.; Basak, S.; Li, Z.; Wagemaker, M.
14
15 3859 Accessing the bottleneck in all-solid state batteries, lithium-ion transport over the
16
17 3860 solid-electrolyte-electrode interface. *Nature Communications* **2017**, *8*, 1086.
18
19
20 3861 (292) Xu, K. Nonaqueous Liquid Electrolytes for Lithium-Based Rechargeable Batteries.
21
22 3862 *Chemical Reviews* **2004**, *104*, 4303–4418.
23
24
25 3863 (293) Xu, K. Electrolytes and interphases in Li-ion batteries and beyond. *Chemical Reviews*
26
27 3864 **2014**, *114*, 11503–11618.
28
29
30 3865 (294) Maier, J. Ionic conduction in space charge regions. *Prog. Sol. Stat. Chem.* **1995**, *23*,
31
32 3866 171 – 263.
33
34
35 3867 (295) Mebane, D. S. A variational approach to surface cation segregation in mixed conduct-
36
37 3868 ing perovskites. *Comp. Mater. Sci.* **2015**, *103*, 231 – 236.
38
39
40 3869 (296) Mebane, D. S.; De Souza, R. A. A generalised space-charge theory for extended defects
41
42 3870 in oxygen-ion conducting electrolytes: from dilute to concentrated solid solutions.
43
44 3871 *Energy Environ. Sci.* **2015**, *8*, 2935–2940.
45
46
47 3872 (297) Tong, X.; Mebane, D. S.; De Souza, R. A. Analyzing the grain-boundary resistance
48
49 3873 of oxide-ion conducting electrolytes: Poisson–Cahn vs Poisson–Boltzmann theories. *J.*
50
51 3874 *Amer. Ceram. Soc.* **2020**, *103*, 5–22.
52
53
54 3875 (298) Lund, J.; Vikrant, K.; Bishop, C.; Rheinheimer, W.; García, R. Thermodynamically
55
56 3876 consistent variational principles for charged interfaces. *Acta Materialia* **2021**, *205*,
57
58 3877 116525.
59
60

- 1
2
3
4 3878 (299) Bazant, M. Z.; Storey, B. D.; Kornyshev, A. A. Double layer in ionic liquids: Over-
5 3879 screening versus crowding. *Physical review letters* **2011**, *106*, 046102.
- 6
7
8 3880 (300) Perkin, S. Ionic liquids in confined geometries. *Phys. Chem. Chem. Phys.* **2012**, *14*,
9 3881 5052–5062.
- 10
11
12
13 3882 (301) Groves, T. S.; Perez-Martinez, C. S.; Lhermerout, R.; Perkin, S. Surface Forces and
14 3883 Structure in a Water-in-Salt Electrolyte. *The Journal of Physical Chemistry Letters*
15 3884 **2021**, *12*, 1702–1707.
- 16
17
18
19
20 3885 (302) Bowers, J.; Vergara-Gutierrez, M. C.; Webster, J. R. P. Surface Ordering of Am-
21 3886 phiphilic Ionic Liquids. *Langmuir* **2004**, *20*, 309–312.
- 22
23
24 3887 (303) Sloutskin, E.; Ocko, B. M.; Tamam, L.; Kuzmenko, I.; Gog, T.; Deutsch, M. Surface
25 3888 Layering in Ionic Liquids: An X-ray Reflectivity Study. *Journal of the American*
26 3889 *Chemical Society* **2005**, *127*, 7796–7804.
- 27
28
29
30
31 3890 (304) Dean, J. M.; Coles, S. W.; Saunders, W. R.; McCluskey, A. R.; Wolf, M. J.;
32 3891 Walker, A. B.; Morgan, B. J. Overscreening and Underscreening in Solid-Electrolyte
33 3892 Grain Boundary Space-Charge Layers. *Phys. Rev. Lett.* **2021**, *127*, 135502.
- 34
35
36
37
38 3893 (305) Valøen, L. O.; Reimers, J. N. Transport properties of LiPF₆-based Li-ion battery
39 3894 electrolytes. *Journal of The Electrochemical Society* **2005**, *152*, A882.
- 40
41
42
43 3895 (306) Yamada, Y.; Yaegashi, M.; Abe, T.; Yamada, A. A superconcentrated ether electrolyte
44 3896 for fast-charging Li-ion batteries. *Chem. Commun.* **2013**, *49*, 11194.
- 45
46
47
48 3897 (307) MacFarlane, D. R.; Tachikawa, N.; Forsyth, M.; Pringle, J. M.; Howlett, P. C.; El-
49 3898 liott, G. D.; Davis, J. H.; Watanabe, M.; Simon, P.; Angell, C. A. Energy applications
50 3899 of ionic liquids. *Energy & Environmental Science* **2014**, *7*, 232–250.
- 51
52
53
54 3900 (308) Suo, L.; Borodin, O.; Sun, W.; Fan, X.; Yang, C.; Wang, F.; Gao, T.; Ma, Z.;
55 3901 Schroeder, M.; von Cresce, A., et al. Advanced high-voltage aqueous lithium-ion bat-

- 3902 tery enabled by “water-in-bisalt” electrolyte. *Angewandte Chemie* **2016**, *128*, 7252–
3903 7257.
- 3904 (309) Qian, J.; Henderson, W. A.; Xu, W.; Bhattacharya, P.; Engelhard, M.; Borodin, O.;
3905 Zhang, J.-G. High rate and stable cycling of lithium metal anode. *Nature communi-*
3906 *cations* **2015**, *6*, 1–9.
- 3907 (310) Kim, H.; Wu, F.; Lee, J. T.; Nitta, N.; Lin, H.-T.; Oschatz, M.; Cho, W. I.; Kaskel, S.;
3908 Borodin, O.; Yushin, G. In situ formation of protective coatings on sulfur cathodes
3909 in lithium batteries with LiFSI-based organic electrolytes. *Advanced energy materials*
3910 **2015**, *5*, 1401792.
- 3911 (311) Zhou, X.; Zhou, J.; Yin, Y. *Modeling and Diagnostics of Polymer Electrolyte Fuel*
3912 *Cells*; Springer, 2009; pp 307–380.
- 3913 (312) Enderby, J.; Neilson, G. The structure of electrolyte solutions. *Reports on Progress in*
3914 *Physics* **1981**, *44*, 593.
- 3915 (313) Fujie, T.; Takenaka, N.; Suzuki, Y.; Nagaoka, M. Red Moon methodology compat-
3916 ible with quantum mechanics/molecular mechanics framework: Application to solid
3917 electrolyte interphase film formation in lithium-ion battery system. *The Journal of*
3918 *Chemical Physics* **2018**, *149*, 044113.
- 3919 (314) Koch, V. R.; Dominey, L. A.; Nanjundiah, C.; Ondrechen, M. J. The Intrinsic Anodic
3920 Stability of Several Anions Comprising Solvent-Free Ionic Liquids. *Journal of The*
3921 *Electrochemical Society* **1996**, *143*, 798–803.
- 3922 (315) Ong, S. P.; Andreussi, O.; Wu, Y.; Marzari, N.; Ceder, G. Electrochemical windows
3923 of room-temperature ionic liquids from molecular dynamics and density functional
3924 theory calculations. *Chemistry of Materials* **2011**, *23*, 2979–2986.

- 1
2
3
4 3925 (316) Vuilleumier, R.; Sprik, M. Electronic properties of hard and soft ions in solution:
5 3926 Aqueous Na⁺ and Ag⁺ compared. *The Journal of Chemical Physics* **2001**, *115*, 3454–
6 3468.
7 3927
8
9
10 3928 (317) Blumberger, J.; Tavernelli, I.; Klein, M. L.; Sprik, M. Diabatic free energy curves
11 and coordination fluctuations for the aqueous Ag⁺/Ag²⁺ redox couple: A biased
12 3929 Born-Oppenheimer molecular dynamics investigation. *The Journal of chemical physics*
13 3930 **2006**, *124*, 064507.
14 3931
15
16
17
18 3932 (318) Blumberger, J.; Bernasconi, L.; Tavernelli, I.; Vuilleumier, R.; Sprik, M. Electronic
19 structure and solvation of copper and silver ions: a theoretical picture of a model
20 3933 aqueous redox reaction. *Journal of the American Chemical Society* **2004**, *126*, 3928–
21 3934 3938.
22 3935
23
24
25
26
27 3936 (319) VandeVondele, J.; Sulpizi, M.; Sprik, M. From solvent fluctuations to quantitative
28 redox properties of quinones in methanol and acetonitrile. *Angewandte Chemie* **2006**,
29 3937 *118*, 1970–1972.
30 3938
31
32
33
34 3939 (320) Lynden-Bell, R. Can Marcus theory be applied to redox processes in ionic liquids?
35 A comparative simulation study of dimethylimidazolium liquids and acetonitrile. *The*
36 3940 *Journal of Physical Chemistry B* **2007**, *111*, 10800–10806.
37 3941
38
39
40
41 3942 (321) Ganesh, P.; Jiang, D.-E.; Kent, P. R. Accurate static and dynamic properties of liquid
42 electrolytes for Li-ion batteries from ab initio molecular dynamics. *Journal of Physical*
43 3943 *Chemistry B* **2011**, *115*, 3085–3090.
44 3944
45
46
47
48 3945 (322) Kameda, Y.; Umebayashi, Y.; Takeuchi, M.; Wahab, M. A.; Fukuda, S.; Ishiguro, S. I.;
49 Sasaki, M.; Amo, Y.; Usuki, T. Solvation structure of Li⁺ in concentrated LiPF₆-
50 3946 propylene carbonate solutions. *Journal of Physical Chemistry B* **2007**, *111*, 6104–
51 3947 6109.
52 3948
53
54
55
56
57
58
59
60

- 1
2
3 3949 (323) Soetens, J.-C.; Millot, C.; Maigret, B. Molecular Dynamics Simulation of Li^+BF_4^-
4 in Ethylene Carbonate, Propylene Carbonate, and Dimethyl Carbonate Solvents. *J.*
5 3950 *Phys. Chem. A* **1998**, *102*, 1055–1061.
6
7 3951
8
9
10 3952 (324) Lespes, N.; Filhol, J.-S. Using implicit solvent in *ab initio* electrochemical modeling:
11 investigating Li^+/Li electrochemistry at a Li/solvent interface. *Journal of chemical*
12 3953 *theory and computation* **2015**, *11*, 3375–3382.
13
14 3954
15
16 3955 (325) Morgan, B. J.; Watson, G. W. Role of Lithium Ordering in the Li_xTiO_2 Anatase \rightarrow
17 Titanate Phase Transition. *J. Phys. Chem. Lett.* **2011**, *2*, 1657–1661.
18 3956
19
20
21 3957 (326) Zhao, X.-G.; Dalpian, G. M.; Wang, Z.; Zunger, A. Polymorphous nature of cubic
22 halide perovskites. *Phys. Rev. B* **2020**, *101*, 155137.
23 3958
24
25
26 3959 (327) Yeh, I.-C.; Hummer, G. System-Size Dependence of Diffusion Coefficients and Vis-
27 cosities from Molecular Dynamics Simulations with Periodic Boundary Conditions. *J.*
28 3960 *Phys. Chem. B* **2004**, *108*, 15873–15879.
29 3961
30
31
32 3962 (328) Botan, A.; Marry, V.; Rotenberg, B. Diffusion in bulk liquids: finite-size effects in
33 anisotropic systems. *Molecular Physics* **2015**, *113*, 2674–2679.
34 3963
35
36
37 3964 (329) Horbach, J.; Kob, W.; Binder, K.; Angell, C. A. Finite size effects in simulations of
38 glass dynamics. *Phys. Rev. E* **1996**, *54*, R5897–R5900.
39 3965
40
41
42 3966 (330) Coles, S. W.; Park, C.; Nikam, R.; Kanduč, M.; Dzubiella, J.; Rotenberg, B. Correla-
43 tion Length in Concentrated Electrolytes: Insights from All-Atom Molecular Dynamics
44 3967 Simulations. *J. Phys. Chem. B* **2020**, *124*, 1778–1786.
45 3968
46
47
48 3969 (331) Frenkel, D.; Smit, B. *Understanding molecular simulation*; Academic Press, 2002.
49
50
51 3970 (332) Lindahl,; Abraham,; Hess,; van der Spoel, GROMACS 2021 Manual. **2021**,
52
53
54 3971 (333) Canongia Lopes, J. N.; Pádua, A. A. H. CL&P: A generic and systematic force field
55 for ionic liquids modeling. *Theor Chem Acc* **2012**, *131*, 1129.
56 3972
57
58
59
60

- 1
2
3
4 3973 (334) Jorgensen, W. L.; Maxwell, D. S.; Tirado-Rives, J. Development and Testing of the
5 3974 OPLS All-Atom Force Field on Conformational Energetics and Properties of Organic
6
7 3975 Liquids. *J. Am. Chem. Soc.* **1996**, *118*, 11225–11236.
8
9
10 3976 (335) Hess, B.; Bekker, H.; Berendsen, H. J. C.; Fraaije, J. G. E. M. LINCS: A linear con-
11
12 3977 straint solver for molecular simulations. *Journal of Computational Chemistry* **1997**,
13
14 3978 *18*, 1463–1472.
15
16
17 3979 (336) Ryckaert, J.-P.; Ciccotti, G.; Berendsen, H. J. C. Numerical integration of the cartesian
18
19 3980 equations of motion of a system with constraints: molecular dynamics of n-alkanes.
20
21 3981 *Journal of Computational Physics* **1977**, *23*, 327–341.
22
23
24 3982 (337) Andersen, H. C. Rattle: A “velocity” version of the shake algorithm for molecular
25
26 3983 dynamics calculations. *Journal of Computational Physics* **1983**, *52*, 24–34.
27
28
29 3984 (338) Ewald, P. P. Die Berechnung optischer und elektrostatischer Gitterpotentiale. *Annalen*
30
31 3985 *der Physik* **1921**, *369*, 253–287.
32
33
34 3986 (339) Darden, T.; York, D.; Pedersen, L. Particle mesh Ewald: An N.log(N) method for
35
36 3987 Ewald sums in large systems. *J. Chem. Phys.* **1993**, *98*, 10089–10092.
37
38
39 3988 (340) Deserno, M.; Holm, C. How to mesh up Ewald sums. II. An accurate error estimate for
40
41 3989 the particle–particle–particle-mesh algorithm. *J. Chem. Phys.* **1998**, *109*, 7694–7701.
42
43
44 3990 (341) Yeh, I.-C.; Berkowitz, M. L. Ewald summation for systems with slab geometry. *J.*
45
46 3991 *Chem. Phys.* **1999**, *111*, 3155–3162.
47
48
49 3992 (342) Canongia Lopes, J. N.; Deschamps, J.; Pádua, A. A. H. Modeling Ionic Liquids Using
50
51 3993 a Systematic All-Atom Force Field. *J. Phys. Chem. B* **2004**, *108*, 2038–2047.
52
53
54 3994 (343) Canongia Lopes, J. N.; Pádua, A. A. H. Molecular Force Field for Ionic Liquids Com-
55
56 3995 posed of Triflate or Bistriflylimide Anions. *J. Phys. Chem. B* **2004**, *108*, 16893–16898.
57
58
59
60

- 1
2
3
4 3996 (344) Canongia Lopes, J. N.; Pádua, A. A. H. Molecular Force Field for Ionic Liquids III:
5 3997 Imidazolium, Pyridinium, and Phosphonium Cations; Chloride, Bromide, and Di-
6 cyanamide Anions. *J. Phys. Chem. B* **2006**, *110*, 19586–19592.
7 3998
8
9
10 3999 (345) Spackman, M. A. Potential derived charges using a geodesic point selection scheme.
11 *Journal of Computational Chemistry* **1996**, *17*, 1–18.
12 4000
13
14
15 4001 (346) Breneman, C. M.; Wiberg, K. B. Determining atom-centered monopoles from molec-
16 ular electrostatic potentials. The need for high sampling density in formamide confor-
17 4002 mational analysis. *Journal of Computational Chemistry* **1990**, *11*, 361–373.
18 4003
19
20
21
22 4004 (347) Singh, U. C.; Kollman, P. A. An approach to computing electrostatic charges for
23 molecules. *Journal of Computational Chemistry* **1984**, *5*, 129–145.
24 4005
25
26
27 4006 (348) Schröder, C. Comparing reduced partial charge models with polarizable simulations
28 of ionic liquids. *Phys. Chem. Chem. Phys.* **2012**, *14*, 3089–3102.
29 4007
30
31
32 4008 (349) Schröder, C.; Lyons, A.; Rick, S. W. Polarizable MD simulations of ionic liquids:
33 How does additional charge transfer change the dynamics? *Phys. Chem. Chem. Phys.*
34 4009 **2020**, *22*, 467–477.
35 4010
36
37
38 4011 (350) Shimizu, K.; Freitas, A. A.; Atkin, R.; Warr, G. G.; FitzGerald, P. A.; Doi, H.;
39 Saito, S.; Ueno, K.; Umebayashi, Y.; Watanabe, M.; Lopes, J. N. C. Structural and
40 4012 aggregate analyses of (Li salt + glyme) mixtures: the complex nature of solvate ionic
41 4013 liquids. *Phys. Chem. Chem. Phys.* **2015**, *17*, 22321–22335.
42 4014
43
44
45
46
47 4015 (351) Sangster, M.; Dixon, M. Interionic potentials in alkali halides and their use in simula-
48 tions of the molten salts. *Advances in Physics* **1976**, *25*, 247–342.
49 4016
50
51
52 4017 (352) Madden, P. A.; Wilson, M. “Covalent” effects in “ionic” systems. *Chem. Soc. Rev.*
53 **1996**, *25*, 339–350.
54 4018
55
56
57
58
59
60

- 1
2
3
4 4019 (353) Borodin, O. Polarizable Force Field Development and Molecular Dynamics Simulations
5
6 4020 of Ionic Liquids. *J. Phys. Chem. B* **2009**, *113*, 11463–11478.
7
- 8
9 4021 (354) Borodin, O.; Smith, G. D. LiTFSI Structure and Transport in Ethylene Carbonate
10
11 4022 from Molecular Dynamics Simulations. *J. Phys. Chem. B* **2006**, *110*, 4971–4977.
12
- 13 4023 (355) Bedrov, D.; Piquemal, J.-P.; Borodin, O.; MacKerell, A. D.; Roux, B.; Schröder, C.
14
15 4024 Molecular Dynamics Simulations of Ionic Liquids and Electrolytes Using Polarizable
16
17 4025 Force Fields. *Chem. Rev.* **2019**, *119*, 7940–7995.
18
- 19
20 4026 (356) Bedrov, D.; Borodin, O.; Li, Z.; Smith, G. D. Influence of Polarization on Structural,
21
22 4027 Thermodynamic, and Dynamic Properties of Ionic Liquids Obtained from Molecular
23
24 4028 Dynamics Simulations. *J. Phys. Chem. B* **2010**, *114*, 4984–4997.
25
- 26
27 4029 (357) Marin-Lafèche, A.; Haefele, M.; Scalfi, L.; Coretti, A.; Dufils, T.; Jeanmairat, G.;
28
29 4030 Reed, S. K.; Alessandra, S.; Berthin, R.; Bacon, C.; Bonella, S.; Rotenberg, B.; Mad-
30
31 4031 den, P. A.; Salanne, M. MetalWalls: A classical molecular dynamics software dedicated
32
33 4032 to the simulation of electrochemical systems. *Journal of Open Source Software* **2020**,
34
35 4033 *5*, 2373.
36
- 37
38 4034 (358) Mamatkulov, S.; Fyta, M.; Netz, R. R. Force fields for divalent cations based on
39
40 4035 single-ion and ion-pair properties. *J. Chem. Phys.* **2013**, *138*, 024505.
41
- 42
43 4036 (359) Mamatkulov, S.; Schwierz, N. Force fields for monovalent and divalent metal cations in
44
45 4037 TIP3P water based on thermodynamic and kinetic properties. *J. Chem. Phys.* **2018**,
46
47 4038 *148*, 074504.
48
- 49
50 4039 (360) Pethes, I. A comparison of classical interatomic potentials applied to highly concen-
51
52 4040 trated aqueous lithium chloride solutions. *Journal of Molecular Liquids* **2017**, *242*,
53
54 4041 845–858.
55
56
57
58
59
60

- 1
2
3
4 4042 (361) Hanke, C. G.; Price, S. L.; Lynden-Bell, R. M. Intermolecular potentials for simulations
5
6 4043 of liquid imidazolium salts. *Molecular Physics* **2001**, *99*, 801–809.
7
8
9 4044 (362) Tsuzuki, S.; Shinoda, W.; Saito, H.; Mikami, M.; Tokuda, H.; Watanabe, M. Molec-
10
11 4045 ular Dynamics Simulations of Ionic Liquids: Cation and Anion Dependence of Self-
12
13 4046 Diffusion Coefficients of Ions. *J. Phys. Chem. B* **2009**, *113*, 10641–10649.
14
15 4047 (363) Migliorati, V.; Serva, A.; Aquilanti, G.; Olivi, L.; Pascarelli, S.; Mathon, O.;
16
17 4048 D’Angelo, P. Combining EXAFS spectroscopy and molecular dynamics simulations
18
19 4049 to understand the structural and dynamic properties of an imidazolium iodide ionic
20
21 4050 liquid. *Physical Chemistry Chemical Physics* **2015**, *17*, 2464–2474.
22
23
24 4051 (364) Chaudhari, M. I.; Muralidharan, A.; Pratt, L. R.; Rempe, S. B. Assessment of Simple
25
26 4052 Models for Molecular Simulation of Ethylene Carbonate and Propylene Carbonate as
27
28 4053 Solvents for Electrolyte Solutions. *Top Curr Chem (Z)* **2018**, *376*, 376.
29
30
31 4054 (365) Smith, A. M.; Lee, A. A.; Perkin, S. The Electrostatic Screening Length in Con-
32
33 4055 centrated Electrolytes Increases with Concentration. *J. Phys. Chem. Lett.* **2016**, *7*,
34
35 4056 2157–2163.
36
37
38 4057 (366) Gaddam, P.; Ducker, W. Electrostatic Screening Length in Concentrated Salt Solu-
39
40 4058 tions. *Langmuir* **2019**, *35*, 5719–5727.
41
42
43 4059 (367) Zeman, J.; Kondrat, S.; Holm, C. Bulk ionic screening lengths from extremely large-
44
45 4060 scale molecular dynamics simulations. *Chem. Commun.* **2020**, *56*, 15635–15638.
46
47
48 4061 (368) Krucker-Velasquez, E.; Swan, J. W. Underscreening and hidden ion structures in large
49
50 4062 scale simulations of concentrated electrolytes. *The Journal of Chemical Physics* **2021**,
51
52 4063 *155*, 134903.
53
54 4064 (369) Jeanmairet, G.; Rotenberg, B.; Borgis, D.; Salanne, M. Study of a water-graphene
55
56
57
58
59
60

- 1
2
3
4 4065 capacitor with molecular density functional theory. *The Journal of chemical physics*
5 4066 **2019**, *151*, 124111.
6
7
8 4067 (370) Cats, P.; Evans, R.; Härtel, A.; van Roij, R. Primitive model electrolytes in the near
9
10 4068 and far field: Decay lengths from DFT and simulations. *The Journal of Chemical*
11
12 4069 *Physics* **2021**, *154*, 124504.
13
14
15 4070 (371) Merlet, C.; Péan, C.; Rotenberg, B.; Madden, P. A.; Daffos, B.; Taberna, P.-L.; Si-
16
17 4071 mon, P.; Salanne, M. Highly confined ions store charge more efficiently in supercapac-
18
19 4072 itors. *Nature Communications* **2013**, *4*, 2701.
20
21
22 4073 (372) Coles, S. W.; Mishin, M.; Perkin, S.; V. Fedorov, M.; B. Ivaništšev, V. The nanostruc-
23
24 4074 ture of a lithium glyme solvate ionic liquid at electrified interfaces. *Physical Chemistry*
25
26 4075 *Chemical Physics* **2017**, *19*, 11004–11010.
27
28
29 4076 (373) Coles, S. W.; Ivaništšev, V. B. Simulation of a Solvate Ionic Liquid at a Polarizable
30
31 4077 Electrode with a Constant Potential. *J. Phys. Chem. C* **2019**, *123*, 3935–3943.
32
33
34 4078 (374) Sergeev, A. V.; Chertovich, A. V.; Itkis, D. M.; Sen, A.; Gross, A.; Khokhlov, A. R.
35
36 4079 Electrode/Electrolyte Interface in the Li–O₂ Battery: Insight from Molecular Dynam-
37
38 4080 ics Study. *J. Phys. Chem. C* **2017**, *121*, 14463–14469.
39
40
41 4081 (375) Schröder, C. Collective translational motions and cage relaxations in molecular ionic
42
43 4082 liquids. *J. Chem. Phys.* **2011**, *135*, 024502.
44
45
46 4083 (376) Schröder, C.; Steinhauser, O. On the dielectric conductivity of molecular ionic liquids.
47
48 4084 *J. Chem. Phys.* **2009**, *131*, 114504.
49
50
51 4085 (377) Hayamizu, K.; Aihara, Y.; Arai, S.; Martinez, C. G. Pulse-gradient spin-echo ¹H, ⁷Li,
52
53 4086 and ¹⁹F NMR diffusion and ionic conductivity measurements of 14 organic electrolytes
54
55 4087 containing LiN(SO₂CF₃)₂. *Journal of Physical Chemistry B* **1999**, *103*, 519–524.
56
57
58
59
60

- 1
2
3
4 4088 (378) Lesch, V.; Li, Z.; Bedrov, D.; Borodin, O.; Heuer, A. The influence of cations on
5 4089 lithium ion coordination and transport in ionic liquid electrolytes: a MD simulation
6
7 4090 study. *Phys. Chem. Chem. Phys.* **2015**, *18*, 382–392.
8
9
10 4091 (379) Borodin, O.; Smith, G. D.; Henderson, W. Li⁺ Cation Environment, Transport, and
11
12 4092 Mechanical Properties of the LiTFSI Doped N-Methyl-N-alkylpyrrolidinium⁺TFSI⁻
13
14 4093 Ionic Liquids. *J. Phys. Chem. B* **2006**, *110*, 16879–16886.
15
16
17 4094 (380) Borodin, O.; Smith, G. D. Li⁺ Transport Mechanism in Oligo(Ethylene Oxide)s Com-
18
19 4095 pared to Carbonates. *J Solution Chem* **2007**, *36*, 803–813.
20
21
22 4096 (381) Onsager, L.; Kim, S. K. Wien Effect in Simple Strong Electrolytes. *The Journal of*
23
24 4097 *Physical Chemistry* **1957**, *61*, 198–215.
25
26
27 4098 (382) Lesnicki, D.; Gao, C. Y.; Rotenberg, B.; Limmer, D. T. Field-Dependent Ionic Con-
28
29 4099 ductivities from Generalized Fluctuation-Dissipation Relations. *Phys. Rev. Lett.* **2020**,
30
31 4100 *124*, 206001.
32
33
34 4101 (383) Jones, P.; Coupette, F.; Härtel, A.; Lee, A. A. Bayesian unsupervised learning reveals
35
36 4102 hidden structure in concentrated electrolytes. *The Journal of Chemical Physics* **2021**,
37
38 4103 *154*, 134902.
39
40 4104 (384) Skarmoutsos, I.; Ponnuchamy, V.; Vetere, V.; Mossa, S. Li⁺ Solvation in Pure, Binary,
41
42 4105 and Ternary Mixtures of Organic Carbonate Electrolytes. *J. Phys. Chem. C* **2015**,
43
44 4106 *119*, 4502–4515.
45
46
47 4107 (385) Takeuchi, M.; Matubayasi, N.; Kameda, Y.; Minofar, B.; Ichi Ishiguro, S.; Ume-
48
49 4108 bayashi, Y. Free-Energy and Structural Analysis of Ion Solvation and Contact Ion-Pair
50
51 4109 Formation of Li⁺ with BF₄⁻ and PF₆⁻ in Water and Carbonate Solvents. *J. Phys. Chem.*
52
53 4110 *B* **2012**, *116*, 6476–6487.
54
55
56
57
58
59
60

- 1
2
3
4 4111 (386) Lazaridis, T. Inhomogeneous Fluid Approach to Solvation Thermodynamics. 1. The-
5 4112 ory. *J. Phys. Chem. B* **1998**, *102*, 3531–3541.
- 6
7
8 4113 (387) Hall, D. S.; Self, J.; Dahn, J. R. Dielectric Constants for Quantum Chemistry and
9 4114 Li-Ion Batteries: Solvent Blends of Ethylene Carbonate and Ethyl Methyl Carbonate.
10 4115 *Journal of Physical Chemistry C* **2015**, *119*, 22322–22330.
- 11
12
13
14
15 4116 (388) Naejus, R.; Damas, C.; Lemordant, D.; Coudert, R.; Willmann, P. Excess thermody-
16 4117 namic properties of the ethylene carbonate-trifluoroethyl methyl carbonate and propy-
17 4118 lene carbonate-trifluoroethyl methyl carbonate systems at $T = (298.15 \text{ or } 315.15) \text{ K}$.
18 4119 *Journal of Chemical Thermodynamics* **2002**, *34*, 795–806.
- 19
20
21
22
23
24 4120 (389) Stewart, S.; Newman, J. Measuring the salt activity coefficient in lithium-battery
25 4121 electrolytes. *Journal of the Electrochemical Society* **2008**, *155*, 458–463.
- 26
27
28
29 4122 (390) Debye, P.; Hückel, E. On the theory of electrolytes. II Limiting law for electric con-
30 4123 ductivity. *Physikalische Zeitschrift* **1923**, *24*, 305–325.
- 31
32
33
34 4124 (391) Merlet, C.; Péan, C.; Rotenberg, B.; Madden, P. A.; Simon, P.; Salanne, M. Simulating
35 4125 Supercapacitors: Can We Model Electrodes As Constant Charge Surfaces? *J. Phys.*
36 4126 *Chem. Lett.* **2013**, *4*, 264–268.
- 37
38
39
40 4127 (392) Chowdhury, A. U.; Muralidharan, N.; Daniel, C.; Amin, R.; Belharouak, I. Probing
41 4128 the electrolyte/electrode interface with vibrational sum frequency generation spec-
42 4129 troscopy: A review. *Journal of Power Sources* **2021**, *506*, 230173.
- 43
44
45
46
47 4130 (393) Zhang, Z.; Said, S.; Smith, K.; Jervis, R.; Howard, C. A.; Shearing, P. R.; Brett, D.
48 4131 J. L.; Miller, T. S. Characterizing Batteries by In Situ Electrochemical Atomic Force
49 4132 Microscopy: A Critical Review. *Advanced Energy Materials* **2021**, *n/a*, 2101518.
- 50
51
52
53
54 4133 (394) Perkin, S.; Chai, L.; Kampf, N.; Raviv, U.; Briscoe, W.; Dunlop, I.; Titmuss, S.;
55 4134 Seo, M.; Kumacheva, E.; Klein, J. Forces between Mica Surfaces, Prepared in Different

- 1
2
3
4 4135 Ways, Across Aqueous and Nonaqueous Liquids Confined to Molecularly Thin Films.
5 4136 *Langmuir* **2006**, *22*, 6142–6152.
6
7
8 4137 (395) Scalfi, L.; Dufils, T.; Reeves, K. G.; Rotenberg, B.; Salanne, M. A semiclassical
9
10 4138 Thomas–Fermi model to tune the metallicity of electrodes in molecular simulations.
11
12 4139 *J. Chem. Phys.* **2020**, *153*, 174704.
13
14
15 4140 (396) Vatamanu, J.; Borodin, O. Ramifications of Water-in-Salt Interfacial Structure at
16
17 4141 Charged Electrodes for Electrolyte Electrochemical Stability. *J. Phys. Chem. Lett.*
18
19 4142 **2017**, *8*, 4362–4367.
20
21
22 4143 (397) Li, Z.; Jeanmairet, G.; Méndez-Morales, T.; Rotenberg, B.; Salanne, M. Capacitive
23
24 4144 Performance of Water-in-Salt Electrolytes in Supercapacitors: A Simulation Study. *J.*
25
26 4145 *Phys. Chem. C* **2018**, *122*, 23917–23924.
27
28
29 4146 (398) Vatamanu, J.; Borodin, O.; Smith, G. D. Molecular dynamics simulations of atomically
30
31 4147 flat and nanoporous electrodes with a molten salt electrolyte. **2009**, *12*, 170–182.
32
33
34 4148 (399) Merlet, C.; Rotenberg, B.; Madden, P. A.; Taberna, P.-L.; Simon, P.; Gogotsi, Y.;
35
36 4149 Salanne, M. On the molecular origin of supercapacitance in nanoporous carbon elec-
37
38 4150 trodes. *Nature Materials* **2012**, *11*, 306–310.
39
40
41 4151 (400) Vatamanu, J.; Cao, L.; Borodin, O.; Bedrov, D.; Smith, G. D. On the Influence of Sur-
42
43 4152 face Topography on the Electric Double Layer Structure and Differential Capacitance
44
45 4153 of Graphite/Ionic Liquid Interfaces. *J. Phys. Chem. Lett.* **2011**, *2*, 2267–2272.
46
47
48 4154 (401) Borodin, O.; Bedrov, D. Interfacial Structure and Dynamics of the Lithium Alkyl
49
50 4155 Dicarboxylate SEI Components in Contact with the Lithium Battery Electrolyte. *J.*
51
52 4156 *Phys. Chem. C* **2014**, *118*, 18362–18371.
53
54
55 4157 (402) Simoncelli, M.; Ganfoud, N.; Sene, A.; Haefele, M.; Daffos, B.; Taberna, P.-L.;
56
57 4158 Salanne, M.; Simon, P.; Rotenberg, B. Blue Energy and Desalination with Nanoporous
58
59
60

- 1
2
3 4159 Carbon Electrodes: Capacitance from Molecular Simulations to Continuous Models.
4
5 4160 *Phys. Rev. X* **2018**, *8*, 021024.
6
7
8 4161 (403) Suo, L.; Borodin, O.; Gao, T.; Olguin, M.; Ho, J.; Fan, X.; Luo, C.; Wang, C.; Xu, K.
9
10 4162 “Water-in-salt” electrolyte enables high-voltage aqueous lithium-ion chemistries. *Sci-*
11
12 4163 *ence* **2015**, *350*, 938–943.
13
14
15 4164 (404) Chen, M.; Feng, G.; Qiao, R. Water-in-salt electrolytes: An interfacial perspective.
16
17 4165 *Current Opinion in Colloid & Interface Science* **2020**, *47*, 99–110.
18
19
20 4166 (405) Li, Z.; Bouchal, R.; Mendez-Morales, T.; Rollet, A.-L.; Rizzi, C.; Le Vot, S.; Favier, F.;
21
22 4167 Rotenberg, B.; Borodin, O.; Fontaine, O., et al. Transport properties of Li-TFSI water-
23
24 4168 in-salt electrolytes. *The Journal of Physical Chemistry B* **2019**, *123*, 10514–10521.
25
26
27 4169 (406) McCurry, J. Samsung blames two separate battery faults for Galaxy Note
28
29 4170 7 fires. 2017; [http://www.theguardian.com/technology/2017/jan/23/
30
31 4171 samsung-blames-faulty-batteries-for-causing-galaxy-note-7-fires](http://www.theguardian.com/technology/2017/jan/23/samsung-blames-faulty-batteries-for-causing-galaxy-note-7-fires).
32
33
34 4172 (407) Zhang, S. S. Liquid electrolyte lithium/sulfur battery: Fundamental chemistry, prob-
35
36 4173 lems, and solutions. *Journal of Power Sources* **2013**, *231*, 153–162.
37
38
39 4174 (408) Wu, X.; Pan, K.; Jia, M.; Ren, Y.; He, H.; Zhang, L.; Zhang, S. Electrolyte for lithium
40
41 4175 protection: From liquid to solid. *Green Energy and Environment* **2019**, *4*, 360–374.
42
43
44 4176 (409) Kushima, A.; So, K. P.; Su, C.; Bai, P.; Kuriyama, N.; Maebashi, T.; Fujiwara, Y.;
45
46 4177 Bazant, M. Z.; Li, J. Liquid cell transmission electron microscopy observation of
47
48 4178 lithium metal growth and dissolution: Root growth, dead lithium and lithium flot-
49
50 4179 sams. *Nano Energy* **2017**, *32*, 271–279.
51
52
53 4180 (410) Lin, D.; Liu, Y.; Li, Y.; Li, Y.; Pei, A.; Xie, J.; Huang, W.; Cui, Y. Fast galvanic
54
55 4181 lithium corrosion involving a Kirkendall-type mechanism. *Nature chemistry* **2019**, *11*,
56
57 4182 382–389.
58
59
60

- 1
2
3 4183 (411) Hallinan Jr, D. T.; Balsara, N. P. Polymer electrolytes. *Annual review of materials*
4 4184 *research* **2013**, *43*, 503–525.
- 5
6
7
8 4185 (412) Popovic, J. Chemistry of Soft Matter Battery Electrolytes. *Encyclopedia of Inorganic*
9 4186 *and Bioinorganic Chemistry* **2011**, 1–11.
- 10
11
12
13 4187 (413) Shao, Y.; Knijff, L.; Dietrich, F. M.; Hermansson, K.; Zhang, C. Modelling Bulk
14 4188 Electrolytes and Electrolyte Interfaces with Atomistic Machine Learning. *Batteries &*
15 4189 *Supercaps* **2021**, *4*, 585–595.
- 16
17
18
19
20 4190 (414) Hellström, M.; Behler, J. Concentration-dependent proton transfer mechanisms in
21 4191 aqueous NaOH solutions: From acceptor-driven to donor-driven and back. *The journal*
22 4192 *of physical chemistry letters* **2016**, *7*, 3302–3306.
- 23
24
25
26 4193 (415) Tovey, S.; Narayanan Krishnamoorthy, A.; Sivaraman, G.; Guo, J.; Benmore, C.;
27 4194 Heuer, A.; Holm, C. DFT Accurate Interatomic Potential for Molten NaCl from Ma-
28 4195 chine Learning. *The Journal of Physical Chemistry C* **2020**, *124*, 25760–25768.
- 29
30
31
32
33 4196 (416) Fedkin, M. V.; Shin, Y. K.; Dasgupta, N.; Yeon, J.; Zhang, W.; Van Duin, D.;
34 4197 Van Duin, A. C.; Mori, K.; Fujiwara, A.; Machida, M., et al. Development of the
35 4198 ReaxFF Methodology for Electrolyte–Water Systems. *The Journal of Physical Chem-*
36 4199 *istry A* **2019**, *123*, 2125–2141.
- 37
38
39
40
41
42 4200 (417) Hossain, M. J.; Pawar, G.; Liaw, B.; Gering, K. L.; Dufek, E. J.; van Duin, A. C.
43 4201 Lithium-electrolyte solvation and reaction in the electrolyte of a lithium ion battery:
44 4202 A ReaxFF reactive force field study. *The Journal of chemical physics* **2020**, *152*,
45 4203 184301.
- 46
47
48
49
50
51 4204 (418) Forsman, J.; Woodward, C. E.; Trulsson, M. A Classical Density Functional Theory
52 4205 of Ionic Liquids. *J. Phys. Chem. B* **2011**, *115*, 4606–4612.
- 53
54
55
56
57
58
59
60

- 1
2
3
4 4206 (419) Jeanmairet, G.; Rotenberg, B.; Levesque, M.; Borgis, D.; Salanne, M. A molecular
5 4207 density functional theory approach to electron transfer reactions. *Chemical science*
6
7 4208 **2019**, *10*, 2130–2143.
- 8
9
10 4209 (420) Jie, Y.; Ren, X.; Cao, R.; Cai, W.; Jiao, S. Advanced liquid electrolytes for rechargeable
11
12 4210 Li metal batteries. *Advanced Functional Materials* **2020**, *30*, 1910777.
- 13
14
15 4211 (421) Francis, C. F.; Kyratzis, I. L.; Best, A. S. Lithium-Ion Battery Separators for Ionic-
16
17 4212 Liquid Electrolytes: A Review. *Advanced Materials* **2020**, *32*, 1904205.
- 18
19
20 4213 (422) Xiong, S.; Regula, M.; Wang, D.; Song, J. Toward better lithium–sulfur batteries:
21
22 4214 functional non-aqueous liquid electrolytes. *Electrochemical Energy Reviews* **2018**, *1*,
23
24 4215 388–402.
- 25
26
27 4216 (423) Culver, S. P.; Koerver, R.; Krauskopf, T.; Zeier, W. G. Designing Ionic Conductors:
28
29 4217 The Interplay between Structural Phenomena and Interfaces in Thiophosphate-Based
30
31 4218 Solid-State Batteries. *Chemistry of Materials* **2018**, *30*, 4179–4192.
- 32
33
34 4219 (424) Famprakis, T.; Canepa, P.; Dawson, J. A.; Islam, M. S.; Masquelier, C. Fundamentals
35
36 4220 of inorganic solid-state electrolytes for batteries. *Nature Materials* **2019**, *18*, 1278–
37
38 4221 1291.
- 39
40 4222 (425) Goodenough, J. B.; Park, K.-S. The Li-Ion Rechargeable Battery: A Perspective.
41
42 4223 *Journal of the American Chemical Society* **2013**, *135*, 1167–1176.
- 43
44
45 4224 (426) Dirican, M.; Yan, C.; Zhu, P.; Zhang, X. Composite solid electrolytes for all-solid-state
46
47 4225 lithium batteries. *Materials Science and Engineering: R: Reports* **2019**, *136*, 27 – 46.
- 48
49
50 4226 (427) Han, L.; Lehmann, M. L.; Zhu, J.; Liu, T.; Zhou, Z.; Tang, X.; Heish, C.-T.;
51
52 4227 Sokolov, A. P.; Cao, P.; Chen, X. C., et al. Recent Developments and Challenges
53
54 4228 in Hybrid Solid Electrolytes for Lithium-Ion Batteries. *Frontiers in Energy Research*
55
56 4229 **2020**, *8*, 202.

- 1
2
3 4230 (428) Manthiram, A.; Yu, X.; Wang, S. Lithium battery chemistries enabled by solid-state
4 electrolytes. *Nature Reviews Materials* **2017**, *2*, 1–16.
5 4231
6
7
8 4232 (429) Faraday, M. IV. Experimental researches in electricity.–Third series. *Philosophical*
9
10 4233 *Transactions of the Royal Society of London* **1833**, *123*, 23–54.
11
12
13 4234 (430) Armand, M.; Tarascon, J.-M. Building better batteries. *Nature* **2008**, *451*, 652–657.
14
15 4235 (431) Sudworth, J. The sodium/nickel chloride (ZEBRA) battery. *Journal of Power Sources*
16
17 4236 **2001**, *100*, 149 – 163.
18
19
20 4237 (432) Oshima, T.; Kajita, M.; Okuno, A. Development of sodium-sulfur batteries. *Interna-*
21
22 4238 *tional Journal of Applied Ceramic Technology* **2004**, *1*, 269–276.
23
24
25 4239 (433) Capasso, C.; Veneri, O. Experimental analysis of a zebra battery based propulsion
26
27 4240 system for urban bus under dynamic conditions. *Energy Procedia* **2014**, *61*, 1138–
28
29 4241 1141.
30
31 4242 (434) Dudney, N.; Bates, J.; Zuhr, R.; Luck, C.; Robertson, J. Sputtering of lithium com-
32
33 4243 pounds for preparation of electrolyte thin films. *solid state ionics* **1992**, *53*, 655–661.
34
35
36 4244 (435) Bates, J.; Dudney, N.; Gruzalski, G.; Zuhr, R.; Choudhury, A.; Luck, C.; Robertson, J.
37
38 4245 Electrical properties of amorphous lithium electrolyte thin films. *Solid state ionics*
39
40 4246 **1992**, *53*, 647–654.
41
42
43 4247 (436) Inaguma, Y.; Liqun, C.; Itoh, M.; Nakamura, T.; Uchida, T.; Ikuta, H.; Wakihara, M.
44
45 4248 High ionic conductivity in lithium lanthanum titanate. *Solid State Communications*
46
47 4249 **1993**, *86*, 689–693.
48
49
50 4250 (437) Kasper, H. Series of rare earth garnets $\text{Ln}_3^{3+}\text{M}_2\text{Li}_3^+\text{O}_{12}$ (M= Te, W). *Inorganic Chem-*
51
52 4251 *istry* **1969**, *8*, 1000–1002.
53
54 4252 (438) Mazza, D. Remarks on a ternary phase in the $\text{La}_2\text{O}_3\text{□Me}_2\text{O}_5\text{□Li}_2\text{O}$ system (Me= Nb,
55
56 4253 Ta). *Materials Letters* **1988**, *7*, 205–207.
57
58
59
60

- 1
2
3
4 4254 (439) Kennedy, J. H.; Sahami, S.; Shea, S. W.; Zhang, Z. Preparation and conductivity
5 4255 measurements of $\text{SiS}_2\text{-Li}_2\text{S}$ glasses doped with LiBr and LiCl. *Solid State Ionics* **1986**,
6 4256 *18*, 368–371.
7
8
9
10 4257 (440) Ivanov-Shits, A.; Sigaryov, S. Ionic conductivity in LISICON-type materials. *Solid*
11 4258 *state ionics* **1988**, *27*, 89–100.
12
13
14
15 4259 (441) Lang, B.; Ziebarth, B.; Elsässer, C. Lithium ion conduction in $\text{LiTi}_2(\text{PO}_4)_3$ and related
16 4260 compounds based on the NASICON structure: a first-principles study. *Chemistry of*
17 4261 *Materials* **2015**, *27*, 5040–5048.
18
19
20
21
22 4262 (442) De Klerk, N. J.; Rosłoń, I.; Wagemaker, M. Diffusion mechanism of Li argyrodite
23 4263 solid electrolytes for Li-ion batteries and prediction of optimized halogen doping: the
24 4264 effect of Li vacancies, halogens, and halogen disorder. *Chemistry of Materials* **2016**,
25 4265 *28*, 7955–7963.
26
27
28
29
30 4266 (443) Dawson, J. A.; Attari, T. S.; Chen, H.; Emge, S. P.; Johnston, K. E.; Islam, M. S. Elu-
31 4267 cidating lithium-ion and proton dynamics in anti-perovskite solid electrolytes. *Energy*
32 4268 *& Environmental Science* **2018**, *11*, 2993–3002.
33
34
35
36
37 4269 (444) Ahiavi, E.; Dawson, J. A.; Kudu, U.; Courty, M.; Islam, M. S.; Clemens, O.; Masque-
38 4270 lier, C.; Famprikis, T. Mechanochemical synthesis and ion transport properties of
39 4271 Na_3OX (X= Cl, Br, I and BH_4) antiperovskite solid electrolytes. *Journal of Power*
40 4272 *Sources* **2020**, *471*, 228489.
41
42
43
44
45
46 4273 (445) Fenton, D. Complexes of alkali metal ions with poly (ethylene oxide). *Polymer* **1973**,
47 4274 *14*, 589.
48
49
50
51 4275 (446) Abraham, K.; Alamgir, M. Li^+ -conductive solid polymer electrolytes with liquid-like
52 4276 conductivity. *J. Electrochem. Soc* **1990**, *137*, 1657.
53
54
55
56
57
58
59
60

- 1
2
3
4 4277 (447) Dautzenberg, G.; Croce, F.; Passerini, S.; Scrosati, B. Characterization of PAN-based
5 4278 gel electrolytes. electrochemical stability and lithium cyclability. *Chemistry of mate-*
6 4279 *rials* **1994**, *6*, 538–542.
- 7
8
9
10 4280 (448) Arcella, V.; Sanguineti, A.; Quartarone, E.; Mustarelli, P. Vinylidene fluoride–
11 4281 hexafluoropropylene copolymers as hybrid electrolyte components for lithium batter-
12 4282 ies. *Journal of power sources* **1999**, *81*, 790–794.
- 13
14
15
16
17 4283 (449) Kataoka, H.; Saito, Y.; Sakai, T.; Quartarone, E.; Mustarelli, P. Conduction mecha-
18 4284 nisms of PVDF-type gel polymer electrolytes of lithium prepared by a phase inversion
19 4285 process. *The Journal of Physical Chemistry B* **2000**, *104*, 11460–11464.
- 20
21
22
23
24 4286 (450) Li, W.; Zhu, Z.; Shen, W.; Tang, J.; Yang, G.; Xu, Z. A novel PVdF-based composite
25 4287 gel polymer electrolyte doped with ionomer modified graphene oxide. *RSC Advances*
26 4288 **2016**, *6*, 97338–97345.
- 27
28
29
30 4289 (451) Appetecchi, G.; Croce, F.; Scrosati, B. Kinetics and stability of the lithium electrode
31 4290 in poly (methylmethacrylate)-based gel electrolytes. *Electrochimica Acta* **1995**, *40*,
32 4291 991–997.
- 33
34
35
36
37 4292 (452) Bohnke, O.; Frand, G.; Rezrazi, M.; Rousselot, C.; Truche, C. Fast ion transport in
38 4293 new lithium electrolytes gelled with PMMA. 1. Influence of polymer concentration.
39 4294 *Solid State Ionics* **1993**, *66*, 97–104.
- 40
41
42
43
44 4295 (453) Abbrent, S.; Plestil, J.; Hlavata, D.; Lindgren, J.; Tegenfeldt, J.; Wendsjö, Å. Crys-
45 4296 tallinity and morphology of PVdF–HFP-based gel electrolytes. *Polymer* **2001**, *42*,
46 4297 1407–1416.
- 47
48
49
50
51 4298 (454) Park, M.-S.; Hyun, S.-H.; Nam, S.-C.; Cho, S. B. Performance evaluation of printed
52 4299 LiCoO₂ cathodes with PVDF-HFP gel electrolyte for lithium ion microbatteries. *Elec-*
53 4300 *trochimica Acta* **2008**, *53*, 5523–5527.
- 54
55
56
57
58
59
60

- 1
2
3
4 4301 (455) Yang, C.-C.; Lian, Z.-Y.; Lin, S.; Shih, J.-Y.; Chen, W.-H. Preparation and application
5 4302 of PVDF-HFP composite polymer electrolytes in $\text{LiNi}_{0.5}\text{Co}_{0.2}\text{Mn}_{0.3}\text{O}_2$ lithium-polymer
6
7 4303 batteries. *Electrochimica Acta* **2014**, *134*, 258–265.
8
9
10 4304 (456) Zhou, W.; Wang, S.; Li, Y.; Xin, S.; Manthiram, A.; Goodenough, J. B. Plating a
11
12 4305 dendrite-free lithium anode with a polymer/ceramic/polymer sandwich electrolyte.
13
14 4306 *Journal of the American Chemical Society* **2016**, *138*, 9385–9388.
15
16
17 4307 (457) Zhang, T.; He, W.; Zhang, W.; Wang, T.; Li, P.; Sun, Z.; Yu, X. Designing composite
18
19 4308 solid-state electrolytes for high performance lithium ion or lithium metal batteries.
20
21 4309 *Chem. Sci.* **2020**, *11*, 8686–8707.
22
23
24 4310 (458) Uvarov, N. Composite solid electrolytes: recent advances and design strategies. *Jour-*
25
26 4311 *nal of Solid State Electrochemistry* **2011**, *15*, 367–389.
27
28
29 4312 (459) Wilkening, M.; Indris, S.; Heitjans, P. Heterogeneous lithium diffusion in nanocryst-
30
31 4313 talline $\text{Li}_2\text{O}:\text{Al}_2\text{O}_3$ composites. *Phys. Chem. Chem. Phys.* **2003**, *5*, 2225–2231.
32
33
34 4314 (460) Heitjans, P.; Indris, S. Diffusion and ionic conduction in nanocrystalline ceramics.
35
36 4315 *Journal of Physics: Condensed Matter* **2003**, *15*, R1257–R1289.
37
38
39 4316 (461) Indris, S.; Heitjans, P.; Roman, H. E.; Bunde, A. Nanocrystalline versus Microcrys-
40
41 4317 talline $\text{Li}_2\text{O}:\text{B}_2\text{O}_3$ Composites: Anomalous Ionic Conductivities and Percolation The-
42
43 4318 ory. *Phys. Rev. Lett.* **2000**, *84*, 2889–2892.
44
45
46 4319 (462) Indris, S.; Heitjans, P. Heterogeneous ^7Li NMR relaxation in nanocrystalline
47
48 4320 $\text{Li}_2\text{O}:\text{B}_2\text{O}_3$ composites. *Journal of Non-Crystalline Solids* **2002**, *307-310*, 555 – 564.
49
50
51 4321 (463) Blanchard, D.; Nale, A.; Sveinbjörnsson, D.; Eggenhuisen, T. M.; Verkuijlen, M. H.;
52
53 4322 Vegge, T.; Kentgens, A. P.; de Jongh, P. E. Nanoconfined LiBH_4 as a fast lithium ion
54
55 4323 conductor. *Advanced Functional Materials* **2015**, *25*, 184–192.
56
57
58
59
60

- 1
2
3
4 4324 (464) Liang, C. Conduction characteristics of the lithium iodide-aluminum oxide solid elec-
5
6 4325 trolytes. *Journal of the Electrochemical Society* **1973**, *120*, 1289.
7
8 4326 (465) Phipps, J.; Whitmore, D. Ion transport in LiSiO₂ composites. *Solid State Ionics*
9
10 4327 **1983**, *9*, 123–130.
11
12
13 4328 (466) Uvarov, N.; Isupov, V.; Sharma, V.; Shukla, A. Effect of morphology and particle size
14
15 4329 on the ionic conductivities of composite solid electrolytes. *Solid State Ionics* **1992**, *51*,
16
17 4330 41–52.
18
19
20 4331 (467) Pradel, A.; Ribes, M. Electrical properties of lithium conductive silicon sulfide glasses
21
22 4332 prepared by twin roller quenching. *Solid State Ionics* **1986**, *18*, 351–355.
23
24
25 4333 (468) Kanno, R. Synthesis of a new lithium ionic conductor, thio-LISICON–lithium germa-
26
27 4334 nium sulfide system. *Solid State Ionics* **2000**, *130*, 97–104.
28
29
30 4335 (469) Murayama, M. Synthesis of New Lithium Ionic Conductor Thio-LISICON—Lithium
31
32 4336 Silicon Sulfides System. *Journal of Solid State Chemistry* **2002**, *168*, 140–148.
33
34
35 4337 (470) Murayama, M.; Sonoyama, N.; Yamada, A.; Kanno, R. Material design of new lithium
36
37 4338 ionic conductor, thio-LISICON, in the Li₂S–P₂S₅ system. *Solid State Ionics* **2004**, *170*,
38
39 4339 173–180.
40
41
42 4340 (471) Minafra, N.; Culver, S. P.; Li, C.; Senyshyn, A.; Zeier, W. G. Influence of the
43
44 4341 Lithium Substructure on the Diffusion Pathways and Transport Properties of the
45
46 4342 Thio-LISICON Li₄Ge_{1-x}Sn_xS₄. *Chemistry of Materials* **2019**, *31*, 3794–3802.
47
48
49 4343 (472) Bron, P.; Johansson, S.; Zick, K.; Schmedt auf der Günne, J.; Dehnen, S.; Roling, B.
50
51 4344 Li₁₀SnP₂S₁₂: An Affordable Lithium Superionic Conductor. *Journal of the American*
52
53 4345 *Chemical Society* **2013**, *135*, 15694–15697.
54
55 4346 (473) Whiteley, J. M.; Woo, J. H.; Hu, E.; Nam, K.-W.; Lee, S.-H. Empowering the Lithium
56
57
58
59
60

- 1
2
3 4347 Metal Battery through a Silicon-Based Superionic Conductor. *Journal of The Electrochemical Society* **2014**, *161*, A1812–A1817.
4
5 4348
6
7
8 4349 (474) Huang, W.; Yoshino, K.; Hori, S.; Suzuki, K.; Yonemura, M.; Hirayama, M.; Kanno, R.
9
10 4350 Superionic lithium conductor with a cubic argyrodite-type structure in the Li–Al–Si–S
11
12 4351 system. *Journal of Solid State Chemistry* **2019**, *270*, 487–492.
13
14
15 4352 (475) Yamane, H.; Shibata, M.; Shimane, Y.; Junke, T.; Seino, Y.; Adams, S.; Minami, K.;
16
17 4353 Hayashi, A.; Tatsumisago, M. Crystal structure of a superionic conductor, $\text{Li}_7\text{P}_3\text{S}_{11}$.
18
19 4354 *Solid State Ionics* **2007**, *178*, 1163–1167.
20
21
22 4355 (476) Homma, K.; Yonemura, M.; Kobayashi, T.; Nagao, M.; Hirayama, M.; Kanno, R.
23
24 4356 Crystal structure and phase transitions of the lithium ionic conductor Li_3PS_4 . *Solid*
25
26 4357 *State Ionics* **2011**, *182*, 53–58.
27
28
29 4358 (477) Minami, T.; Hayashi, A.; Tatsumisago, M. Recent progress of glass and glass-ceramics
30
31 4359 as solid electrolytes for lithium secondary batteries. *Solid State Ionics* **2006**, *177*,
32
33 4360 2715–2720.
34
35
36 4361 (478) Bai, X.; Duan, Y.; Zhuang, W.; Yang, R.; Wang, J. Research progress in Li-argyrodite-
37
38 4362 based solid-state electrolytes. *Journal of Materials Chemistry A* **2020**, *8*, 25663–25686.
39
40
41 4363 (479) Minafra, N.; Hogrefe, K.; Barbon, F.; Helm, B.; Li, C.; Wilkening, H. M. R.;
42
43 4364 Zeier, W. G. Two-Dimensional Substitution: Toward a Better Understanding of the
44
45 4365 Structure–Transport Correlations in the Li-Superionic Thio-LISICONS. *Chemistry of*
46
47 4366 *Materials* **2021**, *33*, 727–740.
48
49 4367 (480) Bhandari, A.; Bhattacharya, J. Origin of Fast Ion Conduction in $\text{Li}_{10}\text{GeP}_2\text{S}_{12}$, a
50
51 4368 Superionic Conductor. *Journal of Physical Chemistry C* **2016**, *120*.
52
53
54 4369 (481) Mo, Y.; Ong, S. P.; Ceder, G. First Principles Study of the $\text{Li}_{10}\text{GeP}_2\text{S}_{12}$ Lithium Super
55
56 4370 Ionic Conductor Material. *Chemistry of Materials* **2012**, *24*, 15–17.
57
58
59
60

- 1
2
3
4 4371 (482) Kraft, M. A.; Ohno, S.; Zinkevich, T.; Koerver, R.; Culver, S. P.; Fuchs, T.;
5 4372 Senyshyn, A.; Indris, S.; Morgan, B. J.; Zeier, W. G. Inducing High Ionic Conductivity
6 in the Lithium Superionic Argyrodites $\text{Li}_{6+x}\text{P}_{1-x}\text{Ge}_x\text{S}_5\text{I}$ for All-Solid-State Batteries.
7 4373 *Journal of the American Chemical Society* **2018**, *140*, 16330–16339.
8 4374
- 9
10
11
12 4375 (483) Deiseroth, H.-J.; Kong, S.-T.; Eckert, H.; Vannahme, J.; Reiner, C.; Zaiβ, T.;
13 4376 Schlosser, M. $\text{Li}_6\text{PS}_5\text{X}$: A Class of Crystalline Li-Rich Solids With an Unusually High
14 Li^+ Mobility. *Angewandte Chemie International Edition* **2008**, *47*, 755–758.
15 4377
- 16
17
18
19 4378 (484) Kraft, M. A.; Culver, S. P.; Calderon, M.; Böcher, F.; Krauskopf, T.; Senyshyn, A.;
20 4379 Dietrich, C.; Zevalkink, A.; Janek, J.; Zeier, W. G. Influence of lattice polarizability
21 on the ionic conductivity in the lithium superionic argyrodites $\text{Li}_6\text{PS}_5\text{X}$ ($X = \text{Cl}, \text{Br},$
22 4380 I). *Journal of the American Chemical Society* **2017**, *139*, 10909–10918.
23 4381
- 24
25
26
27
28 4382 (485) Minafra, N.; Culver, S. P.; Krauskopf, T.; Senyshyn, A.; Zeier, W. G. Effect of Si
29 substitution on the structural and transport properties of superionic Li-argyrodites.
30 4383 *Journal of Materials Chemistry A* **2018**, *6*, 645–651.
31 4384
- 32
33
34 4385 (486) Adeli, P.; Bazak, J. D.; Park, K. H.; Kochetkov, I.; Huq, A.; Goward, G. R.;
35 4386 Nazar, L. F. Boosting solid-state diffusivity and conductivity in lithium superionic
36 argyrodites by halide substitution. *Angewandte Chemie International Edition* **2019**,
37 4387 *58*, 8681–8686.
38 4388
- 39
40
41
42
43 4389 (487) Kuhn, A.; Duppel, V.; Lotsch, B. V. Tetragonal $\text{Li}_{10}\text{GeP}_2\text{S}_{12}$ – exploring the Li ion
44 dynamics in LGPS Li electrolytes. *Energy Environ. Sci.* **2013**, *6*, 3548–3552.
45 4390
- 46
47
48 4391 (488) Xu, M.; Ding, J.; Ma, E. One-dimensional stringlike cooperative migration of lithium
49 ions in an ultrafast ionic conductor. *Applied Physics Letters* **2012**, *101*, 031901.
50 4392
- 51
52
53 4393 (489) Adams, S.; Prasada Rao, R. Structural requirements for fast lithium ion migration in
54 $\text{Li}_{10}\text{GeP}_2\text{S}_{12}$. *Journal of Materials Chemistry* **2012**, *22*, 7687.
55 4394

- 1
2
3
4 4395 (490) Kuhn, A.; Köhler, J.; Lotsch, B. V. Single-crystal X-ray structure analysis of the
5
6 4396 superionic conductor $\text{Li}_{10}\text{GeP}_2\text{S}_{12}$. *Phys. Chem. Chem. Phys.* **2013**, *15*, 11620–2.
7
8 4397 (491) Zhou, L.; Minafra, N.; Zeier, W. G.; Nazar, L. F. Innovative Approaches to Li-
9
10 4398 Argyrodite Solid Electrolytes for All-Solid-State Lithium Batteries. *Accounts of Chem-*
11
12 4399 *ical Research* **2021**, 19002–19013.
13
14
15 4400 (492) Bachman, J. C.; Muy, S.; Grimaud, A.; Chang, H.-H.; Pour, N.; Lux, S. F.;
16
17 4401 Paschos, O.; Maglia, F.; Lupart, S.; Lamp, P., et al. Inorganic solid-state electrolytes
18
19 4402 for lithium batteries: mechanisms and properties governing ion conduction. *Chemical*
20
21 4403 *reviews* **2016**, *116*, 140–162.
22
23
24 4404 (493) Ohno, S.; Helm, B.; Fuchs, T.; Dewald, G.; Kraft, M. A.; Culver, S. P.; Senyshyn, A.;
25
26 4405 Zeier, W. G. Further Evidence for Energy Landscape Flattening in the Superionic
27
28 4406 Argyrodites $\text{Li}_{6+x}\text{P}_{1-x}\text{M}_x\text{S}_5\text{I}$ (M= Si, Ge, Sn). *Chemistry of Materials* **2019**, *31*, 4936–
29
30 4407 4944.
31
32
33 4408 (494) Zhao, F.; Liang, J.; Yu, C.; Sun, Q.; Li, X.; Adair, K.; Wang, C.; Zhao, Y.; Zhang, S.;
34
35 4409 Li, W., et al. A Versatile Sn-Substituted Argyrodite Sulfide Electrolyte for All-Solid-
36
37 4410 State Li Metal Batteries. *Adv. Energy Mater.* **2020**, *10*, 1903422.
38
39
40 4411 (495) Zhou, L.; Assoud, A.; Zhang, Q.; Wu, X.; Nazar, L. F. New Family of Argyrodite
41
42 4412 Thioantimonate Lithium Superionic Conductors. *J. Am. Chem. Soc.* **2019**, *141*,
43
44 4413 19002–19013.
45
46 4414 (496) Zhou, L.; Park, K.-H.; Sun, X.; Lalère, F.; Adermann, T.; Hartmann, P.; Nazar, L. F.
47
48 4415 Solvent-Engineered Design of Argyrodite $\text{Li}_6\text{PS}_5\text{X}$ ($X = \text{Cl}, \text{Br}, \text{I}$) Solid Electrolytes
49
50 4416 with High Ionic Conductivity. *ACS Energy Letters* **2019**, *4*, 265–270.
51
52
53 4417 (497) Wang, P.; Liu, H.; Patel, S.; Feng, X.; Chien, P.-H.; Wang, Y.; Hu, Y.-Y. Fast Ion
54
55 4418 Conduction and Its Origin in $\text{Li}_{6-x}\text{PS}_{5-x}\text{Br}_{1+x}$. *Chem. Mater.* **2020**, *32*, 3833–3840.
56
57
58
59
60

- 1
2
3 4419 (498) Morgan, B. J. Mechanistic Origin of Superionic Lithium Diffusion in Anion-Disordered
4
5 4420 $\text{Li}_6\text{PS}_5\text{X}$ Argyrodites. *Chem. Mater.* **2021**, *33*, 2004–2018.
6
7
8 4421 (499) Kuhs, W.; Nitsche, R.; Scheunemann, K. The argyrodites– A new family of tetrahe-
9
10 4422 drally close-packed structures. *Materials Research Bulletin* **1979**, *14*, 241–248.
11
12
13 4423 (500) Gautam, A.; Sadowski, M.; Ghidui, M.; Minafra, N.; Senyshyn, A.; Albe, K.;
14
15 4424 Zeier, W. G. Engineering the Site-Disorder and Lithium Distribution in the Lithium
16
17 4425 Superionic Argyrodite $\text{Li}_6\text{PS}_5\text{Br}$. *Advanced Energy Materials* *11*, 2003369.
18
19
20 4426 (501) Minafra, N.; Kraft, M.; Bernges, T.; Li, C.; Schlem, R.; Morgan, B.; Zeier, W. On the
21
22 4427 Local Charge Inhomogeneity and Lithium Distribution in the Superionic Argyrodites
23
24 4428 $\text{Li}_6\text{PS}_5\text{X}$ (X = Cl, Br, I). **2020**,
25
26
27 4429 (502) Deng, Z.; Zhu, Z.; Chu, I.-H.; Ong, S. P. Data-Driven First-Principles Methods for
28
29 4430 the Study and Design of Alkali Superionic Conductors. *Chemistry of Materials* **2017**,
30
31 4431 *29*, 281–288.
32
33
34 4432 (503) Yu, C. et al. Superionic conductivity in lithium argyrodite solid-state electrolyte by
35
36 4433 controlled Cl-doping. *Nano Energy* **2020**, *69*, 104396.
37
38
39 4434 (504) Feng, X.; Chien, P.-H.; Wang, Y.; Patel, S.; Wang, P.; Liu, H.; Immediato-Scuotto, M.;
40
41 4435 Hu, Y.-Y. Enhanced ion conduction by enforcing structural disorder in Li-deficient
42
43 4436 argyrodites $\text{Li}_{6-x}\text{PS}_{5-x}\text{Cl}_{1+x}$. *Energy Storage Materials* **2020**, *30*, 67 – 73.
44
45
46 4437 (505) Yu, C.; Hageman, J.; Ganapathy, S.; van Eijck, L.; Zhang, L.; Adair, K. R.; Sun, X.;
47
48 4438 Wagemaker, M. Tailoring $\text{Li}_6\text{PS}_5\text{Br}$ ionic conductivity and understanding of its role
49
50 4439 in cathode mixtures for high performance all-solid-state Li–S batteries. *Journal of*
51
52 4440 *Materials Chemistry A* **2019**, *7*, 10412–10421.
53
54
55 4441 (506) Murugan, R.; Thangadurai, V.; Weppner, W. Fast lithium ion conduction in garnet-
56
57 4442 type $\text{Li}_7\text{La}_3\text{Zr}_2\text{O}_{12}$. *Angewandte Chemie - International Edition* **2007**, *46*, 7778–7781.
58
59
60

- 1
2
3 4443 (507) Ni, J. E.; Case, E. D.; Sakamoto, J. S.; Rangasamy, E.; Wolfenstine, J. B. Room
4 4444 temperature elastic moduli and Vickers hardness of hot-pressed LLZO cubic garnet.
5 4445 *Journal of Materials Science* **2012**, *47*, 7978–7985.
6
7
8
9
10 4446 (508) Zhu, Y.; He, X.; Mo, Y. First principles study on electrochemical and chemical stability
11 4447 of solid electrolyte-electrode interfaces in all-solid-state Li-ion batteries. *Journal of*
12 4448 *Materials Chemistry A* **2016**, *4*, 3253–3266.
13
14
15
16
17 4449 (509) Binninger, T.; Marcolongo, A.; Mottet, M.; Weber, V.; Laino, T. Comparison of com-
18 4450 putational methods for the electrochemical stability window of solid-state electrolyte
19 4451 materials. *Journal of Materials Chemistry A* **2020**, *8*, 1347–1359.
20
21
22
23 4452 (510) Geiger, C. A.; Alekseev, E.; Lazic, B.; Fisch, M.; Armbruster, T.; Langner, R.;
24 4453 Fechtelkord, M.; Kim, N.; Pettke, T.; Weppner, W. Crystal chemistry and stability of
25 4454 “Li₇La₃Zr₂O₁₂” garnet: A fast lithium-ion conductor. *Inorganic Chemistry* **2011**, *50*,
26 4455 1089–1097.
27
28
29
30
31
32 4456 (511) Rangasamy, E.; Wolfenstine, J.; Sakamoto, J. The role of Al and Li concentration on
33 4457 the formation of cubic garnet solid electrolyte of nominal composition Li₇La₃Zr₂O₁₂.
34 4458 *Solid State Ionics* **2012**, *206*, 28–32.
35
36
37
38
39 4459 (512) Ren, Y.; Shen, Y.; Lin, Y.; Nan, C. W. Direct observation of lithium dendrites inside
40 4460 garnet-type lithium-ion solid electrolyte. *Electrochemistry Communications* **2015**, *57*,
41 4461 27–30.
42
43
44
45
46 4462 (513) Sudo, R.; Nakata, Y.; Ishiguro, K.; Matsui, M.; Hirano, A.; Takeda, Y.; Yamamoto, O.;
47 4463 Imanishi, N. Interface behavior between garnet-type lithium-conducting solid elec-
48 4464 trolyte and lithium metal. *Solid State Ionics* **2014**, *262*, 151–154.
49
50
51
52 4465 (514) Cheng, E. J.; Sharafi, A.; Sakamoto, J. Intergranular Li metal propagation through
53 4466 polycrystalline Li_{6.25}Al_{0.25}La₃Zr₂O₁₂ ceramic electrolyte. *Electrochimica Acta* **2017**,
54 4467 *223*, 85–91.
55
56
57
58
59
60

- 1
2
3 4468 (515) Kim, S.; Jung, C.; Kim, H.; Thomas-Alyea, K. E.; Yoon, G.; Kim, B.; Badding, M. E.;
4
5 4469 Song, Z.; Chang, J. M.; Kim, J.; Im, D.; Kang, K. The Role of Interlayer Chemistry in
6
7 4470 Li-Metal Growth through a Garnet-Type Solid Electrolyte. *Advanced Energy Materials*
8
9 4471 **2020**, *10*, 1903993.
- 10
11
12 4472 (516) Canepa, P.; Dawson, J. A.; Sai Gautam, G.; Statham, J. M.; Parker, S. C.; Islam, M. S.
13
14 4473 Particle Morphology and Lithium Segregation to Surfaces of the $\text{Li}_7\text{La}_3\text{Zr}_2\text{O}_{12}$ Solid
15
16 4474 Electrolyte. *Chemistry of Materials* **2018**, *30*, 3019–3027.
- 17
18
19 4475 (517) Tian, H. K.; Xu, B.; Qi, Y. Computational study of lithium nucleation tendency in
20
21 4476 $\text{Li}_7\text{La}_3\text{Zr}_2\text{O}_{12}$ (LLZO) and rational design of interlayer materials to prevent lithium
22
23 4477 dendrites. *Journal of Power Sources* **2018**, *392*, 79–86.
- 24
25
26 4478 (518) Gao, B.; Jalem, R.; Tateyama, Y. Surface-Dependent Stability of the Interface between
27
28 4479 Garnet $\text{Li}_7\text{La}_3\text{Zr}_2\text{O}_{12}$ and the Li Metal in the All-Solid-State Battery from First-
29
30 4480 Principles Calculations. *ACS Applied Materials & Interfaces* **2020**, *12*, 16350–16358.
- 31
32
33 4481 (519) Ma, C.; Cheng, Y.; Yin, K.; Luo, J.; Sharafi, A.; Sakamoto, J.; Li, J.; More, K. L.;
34
35 4482 Dudney, N. J.; Chi, M. Interfacial Stability of Li Metal–Solid Electrolyte Elucidated
36
37 4483 via in Situ Electron Microscopy. *Nano Letters* **2016**, *16*, 7030–7036.
- 38
39
40 4484 (520) Rettenwander, D.; Wagner, R.; Reyer, A.; Bonta, M.; Cheng, L.; Doeff, M. M.;
41
42 4485 Limbeck, A.; Wilkening, M.; Amthauer, G. Interface instability of fe-stabilized
43
44 4486 $\text{Li}_7\text{La}_3\text{Zr}_2\text{O}_{12}$ versus li metal. *Journal of Physical Chemistry C* **2018**, *122*, 3780–3785.
- 45
46 4487 (521) Shen, F.; Dixit, M. B.; Xiao, X.; Hatzell, K. B. Effect of Pore Connectivity on Li
47
48 4488 Dendrite Propagation within LLZO Electrolytes Observed with Synchrotron X-ray
49
50 4489 Tomography. *ACS Energy Letters* **2018**, *3*, 1056–1061.
- 51
52
53 4490 (522) Aguesse, F.; Manalastas, W.; Buannic, L.; Del Amo, J. M. L.; Singh, G.; Llordés, A.;
54
55 4491 Kilner, J. Investigating the dendritic growth during full cell cycling of garnet elec-

- 1
2
3
4 4492 trolite in direct contact with Li metal. *ACS Applied Materials and Interfaces* **2017**,
5 4493 *9*, 3808–3816.
6
7
8 4494 (523) Krauskopf, T.; Hartmann, H.; Zeier, W. G.; Janek, J. Toward a Fundamental Un-
9
10 4495 derstanding of the Lithium Metal Anode in Solid-State Batteries - An Electrochemo-
11
12 4496 Mechanical Study on the Garnet-Type Solid Electrolyte $\text{Li}_{6.25}\text{Al}_{0.25}\text{La}_3\text{Zr}_2\text{O}_{12}$. *ACS*
13
14 4497 *Applied Materials and Interfaces* **2019**, *11*, 14463–14477.
15
16
17 4498 (524) Zhu, Y.; Connell, J. G.; Tepavcevic, S.; Zapol, P.; Garcia-Mendez, R.; Tay-
18
19 4499 lor, N. J.; Sakamoto, J.; Ingram, B. J.; Curtiss, L. A.; Freeland, J. W.; Fong, D. D.;
20
21 4500 Markovic, N. M. Dopant-Dependent Stability of Garnet Solid Electrolyte Interfaces
22
23 4501 with Lithium Metal. *Advanced Energy Materials* **2019**, *9*, 1–11.
24
25
26 4502 (525) Tsai, C.-L.; Roddatis, V.; Chandran, C. V.; Ma, Q.; Uhlenbruck, S.; Bram, M.; Heit-
27
28 4503 jans, P.; Guillon, O. $\text{Li}_7\text{La}_3\text{Zr}_2\text{O}_{12}$ Interface Modification for Li Dendrite Prevention.
29
30 4504 *ACS Applied Materials & Interfaces* **2016**, *8*, 10617–10626.
31
32
33 4505 (526) Thompson, T.; Yu, S.; Williams, L.; Schmidt, R. D.; Garcia-Mendez, R.; Wolfen-
34
35 4506 stine, J.; Allen, J. L.; Kioupakis, E.; Siegel, D. J.; Sakamoto, J. Electrochemical
36
37 4507 Window of the Li-Ion Solid Electrolyte $\text{Li}_7\text{La}_3\text{Zr}_2\text{O}_{12}$. *ACS Energy Letters* **2017**, *2*,
38
39 4508 462–468.
40
41
42 4509 (527) Yu, S.; Schmidt, R. D.; Garcia-Mendez, R.; Herbert, E.; Dudney, N. J.; Wolfen-
43
44 4510 stine, J. B.; Sakamoto, J.; Siegel, D. J. Elastic Properties of the Solid Electrolyte
45
46 4511 $\text{Li}_7\text{La}_3\text{Zr}_2\text{O}_{12}$ (LLZO). *Chemistry of Materials* **2016**, *28*, 197–206.
47
48
49 4512 (528) Wang, Y.; Lv, J.; Zhu, L.; Ma, Y. CALYPSO: A method for crystal structure predic-
50
51 4513 tion. *Computer Physics Communications* **2012**, *183*, 2063–2070.
52
53
54 4514 (529) Gao, B.; Gao, P.; Lu, S.; Lv, J.; Wang, Y.; Ma, Y. Interface structure prediction via
55
56 4515 CALYPSO method. *Science Bulletin* **2019**, *64*, 301–309.
57
58
59
60

- 1
2
3
4 4516 (530) Han, F.; Westover, A. S.; Yue, J.; Fan, X.; Wang, F.; Chi, M.; Leonard, D. N.;
5 4517 Dudney, N. J.; Wang, H.; Wang, C. High electronic conductivity as the origin of
6 lithium dendrite formation within solid electrolytes. *Nature Energy* **2019**, *4*, 187–196.
7 4518
8
9
10 4519 (531) Squires, A.; Davies, D.; Kim, S.; Scanlon, D.; Walsh, A.; Morgan, B. Low Electronic
11 Conductivity of $\text{Li}_7\text{La}_3\text{Zr}_2\text{O}_{12}$ (LLZO) Solid Electrolytes from First Principles. **2020**,
12 4520
13
14
15 4521 (532) Xu, M.; Park, M. S.; Lee, J. M.; Kim, T. Y.; Park, Y. S.; Ma, E. Mechanisms of Li^+
16 transport in garnet-type cubic $\text{Li}_{3+x}\text{La}_3\text{M}_2\text{O}_{12}$ ($M = \text{Te}, \text{Nb}, \text{Zr}$). *Physical Review B*
17 4522
18 **2012**, *85*, 052301.
19 4523
20
21
22 4524 (533) Burbano, M.; Carlier, D.; Boucher, F.; Morgan, B. J.; Salanne, M. Sparse Cyclic Exci-
23 tations Explain the Low Ionic Conductivity of Stoichiometric $\text{Li}_7\text{La}_3\text{Zr}_2\text{O}_{12}$. *Physical*
24 4525
25 *Review Letters* **2016**, *116*, 1–6.
26 4526
27
28
29 4527 (534) Meier, K.; Laino, T.; Curioni, A. Solid-state electrolytes: Revealing the mechanisms
30 of Li-Ion conduction in tetragonal and cubic LLZO by first-principles calculations.
31 4528
32 *Journal of Physical Chemistry C* **2014**, *118*, 6668–6679.
33 4529
34
35
36 4530 (535) Jalem, R.; Yamamoto, Y.; Shiiba, H.; Nakayama, M.; Munakata, H.; Kasuga, T.;
37 Kanamura, K. Concerted migration mechanism in the Li ion dynamics of garnet-type
38 4531
39 $\text{Li}_7\text{La}_3\text{Zr}_2\text{O}_{12}$. *Chemistry of Materials* **2013**, *25*, 425–430.
40 4532
41
42
43 4533 (536) Rettenwander, D.; Blaha, P.; Laskowski, R.; Schwarz, K.; Bottke, P.; Wilkening, M.;
44 Geiger, C. A.; Amthauer, G. DFT study of the role of Al^{3+} in the fast ion-conductor
45 4534
46 $\text{Li}_{7-3x}\text{Al}_{3+x}\text{La}_3\text{Zr}_2\text{O}_{12}$ garnet. *Chemistry of Materials* 2617–2623.
47 4535
48
49 4536 (537) Rettenwander, D.; Redhammer, G.; Preishuber-Pflügl, F.; Cheng, L.; Miara, L.; Wag-
50 ner, R.; Welzl, A.; Suard, E.; Doeff, M. M.; Wilkening, M.; Fleig, J.; Amthauer, G.
51 4537
52 Structural and Electrochemical Consequences of Al and Ga Cosubstitution in
53 4538
54 $\text{Li}_7\text{La}_3\text{Zr}_2\text{O}_{12}$ Solid Electrolytes. *Chemistry of Materials* **2016**, *28*, 2384–2392.
55 4539
56
57
58
59
60

- 1
2
3
4 4540 (538) Bonilla, M. R.; García Daza, F. A.; Carrasco, J.; Akhmatskaya, E. Exploring Li-ion
5
6 4541 conductivity in cubic, tetragonal and mixed-phase Al-substituted $\text{Li}_7\text{La}_3\text{Zr}_2\text{O}_{12}$ using
7
8 4542 atomistic simulations and effective medium theory. *Acta Materialia* **2019**, *175*, 426–
9
10 4543 435.
- 11
12 4544 (539) Awaka, J.; Kijima, N.; Hayakawa, H.; Akimoto, J. Synthesis and structure analysis of
13
14 4545 tetragonal $\text{Li}_7\text{La}_3\text{Zr}_2\text{O}_{12}$ with the garnet-related type structure. *Journal of Solid State*
15
16 4546 *Chemistry* **2009**, *182*, 2046–2052.
- 17
18
19 4547 (540) Hayamizu, K.; Seki, S.; Haishi, T. Lithium ion micrometer diffusion in a garnet-type
20
21 4548 cubic $\text{Li}_7\text{La}_3\text{Zr}_2\text{O}_{12}$ (LLZO) studied using ^7Li NMR spectroscopy. *The Journal of*
22
23 4549 *Chemical Physics* **2017**, *146*, 024701.
- 24
25
26 4550 (541) Brugge, R. H.; Chater, R. J.; Kilner, J. A.; Aguadero, A. Experimental determination
27
28 4551 of Li diffusivity in LLZO using isotopic exchange and FIB-SIMS. *Journal of Physics:*
29
30 4552 *Energy* **2021**, *3*, 034001.
- 31
32
33 4553 (542) Sharafi, A.; Yu, S.; Naguib, M.; Lee, M.; Ma, C.; Meyer, H. M.; Nanda, J.; Chi, M.;
34
35 4554 Siegel, D. J.; Sakamoto, J. Impact of air exposure and surface chemistry on Li-
36
37 4555 $\text{Li}_7\text{La}_3\text{Zr}_2\text{O}_{12}$ interfacial resistance. *Journal of Materials Chemistry A* **2017**, *5*, 13475–
38
39 4556 13487.
- 40
41
42 4557 (543) Islam, M. M.; Bredow, T.; Heitjans, P. The ionic conductivity in lithium-boron oxide
43
44 4558 materials and its relation to structural, electronic and defect properties: insights from
45
46 4559 theory. *Journal of Physics: Condensed Matter* **2012**, *24*, 203201.
- 47
48
49 4560 (544) Islam, M. M.; Bredow, T.; Indris, S.; Heitjans, P. Enhanced Conductivity at the
50
51 4561 Interface of $\text{Li}_2\text{O}:\text{B}_2\text{O}_3$ Nanocomposites: Atomistic Models. *Phys. Rev. Lett.* **2007**,
52
53 4562 *99*, 145502.
- 54
55 4563 (545) Baggio, B. F.; Grunder, Y. In Situ X-Ray Techniques for Electrochemical Interfaces.

- 1
2
3
4 4564 *Annual Review of Analytical Chemistry* **2021**, *14*, DOI: 10.1146/annurev-anchem-
5 4565 091020-100631.
6
7
8 4566 (546) Claessen, R.; Sing, M.; Paul, M.; Berner, G.; Wetscherek, A.; Müller, A.; Drube, W.
9
10 4567 Hard x-ray photoelectron spectroscopy of oxide hybrid and heterostructures: a new
11
12 4568 method for the study of buried interfaces. *New Journal of Physics* **2009**, *11*, 125007.
13
14
15 4569 (547) Thangadurai, V.; Weppner, W. $\text{Li}_6\text{AlLa}_2\text{Ta}_2\text{O}_{12}$ (A=Sr, Ba): Novel garnet-like oxides
16
17 4570 for fast lithium ion conduction. *Advanced Functional Materials* **2005**, *15*, 107–112.
18
19
20 4571 (548) Liu, Z.; Fu, W.; Payzant, E. A.; Yu, X.; Wu, Z.; Dudney, N. J.; Kiggans, J.; Hong, K.;
21
22 4572 Rondinone, A. J.; Liang, C. Anomalous High Ionic Conductivity of Nanoporous β -Li
23
24 4573 PS_4 . *Journal of the American Chemical Society* **2013**, *135*, 975–978.
25
26
27 4574 (549) Kobayashi, T.; Yamada, A.; Kanno, R. Interfacial reactions at electrode/electrolyte
28
29 4575 boundary in all solid-state lithium battery using inorganic solid electrolyte, thio-
30
31 4576 LISICON. *Electrochimica Acta* **2008**, *53*, 5045–5050.
32
33
34 4577 (550) Takada, K.; Ohta, N.; Zhang, L.; Fukuda, K.; Sakaguchi, I.; Ma, R.; Osada, M.;
35
36 4578 Sasaki, T. Interfacial modification for high-power solid-state lithium batteries. *Solid*
37
38 4579 *State Ionics* 1333–1337.
39
40
41 4580 (551) Sakuda, A.; Hayashi, A.; Tatsumisago, M. Interfacial observation between LiCoO_2
42
43 4581 electrode and $\text{Li}_2\text{S-P}_2\text{S}_5$ solid electrolytes of all-solid-state lithium secondary batteries
44
45 4582 using transmission electron microscopy. *Chemistry of Materials* **2010**, *22*, 949–956.
46
47
48 4583 (552) Okuno, Y.; Haruyama, J.; Tateyama, Y. Comparative study on sulfide and oxide
49
50 4584 electrolyte interfaces with cathodes in all-solid-state battery via first-principles calcu-
51
52 4585 lations. *ACS Applied Energy Materials* **2020**, *3*, 11061–11072.
53
54
55 4586 (553) Sharafi, A.; Kazyak, E.; Davis, A. L.; Yu, S.; Thompson, T.; Siegel, D. J.; Das-
56
57 4587 gupta, N. P.; Sakamoto, J. Surface Chemistry Mechanism of Ultra-Low Interfacial

- 1
2
3 4588 Resistance in the Solid-State Electrolyte $\text{Li}_7\text{La}_3\text{Zr}_2\text{O}_{12}$. *Chemistry of Materials* **2017**,
4 4589 *29*, 7961–7968.
- 5
6
7
8 4590 (554) Jiang, Z.; Han, Q.; Wang, S.; Wang, H. Reducing the Interfacial Resistance in
9 4591 All-Solid-State Lithium Batteries Based on Oxide Ceramic Electrolytes. *ChemElec-*
10 4592 *troChem* **2019**, *6*, 2970–2983.
- 11
12
13
14
15 4593 (555) Lepley, N. D.; Holzwarth, N. A. Modeling interfaces between solids: Application to
16 4594 Li battery materials. *Physical Review B - Condensed Matter and Materials Physics*
17 4595 **2015**, *92*, 1–15.
- 18
19
20
21
22 4596 (556) Zhang, Y. Q.; Tian, Y.; Xiao, Y.; Miara, L. J.; Aihara, Y.; Tsujimura, T.; Shi, T.;
23 4597 Scott, M. C.; Ceder, G. Direct Visualization of the Interfacial Degradation of Cathode
24 4598 Coatings in Solid State Batteries: A Combined Experimental and Computational
25 4599 Study. *Advanced Energy Materials* **2020**, *10*.
- 26
27
28
29
30 4600 (557) Xiao, Y.; Miara, L. J.; Wang, Y.; Ceder, G. Computational Screening of Cathode
31 4601 Coatings for Solid-State Batteries. *Joule* **2019**, *3*, 1252–1275.
- 32
33
34
35 4602 (558) Sang, J.; Yu, Y.; Wang, Z.; Shao, G. Theoretical formulation of $\text{Li}_{3a+b}\text{N}_a\text{X}_b$ (X =
36 4603 halogen) as a potential artificial solid electrolyte interphase (ASEI) to protect the Li
37 4604 anode. *Physical Chemistry Chemical Physics* **2020**, *22*, 12918–12928.
- 38
39
40
41
42 4605 (559) Glass, C. W.; Oganov, A. R.; Hansen, N. USPEX-Evolutionary crystal structure pre-
43 4606 diction. *Computer Physics Communications* **2006**, *175*, 713–720.
- 44
45
46
47 4607 (560) Oganov, A. R.; Glass, C. W. Crystal structure prediction using ab initio evolutionary
48 4608 techniques: Principles and applications. *Journal of Chemical Physics* **2006**, *124*.
- 49
50
51
52 4609 (561) Parlinski, K.; Li, Z. Q.; Kawazoe, Y. First-principles determination of the soft mode
53 4610 in cubic ZrO_2 . *Physical Review Letters* **1997**, *78*, 4063–4066.
- 54
55
56
57
58
59
60

- 1
2
3 4611 (562) Togo, A.; Oba, F.; Tanaka, I. First-principles calculations of the ferroelastic transi-
4 4612 tion between rutile-type and CaCl₂-type SiO₂ at high pressures. *Physical Review B -*
5 4613 *Condensed Matter and Materials Physics* **2008**, *78*, 1–9.
- 6
7
8
9
10 4614 (563) Hart, G. L.; Forcade, R. W. Algorithm for generating derivative structures. *Physical*
11 4615 *Review B - Condensed Matter and Materials Physics* **2008**, *77*, 1–12.
- 12
13
14
15 4616 (564) Sang, L.; Kisson, N.; Wen, F. Characterizations of dynamic interfaces in all-solid
16 4617 lithium batteries. *Journal of Power Sources* **2021**, *506*.
- 18
19
20 4618 (565) Schnell, J.; Knörzer, H.; Imbsweiler, A. J.; Reinhart, G. Solid versus Liquid—A
21 4619 Bottom-Up Calculation Model to Analyze the Manufacturing Cost of Future High-
22 4620 Energy Batteries. *Energy Technology* **2020**, *8*, 1901237.
- 23
24
25
26 4621 (566) Kato, Y.; Hori, S.; Saito, T.; Suzuki, K.; Hirayama, M.; Mitsui, A.; Yonemura, M.;
27 4622 Iba, H.; Kanno, R. High-power all-solid-state batteries using sulfide superionic con-
28 4623 ductors. *Nature Energy* **2016**, *1*, 1–7.
- 29
30
31
32
33 4624 (567) Kim, K. J.; Balaish, M.; Wadaguchi, M.; Kong, L.; Rupp, J. L. Solid-State Li–Metal
34 4625 Batteries: Challenges and Horizons of Oxide and Sulfide Solid Electrolytes and Their
35 4626 Interfaces. *Advanced Energy Materials* **2021**, *11*, 2002689.
- 36
37
38
39
40 4627 (568) Albertus, P.; Babinec, S.; Litzelman, S.; Newman, A. Status and challenges in enabling
41 4628 the lithium metal electrode for high-energy and low-cost rechargeable batteries. *Nature*
42 4629 *Energy* **2018**, *3*, 16–21.
- 43
44
45
46
47 4630 (569) Rodney, D.; Ventelon, L.; Clouet, E.; Pizzagalli, L.; Willaime, F. Ab initio modeling
48 4631 of dislocation core properties in metals and semiconductors. *Acta Materialia* **2017**,
49 4632 *124*, 633–659.
- 50
51
52
53
54 4633 (570) Clouet, E. In *Handbook of Materials Modeling: Methods: Theory and Modeling*; An-
55 4634 dreoni, W., Yip, S., Eds.; Springer International Publishing, 2020; pp 1503–1524.

- 1
2
3
4 4635 (571) Chen, H.; Liu, Q. Y.; Jing, M. X.; Chen, F.; Yuan, W. Y.; Ju, B. W.; Tu, F. Y.;
5 4636 Shen, X. Q.; Qin, S. B. Improved Interface Stability and Room-Temperature Per-
6
7 4637 formance of Solid-State Lithium Batteries by Integrating Cathode/Electrolyte and
8
9 4638 Graphite Coating. *ACS Applied Materials and Interfaces* **2020**, *12*, 15120–15127.
- 11
12 4639 (572) Ito, Y.; Yamakawa, S.; Hayashi, A.; Tatsumisago, M. Effects of the microstructure
13
14 4640 of solid-electrolyte-coated LiCoO₂ on its discharge properties in all-solid-state lithium
15
16 4641 batteries. *Journal of Materials Chemistry A* **2017**, *5*, 10658–10668.
- 18
19 4642 (573) Yin, Y.; Jiang, C.-S.; Guthrey, H.; Xiao, C.; Seitzman, N.; Ban, C.; Al-Jassim, M.
20
21 4643 Improved Stability and Cyclability of Ceramic Solid Electrolyte by Coating Polymer.
22
23 4644 *Journal of The Electrochemical Society* **2020**, *167*, 020519.
- 25
26 4645 (574) Ji, X.; Hou, S.; Wang, P.; He, X.; Piao, N.; Chen, J.; Fan, X.; Wang, C. Solid-State
27
28 4646 Electrolyte Design for Lithium Dendrite Suppression. *Advanced Materials* **2020**, *32*.
- 30
31 4647 (575) Li, H.; Lian, F.; Meng, N.; Xiong, C.; Wu, N.; Xu, B.; Li, Y. Constructing Elec-
32
33 4648 tronic and Ionic Dual Conductive Polymeric Interface in the Cathode for High-Energy-
34
35 4649 Density Solid-State Batteries. *Advanced Functional Materials* **2021**, *31*, 2008487.
- 37
38 4650 (576) Yi, J.; He, P.; Liu, H.; Ni, H.; Bai, Z.; Fan, L. Z. Manipulating interfacial stability
39
40 4651 of LiNi_{0.5}Co_{0.3}Mn_{0.2}O₂ cathode with sulfide electrolyte by nanosized LLTO coating to
41
42 4652 achieve high-performance all-solid-state lithium batteries. *Journal of Energy Chem-*
43
44 4653 *istry* **2021**, *52*, 202–209.
- 46
47 4654 (577) Dai, H.; Chen, Y.; Xu, W.; Hu, Z.; Gu, J.; Wei, X.; Xie, F.; Zhang, W.; Wei, W.;
48
49 4655 Guo, R.; Zhang, G. A Review of Modification Methods of Solid Electrolytes for All-
50
51 4656 Solid-State Sodium-Ion Batteries. *Energy Technology* **2021**, *9*, 1–13.
- 53
54 4657 (578) High Voltage Stable Polyoxalate Catholyte with Cathode Coating for All-Solid-State
55
56 4658 Li-Metal/NMC622 Batteries. *Advanced Energy Materials* **2020**, *10*, 1–11.

- 1
2
3
4 4659 (579) Jing, M. X.; Yuan, W. Y.; Shen, X. Q.; Zhang, L. K.; Yang, H.; Liu, Q. Y.; Chen, F.;
5 4660 Liu, M. Q.; Ji, Y. S. Highly efficient interface modification between poly(propylene
6 4661 carbonate)-based solid electrolytes and a lithium anode by facile graphite coating.
7 4662 *ACS Sustainable Chemistry and Engineering* **2020**, *8*, 17106–17115.
- 11
12 4663 (580) Wang, C.; Sun, X.; Yang, L.; Song, D.; Wu, Y.; Ohsaka, T.; Matsumoto, F.; Wu, J.
13 4664 In Situ Ion-Conducting Protective Layer Strategy to Stable Lithium Metal Anode for
14 4665 All-Solid-State Sulfide-Based Lithium Metal Batteries. *Advanced Materials Interfaces*
15 4666 **2021**, *8*, 1–10.
- 20
21 4667 (581) Zhao, F. et al. Tuning bifunctional interface for advanced sulfide-based all-solid-state
22 4668 batteries. *Energy Storage Materials* **2020**, *33*, 139–146.
- 25
26 4669 (582) Zhao, B.; Feng, X.; Yu, M.; Wang, W.; Hao, S.; Chen, H.; Huang, Y.; Gong, W.;
27 4670 Liu, L.; Qiu, H. Interfacial modification enabled room temperature solid-state lithium–
28 4671 metal batteries. *Ionics* **2021**, *27*, 1569–1578.
- 32
33 4672 (583) Liang, J. et al. Stabilizing and understanding the interface between nickel-rich cathode
34 4673 and PEO-based electrolyte by lithium niobium oxide coating for high-performance all-
35 4674 solid-state batteries. *Nano Energy* **2020**, *78*, 105107.
- 39
40 4675 (584) Zhang, Q.; Bruck, A. M.; Stavola, A. M.; Liang, W.; Aurora, P.; Gallaway, J. W.
41 4676 Enhanced Electrochemical Stability of Sulfide-Based $\text{LiNi}_{0.8}\text{Mn}_{0.1}\text{Co}_{0.1}\text{O}_2$ All-Solid-
42 4677 State Batteries by Ti Surface Doping. *Batteries & Supercaps* **2020**, 1–8.
- 45
46 4678 (585) Mizushima, K.; Jones, P.; Wiseman, P.; Goodenough, J. B. Li_xCoO_2 ($0 < x < -1$): A
47 4679 new cathode material for batteries of high energy density. *Materials Research Bulletin*
48 4680 **1980**, *15*, 783–789.
- 52
53 4681 (586) Rozier, P.; Tarascon, J. M. Li-rich layered oxide cathodes for next-generation Li-ion
54 4682 batteries: chances and challenges. *Journal of The Electrochemical Society* **2015**, *162*,
55 4683 A2490.

- 1
2
3
4 4684 (587) Whittingham, M. S. Materials challenges facing electrical energy storage. *MRS Bul-*
5 4685 *letin* **2008**, *33*, 411–419.
6
7
8 4686 (588) Dunn, B.; Kamath, H.; Tarascon, J.-M. Electrical energy storage for the grid: a battery
9 4687 of choices. *Science* **2011**, *334*, 928–935.
10
11
12
13 4688 (589) Liu, J.; Zhang, J.-G.; Yang, Z.; Lemmon, J. P.; Imhoff, C.; Graff, G. L.; Li, L.;
14 4689 Hu, J.; Wang, C.; Xiao, J., et al. Materials science and materials chemistry for large
15 4690 scale electrochemical energy storage: from transportation to electrical grid. *Advanced*
16 4691 *Functional Materials* **2013**, *23*, 929–946.
17
18
19
20
21
22 4692 (590) Palacin, M. R. Recent advances in rechargeable battery materials: a chemist's per-
23 4693 spective. *Chemical Society Reviews* **2009**, *38*, 2565–2575.
24
25
26 4694 (591) Masquelier, C.; Croguennec, L. Polyanionic (phosphates, silicates, sulfates) frame-
27 4695 works as electrode materials for rechargeable Li (or Na) batteries. *Chemical Reviews*
28 4696 **2013**, *113*, 6552–6591.
29
30
31
32
33 4697 (592) Bruce, P. G.; Freunberger, S. A.; Hardwick, L. J.; Tarascon, J.-M. Li–O₂ and Li–S
34 4698 batteries with high energy storage. *Nature materials* **2012**, *11*, 19.
35
36
37
38 4699 (593) Scrosati, B.; Hassoun, J.; Sun, Y.-K. Lithium-ion batteries. A look into the future.
39 4700 *Energy & Environmental Science* **2011**, *4*, 3287–3295.
40
41
42
43 4701 (594) Etacheri, V.; Marom, R.; Elazari, R.; Salitra, G.; Aurbach, D. Challenges in the
44 4702 development of advanced Li-ion batteries: a review. *Energy & Environmental Science*
45 4703 **2011**, *4*, 3243–3262.
46
47
48
49 4704 (595) Takada, K. Progress and prospective of solid-state lithium batteries. *Acta Materialia*
50 4705 **2013**, *61*, 759–770.
51
52
53
54 4706 (596) Fergus, J. W. Recent developments in cathode materials for lithium ion batteries.
55 4707 *Journal of power sources* **2010**, *195*, 939–954.
56
57
58
59
60

- 1
2
3 4708 (597) Ellis, B. L.; Lee, K. T.; Nazar, L. F. Positive electrode materials for Li-ion and Li-
4
5 4709 batteries. *Chemistry of materials* **2010**, *22*, 691–714.
6
7
8 4710 (598) He, P.; Yu, H.; Zhou, H., et al. Layered lithium transition metal oxide cathodes towards
9
10 4711 high energy lithium-ion batteries. *Journal of Materials Chemistry* **2012**, *22*, 3680–
11
12 4712 3695.
13
14
15 4713 (599) Zaghbi, K.; Guerfi, A.; Hovington, P.; Vijn, A.; Trudeau, M.; Mauger, A.; Good-
16
17 4714 enough, J.; Julien, C. Review and analysis of nanostructured olivine-based lithium
18
19 4715 rechargeable batteries: Status and trends. *Journal of Power Sources* **2013**, *232*,
20
21 4716 357–369.
22
23
24 4717 (600) Ellis, B. L.; Nazar, L. F. Sodium and sodium-ion energy storage batteries. *Current*
25
26 4718 *Opinion in Solid State and Materials Science* **2012**, *16*, 168–177.
27
28
29 4719 (601) Kim, S.-W.; Seo, D.-H.; Ma, X.; Ceder, G.; Kang, K. Electrode materials for recharge-
30
31 4720 able sodium-ion batteries: potential alternatives to current lithium-ion batteries. *Ad-*
32
33 4721 *vanced Energy Materials* **2012**, *2*, 710–721.
34
35
36 4722 (602) Palomares, V.; Serras, P.; Villaluenga, I.; Hueso, K. B.; Carretero-González, J.;
37
38 4723 Rojo, T. Na-ion batteries, recent advances and present challenges to become low cost
39
40 4724 energy storage systems. *Energy & Environmental Science* **2012**, *5*, 5884–5901.
41
42
43 4725 (603) Fergus, J. W. Ion transport in sodium ion conducting solid electrolytes. *Solid State*
44
45 4726 *Ionics* **2012**, *227*, 102–112.
46
47
48 4727 (604) Yabuuchi, N.; Kajiyama, M.; Iwatate, J.; Nishikawa, H.; Hitomi, S.; Okuyama, R.;
49
50 4728 Usui, R.; Yamada, Y.; Komaba, S. P2-type $\text{Na}_x[\text{Fe}_{1/2}\text{Mn}_{1/2}]\text{O}_2$ made from earth-
51
52 4729 abundant elements for rechargeable Na batteries. *Nature materials* **2012**, *11*, 512–517.
53
54 4730 (605) Daniel, C.; Mohanty, D.; Li, J.; Wood, D. L. Cathode materials review. **2014**, *1597*,
55
56 4731 26–43.
57
58
59
60

- 1
2
3 4732 (606) Islam, M. S.; Fisher, C. A. Lithium and sodium battery cathode materials: computa-
4
5 4733 tional insights into voltage, diffusion and nanostructural properties. *Chemical Society*
6
7 4734 *Reviews* **2014**, *43*, 185–204.
8
9
10 4735 (607) Myung, S.-T.; Maglia, F.; Park, K.-J.; Yoon, C. S.; Lamp, P.; Kim, S.-J.; Sun, Y.-K.
11
12 4736 Nickel-rich layered cathode materials for automotive lithium-ion batteries: achieve-
13
14 4737 ments and perspectives. *ACS Energy Letters* **2017**, *2*, 196–223.
15
16
17 4738 (608) Mo, J. Y.; Jeon, W. The impact of electric vehicle demand and battery recycling on
18
19 4739 price dynamics of lithium-ion battery cathode materials: A vector error correction
20
21 4740 model (VECM) analysis. *Sustainability* **2018**, *10*, 2870.
22
23
24 4741 (609) Goonetilleke, D.; Sharma, N.; Pang, W. K.; Peterson, V. K.; Petibon, R.;
25
26 4742 Li, J.; Dahn, J. Structural Evolution and High-Voltage Structural Stability of
27
28 4743 $\text{Li}(\text{Ni}_x\text{Mn}_y\text{Co}_z)\text{O}_2$ Electrodes. *Chemistry of Materials* **2018**, *31*, 376–386.
29
30
31 4744 (610) Chen, Z.; Lu, Z.; Dahn, J. Staging phase transitions in Li_xCoO_2 . *Journal of the Elec-*
32
33 4745 *trochemical Society* **2002**, *149*, A1604.
34
35
36 4746 (611) Min, K.; Kim, K.; Jung, C.; Seo, S.-W.; Song, Y. Y.; Lee, H. S.; Shin, J.; Cho, E. A
37
38 4747 comparative study of structural changes in lithium nickel cobalt manganese oxide as
39
40 4748 a function of Ni content during delithiation process. *Journal of Power Sources* **2016**,
41
42 4749 *315*, 111–119.
43
44
45 4750 (612) Tian, Z.; Yu, H.; Zhang, Z.; Xu, X. Performance Improvements of Cobalt Oxide
46
47 4751 Cathodes for Rechargeable Lithium Batteries. *ChemBioEng Reviews* **2018**, *5*, 111–
48
49 4752 118.
50
51 4753 (613) Paulsen, J.; Thomas, C.; Dahn, J. O_2 Structure $\text{Li}_{2/3}[\text{Ni}_{1/3}\text{Mn}_{2/3}]\text{O}_2$: A New Layered
52
53 4754 Cathode Material for Rechargeable Lithium Batteries. I. Electrochemical Properties.
54
55 4755 *Journal of the Electrochemical Society* **2000**, *147*, 861.
56
57
58
59
60

- 1
2
3
4 4756 (614) Paulsen, J.; Dahn, J. O₂-Type Li_{2/3}[Ni_{1/3}Mn_{2/3}]O₂: A New Layered Cathode Mate-
5 4757 rial for Rechargeable Lithium Batteries II. Structure, Composition, and Properties.
6
7 4758 *Journal of the Electrochemical Society* **2000**, *147*, 2478.
8
9
10 4759 (615) Lu, Z.; MacNeil, D.; Dahn, J. Layered Li[Ni_xCo_{1-2x}Mn_x]O₂ Cathode materials for
11
12 4760 lithium-ion batteries. *Electrochemical and Solid State Letters* **2001**, *4*, A200.
13
14
15 4761 (616) Ohzuku, T.; Makimura, Y. Layered lithium insertion material of LiNi_{1/2}Mn_{1/2}O₂: A
16
17 4762 possible alternative to LiCoO₂ for advanced lithium-ion batteries. *Chemistry Letters*
18
19 4763 **2001**, *30*, 744–745.
20
21
22 4764 (617) Duan, Y.; Yang, L.; Zhang, M.-J.; Chen, Z.; Bai, J.; Amine, K.; Pan, F.; Wang, F.
23
24 4765 Insights into Li/Ni ordering and surface reconstruction during synthesis of Ni-rich
25
26 4766 layered oxides. *Journal of Materials Chemistry A* **2019**, *7*, 513–519.
27
28
29 4767 (618) Zhang, N.; Li, J.; Li, H.; Liu, A.; Huang, Q.; Ma, L.; Li, Y.; Dahn, J. R. Structural,
30
31 4768 Electrochemical, and Thermal Properties of Nickel-Rich LiNi_xMn_yCo_zO₂ Materials.
32
33 4769 *Chemistry of Materials* **2018**, *30*, 8852–8860.
34
35
36 4770 (619) Azevedo, M.; Campagnol, N.; Hagenbruch, T.; Hoffman, K.; Lala, A.; Ramsbot-
37
38 4771 tom, O. *Metals and Mining* **2018**, [https://www.mckinsey.com/industries/metals-and-](https://www.mckinsey.com/industries/metals-and-mining/our-insights/lithium-and-cobalt-a-tale-of-two-commodities)
39
40 4772 [mining/our-insights/lithium-and-cobalt-a-tale-of-two-commodities](https://www.mckinsey.com/industries/metals-and-mining/our-insights/lithium-and-cobalt-a-tale-of-two-commodities).
41
42
43 4773 (620) Sathiya, M.; Rousse, G.; Ramesha, K.; Laisa, C.; Vezin, H.; Sougrati, M. T.; Dou-
44
45 4774 blet, M.-L.; Foix, D.; Gonbeau, D.; Walker, W., et al. Reversible anionic redox chem-
46
47 4775 istry in high-capacity layered-oxide electrodes. *Nature materials* **2013**, *12*, 827–835.
48
49 4776 (621) Lee, J.; Urban, A.; Li, X.; Su, D.; Hautier, G.; Ceder, G. Unlocking the potential of
50
51 4777 cation-disordered oxides for rechargeable lithium batteries. *Science* **2014**, *343*, 519–
52
53 4778 522.
54
55
56
57
58
59
60

- 1
2
3
4 4779 (622) Oishi, M.; Yogi, C.; Watanabe, I.; Ohta, T.; Orikasa, Y.; Uchimoto, Y.; Ogumi, Z.
5
6 4780 Direct observation of reversible charge compensation by oxygen ion in Li-rich man-
7
8 4781 ganese layered oxide positive electrode material, $\text{Li}_{1.16}\text{Ni}_{0.15}\text{Co}_{0.19}\text{Mn}_{0.50}\text{O}_2$. *Journal of*
9
10 4782 *Power Sources* **2015**, *276*, 89–94.
- 11
12 4783 (623) Seo, D.-H.; Lee, J.; Urban, A.; Malik, R.; Kang, S.; Ceder, G. The structural and
13
14 4784 chemical origin of the oxygen redox activity in layered and cation-disordered Li-excess
15
16 4785 cathode materials. *Nature Chemistry* **2016**, *8*, 692–697.
- 17
18
19 4786 (624) Gent, W. E. et al. Coupling between oxygen redox and cation migration explains un-
20
21 4787 usual electrochemistry in lithium-rich layered oxides. *Nature Communications* **2017**,
22
23 4788 *8*, 2091.
- 24
25
26 4789 (625) Assat, G.; Tarascon, J.-M. Fundamental understanding and practical challenges of
27
28 4790 anionic redox activity in Li-ion batteries. *Nature Energy* **2018**, *3*, 373–386.
- 29
30
31 4791 (626) Naylor, A. J.; Makkos, E.; Maibach, J.; Guerrini, N.; Sobkowiak, A.; Björklund, E.;
32
33 4792 Lozano, J. G.; Menon, A. S.; Younesi, R.; Roberts, M. R., et al. Depth-dependent
34
35 4793 oxygen redox activity in lithium-rich layered oxide cathodes. *Journal of Materials*
36
37 4794 *Chemistry A* **2019**, *7*, 25355–25368.
- 38
39 4795 (627) House, R. A.; Maitra, U.; Pérez-Osorio, M. A.; Lozano, J. G.; Jin, L.; Somerville, J. W.;
40
41 4796 Duda, L. C.; Nag, A.; Walters, A.; Zhou, K.-J.; Roberts, M. R.; Bruce, P. G. Super-
42
43 4797 structure control of first-cycle voltage hysteresis in oxygen-redox cathodes. *Nature*
44
45 4798 **2020**, *577*, 502–508.
- 46
47
48 4799 (628) House, R. A.; Rees, G. J.; Pérez-Osorio, M. A.; Marie, J. J.; Boivin, E.; Robert-
49
50 4800 son, A. W.; Nag, A.; Garcia-Fernandez, M.; Zhou, K. J.; Bruce, P. G. First-cycle
51
52 4801 voltage hysteresis in Li-rich 3d cathodes associated with molecular O_2 trapped in the
53
54 4802 bulk. *Nature Energy* **2020**, *5*, 777–785.

- 1
2
3
4 4803 (629) Hy, S.; Liu, H.; Zhang, M.; Qian, D.; Hwang, B.-J.; Meng, Y. S. Performance and
5 4804 design considerations for lithium excess layered oxide positive electrode materials for
6
7 4805 lithium ion batteries. *Energy & Environmental Science* **2016**, *9*, 1931–1954.
8
9
10 4806 (630) Urban, A.; Lee, J.; Ceder, G. The Configurational Space of Rocksalt-Type Oxides
11
12 4807 for High-Capacity Lithium Battery Electrodes. *Advanced Energy Materials* **2014**, *4*,
13
14 4808 1400478.
15
16
17 4809 (631) Lee, J.; Seo, D.-H.; Balasubramanian, M.; Twu, N.; Li, X.; Ceder, G. A new
18
19 4810 class of high capacity cation-disordered oxides for rechargeable lithium batteries:
20
21 4811 Li–Ni–Ti–Mo oxides. *Energy & Environmental Science* **2015**, *8*, 3255–3265.
22
23
24 4812 (632) Yabuuchi, N.; Nakayama, M.; Takeuchi, M.; Komaba, S.; Hashimoto, Y.; Mukai, T.;
25
26 4813 Shiiba, H.; Sato, K.; Kobayashi, Y.; Nakao, A.; Yonemura, M.; Yamanaka, K.; Mit-
27
28 4814 suhara, K.; Ohta, T. Origin of stabilization and destabilization in solid-state redox
29
30 4815 reaction of oxide ions for lithium-ion batteries. *Nature Communications* **2016**, *7*, 1–
31
32 4816 10.
33
34
35 4817 (633) Freire, M.; Kosova, N. V.; Jordy, C.; Chateigner, D.; Lebedev, O. I.; Maignan, A.;
36
37 4818 Pralong, V. A new active Li–Mn–O compound for high energy density Li-ion batteries.
38
39 4819 *Nature Materials* **2016**, *15*, 173–177.
40
41
42 4820 (634) Yao, Z.; Kim, S.; He, J.; Hegde, V. I.; Wolverton, C. Interplay of cation and anion redox
43
44 4821 in $\text{Li}_4\text{Mn}_2\text{O}_5$ cathode material and prediction of improved $\text{Li}_4(\text{Mn},\text{M})_2\text{O}_5$ electrodes
45
46 4822 for Li-ion batteries. *Science Advances* **2018**, *4*, eaao6754.
47
48
49 4823 (635) Bhandari, A.; Jindal, P.; Bhattacharya, J. Discovery of new ground state structures
50
51 4824 for $\text{Li}_4\text{Mn}_2\text{O}_5$ and V_2O_5 from first principles. *Computational Materials Science* **2019**,
52
53 4825 *159*, 454–459.
54
55 4826 (636) Nakajima, M.; Yabuuchi, N. Lithium-Excess Cation-Disordered Rocksalt-Type Oxide
56
57
58
59
60

- 1
2
3
4 4827 with Nanoscale Phase Segregation: $\text{Li}_{1.25}\text{Nb}_{0.25}\text{V}_{0.5}\text{O}_2$. *Chemistry of Materials* **2017**,
5 4828 *29*, 6927–6935.
6
7
8 4829 (637) Yabuuchi, N.; Takeuchi, M.; Nakayama, M.; Shiiba, H.; Ogawa, M.; Nakayama, K.;
9
10 4830 Ohta, T.; Endo, D.; Ozaki, T.; Inamasu, T.; Sato, K.; Komaba, S. High-capacity
11
12 4831 electrode materials for rechargeable lithium batteries: Li_3NbO_4 -based system with
13
14 4832 cation-disordered rocksalt structure. *Proceedings of the National Academy of Sciences*
15
16 4833 **2015**, *112*, 7650–7655.
17
18
19 4834 (638) Wang, R.; Li, X.; Liu, L.; Lee, J.; Seo, D.-H.; Bo, S.-H.; Urban, A.; Ceder, G. A
20
21 4835 disordered rock-salt Li-excess cathode material with high capacity and substantial
22
23 4836 oxygen redox activity: $\text{Li}_{1.25}\text{Nb}_{0.25}\text{Mn}_{0.5}\text{O}_2$. *Electrochemistry Communications* **2015**,
24
25 4837 *60*, 70–73.
26
27
28 4838 (639) Sharpe, R.; House, R. A.; Clarke, M. J.; Forstermann, D.; Marie, J.-J.; Cibin, G.;
29
30 4839 Zhou, K.-J.; Playford, H. Y.; Bruce, P. G.; Islam, M. S. Redox Chemistry and the
31
32 4840 Role of Trapped Molecular O_2 in Li-Rich Disordered Rocksalt Oxyfluoride Cathodes.
33
34 4841 *J. Am. Chem. Soc.* **2020**, *142*, 21799–21809.
35
36
37 4842 (640) House, R. A.; Jin, L.; Maitra, U.; Tsuruta, K.; Somerville, J. W.; Förstermann, D. P.;
38
39 4843 Massel, F.; Duda, L.; Roberts, M. R.; Bruce, P. G. Lithium manganese oxyfluoride
40
41 4844 as a new cathode material exhibiting oxygen redox. *Energy & Environmental Science*
42
43 4845 **2018**, *11*, 926–932.
44
45
46 4846 (641) Lun, Z.; Ouyang, B.; Cai, Z.; Clément, R. J.; Kwon, D.-H.; Huang, J.; Papp, J. K.;
47
48 4847 Balasubramanian, M.; Tian, Y.; McCloskey, B. D.; Ji, H.; Kim, H.; Kitchaev, D. A.;
49
50 4848 Ceder, G. Design Principles for High-Capacity Mn-Based Cation-Disordered Rocksalt
51
52 4849 Cathodes. *Chem* 153–168.
53
54 4850 (642) Chen, R.; Ren, S.; Yavuz, M.; Guda, A. A.; Shapovalov, V.; Witter, R.; Fichtner, M.;

- 1
2
3
4 4851 Hahn, H. Li⁺ intercalation in isostructural Li₂VO₃ and Li₂VO₂F with O²⁻ and mixed
5 4852 O²⁻/F⁻ anions. *Physical Chemistry Chemical Physics* **2015**, *17*, 17288–17295.
6
7
8 4853 (643) Chen, R.; Ren, S.; Knapp, M.; Wang, D.; Witter, R.; Fichtner, M.; Hahn, H. Dis-
9
10 4854 ordered Lithium-Rich Oxyfluoride as a Stable Host for Enhanced Li⁺ Intercalation
11
12 4855 Storage. *Advanced Energy Materials* **2015**, *5*, 1401814.
13
14
15 4856 (644) Baur, C. et al. Improved cycling stability in high-capacity Li-rich vanadium containing
16
17 4857 disordered rock salt oxyfluoride cathodes. *Journal of Materials Chemistry A* **2019**, *7*,
18
19 4858 21244–21253.
20
21
22 4859 (645) Cambaz, M. A.; Vinayan, B. P.; Pervez, S. A.; Johnsen, R. E.; Geßwein, H.;
23
24 4860 Guda, A. A.; Rusalev, Y. V.; Kinyanjui, M. K.; Kaiser, U.; Fichtner, M. Suppress-
25
26 4861 ing Dissolution of Vanadium from Cation-Disordered Li_{2-x}VO₂F via a Concentrated
27
28 4862 Electrolyte Approach. *Chemistry of Materials* **2019**, *31*, 7941–7950.
29
30
31 4863 (646) Baur, C.; Lacatusu, M.-E.; Fichtner, M.; Johnsen, R. E. Insights into Structural Trans-
32
33 4864 formations in the Local Structure of Li₂VO₂F Using Operando X-ray Diffraction and
34
35 4865 Total Scattering: Amorphization and Recrystallization. *ACS Applied Materials & In-*
36
37 4866 *terfaces* **2020**, *12*, 27010–27016.
38
39 4867 (647) Källquist, I.; Naylor, A. J.; Baur, C.; Chable, J.; Kullgren, J.; Fichtner, M.; Ed-
40
41 4868 ström, K.; Brandell, D.; Hahlin, M. Degradation Mechanisms in Li₂VO₂F Li-Rich
42
43 4869 Disordered Rock-Salt Cathodes. *Chemistry of Materials* **2019**, *31*, 6084–6096.
44
45
46 4870 (648) Chang, J. H.; Baur, C.; Mba, J.-M. A.; Arçon, D.; Mali, G.; Alwast, D.; Behm, R. J.;
47
48 4871 Fichtner, M.; Vegge, T.; Lastra, J. M. G. Superoxide Formation in Li₂VO₂F Cathode
49
50 4872 Material – a Combined Computational and Experimental Investigation of Anionic
51
52 4873 Redox Activity. *Journal of Materials Chemistry A* **2020**, *8*, 16551–16559.
53
54
55 4874 (649) Lee, J.; Kitchaev, D. A.; Kwon, D.-H.; Lee, C.-W.; Papp, J. K.; Liu, Y.-S.; Lun, Z.; Clé-
56
57 4875 ment, R. J.; Shi, T.; McCloskey, B. D.; Guo, J.; Balasubramanian, M.; Ceder, G. Re-

- 4876 versible $\text{Mn}^{2+}/\text{Mn}^{4+}$ double redox in lithium-excess cathode materials. *Nature* **2018**,
4877 556, 185–190.
- 4878 (650) Freire, M.; Lebedev, O.; Maignan, A.; Jordy, C.; Pralong, V. Nanostructured Li_2MnO_3 :
4879 a disordered rock salt type structure for high energy density Li ion batteries. *Journal*
4880 *of Materials Chemistry A* **2017**, 5, 21898–21902.
- 4881 (651) Jacquet, Q.; Iadecola, A.; Saubanere, M.; Li, H.; Berg, E. J.; Rousse, G.; Cabana, J.;
4882 Doublet, M. L.; Tarascon, J. M. Charge Transfer Band Gap as an Indicator of Hys-
4883 teresis in Li-Disordered Rock Salt Cathodes for Li-Ion Batteries. *J. Am. Chem. Soc.*
4884 **2019**, 141, 11452–11464.
- 4885 (652) Clément, R.; Lun, Z.; Ceder, G. Cation-disordered rocksalt transition metal oxides and
4886 oxyfluorides for high energy lithium-ion cathodes. *Energy & Environmental Science*
4887 **2020**, 13, 345–373.
- 4888 (653) Nyttén, A.; Abouimrane, A.; Armand, M.; Gustafsson, T.; Thomas, J. O. Electrochem-
4889 ical performance of $\text{Li}_2\text{FeSiO}_4$ as a new Li-battery cathode material. *Electrochemistry*
4890 *communications* **2005**, 7, 156–160.
- 4891 (654) Sirisopanaporn, C.; Dominko, R.; Masquelier, C.; Armstrong, A. R.; Mali, G.;
4892 Bruce, P. G. Polymorphism in $\text{Li}_2(\text{Fe,Mn})\text{SiO}_4$: A combined diffraction and NMR
4893 study. *Journal of Materials Chemistry* **2011**, 21, 17823–17831.
- 4894 (655) Islam, M. S.; Dominko, R.; Masquelier, C.; Sirisopanaporn, C.; Armstrong, A. R.;
4895 Bruce, P. G. Silicate cathodes for lithium batteries: alternatives to phosphates? *Jour-*
4896 *nal of Materials Chemistry* **2011**, 21, 9811–9818.
- 4897 (656) Padhi, A.; Nanjundaswamy, K.; Masquelier, C.; Goodenough, J. Mapping of transition
4898 metal redox energies in phosphates with NASICON structure by lithium intercalation.
4899 *Journal of the Electrochemical Society* **1997**, 144, 2581.

- 1
2
3
4 4900 (657) Tygesen, A. S.; Chang, J. H.; Vegge, T.; García-Lastra, J. M. Computational frame-
5 4901 work for a systematic investigation of anionic redox process in Li-rich compounds. *npj*
6
7 4902 *Computational Materials* **2020**, *6*, 1–9.
8
9
10 4903 (658) Armstrong, A. R.; Bruce, P. G. Synthesis of layered LiMnO_2 as an electrode for
11
12 4904 rechargeable lithium batteries. *Nature* **1996**, *381*, 499–500.
13
14
15 4905 (659) Mosbah, A.; Verbaere, A.; Tournoux, M. Phases Li_xMnO_2 rattachees au type spinelle.
16
17 4906 *Materials research bulletin* **1983**, *18*, 1375–1381.
18
19
20 4907 (660) Dittrich, G.; Hoppe, R. Zur Kristallstruktur von LiMnO_2 . *Zeitschrift für anorganische*
21
22 4908 *und allgemeine Chemie* **1969**, *368*, 262–270.
23
24
25 4909 (661) Gao, P.; Ishikawa, R.; Tochigi, E.; Kumamoto, A.; Shibata, N.; Ikuhara, Y. Atomic-
26
27 4910 Scale Tracking of a Phase Transition from Spinel to Rocksalt in Lithium Manganese
28
29 4911 Oxide. *Chemistry of Materials* **2017**, *29*, 1006–1013.
30
31 4912 (662) Chen, B.; Ben, L.; Yu, H.; Chen, Y.; Huang, X. Understanding Surface Structural
32
33 4913 Stabilization of the High-Temperature and High-Voltage Cycling Performance of Al^{3+} -
34
35 4914 Modified LiMn_2O_4 Cathode Material. *ACS Applied Materials & Interfaces* **2018**, *10*,
36
37 4915 550–559.
38
39
40 4916 (663) Reed, J.; Ceder, G.; Van Der Ven, A. Layered-to-spinel phase transition in Li_xMnO_2 .
41
42 4917 *Electrochemical and Solid State Letters* **2001**, *4*, A78.
43
44
45 4918 (664) Bruce, P. G.; Scrosati, B.; Tarascon, J.-M. Nanomaterials for rechargeable lithium
46
47 4919 batteries. *Angewandte Chemie International Edition* **2008**, *47*, 2930–2946.
48
49
50 4920 (665) Franger, S.; Benoit, C.; Bourbon, C.; Le Cras, F. Chemistry and electrochemistry of
51
52 4921 composite LiFePO_4 materials for secondary lithium batteries. *Journal of Physics and*
53
54 4922 *Chemistry of Solids* **2006**, *67*, 1338–1342.
55
56
57
58
59
60

- 1
2
3
4 4923 (666) Ellis, B.; Kan, W. H.; Makahnouk, W.; Nazar, L. Synthesis of nanocrystals and mor-
5
6 4924 phology control of hydrothermally prepared LiFePO₄. *Journal of Materials Chemistry*
7
8 4925 **2007**, *17*, 3248–3254.
- 9
10 4926 (667) Malik, R.; Burch, D.; Bazant, M.; Ceder, G. Particle size dependence of the ionic
11
12 4927 diffusivity. *Nano letters* **2010**, *10*, 4123–4127.
- 13
14
15 4928 (668) Ledwaba, R. S.; Ngoepe, P.; Sayle, D. Modeling Diffusion-Induced Stress In Li-Mn-O
16
17 4929 Nanocomposite Cathode Materials. APS March Meeting Abstracts. 2018; p E20.006.
- 18
19
20 4930 (669) Sayle, T. X.; Maphanga, R. R.; Ngoepe, P. E.; Sayle, D. C. Predicting the electrochem-
21
22 4931 ical properties of MnO₂ nanomaterials used in rechargeable Li batteries: simulating
23
24 4932 nanostructure at the atomistic level. *Journal of the American Chemical Society* **2009**,
25
26 4933 *131*, 6161–6173.
- 27
28
29 4934 (670) Gupta, P. K.; Bhandari, A.; Bhattacharya, J.; Pala, R. G. S. Correlating Voltage
30
31 4935 Profile to Molecular Transformations in Ramsdellite MnO₂ and Its Implication for
32
33 4936 Polymorph Engineering of Lithium Ion Battery Cathodes. *The Journal of Physical*
34
35 4937 *Chemistry C* **2018**, *122*, 11689–11700.
- 36
37
38 4938 (671) Gupta, P. K.; Bhandari, A.; Bhattacharya, J.; Ganesh S Pala, R. Higher voltage,
39
40 4939 wider voltage plateau, longer cycle life, and faster kinetics via thermally modulated
41
42 4940 interfaces between Ramsdellite and Pyrolusite MnO₂ for lithium-ion battery cathodes.
43
44 4941 *Journal of Power Sources* **2020**, *450*, 227619.
- 45
46 4942 (672) Moriwake, H.; Kuwabara, A.; Fisher, C. A.; Huang, R.; Hitosugi, T.; Ikuhara, Y. H.;
47
48 4943 Oki, H.; Ikuhara, Y. First-Principles Calculations of Lithium-Ion Migration at a Co-
49
50 4944 herent Grain Boundary in a Cathode Material, LiCoO₂. *Advanced Materials* **2013**,
51
52 4945 *25*, 618–622.
- 53
54
55 4946 (673) Dixit, M.; Engel, H.; Eitan, R.; Aurbach, D.; Levi, M. D.; Kosa, M.; Major, D. T.

- 4947 Classical and Quantum Modeling of Li and Na Diffusion in FePO_4 . *The Journal of*
4948 *Physical Chemistry C* **2015**, *119*, 15801–15809.
- 4949 (674) Morgan, D.; Van der Ven, A.; Ceder, G. Li Conductivity in Li_xMPO_4
4950 (M=Mn,Fe,Co,Ni) Olivine Materials. *Electrochemical and Solid-State Letters* **2004**,
4951 *7*, A30–A32.
- 4952 (675) Ouyang, C.; Shi, S.; Wang, Z.; Huang, X.; Chen, L. First-principles study of Li ion
4953 diffusion in LiFePO_4 . *Physical Review B* **2004**, *69*, 104303.
- 4954 (676) Islam, M. S.; Driscoll, D. J.; Fisher, C. A. J.; Slater, P. R. Atomic-scale investigation of
4955 defects, dopants, and lithium transport in the LiFePO_4 olivine-type battery material.
4956 *Chemistry of Materials* **2005**, *17*, 5085–5092.
- 4957 (677) Amin, R.; Balaya, P.; Maier, J. Anisotropy of electronic and ionic transport in LiFePO_4
4958 single crystals. *Electrochemical and Solid State Letters* **2006**, *10*, A13.
- 4959 (678) Van der Ven, A.; Ceder, G. Lithium diffusion in layered Li_xCoO_2 . *Electrochemical and*
4960 *Solid State Letters* **2000**, *3*, 301.
- 4961 (679) Thackeray, M. M. Manganese oxides for lithium batteries. *Progress in Solid State*
4962 *Chemistry* **1997**, *25*, 1–71.
- 4963 (680) Proell, J.; Kohler, R.; Mangang, A.; Ulrich, S.; Ziebert, C.; Pfleging, W. 3D structures
4964 in battery materials. *Journal of Laser Micro Nanoengineering* **2012**, *7*, 97.
- 4965 (681) Nishimura, S.-i.; Kobayashi, G.; Ohoyama, K.; Kanno, R.; Yashima, M.; Yamada, A.
4966 Experimental visualization of lithium diffusion in Li_xFePO_4 . *Nature materials* **2008**,
4967 *7*, 707–711.
- 4968 (682) Van der Ven, A.; Thomas, J. C.; Xu, Q.; Swoboda, B.; Morgan, D. Nondilute diffusion
4969 from first principles: Li diffusion in Li_xTiS_2 . *Physical Review B* **2008**, *78*, 104306.

- 1
2
3
4 4970 (683) Bhattacharya, J.; Van der Ven, A. First-principles study of competing mechanisms of
5
6 4971 nondilute Li diffusion in spinel Li_xTiS_2 . *Physical Review B* **2011**, *83*, 144302.
7
8
9 4972 (684) Bhattacharya, J.; Van der Ven, A. Phase stability and nondilute Li diffusion in spinel
10
11 4973 $\text{Li}_{1+x}\text{Ti}_2\text{O}_4$. *Physical Review B* **2010**, *81*, 104304.
12
13 4974 (685) Van Der Ven, A.; Bhattacharya, J.; Belak, A. A. Understanding Li diffusion in Li-
14
15 4975 intercalation compounds. *Accounts of Chemical Research* **2013**, *46*, 1216–1225.
16
17
18 4976 (686) Van der Ven, A.; Ceder, G. Lithium diffusion mechanisms in layered intercalation
19
20 4977 compounds. *Journal of power sources* **2001**, *97*, 529–531.
21
22
23 4978 (687) Choi, S. H.; Shlyakhtin, O.; Kim, J.; Yoon, Y. S. Structural and electrochemical
24
25 4979 properties of $\text{Li}_{1+x}\text{Ni}_{0.5}\text{Mn}_{0.5}\text{O}_{2+\delta}$ ($0 \leq x \leq 0.7$) cathode materials for lithium-ion
26
27 4980 batteries. *Journal of power sources* **2005**, *140*, 355–360.
28
29
30 4981 (688) Kang, K.; Meng, Y. S.; Breger, J.; Grey, C. P.; Ceder, G. Electrodes with high power
31
32 4982 and high capacity for rechargeable lithium batteries. *Science* **2006**, *311*, 977–980.
33
34
35 4983 (689) Laubach, S.; Laubach, S.; Schmidt, P. C.; Gröting, M.; Albe, K.; Jaegermann, W.;
36
37 4984 Wolf, W. Structure, Electronic Structure and Defect Formation Energies of
38
39 4985 $\text{Li}_x\text{Co}_{1-y}\text{Ni}_y\text{O}_2$ as a Function of x ($0 < x < 1$) and y ($y = 0, 0.5, 1$). *Zeitschrift*
40
41 4986 *für Physikalische Chemie* **2009**, *223*, 1327–1340.
42
43
44 4987 (690) Lee, E.; Persson, K. A. Solid-Solution Li Intercalation as a Function of Cation Or-
45
46 4988 der/Disorder in the High-Voltage $\text{Li}_x\text{Ni}_{0.5}\text{Mn}_{1.5}\text{O}_4$ Spinel. *Chemistry of Materials*
47
48 4989 **2013**, *25*, 2885–2889.
49
50
51 4990 (691) Hao, S.; Lu, Z.; Wolverton, C. Quaternary phase diagrams of spinel
52
53 4991 $\text{Li}_y\text{□}_{1-y}\text{Mn}_x\text{Ni}_{2-x}\text{O}_4$ and composite cathode voltages for concentration gradient ma-
54
55 4992 terials. *Physical Review B* **2016**, *94*, 014114.
56
57
58
59
60

- 1
2
3 4993 (692) Capsoni, D.; Bini, M.; Chiodelli, G.; Mustarelli, P.; Massarotti, V.; Azzoni, C. B.;
4
5 4994 Mozzati, M. C.; Linati, L. Inhibition of Jahn-Teller Cooperative Distortion in LiMn_2O_4
6
7 4995 Spinel by Ga^{3+} Doping. *The Journal of Physical Chemistry B* **2002**, *106*, 7432–7438.
8
9
10 4996 (693) Singh, G.; Gupta, S.; Prasad, R.; Auluck, S.; Gupta, R.; Sil, A. Suppression of Jahn–
11
12 4997 Teller distortion by chromium and magnesium doping in spinel LiMn_2O_4 : A first–
13
14 4998 principles study using GGA and GGA+U. *Journal of Physics and Chemistry of Solids*
15
16 4999 **2009**, *70*, 1200–1206.
17
18
19 5000 (694) Padhi, A.; Nanjundaswamy, K.; Goodenough, J. Phospho-olivines as positive-electrode
20
21 5001 materials for rechargeable lithium batteries. *Journal of the Electrochemical Society*
22
23 5002 **1997**, *144*, 1188–1194.
24
25
26 5003 (695) Thackeray, M. M.; David, W. I. F.; Bruce, P. G.; Goodenough, P. G. Lithium Insertion
27
28 5004 into Manganese Spinels. *Materials Research Bulletin* **1983**, *18*, 461–472.
29
30
31 5005 (696) Koga, H.; Croguennec, L.; Menetrier, M.; Douhiol, K.; Belin, S.; Bourgeois, L.;
32
33 5006 Suard, E.; Weill, F. Reversible Oxygen Participation to the Redox Processes Revealed
34
35 5007 for $\text{Li}_{1.20}\text{Mn}_{0.54}\text{Co}_{0.13}\text{Ni}_{0.13}\text{O}_2$. *J. Electrochem. Soc.* **2013**, *160*, A786–A792.
36
37
38 5008 (697) Sathiya, M.; Lerich, J.-B.; Salager, E.; Gourier, D.; Tarascon, J.-M.; Vezin, H. Electron
39
40 5009 paramagnetic resonance imaging for real-time monitoring of Li-ion batteries. *Nat.*
41
42 5010 *Commun.* **2015**, *6*, 6276.
43
44
45 5011 (698) McCalla, E.; Abakumov, A. M.; Saubanère, M.; Foix, D.; Berg, E. J.; Rouse, G.;
46
47 5012 Doublet, M.-L.; Gonbeau, D.; Novák, P.; Van Tendeloo, G., et al. Visualization of OO
48
49 5013 peroxo-like dimers in high-capacity layered oxides for Li-ion batteries. *Science* **2015**,
50
51 5014 *350*, 1516–1521.
52
53
54 5015 (699) Cao, T.; Shi, C.; Zhao, N.; He, C.; Li, J.; Liu, E. Understanding the Electrochemi-
55
56 5016 cal Properties of Li-Rich Cathode Materials from First-Principles Calculations. *The*
57
58 5017 *Journal of Physical Chemistry C* **2015**, *119*, 28749–28756.
59
60

- 1
2
3
4 5018 (700) Shimoda, K.; Minato, T.; Nakanishi, K.; Komatsu, H.; Matsunaga, T.; Tanida, H.;
5
6 5019 Arai, H.; Ukyo, Y.; Uchimoto, Y.; Ogumi, Z. Oxidation behaviour of lattice oxygen
7
8 5020 in Li-rich manganese-based layered oxide studied by hard X-ray photoelectron spec-
9
10 5021 troscopy. *J. Mater. Chem. A* **2016**, *4*, 5909–5916.
- 11
12 5022 (701) Chen, H.; Islam, M. S. Lithium Extraction Mechanism in Li-Rich Li_2MnO_3 Involving
13
14 5023 Oxygen Hole Formation and Dimerization. *Chemistry of Materials* **2016**, *28*, 6656–
15
16 5024 6663.
- 17
18
19 5025 (702) Luo, K.; Roberts, M. R.; Hao, R.; Guerrini, N.; Pickup, D. M.; Liu, Y.-S.; Edström, K.;
20
21 5026 Guo, J.; Chadwick, A. V.; Duda, L. C.; Bruce, P. G. Charge-compensation in 3d-
22
23 5027 transition-metal-oxide intercalation cathodes through the generation of localized elec-
24
25 5028 tron holes on oxygen. *Nature Chemistry* **2016**, *8*, 684–691.
- 26
27
28 5029 (703) Muhammad, S.; Kim, H.; Kim, Y.; Kim, D.; Song, J. H.; Yoon, J.; Park, J.-H.;
29
30 5030 Ahn, S.-J.; Kang, S.-H.; Thackeray, M. M.; Yoon, W.-S. Evidence of reversible oxy-
31
32 5031 gen participation in anomalously high capacity Li- and Mn-rich cathodes for Li-ion
33
34 5032 batteries. *Nano Energy* **2016**, *21*, 172–184.
- 35
36 5033 (704) Zhan, C. et al. Enabling the high capacity of lithium-rich anti-fluorite lithium iron
37
38 5034 oxide by simultaneous anionic and cationic redox. *Nature Energy* **2017**, *2*, 963–971.
- 39
40
41 5035 (705) Zheng, J.; Myeong, S.; Cho, W.; Yan, P.; Xiao, J.; Wang, C.; Cho, J.; Zhang, J. G. Li-
42
43 5036 and Mn-Rich Cathode Materials: Challenges to Commercialization. **2017**, *7*, 1601284.
- 44
45
46 5037 (706) Ben Yahia, M.; Vergnet, J.; Saubanère, M.; Doublet, M.-L. Unified picture of anionic
47
48 5038 redox in Li/Na-ion batteries. *Nature Materials* **2019**, *18*, 496–502.
- 49
50
51 5039 (707) Hua, W.; Wang, S.; Knapp, M.; Leake, S. J.; Senyshyn, A.; Richter, C.; Yavuz, M.;
52
53 5040 Binder, J. R.; Grey, C. P.; Ehrenberg, H.; Indris, S.; Schwarz, B. Structural insights
54
55 5041 into the formation and voltage degradation of lithium- and manganese-rich layered
56
57 5042 oxides. *Nature Communications* **2019**, *10*, 5365.

- 1
2
3 5043 (708) Li, L.; Castro, F. C.; Park, J. S.; Li, H.; Lee, E.; Boyko, T. D.; Freeland, Z., J.
4 5044 W. and Yao; Fister, T. T.; Vinson, J.; Shirley, E. L.; Wolverton, C.; Cabana, J.;
5 5045 Dravid, V. P.; M., T. M.; Chan, M. K. Y. Probing Electrochemically Induced Struc-
6 5046 tural Evolution and Oxygen Redox Reactions in Layered Lithium Iridate. *Chem.*
7 5047 *Mater.* **2019**, *31*, 4341–4352.
- 13
14 5048 (709) Eum, D.; Kim, B.; Kim, S. J.; Park, H.; Wu, J.; Cho, S.-P.; Yoon, G.; Lee, M. H.;
15 5049 Jung, S.-K.; Yang, W., et al. Voltage decay and redox asymmetry mitigation by re-
16 5050 versible cation migration in lithium-rich layered oxide electrodes. *Nature materials*
17 5051 **2020**, *19*, 419–427.
- 22
23 5052 (710) Gent, W. E.; Abate, I. I.; Yang, W.; Nazar, L. F.; Chueh, W. C. Design Rules for
24 5053 High-Valent Redox in Intercalation Electrodes. **2020**, *4*, 1369–1397.
- 26
27 5054 (711) Sathiya, M.; Ramesha, K.; Rousse, G.; Foix, D.; Gonbeau, D.; Prakash, A. S.; Dou-
28 5055 blet, M. L.; Hemalatha, K.; Tarascon, J. M. High performance $\text{Li}_2\text{Ru}_{1-y}\text{Mn}_y\text{O}_3$ ($0.2 \leq$
29 5056 $y \leq 0.8$) cathode materials for rechargeable lithium-ion batteries: Their understand-
30 5057 ing. *Chemistry of Materials* **2013**, *25*, 1121–1131.
- 35
36 5058 (712) Xiao, R.; Li, H.; Chen, L. Density functional investigation on Li_2MnO_3 . *Chemistry of*
37 5059 *Materials* **2012**, *24*, 4242–4251.
- 39
40
41 5060 (713) Hong, J. et al. Metal–oxygen decoordination stabilizes anion redox in Li-rich oxides.
42 5061 *Nature Materials* **2019**, *18*, 256–265.
- 44
45
46 5062 (714) Davies, D. W.; Morgan, B. J.; Scanlon, D. O.; Walsh, A. Low-cost descriptors of
47 5063 electrostatic and electronic contributions to anion redox activity in batteries. *IOP*
48 5064 *SciNotes* **2020**, *1*, 024805.
- 51
52
53 5065 (715) Xiao, Y.; Liu, T.; Liu, J.; He, L.; Chen, J.; Zhang, J.; Luo, P.; Lu, H.; Wang, R.;
54 5066 Zhu, W., et al. Insight into the origin of lithium/nickel ions exchange in layered Li
55 5067 $(\text{Ni}_x\text{Mn}_y\text{Co}_z)\text{O}_2$ cathode materials. *Nano Energy* **2018**, *49*, 77–85.

- 1
2
3
4 5068 (716) Sun, H.; Zhao, K. Electronic Structure and Comparative Properties of $\text{LiNi}_x\text{Mn}_y\text{Co}_z\text{O}_2$
5
6 5069 Cathode Materials. *The Journal of Physical Chemistry C* **2017**, *121*, 6002–6010.
7
8 5070 (717) Dixit, M.; Markovsky, B.; Schipper, F.; Aurbach, D.; Major, D. T. Origin of struc-
9
10 5071 tural degradation during cycling and low thermal stability of Ni-rich layered transition
11
12 5072 metal-based electrode materials. *The Journal of Physical Chemistry C* **2017**, *121*,
13
14 5073 22628–22636.
15
16 5074 (718) Hoang, K.; Johannes, M. Defect physics and chemistry in layered mixed transition
17
18 5075 metal oxide cathode materials:(Ni, Co, Mn) vs (Ni, Co, Al). *Chemistry of Materials*
19
20 5076 **2016**, *28*, 1325–1334.
21
22
23 5077 (719) Dixit, M.; Markovsky, B.; Aurbach, D.; Major, D. T. Unraveling the effects of Al
24
25 5078 doping on the electrochemical properties of $\text{LiNi}_{0.5}\text{Co}_{0.2}\text{Mn}_{0.3}\text{O}_2$ using first principles.
26
27 5079 *Journal of The Electrochemical Society* **2017**, *164*, A6359.
28
29
30 5080 (720) Lu, Z.; Donaberger, R.; Dahn, J. Superlattice ordering of Mn, Ni, and Co in layered
31
32 5081 alkali transition metal oxides with P2, P3, and O3 structures. *Chemistry of materials*
33
34 5082 **2000**, *12*, 3583–3590.
35
36
37 5083 (721) Du, T.; Xu, B.; Wu, M.; Liu, G.; Ouyang, C. Insight into the vibrational and ther-
38
39 5084 modynamic properties of layered lithium transition-metal oxides LiMO_2 (M= Co, Ni,
40
41 5085 Mn): a first-principles study. *The Journal of Physical Chemistry C* **2016**, *120*, 5876–
42
43 5086 5882.
44
45
46 5087 (722) Shang, S.; Wang, Y.; Mei, Z.; Hui, X.; Liu, Z. Lattice dynamics, thermodynamics,
47
48 5088 and bonding strength of lithium-ion battery materials LiMPO_4 (M= Mn, Fe, Co, and
49
50 5089 Ni): a comparative first-principles study. *Journal of Materials Chemistry* **2012**, *22*,
51
52 5090 1142–1149.
53
54 5091 (723) Sagotra, A. K.; Chu, D.; Cazorla, C. Influence of lattice dynamics on lithium-ion
55
56 5092 conductivity: A first-principles study. *Physical Review Materials* **2019**, *3*, 035405.
57
58
59
60

- 1
2
3 5093 (724) Puligheddu, M.; Xia, Y.; Chan, M.; Galli, G. Computational prediction of lattice
4 thermal conductivity: A comparison of molecular dynamics and Boltzmann transport
5 5094 approaches. *Physical Review Materials* **2019**, *3*, 085401.
6
7 5095
8
9
10 5096 (725) Mattila, N.; Karttunen, A. J. Lattice thermal conductivity of NaCoO₂ and LiCoO₂
11 intercalation materials studied by hybrid density functional theory. *Materials Research*
12 5097 *Express* **2020**, *7*, 075502.
13
14 5098
15
16
17 5099 (726) Feng, T.; O'Hara, A.; Pantelides, S. T. Quantum prediction of ultra-low thermal
18 conductivity in lithium intercalation materials. *Nano Energy* **2020**, 104916.
19 5100
20
21
22 5101 (727) Qian, X.; Gu, X.; Dresselhaus, M. S.; Yang, R. Anisotropic tuning of graphite ther-
23 mal conductivity by lithium intercalation. *The Journal of Physical Chemistry Letters*
24 5102 **2016**, *7*, 4744–4750.
25
26 5103
27
28
29 5104 (728) Wei, Z.; Yang, F.; Bi, K.; Yang, J.; Chen, Y. Tunable Anisotropic Thermal Conduc-
30 tivity and Elastic Properties in Intercalated Graphite via Lithium Ions. *The Journal*
31 5105 *of Physical Chemistry C* **2018**, *122*, 1447–1455.
32 5106
33
34
35 5107 (729) Xia, Y.; Hegde, V. I.; Pal, K.; Hua, X.; Gaines, D.; Patel, S.; He, J.; Aykol, M.; Wolver-
36 ton, C. High-Throughput Study of Lattice Thermal Conductivity in Binary Rocksalt
37 5108 and Zinc Blende Compounds Including Higher-Order Anharmonicity. *Physical Review*
38 5109 *X* **2020**, *10*, 041029.
39 5110
40
41
42
43
44 5111 (730) Zhang, Q.; Uchaker, E.; Candelaria, S. L.; Cao, G. Nanomaterials for energy conversion
45 and storage. *Chemical Society Reviews* **2013**, *42*, 3127–3171.
46 5112
47
48
49 5113 (731) Kramer, D.; Ceder, G. Tailoring the morphology of LiCoO₂: a first principles study.
50 *Chemistry of Materials* **2009**, *21*, 3799–3809.
51 5114
52
53
54 5115 (732) Xu, B.; Fell, C. R.; Chi, M.; Meng, Y. S. Identifying surface structural changes in
55 layered Li-excess nickel manganese oxides in high voltage lithium ion batteries: A
56 5116
57
58
59
60

- 1
2
3
4 5117 joint experimental and theoretical study. *Energy & Environmental Science* **2011**, *4*,
5 5118 2223–2233.
6
7
8 5119 (733) Dahéron, L.; Martinez, H.; Dedryvere, R.; Baraille, I.; Ménétrier, M.; Denage, C.;
9
10 5120 Delmas, C.; Gonbeau, D. Surface properties of LiCoO₂ investigated by XPS analyses
11
12 5121 and theoretical calculations. *The Journal of Physical Chemistry C* **2009**, *113*, 5843–
13
14 5122 5852.
15
16
17 5123 (734) Kim, Y.; Lee, H.; Kang, S. First-principles and experimental investigation of the
18
19 5124 morphology of layer-structured LiNiO₂ and LiCoO₂. *Journal of Materials Chemistry*
20
21 5125 **2012**, *22*, 12874–12881.
22
23
24 5126 (735) Benedek, R.; Thackeray, M. Simulation of the surface structure of lithium manganese
25
26 5127 oxide spinel. *Physical Review B* **2011**, *83*, 195439.
27
28
29 5128 (736) Karim, A.; Fosse, S.; Persson, K. A. Surface structure and equilibrium particle shape
30
31 5129 of the LiMn₂O₄ spinel from first-principles calculations. *Physical Review B* **2013**, *87*,
32
33 5130 075322.
34
35
36 5131 (737) Leung, K. First-principles modeling of the initial stages of organic solvent decompo-
37
38 5132 sition on Li_xMn₂O₄ (100) surfaces. *The Journal of Physical Chemistry C* **2012**, *116*,
39
40 5133 9852–9861.
41
42
43 5134 (738) Tompsett, D. A.; Parker, S. C.; Bruce, P. G.; Islam, M. S. Nanostructuring of β-MnO₂:
44
45 5135 The important role of surface to bulk ion migration. *Chemistry of materials* **2013**, *25*,
46
47 5136 536–541.
48
49 5137 (739) Qian, D.; Hinuma, Y.; Chen, H.; Du, L.-S.; Carroll, K. J.; Ceder, G.; Grey, C. P.;
50
51 5138 Meng, Y. S. Electronic spin transition in nanosize stoichiometric lithium cobalt oxide.
52
53 5139 *Journal of the American Chemical Society* **2012**, *134*, 6096–6099.
54
55
56
57
58
59
60

- 1
2
3 5140 (740) Hong, L.; Hu, L.; Freeland, J. W.; Cabana, J.; Ögüt, S.; Klie, R. F. Electronic Struc-
4
5 5141 ture of LiCoO₂ Surfaces and Effect of Al Substitution. *The Journal of Physical Chem-*
6
7 5142 *istry C* **2019**, *123*, 8851–8858.
- 8
9
10 5143 (741) Abbaspour-Tamijani, A.; Bennett, J. W.; Jones, D. T.; Cartagena-Gonzalez, N.;
11
12 5144 Jones, Z. R.; Laudadio, E. D.; Hamers, R. J.; Santana, J. A.; Mason, S. E. DFT
13
14 5145 and thermodynamics calculations of surface cation release in LiCoO₂. *Applied Surface*
15
16 5146 *Science* **2020**, *515*, 145865.
- 17
18
19 5147 (742) Deng, Y.-P.; Yin, Z.-W.; Wu, Z.-G.; Zhang, S.-J.; Fu, F.; Zhang, T.; Li, J.-
20
21 5148 T.; Huang, L.; Sun, S.-G. Layered/spinel heterostructured and hierarchical mi-
22
23 5149 cro/nanostructured Li-rich cathode materials with enhanced electrochemical prop-
24
25 5150 erties for Li-ion batteries. *ACS applied materials & interfaces* **2017**, *9*, 21065–21070.
- 26
27
28 5151 (743) Deng, Y.-P.; Fu, F.; Wu, Z.-G.; Yin, Z.-W.; Zhang, T.; Li, J.-T.; Huang, L.; Sun, S.-G.
29
30 5152 Layered/spinel heterostructured Li-rich materials synthesized by a one-step solvother-
31
32 5153 mal strategy with enhanced electrochemical performance for Li-ion batteries. *Journal*
33
34 5154 *of Materials Chemistry A* **2016**, *4*, 257–263.
- 35
36
37 5155 (744) Long, B. R.; Croy, J. R.; Park, J. S.; Wen, J.; Miller, D. J.; Thackeray, M. M. Advances
38
39 5156 in stabilizing ‘layered-layered’ xLi₂MnO₃·(1-x)LiMO₂ (M= Mn, Ni, Co) electrodes
40
41 5157 with a spinel component. *Journal of the Electrochemical Society* **2014**, *161*, A2160.
- 42
43
44 5158 (745) Wang, D.; Belharouak, I.; Zhou, G.; Amine, K. Nanoarchitecture multi-structural
45
46 5159 cathode materials for high capacity lithium batteries. *Advanced Functional Materials*
47
48 5160 **2013**, *23*, 1070–1075.
- 49
50 5161 (746) Warburton, R. E.; Castro, F. C.; Deshpande, S.; Madsen, K. E.; Bassett, K. L.;
51
52 5162 Dos Reis, R.; Gewirth, A. A.; Dravid, V. P.; Greeley, J. Oriented LiMn₂O₄ Particle
53
54 5163 Fracture from Delithiation-Driven Surface Stress. *ACS applied materials & interfaces*
55
56 5164 **2020**, *12*, 49182–49191.

- 1
2
3 5165 (747) Liang, C.; Longo, R. C.; Kong, F.; Zhang, C.; Nie, Y.; Zheng, Y.; Cho, K. Ab
4
5 5166 Initio Study on Surface Segregation and Anisotropy of Ni-Rich $\text{LiNi}_{1-2y}\text{Co}_y\text{Mn}_y\text{O}_2$
6
7 5167 (NCM)($y \leq 0.1$) Cathodes. *ACS applied materials & interfaces* **2018**, *10*, 6673–6680.
8
9
10 5168 (748) Chen, G.; Song, X.; Richardson, T. J. Electron microscopy study of the LiFePO_4 to
11
12 5169 FePO_4 phase transition. *Electrochemical and Solid State Letters* **2006**, *9*, A295.
13
14
15 5170 (749) Islam, M. S. Recent atomistic modelling studies of energy materials: batteries in-
16
17 5171 cluded. *Philosophical Transactions of the Royal Society A: Mathematical, Physical*
18
19 5172 *and Engineering Sciences* **2010**, *368*, 3255–3267.
20
21
22 5173 (750) Tankhilsaikhon, B.; Gorfman, S.; Tungalag, N.; Tuvjargal, N.; Davaasambuu, J.;
23
24 5174 Pietsch, U. *Solid State Phenomena*; 2019; Vol. 288; pp 98–103.
25
26
27 5175 (751) Xu, G.; Zhong, K.; Yang, Y.; Zhang, J.-M.; Huang, Z. Insight into delithiation process
28
29 5176 on the LiFePO_4 (010) surface from a novel viewpoint of the work function. *Solid State*
30
31 5177 *Ionics* **2019**, *338*, 25–30.
32
33
34 5178 (752) Zhang, Y.; Alarco, J. A.; Nerkar, J. Y.; Best, A. S.; Snook, G. A.; Talbot, P. C.;
35
36 5179 Cowie, B. C. Observation of preferential cation doping on the surface of LiFePO_4
37
38 5180 particles and its effect on properties. *ACS Applied Energy Materials* **2020**, *3*, 9158–
39
40 5181 9167.
41
42
43 5182 (753) Li, Y.; Chen, H.; Lim, K.; Deng, H. D.; Lim, J.; Fraggedakis, D.; Attia, P. M.;
44
45 5183 Lee, S. C.; Jin, N.; Moškon, J., et al. Fluid-enhanced surface diffusion controls intra-
46
47 5184 particle phase transformations. *Nature materials* **2018**, *17*, 915–922.
48
49
50 5185 (754) Edström, K.; Gustafsson, T.; Thomas, J. O. The cathode-electrolyte interface in the
51
52 5186 Li-ion battery. *Electrochimica Acta* **2004**, *50*, 397–403.
53
54
55 5187 (755) Bhandari, A.; Bhattacharya, J.; Pala, R. G. S. Adsorption Preference of HF over
56
57 5188 Ethylene Carbonate Leads to Dominant Presence of Fluoride Products in LiFePO_4
58
59
60

- 1
2
3
4 5189 Cathode–Electrolyte Interface in Li-Ion Batteries. *The Journal of Physical Chemistry*
5 5190 *C* **2020**, *124*, 9170–9177.
6
7
8 5191 (756) Tebbe, J. L.; Fuerst, T. F.; Musgrave, C. B. Mechanism of hydrofluoric acid forma-
9
10 5192 tion in ethylene carbonate electrolytes with fluorine salt additives. *Journal of Power*
11
12 5193 *Sources* **2015**, *297*, 427–435.
13
14
15 5194 (757) Tebbe, J. L.; Holder, A. M.; Musgrave, C. B. Mechanisms of LiCoO₂ Cathode Degrada-
16
17 5195 tion by Reaction with HF and Protection by Thin Oxide Coatings. *ACS Applied*
18
19 5196 *Materials and Interfaces* **2015**, *7*, 24265–24278.
20
21
22 5197 (758) Bhandari, A.; Gupta, P. K.; Bhattacharya, J.; Pala, R. G. S. Higher Energy Barrier
23
24 5198 for Interfacial Li-Ion Transfer from EC/LiPF₆ Electrolyte into (010) LiFePO₄ Cathode
25
26 5199 Surface than Bulk Li-Ion Diffusion within Both Cathode and Electrolyte. *Journal of*
27
28 5200 *The Electrochemical Society* **2019**, *166*, A2966–A2972.
29
30
31 5201 (759) Tebbe, J. L.; Fuerst, T. F.; Musgrave, C. B. Degradation of Ethylene Carbonate
32
33 5202 Electrolytes of Lithium Ion Batteries via Ring Opening Activated by LiCoO₂ Cath-
34
35 5203 ode Surfaces and Electrolyte Species. *ACS Applied Materials and Interfaces* **2016**, *8*,
36
37 5204 26664–26674.
38
39 5205 (760) Xu, S.; Luo, G.; Jacobs, R.; Fang, S.; Mahanthappa, M. K.; Hamers, R. J.; Morgan, D.
40
41 5206 Ab Initio Modeling of Electrolyte Molecule Ethylene Carbonate Decomposition Reac-
42
43 5207 tion on Li(Ni,Mn,Co)O₂ Cathode Surface. *ACS Applied Materials & Interfaces* **2017**,
44
45 5208 *9*, 20545–20553.
46
47
48 5209 (761) Malmgren, S.; Rensmo, H.; Gustafsson, T.; Gorgoi, M.; Edström, K. Non-destructive
49
50 5210 depth profiling of the solid electrolyte interphase on LiFePO₄ and graphite electrodes.
51
52 5211 *ECS Transactions* **2010**, *25*, 201–210.
53
54
55 5212 (762) Dathar, G. K. P.; Sheppard, D.; Stevenson, K. J.; Henkelman, G. Calculations of
56
57 5213 Li-Ion Diffusion in Olivine Phosphates. *Chemistry of Materials* **2011**, *23*, 4032–4037.
58
59
60

- 1
2
3 5214 (763) Li, W.; Erickson, E. M.; Manthiram, A. High-nickel layered oxide cathodes for lithium-
4 based automotive batteries. *Nature Energy* **2020**, *5*, 26–34.
5 5215
6
7
8 5216 (764) Li, W.; Dolocan, A.; Oh, P.; Celio, H.; Park, S.; Cho, J.; Manthiram, A. Dynamic
9 behaviour of interphases and its implication on high-energy-density cathode materials
10 5217 in lithium-ion batteries. *Nature communications* **2017**, *8*, 1–10.
11 5218
12
13
14
15 5219 (765) Li, W.; Liu, X.; Celio, H.; Smith, P.; Dolocan, A.; Chi, M.; Manthiram, A. Mn versus
16 Al in layered oxide cathodes in lithium-ion batteries: a comprehensive evaluation on
17 5220 long-term cyclability. *Advanced Energy Materials* **2018**, *8*, 1703154.
18 5221
19
20
21
22 5222 (766) Middlemiss, L. A.; Rennie, A. J.; Sayers, R.; West, A. R. Characterisation of batteries
23 by electrochemical impedance spectroscopy. *Energy Reports* **2020**, *6*, 232–241.
24 5223
25
26
27 5224 (767) Li, J.; Murphy, E.; Winnick, J.; Kohl, P. Studies on the cycle life of commercial lithium
28 ion batteries during rapid charge–discharge cycling. *Journal of Power Sources* **2001**,
29 5225 *102*, 294–301.
30 5226
31
32
33 5227 (768) Song, J.; Lee, H.; Wang, Y.; Wan, C. Two-and three-electrode impedance spectroscopy
34 of lithium-ion batteries. *Journal of Power Sources* **2002**, *111*, 255–267.
35 5228
36
37
38 5229 (769) McTurk, E.; Birkl, C. R.; Roberts, M. R.; Howey, D. A.; Bruce, P. G. Minimally
39 Invasive Insertion of Reference Electrodes into Commercial Lithium-Ion Pouch Cells.
40 5230 *ECS Electrochemistry Letters* **2015**, *4*, A145–A147.
41 5231
42
43
44
45 5232 (770) Belt, J. R.; Bernardi, D. M.; Utgikar, V. Development and Use of a Lithium-Metal
46 Reference Electrode in Aging Studies of Lithium-Ion Batteries. *Journal of The Elec-*
47 5233 *trochemical Society* **2014**, *161*, A1116–A1126.
48 5234
49
50
51
52 5235 (771) Li, J.; Manthiram, A. A Comprehensive Analysis of the Interphasial and Structural
53 Evolution over Long-Term Cycling of Ultrahigh-Nickel Cathodes in Lithium-Ion Bat-
54 5236 teries. *Advanced Energy Materials* **2019**, *9*, 1902731.
55
56 5237
57
58
59
60

- 1
2
3 5238 (772) Kim, J.-S.; Johnson, C. S.; Vaughey, J. T.; Thackeray, M. M.; Hackney, S. A.;
4
5 5239 Yoon, W.; Grey, C. P. Electrochemical and Structural Properties of $x\text{Li}_2\text{M}'\text{O}_3 \cdot (1 -$
6
7 5240 $x)\text{LiMn}_{0.5}\text{Ni}_{0.5}\text{O}_2$ Electrodes for Lithium Batteries ($\text{M}' = \text{Ti, Mn, Zr}$; $0 \leq x \leq 0.3$).
8
9 5241 *Chemistry of Materials* **2004**, *16*, 1996–2006.
- 11
12 5242 (773) Armstrong, A. R.; Holzapfel, M.; Novák, P.; Johnson, C. S.; Kang, S.-H.; Thack-
13
14 5243 eray, M. M.; Bruce, P. G. Demonstrating oxygen loss and associated structural reorga-
15
16 5244 nization in the lithium battery cathode $\text{Li}[\text{Ni}_{0.2}\text{Li}_{0.2}\text{Mn}_{0.6}]\text{O}_2$. *Journal of the American*
17
18 5245 *Chemical Society* **2006**, *128*, 8694–8698.
- 19
20
21 5246 (774) Bhandari, A.; Bhattacharya, J. Review—Manganese Dissolution from Spinel Cathode:
22
23 5247 Few Unanswered Questions. *Journal of The Electrochemical Society* **2016**, *164*, A106–
24
25 5248 A127.
- 26
27 5249 (775) Nakayama, K.; Ishikawa, R.; Kobayashi, S.; Shibata, N.; Ikuhara, Y. Dislocation and
28
29 5250 oxygen-release driven delithiation in Li_2MnO_3 . *Nature Communications* **2020**, *11*,
30
31 5251 4452.
- 32
33
34 5252 (776) Deringer, V. L.; Caro, M. A.; Csányi, G. Machine learning interatomic potentials as
35
36 5253 emerging tools for materials science. *Advanced Materials* **2019**, *31*, 1902765.
- 37
38
39 5254 (777) Assat, G.; Glazier, S. L.; Delacourt, C.; Tarascon, J.-M. Probing the thermal effects
40
41 5255 of voltage hysteresis in anionic redox-based lithium-rich cathodes using isothermal
42
43 5256 calorimetry. *Nature Energy* **2019**, *4*, 647–656.
- 44
45
46 5257 (778) Grimsmann, F.; Brauchle, F.; Gerbert, T.; Gruhle, A.; Knipper, M.; Parisi, J. Hystere-
47
48 5258 sis and current dependence of the thickness change of lithium-ion cells with graphite
49
50 5259 anode. *Journal of Energy Storage* **2017**, *12*, 132–137.
- 51
52
53 5260 (779) Zheng, T.; McKinnon, W. R.; Dahn, J. R. Hysteresis during Lithium Insertion in
54
55 5261 Hydrogen-Containing Carbons. *Journal of The Electrochemical Society* **1996**, *143*,
56
57 5262 2137–2145.

- 1
2
3 5263 (780) Edge, J. S.; O’Kane, S.; Prosser, R.; Kirkaldy, N. D.; Patel, A. N.; Hales, A.; Ghosh, A.;
4
5 5264 Ai, W.; Chen, J.; Jiang, J., et al. Lithium ion battery degradation: what you need to
6
7 5265 know. *Physical Chemistry Chemical Physics* **2021**, *23*, 8200–8221.
8
9
10 5266 (781) Birkel, C. R.; Roberts, M. R.; McTurk, E.; Bruce, P. G.; Howey, D. A. Degradation
11
12 5267 diagnostics for lithium ion cells. *Journal of Power Sources* **2017**, *341*, 373–386.
13
14
15 5268 (782) Zülke, A.; Li, Y.; Keil, P.; Burrell, R.; Belaisch, S.; Nagarathinam, M.; Mercer, M. P.;
16
17 5269 Hoster, H. E. High-Energy Nickel-Cobalt-Aluminium Oxide (NCA) Cells on Idle:
18
19 5270 Anode- versus Cathode-Driven Side Reactions. *Batteries & Supercaps* **2021**, *4*, 934–
20
21 5271 947.
22
23
24 5272 (783) Symington, A. R.; Molinari, M.; Dawson, J. A.; Statham, J. M.; Purton, J.; Canepa, P.;
25
26 5273 Parker, S. C. Elucidating the nature of grain boundary resistance in lithium lanthanum
27
28 5274 titanate. *Journal of Materials Chemistry A* **2021**, *9*, 6487–6498.
29
30
31 5275 (784) Vicent-Luna, J. M.; Ortiz-Roldan, J. M.; Hamad, S.; Tena-Zaera, R.; Calero, S.;
32
33 5276 Anta, J. A. Quantum and classical molecular dynamics of ionic liquid elec-
34
35 5277 trolytes for Na/Li-based batteries: molecular origins of the conductivity behavior.
36
37 5278 *ChemPhysChem* **2016**, *17*, 2473–2481.
38
39
40 5279 (785) Choi, Y.-S.; Park, J.-H.; Ahn, J.-P.; Lee, J.-C. Interfacial reactions in the Li/Si diffu-
41
42 5280 sion couples: origin of anisotropic lithiation of crystalline Si in Li–Si batteries. *Scien-
43
44 5281 tific reports* **2017**, *7*, 1–9.
45
46
47
48
49
50
51
52
53
54
55
56
57
58
59
60